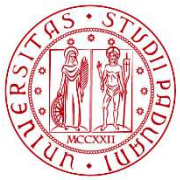

UNIVERSITÀ
DEGLI STUDI
DI PADOVA

Sede Amministrativa: Università degli Studi di Padova

Dipartimento di Ingegneria Industriale

CORSO DI DOTTORATO DI RICERCA IN INGEGNERIA INDUSTRIALE
CURRICOLO: INGEGNERIA DELL'ENERGIA
CICLO XXIX

THEORETICAL AND EXPERIMENTAL STUDY OF ENHANCED HEAT EXCHANGERS FOR AIR CONDITIONING APPLICATIONS

Tesi redatta con il contributo finanziario di Eurapo S.r.l.

Coordinatore: Ch.mo Prof. Paolo Colombo

Supervisore: Ch.mo Prof. Davide Del Col

Dottorando: Marco Rossato


Volume Primo
Parte Prima
Capitolo I
Pagina 1
11-24
CHE PARTENZA!
Schulz

Contents

List of figures

List of tables

Abstract

Nowadays the use of different techniques for the performance enhancement of heat exchangers is widespread and plays an important role in the design of energy systems.
This work focuses on the study of heat exchangers that use extended surfaces to increase the heat transfer coefficient and the heat transfer area of water-to-air, refrigerant-to-air and water-to-refrigerant units.
This work has been possible thanks to the financial support of Eurapo S.r.l.

The present thesis is divided in five Chapters. The first Chapter presents the experimental activity performed in the laboratory of Eurapo S.r.l. in order to determine the thermal performance of a water/air finned tube heat exchanger with three rows and 12 tubes per row. This HX has been tested varying the inlet conditions of water and air, simulating the working conditions in winter (only sensible heat transfer) and summer (sensible and latent heat transfer on the air side when dehumidification is present). Moreover, the same unit has been tested with three different inclination angles with respect to the direction of air flow, in order to investigate the effect of the tilt angle on the thermal performance in devices such as fan coils. Similar tests have been performed also in an enthalpy tunnel, which allowed the measurement of air volumetric flow rate during the heat transfer. This is particularly interesting in order to understand the influence of the condensate moisture and of the tilt angle on the pressure drop, which affects the air mass flow rate and the total heat flow rate exchanged.
The second Chapter reports the experimental activity performed with the aim to investigate the performance of a multiple aluminium minichannels heat exchanger working as evaporator and condenser. A special prototype has been designed, built and instrumented in order to measure pressure drop and quasi local heat transfer coefficient during single and two phase flow with different working fluids having low Global Warming Potential (GWP) as R32 and R1234ze(E). This prototype can be considered as a module of a bar-and-plate heat exchanger, which is an innovative solution for air conditioning applications. The results of these measurements have been compared with the prediction of several literature correlations.
In the third Chapter, a model has been developed in Matlab® to evaluate the thermal performance of finned tubes heat exchangers working with water inside and air outside the tubes. The model divides the heat exchanger in several elements that represent a small length of tube with the corresponding fins attached, and it is able to simulate different circuitries working with and without dehumidification. The heat transfer coefficients on the water and on the air side can be calculated respectively with two and eight different correlations. Using the experimental data obtained during the activity described in Chapter one, it was possible to assess the best predictive correlations for the heat transfer coefficient in the tested finned coil.
A model for a finned coil evaporator was also developed in the fourth Chapter. The model is able to simulate the behaviour of finned tubes heat exchangers working with a refrigerant fluid that evaporates inside the tubes. This allows to evaluate the performance of a dehumidification device working as the evaporator of an inverse cycle machine.
The last Chapter reports the numerical models developed in Matlab® to simulate the performance of bar-and-plate heat exchangers working as evaporators and condensers in refrigerant/water devices.

The experimental analysis reported in the second Chapter allowed to choose the best predictive correlations, while the results of experimental tests on direct expansion systems provided by a different laboratory are used to validate the models.

Sommario

Al giorno d'oggi vi è un crescente interesse all'uso di diverse tecniche per il miglioramento delle prestazioni termiche degli scambiatori di calore e alla progettazione ottimale di sistemi energetici.
Questo lavoro si concentra sullo studio di scambiatori di calore che utilizzano superfici estese per aumentare il coefficiente di scambio termico e l'area di scambio per unità acqua-aria, refrigerante-aria ed acqua-refrigerante.
Questo lavoro è stato possibile grazie al sostegno finanziario di Eurapo S.r.l.

La presente tesi è divisa in cinque Capitoli.
Il primo Capitolo presenta l'attività sperimentale eseguita nel laboratorio di Eurapo S.r.l. su uno scambiatore di calore alettato acqua/aria con tre ranghi e 12 tubi per rango con l'obiettivo di determinarne le prestazioni. Questo scambiatore è stato testato variando le condizioni di ingresso di acqua e aria, simulando le condizioni di lavoro in inverno (solo trasferimento di calore sensibile) e in estate (trasferimento di calore sensibile e latente sul lato aria in presenza di deumidificazione). Inoltre, la stessa unità è stata testata con tre differenti angoli di inclinazione rispetto alla direzione del flusso d'aria, al fine di studiare l'effetto di inclinazione sulle prestazioni termiche in dispositivi quali i ventilconvettori. Le stesse condizioni sono state testate anche in un tunnel entalpico, che ha permesso la misura della portata volumetrica d'aria durante lo scambio termico. Ciò è particolarmente interessante per comprendere l'influenza della portata di condensato e dell'inclinazione sulla caduta di pressione nella batteria alettata, che si riflette nella portata massica di aria e nella portata totale di calore scambiato.
Il secondo Capitolo riporta l'attività sperimentale effettuata per indagare le prestazioni di scambiatori a minicanali in alluminio usati come evaporatori e condensatori. Uno speciale prototipo è stato progettato, costruito e strumentato per misurare la caduta di pressione e il coefficiente di scambio termico quasi-locale durante il deflusso monofase e bifase con diversi fluidi a basso potenziale di riscaldamento globale (GWP) come R32 e R1234ze (E). Questa sezione di prova può essere considerata come un modulo di uno scambiatore di calore bar-and-plate, che è una soluzione innovativa per applicazioni di condizionamento. I risultati di tali misurazioni sono state confrontate con la previsione di numerose correlazioni presenti in letteratura.
Nel terzo Capitolo, è stato sviluppato un modello in Matlab® per valutare le prestazioni termiche di scambiatori di calore a tubi alettati che operano con acqua interna ed aria esterna. Il modello divide lo scambiatore in diversi elementi che rappresentano un piccolo tratto di tubo con le corrispondenti alette, ed è in grado di simulare diverse circuitazioni, con e senza deumidificazione. I coefficienti di scambio termico lato acqua e lato aria vengono calcolati rispettivamente con due e otto correlazioni differenti. Utilizzando i dati sperimentali ottenuti durante l'attività descritta nel primo capitolo, è stato possibile valutare le correlazioni che meglio predicono il coefficiente di scambio termico nella batteria alettata.
Il quarto Capitolo mostra un modello numerico sviluppato per evaporatori a batteria alettata. Questo simula il comportamento di scambiatori di calore a tubi alettati operanti con un fluido frigorigeno che evapora all'interno dei tubi. Questo permette di valutare le prestazioni di sistemi di deumidificazione con macchina a ciclo inverso.

L'ultimo Capitolo riporta i modelli numerici sviluppati in Matlab® per simulare le prestazioni di scambiatori di calore tipo bar-and-plate utilizzati come evaporatori e condensatori in dispositivi refrigerante/acqua. L'analisi sperimentale riportata nel secondo Capitolo ha permesso di scegliere le migliori correlazioni predittive, mentre i risultati delle prove sperimentali effettuate su sistemi ad espansione diretta in un laboratorio differente sono utilizzati per convalidare i modelli.

Introduction

The enhancement of heat transfer plays an important role in the development of air conditioning and refrigeration equipment able to meet the customers request for cheaper, smaller and higher performance systems. There are several techniques to enhance the heat transfer, which are usually divided in active and passive ones, and the number of technical publications and patents in this field shows that both academic and industry have a strong interest in products and systems incorporating enhancement technology.

In air-to-water systems, the use of finned tube heat exchangers (HXs) is widespread and semi-empirical correlations specifically developed for these geometries allow to predict very well the thermal performance of these devices in dry conditions. When the water temperature is lower than the dew point temperature of air, dehumidification occurs and the correlations need to take into account the combined heat and mass transfer. In this case, the process is more complex. Minichannels heat exchangers are another type of compact heat exchangers that use high surface-to-volume ratios to improve their performance. A particular type of them, bar-and-plate HXs, has been used in water-to-compressed air HXs for years, but it has not been employed with an evaporating or a condensing refrigerant.

In the present thesis, the first part experimentally investigates the thermal performance of air-to-water finned tube HXs and bar-and-plate HXs during single and two-phase flow. The experimental activity reported in the first part paves the way for the subsequent development of numerical models able to predict the behaviour of these HXs. Air-to-water, air-to-refrigerant and water-to-refrigerant heat exchangers are considered. The models of finned tube HXs work with and without dehumidification and their structures allow to catch the influence of the circuitry on the thermal performance.

Besides the thermal performance of the systems, there is an increasing interest in refrigerants with a low Global Warming Potential (GWP), because the legislation imposes some limits regarding the GWP of the working fluid and on its amount in the system. This is due to the effect that high GWP substances have on earth climate. The Fourth Assessment Report of the Intergovernmental Panel on Climate Change of the United Nations Framework Convention on Climate Change, stated that, on the basis of existing scientific data, developed countries would need to reduce greenhouse gas emissions by 80 % to 95 % below 1990 levels by 2050 to limit global climate change to a temperature increase of 2 °C and thus prevent undesirable climate effects. The search for alternatives focuses on natural refrigerants and new synthetic refrigerants with low GWP. Natural refrigerants are often toxic (ammonia) or flammable (hydrocarbons) or present some challenges in the design of the system because of their properties (carbon dioxide, water…).

Therefore in the present thesis, we choose to perform the two-phase flow experiments with two low GWP refrigerant, R32 and R1234ze(E). R32 (GWP=675) is a non-toxic fluid that can be used to replace the commonly used refrigerant R410A in air conditioning and heat pump applications. This fluid has interesting properties as a refrigerant, but its flammability now (A2 category of ASHRAE Safety Group) and GWP in the future could limit its applications.

R1234ze(E) has a GWP lower than one, thus it can be considered a long term solution as a replacement for R134a in air conditioning applications, but its thermal performance is lower than that of R32.

1 Heat transfer in air-water heat exchangers: experimentation

1.1 Introduction

In air conditioning applications that use conventional heat exchangers, the thermal resistance in the air side is much bigger than the thermal resistance of the water side. Thus, it is very important to enhance the heat transfer coefficient on the airside. The aims of enhancement techniques is to reduce the volume of the heat exchanger for a given duty, to increase the capacity of an existing heat exchanger and to reduce the approach temperature difference. In a finned tube heat exchanger, round tubes are commonly used and fins are employed either on the outside or on the inside (or both). There are different types of finned coil heat exchangers: the most common in engineering applications are circular fins and flat fins. In this Chapter, a flat fins heat exchanger will be considered.

1.2 Experimental apparatus and test section

In order to obtain experimental data to investigate the performance of these type of heat exchangers, some tests have been performed on a single finned tube HX in the laboratory of Eurapo S.r.l., where a climatic chamber, an enthalpy tunnel and two reverberation rooms are present.

Climatic chamber

The climatic chamber present in the laboratory of Eurapo S.r.l. has been designed to test hydronic systems for air treatment with heat flow rate in the range 0.5 kW – 40 kW during heating (reference conditions: t_{air} = 20°C – UR_{air} = 50%) and 0.5 – 30 kW during cooling with dehumidification (reference conditions: t_{air} = 27°C – UR_{air} = 48%). Tests are performed according to regulation EN 1397:2001 and to standard Eurovent 6/3 (“Thermal test method for fan coil units”) and 6/11 (“Thermal test method for ducted fan coil units”).

Enthalpy tunnel and aeraulic tunnel

In the laboratory of Eurapo S.r.l. two aeraulic tunnels are present: the smaller one measures volumetric flow rate of air ranging between 100 m³/h and 2500 m³/h, while the range of the bigger one is from 120 m³/h to 6000 m³/h. A variable exhaust system allows to increase the pressure drop at the outlet of the tunnel in order to simulate a back pressure in the system due to the piping in the real installation site. The aeraulic tunnels perform the air flow measurement in agreement with the ISO 5801 standard and the standard Eurovent 6/10 (“Air flow test method for ducted fan coil units”). The goal of these two devices is to measure the air flow rate, the absorbed electrical power and the efficiency of different types of fans working with different fan speeds and back pressures at the outlet of the unit.

Connecting the aeraulic tunnel with the climatic chamber is possible to measure the mass flow rate of air during the heat transfer process. In this configuration, the apparatus is also known as enthalpy tunnel, and is of particular interest for the measurement of air flow in summer condition, when the coil is wet and the condensate moisture can block the air passage, causing an additional pressure drop that lead to a different working point for the fan, thus to a different thermal performance of the unit.

Figure 1.1 shows a picture of the fan coil unit installed in the climatic chamber and connected to the aeraulic tunnel for the tests. At the inlet of the fan coil, a sampling tube allows the measurements of temperature and relative humidity of air. Connected to the side of the unit, the inlet and outlet water tubes are visible, with temperature and pressure drop sensors attached close to the unit.
After the plenum, the air enters the aeraulic tunnel, where settling means reduce the turbulence and another sampling tube enables the measurements of temperature and relative humidity of air (Figure 1.2). The core of the aeraulic tunnel is composed by the nozzles, shown in Figure 1.3a: here the air flowing through the small passage area determines a pressure drop that is related to the volumetric flow rate of air. An automatic system to open and close the nozzles (Figure 1.3b) allows to select the proper nozzles for each air flow rate.

Figure 1.1. Experimental set up: climatic chamber with the tested machine connected to the aeraulic tunnel through a plenum.

Figure 1.2. Air sampling tube for the measurement of temperature and humidity of air in the aeraulic tunnel.

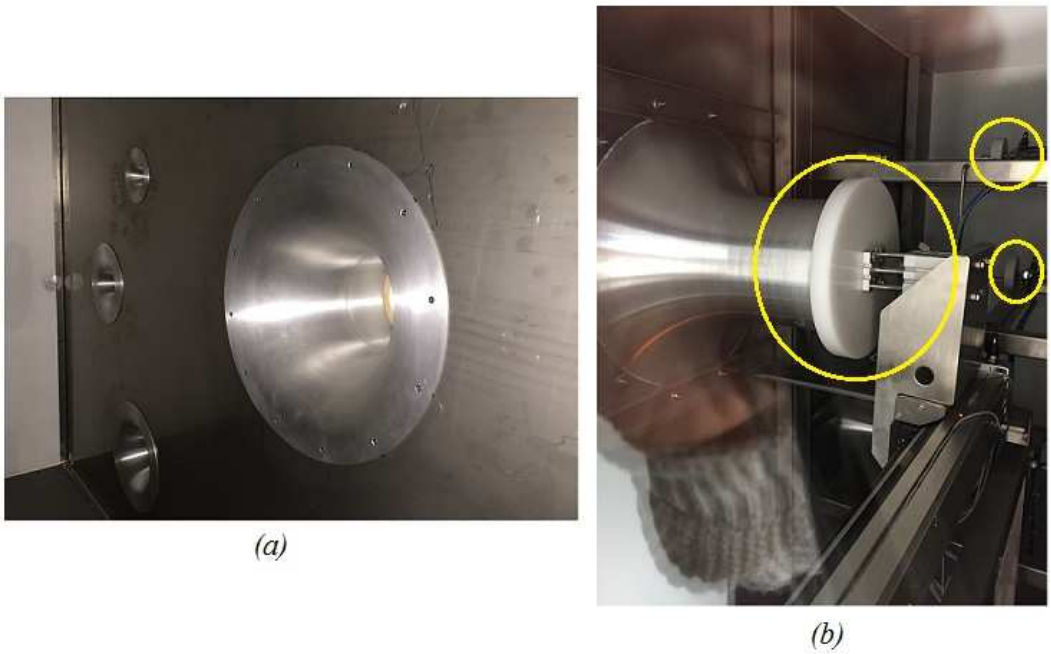

Figure 1.3. (a) Nozzles for air flow rate measurement in the aeraulic tunnel. (b) Automatic system to open and close the nozzles.

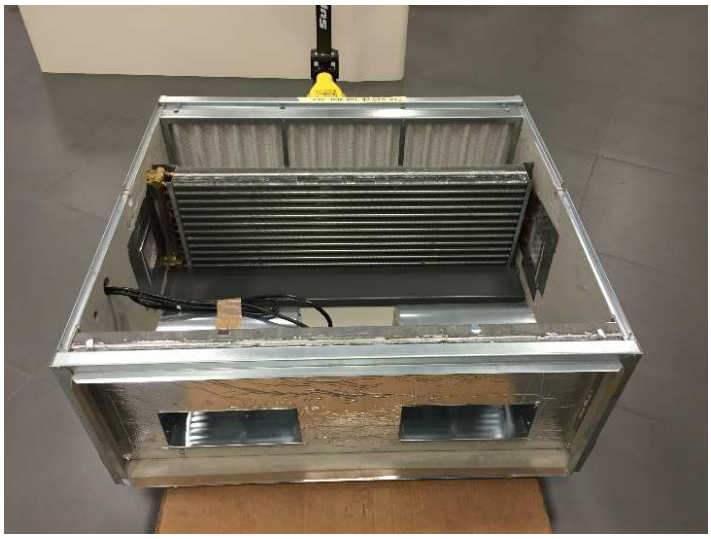

Figure 1.4. Tested machine (EBH 020-3R) with three rows heat exchanger.

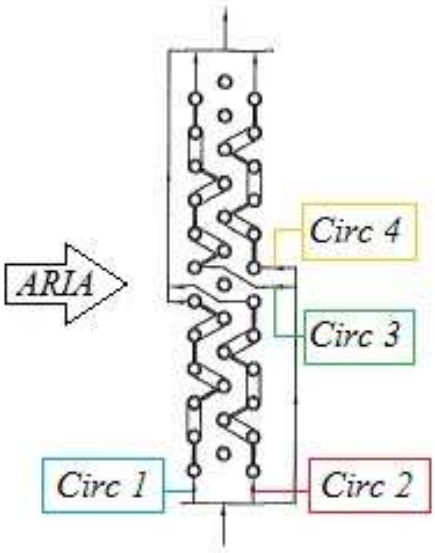

Figure 1.5. Real circuitry of the tested heat exchanger (EBH 020-3R).

Test section

The finned coil heat exchanger tested is EBH 020 – 3R, which has a standard configuration with three row with twelve tubes each, four circuit for water, copper tubes and aluminium fins. Two centrifugal fans let the air flowing with three possible speeds. A picture of the tested unit is reported in Figure 1.4. Under the heat exchanger, the condensate is drained and sent to a balance to obtain its weight during the test. Dividing the condensate weight by the scan time of the test is possible to determine the mass flow rate of condensate moisture and the latent heat flow rate during the test.
Figure 1.5 shows a schematic of the water circuitry of the tested heat exchanger.
In order to measure the temperature distribution of air after the heat exchanger, 10 T-type thermocouples have been installed as reported in Figure 1.6 and Figure 1.7. Eight thermocouples are positioned along the vertical axis of the heat exchanger, where the main differences in temperature occurs, while the other two thermocouples are placed at the same height, in the lateral parts of the outlet section, to check for possible maldistribution of air.

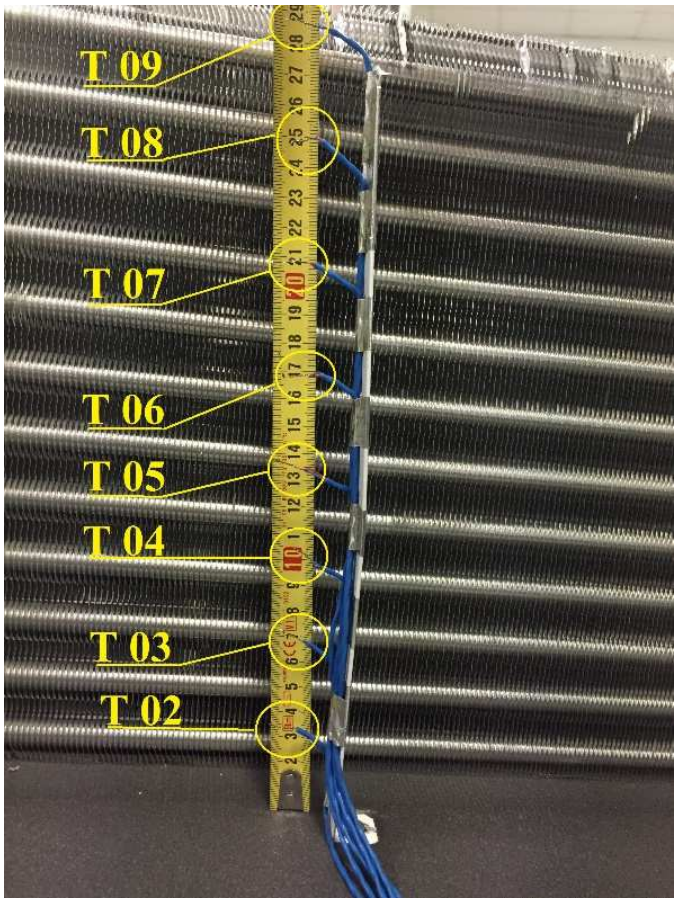

Figure 1.6. Position of thermocouples (T 02 – T 09) used to measure the trend of air temperature at the outlet.

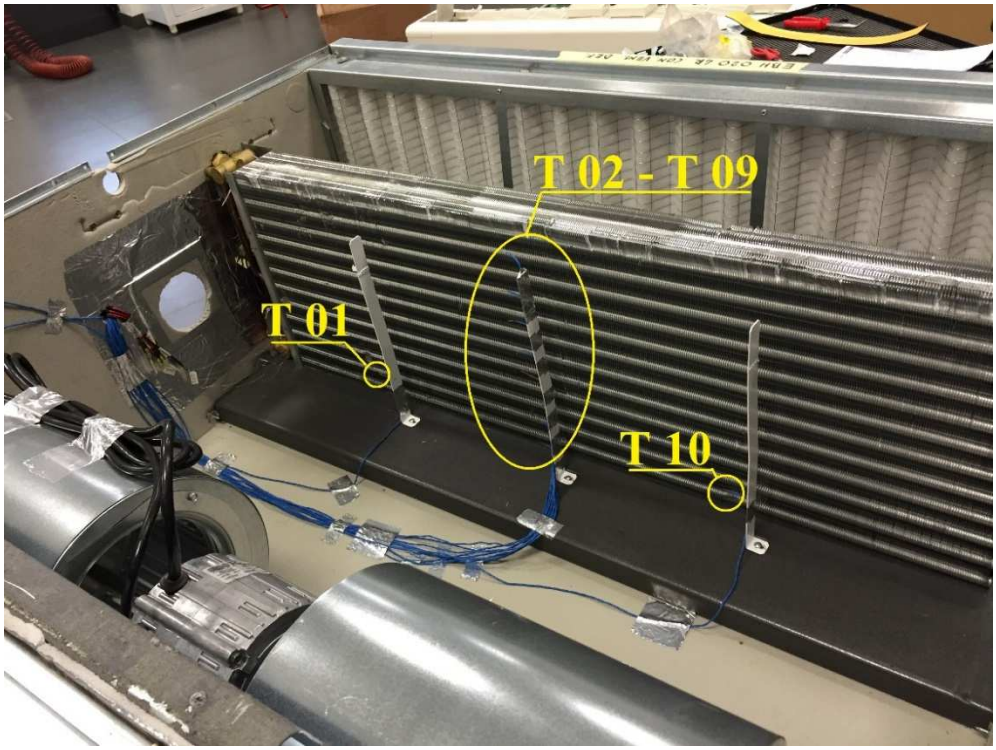

Figure 1.7. Position of all thermocouples (T 01 – T 10) used to measure the trend of air temperature at the outlet.

During the tests in summer conditions, a differential pressure transducer has been installed in order to measure the pressure drop in the heat exchanger on the air side.
The considered finned coil is characterized by a staggered pipe arrangement in the direction of air motion. The main dimensions of the finned coil heat exchanger are available in Table 1.1 and schematically reported in Figure 1.8. In the tested unit, the air flow is maintained by mean of a centrifugal fan with a voltage regulator that allows three different air velocities.
Table 1.2 reports the experimental uncertainty of the different parameters measured during the tests.

Table 1.1. Dimensions of the tested finned tube heat exchanger (EBH 020 – 3R).

Number of Rows	[-]	N_R	3
Number of tubes in each row	[-]	N_t	12
Tube's length	[m]	L	0.875
Fin pitch	[m]	X_f	0.0021
Longitudinal tube pitch	[m]	X_l	0.022
Transverse tube pitch	[m]	X_t	0.025
Fin thickness	[m]	s_f	0.0001
Tube's external diameter	[m]	D_e	0.01009
Tube thickness	[m]	s_t	0.00028
Area on air side	[m²]	A_e	15.03
Area inside tubes	[m²]	A_i	0.943

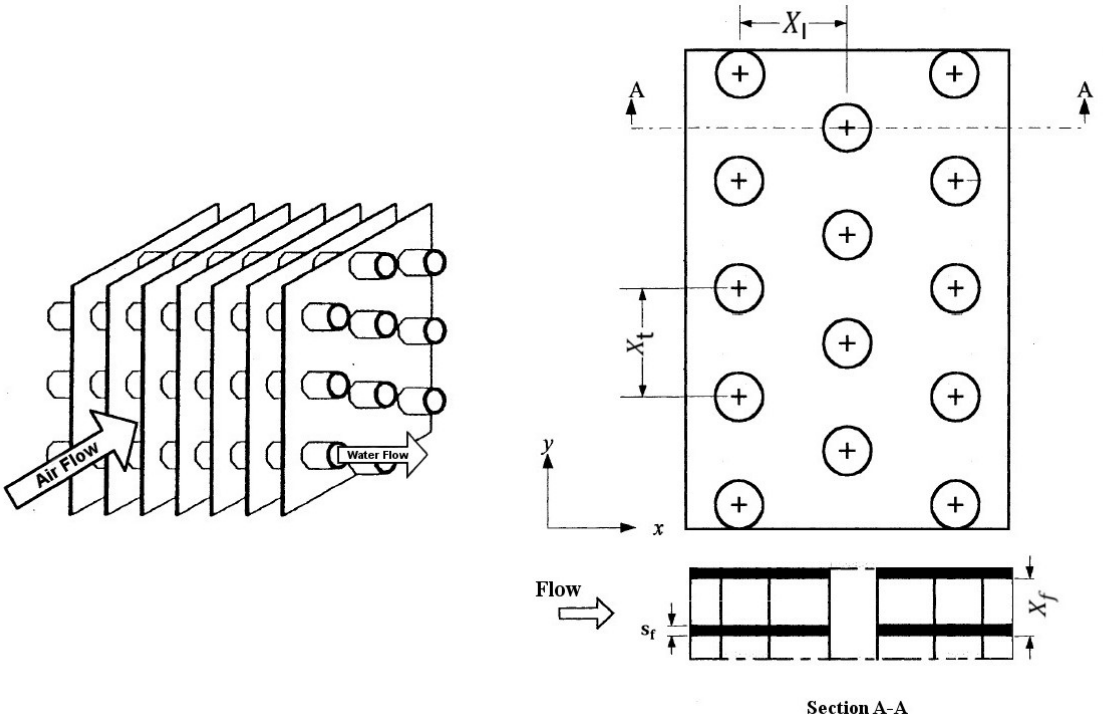

Figure 1.8. Schematic of a finned tube heat exchanger.

Table 1.2. Experimental uncertainty of measured parameters.

	Measured parameter	**Uncertainty**
Air side		
T type thermocouples	Air temperature at the outlet	±0.4 K
Chilled mirror hygrometer	Dew temperature of air at the outlet	±0.2 K
RH capacitive transducer	RH of air in the climatic chamber	±2%
Balance	Condensate weight	±5 g
PT100	Climatic chamber temperature	±0.1 K
Water side		
PT100	Inlet and outlet water temperatures	±0.1 K
Magnetic flow meter	Water flow rate	±0.5%
Pressure transducer	Water pressure drop	±0.5%
Fans		
Wattmeter	Electrical power of fans	±0.2%

Data reduction

The heat flow rate on the water side is evaluated as:

$$Q_{TOT} = \dot{m}_w c_w \left(t_{w,out} - t_{w,in} \right) \tag{1.1}$$

In summer conditions, dehumidification is always present. In order to measure the latent heat exchanged, the condensed water is collected in an external tank and the weight variation during the experimental test is measured as:

$$\Delta m_{cond} = m_{cond,start} - m_{cond,end} \tag{1.2}$$

Where $m_{cond,start}$ and $m_{cond,end}$ correspond to the weight of the tank before and after the considered experimental test, respectively. This quantity is then divided by the test time τ_{test} thus obtaining the condensate flow rate:

$$\dot{m}_{cond} = \frac{\Delta m_{cond}}{\tau_{test}} \tag{1.3}$$

The latent heat associated to the condensate flow rate is given by:

$$Q_{LAT} = \dot{m}_{cond} \cdot h_{fg} \tag{1.4}$$

Where h_{fg} is the latent heat of water.

1.3 Experimental results: vertical configuration

Experimental measurements were carried out using an enthalpy tunnel, located in EURAPO S.r.l., thus verifying the operation of the finned coil examined at different conditions. In particular, the climatic chamber simulates the chosen operational conditions, using an air treatment unit. In winter condition the incoming air is brought to a dry bulb temperature of 20 °C and to a relative humidity of 50%, while in summer condition the air dry bulb temperature is 27 °C and RH=50%. The enthalpy tunnel is meant to measure the air flow that crosses the tested finned coil, using a series of calibrated nozzles. The Reynolds number on the air side is in the range 250 – 600 for all the following tests.

1.3.1 Heat flow rate measurements: winter conditions

During heating tests, hot water flows through the tubes heating the air: the tested conditions are reported in Table 1.3. The main parameters varied are the fan speed, the air temperature and the ΔT between inlet and outlet water temperature.

Figure 1.9 reports the total heat flow rate versus the volumetric flow rate of air for the different inlet conditions. The inlet water temperature is maintained always at 45 °C, thus tests with lower inlet air temperature show higher heat flow rate. Squared markers correspond to tests with 5 K of water temperature gain, while the triangles refer to 10 K of ΔT: this means that the mean temperature of water in these tests is 2.5 K lower, which is the reason for the lower heat flow rate of green triangle with respect to green square markers.

Table 1.3. Conditions for winter tests performed with the finned tube heat exchanger (EBH 020 – 3R).

Test # [-]	Fan speed [-]	T air IN [°C]	T water IN [°C]	ΔT water [°C]
1	MAX	20	45	5
2	Med	20	45	5
3	min	20	45	5
4	MAX	20	45	10
5	Med	20	45	10
6	min	20	45	10
7	MAX	15	45	6
8	Med	15	45	6
9	min	15	45	6
10	MAX	25	45	5
11	min	25	45	5

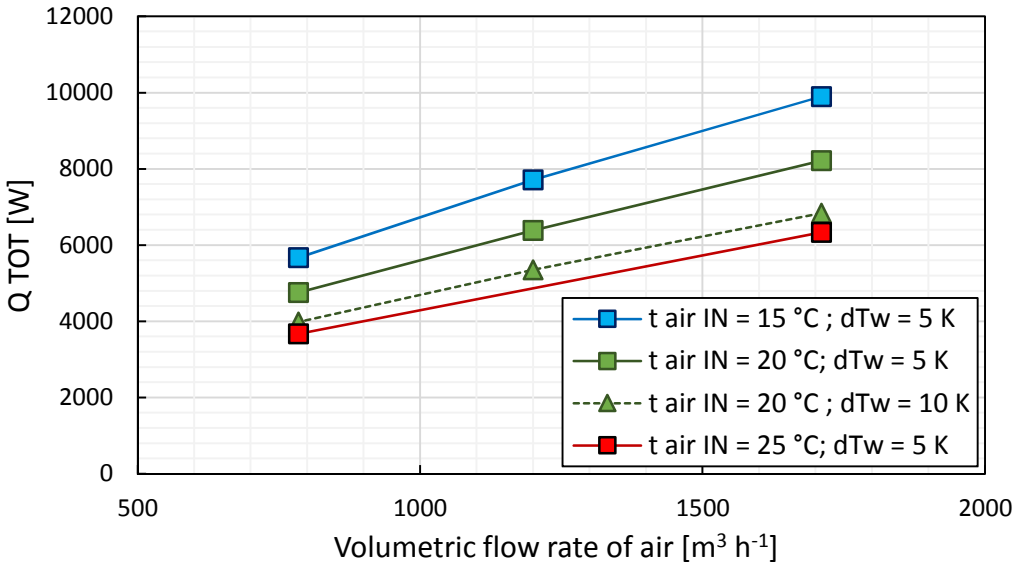

Figure 1.9. Total heat flow rate versus volumetric flow rate of air during tests in winter conditions.

1.3.2 Heat flow rate measurements: summer conditions

When the wall temperature is lower than the wet bulb temperature, the moisture present in the air starts to condensate on the wall, modifying the heat transfer process. The wet bulb temperature strongly depends on the relative humidity of air (RH), thus different values of RH leads to different performance of the unit. Therefore, heating tests investigate the performance of the unit in dry conditions, while the cooling tests are useful to assess the influence of the presence of liquid on the fins. The experimental conditions have been chosen in order to obtain different levels of mass flow rate of condensate (named in Table 1.4 as high, medium and low), maintaining the same temperature for water and air.

Thus, the parameters changed during these tests are the fan speed and the relative humidity of air in the climatic chamber. The values of all the main parameters set for the different tests are reported in Table 1.4.

The three levels of mass flow rate condensate has been chosen so that each level was tested with three fan speed. Moreover the tests have been performed with the three fan speeds for three values RH (66%, 60% and 48%). Two tests have not been performed, because similar to the conditions of tests number 14 and 23.

Figure 1.10 and Figure 1.11 report the latent and total heat flow rate versus the volumetric flow rate of air for tests in summer conditions.

All tests show that higher $\dot{m}_{air}$ lead to higher total heat flow rate, but the effect on the latent heat flow rate depends on the relative humidity of the inlet air: lower RH lead to a smaller variation of the latent heat exchanged when $\dot{m}_{air}$ increases.

Table 1.4. Conditions for summer tests performed with the finned tube heat exchanger (EBH 020 – 3R).

Test #	Fan speed	T air IN	RH air IN	T water IN	ΔT water	Condensate
[-]	[-]	[°C]	[%]	[°C]	[°C]	[-]
12	min	27	82	7	5	High
13	Med	27	72	7	5	High
14	min	27	67	7	5	Medium
15	MAX	27	66	6.5	5.5	High
16	Med	27	66	7	5	
~~≈14~~	~~min~~	~~27~~	~~66~~			
17	MAX	27	60	6.6	5.4	
18	Med	27	60	7	5	Medium
19	min	27	60	7	5	
20	MAX	27	57	7	5	Medium
21	MAX	27	48	7	5	
~~≈23~~	~~Med~~	~~27~~	~~48~~			
22	min	27	48	7	5	Low
23	Med	27	47	7	5	Low
24	MAX	27	46.5	7	5	Low

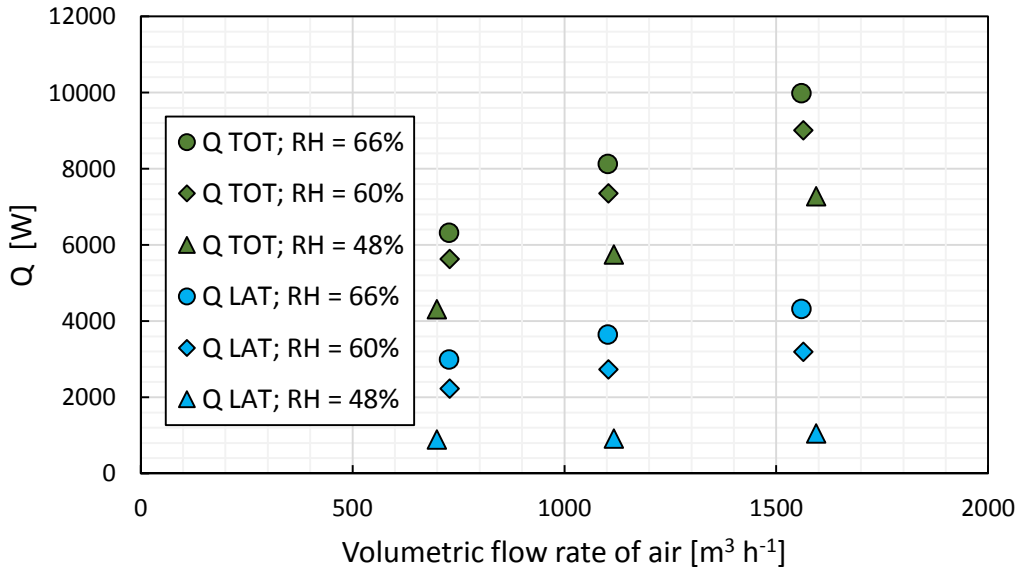

Figure 1.10. Total heat flow rate (green markers) and latent heat flow rate (blue markers) versus volumetric flow rate of air during tests in summer conditions with different inlet RH of air.

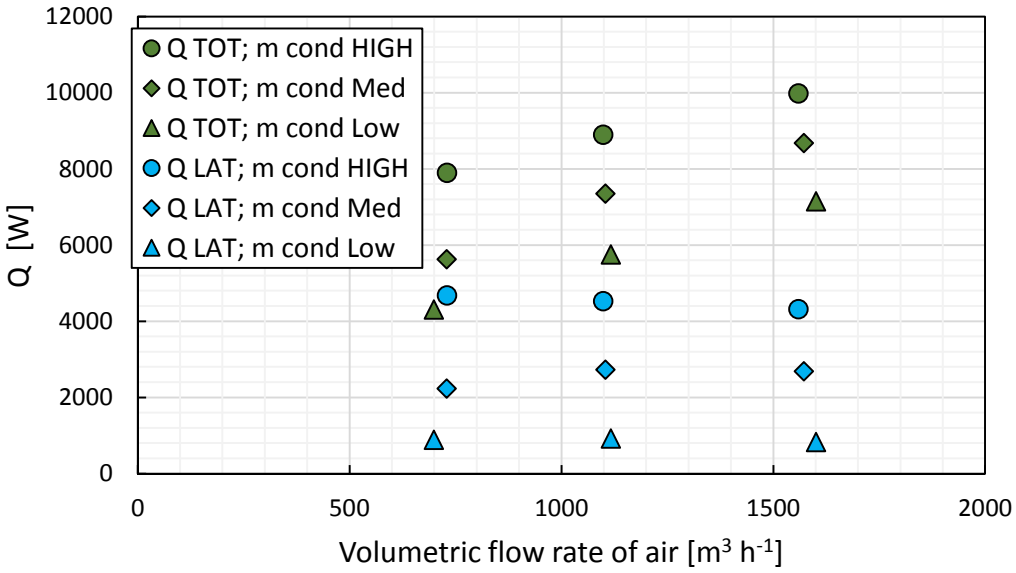

Figure 1.11. Total heat flow rate (green markers) and latent heat flow rate (blue markers) versus volumetric flow rate of air during tests in summer conditions with different mass flow rate of condensate.

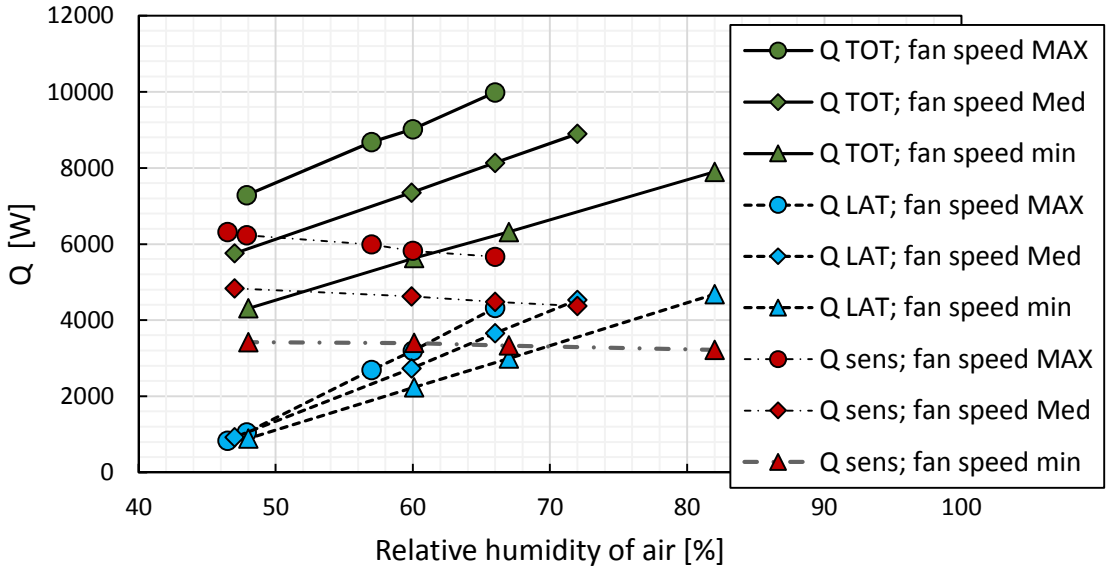

Figure 1.12. Total (green markers), latent (blue markers) and sensible (red markers) heat flow rate versus RH of air during tests in summer conditions with different fan velocities.

Figure 1.12 reports the total (green markers), latent (blue markers) and sensible (red) heat flow rate versus the relative humidity of air with different fan velocities. The total heat flow rate of the three fan speeds increases with the same slope increasing RH. For the lowest speed the gain in total heat flow rate is completely due to the increase in latent heat exchanged, thus the sensible heat exchanged is almost constant. For the other two speeds the latent heat exchanged increases more than the total one, so the sensible heat slightly decreases with RH.

1.3.3 Air mass flow rate measurements

Using the aeraulic tunnel, the air mass flow rate has been measured in dry conditions at the three fan velocities with three different back pressures at the outlet of the unit (0 – 60 – 90 Pa). This is the pressure difference between the outlet of the tested unit and the climatic chamber, which is due to the variable exhaust system that simulates the piping in real installations.
The results of these measurements are reported in Table 1.5 and in Figure 1.13.

Table 1.5. Volumetric flow rate of air during winter tests with three different level of pressure drop after the machine.

Pressure drop [Pa]	**MAX fan speed** [m³/h]	**Med fan speed** [m³/h]	**min fan speed** [m³/h]
0	1710.6	1200.1	784.9
60	1366.4	895	355.8
90	1173.3	675.1	155.9

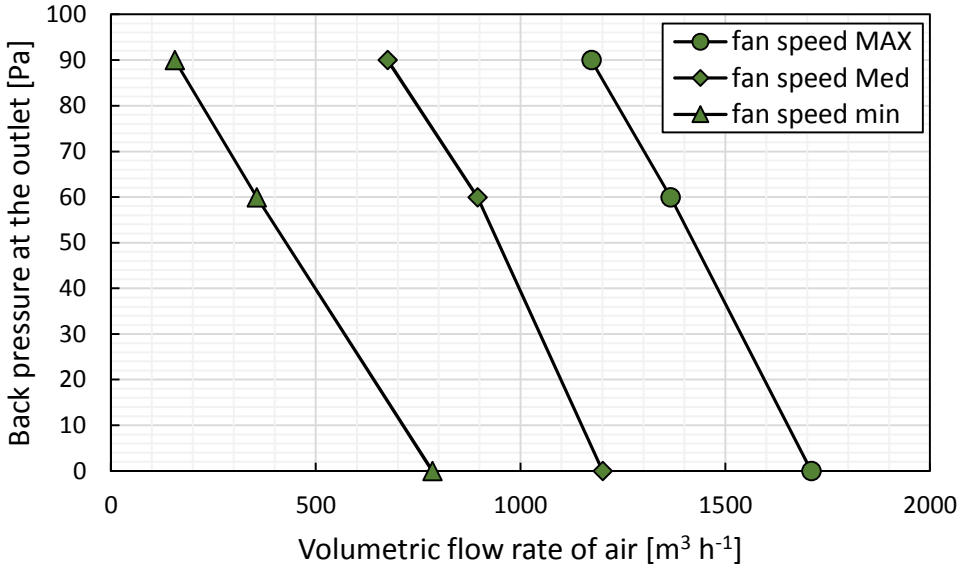

Figure 1.13. Fan curves for different speed of the fan of EBH 020 – 3R with dry unit.

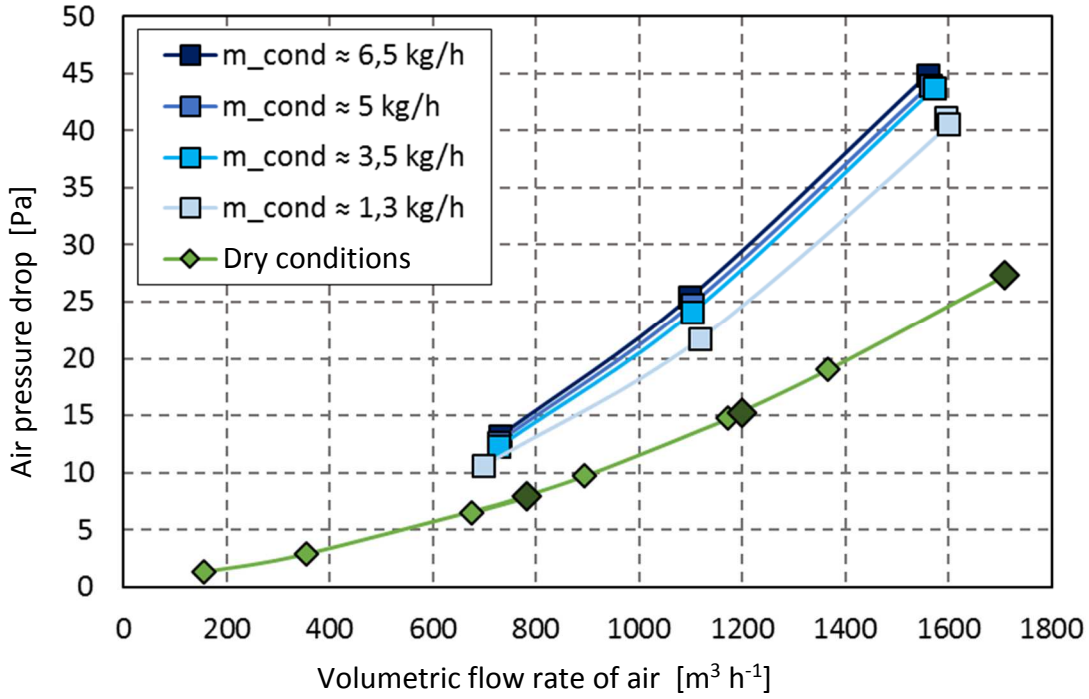

Figure 1.14. Pressure drop of air in the heat exchanger versus mass flow rate of air for tests with and without dehumidification.

Figure 1.14 shows the pressure drop measured between the inlet and outlet of the heat exchanger during the tests performed. The green markers correspond to heating tests, thus with dry conditions, and have the lowest values of pressure drop. Blue markers refer to dehumidification tests, and it is possible to see that higher mass flow rates of condensate lead to higher pressure drop, but even the lowest amount of condensate produces an important increase, while from 3.5 to 6.5 kg/h the difference in the pressure drop is limited. This means that the moisture that condenses on the fin surface causes an obstruction for the air that passes through the coils, but the amount of water that condenses has a weak influence on the additional pressure drop, which is mainly due to the minimum liquid film thickness needed by water to leave the heat exchanger thanks to gravity.

As already mentioned, the enthalpy tunnel allows to measure the volumetric flow rate of air during a thermal test of the unit. Table 1.6 reports the volumetric air flow rate and the corresponding mass flow rate of condensate obtained during the tests performed in summer conditions.
The same results are rearranged in Figure 1.15, where $\dot{m}_{air}$ in the summer tests divided by the mass flow rate in dry conditions is reported versus $\dot{m}_{cond}$ for the three fan speeds tested. As we can see all data have a relative mass flow rate lower than 0.94 with respect to the winter tests. This means that the additional pressure drop due to the presence of water on the fins, lead to a lower $\dot{m}_{air}$. The rate of condensate moisture affects in different ways the different fan speeds: while with the medium and with the highest speed $\dot{m}_{air}$ decreases with $\dot{m}_{cond}$, with the lowest velocity $\dot{m}_{air}$ is almost constant.

Table 1.6. Volumetric flow rate of air and mass flow rate of condensate moisture for the different speed tested in summer condition.

Condensate	**MAX fan speed**		**Med fan speed**		**min fan speed**	
[-]	V_{air} *[m³ s⁻¹]*	$\dot{m}_{cond}$ *[kg h⁻¹]*	V_{air} *[m³ s⁻¹]*	$\dot{m}_{cond}$ *[kg h⁻¹]*	V_{air} *[m³ s⁻¹]*	$\dot{m}_{cond}$ *[kg h⁻¹]*
High	1559,6	6,21	1098,5	6,52	729,6	6,73
Medium	1563,9	4,59	1102,3	5,26	727,6	4,3
Low	1572,4	3,88	1104	3,94	729	3,21
	1593,7	1,51	1117	1,33		
	1600,8	1,2				

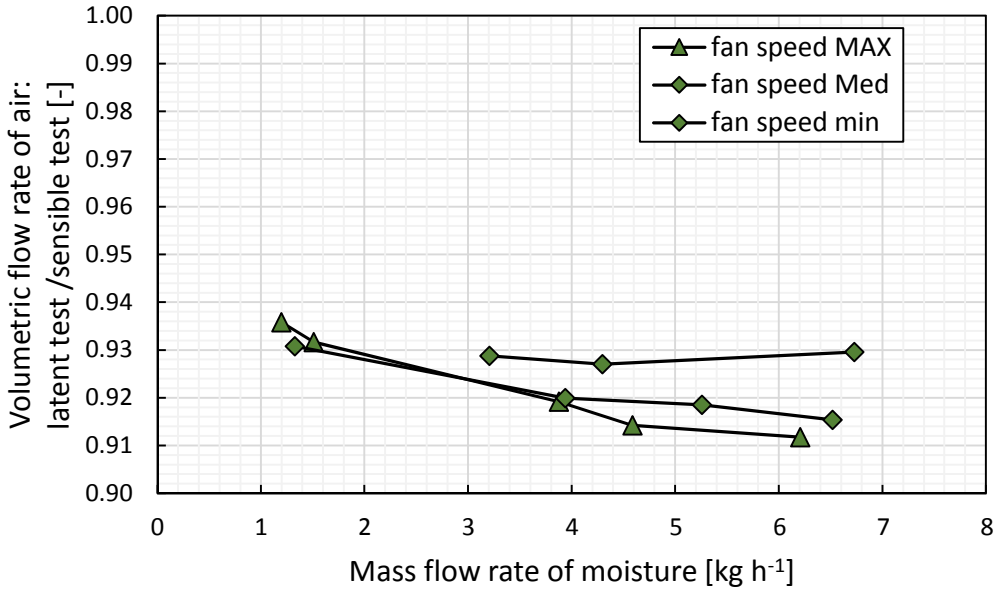

Figure 1.15. Ratio between volumetric flow rate of air in test with and without dehumidification at three different speed of the fan versus the mass flow rate of condensate moisture.

1.4 Experimental results: influence of inclination angle

The air conditioning unit is composed by a fan that provides the air flow, by the fan coil that heats or cools down the air and a finally by a filter meant to purify the air flow from solid particles in suspension. In many applications, the heat exchanger that heats or cools down the air has an inclination with respect to the direction of the air flow, as often happens with fan coil units.

1.4.1 Experimental apparatus

In order to investigate the effect of inclination angle on the thermal performance of finned tube heat exchangers, three different tilted position of the coil have been tested: the first is the classic vertical position, assumed as reference, then two different positions, as illustrated in Figure 1.16. The pictures in Figure 1.17 show the photos of the experimental test section with 30° and 60° of tilt angle.

The tests have been performed with the same heat exchanger tested in paragraph 1.3.
Table 1.7 reports the tested conditions, where the main parameters varied are the fan speed and the tilt angle, with only two thermal situations: winter mode ($t_{w,IN}$ = 45 °C; $t_{air,IN}$ = 20 °C) and summer mode ($t_{w,IN}$ = 7 °C; $t_{air,IN}$ = 27 °C).

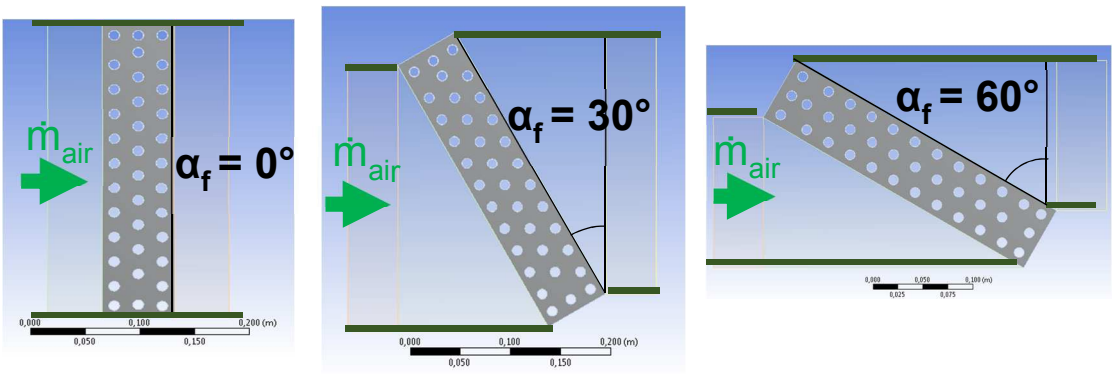

Figure 1.16. Schematic of the three configurations in which the finned tube heat exchanger has been tested.

Figure 1.17. Photos of experimental test section with the finned tube heat exchanger with two different tilt angles.

Table 1.7. Conditions for tests performed with the finned tube heat exchanger (EBH 020 – 3R) with different tilt angles.

	α_f [°]	Fan speed [-]	$t_{water,IN}$ [°C]	Δt_{water} [K]	$t_{air,IN}$ [°C]	$RH_{air,IN}$ [%]
Heating - Winter mode	0 30 60	min – Med – MAX	45	5	20	50
Cooling with dehumidification - Summer mode	0 30 60	min – MAX	7	5	27	48

1.4.2 Air mass flow rate measurements

Figure 1.18 shows the volumetric flow rate of air versus tilt angle for different fan speed during heating and cooling tests performed in the enthalpy tunnel.
The effect of the inclination on the mass flow rate is limited in all the tested conditions.
Figure 1.19 reports the pressure drop versus the air flow. The three series with red markers, referred to winter conditions, have almost the same values of pressure drop, meaning that the tilt angle do not influence the pressure drop. When the heat exchanger is tilted, the cross section of the inlet air conduct is lower, but the passage area through the fins is always the same, thus the air velocity through the tubes is similar in the three tilt conditions.
On the other hand, during cooling conditions the vertical configuration has lower pressure drop with respect to 30° and 60° of tilt angle, which show similar value of Δp.
All the wet tests show higher pressure drop than dry situations, and this is due to the condensate moisture that blocks the air passage. The reason for the higher Δp of tilted tests is probably related to the speed with which the condensate exits the heat exchanger: the inclination angle makes the condensate slower, thus blocking the passage of air even more and increasing the pressure drop.

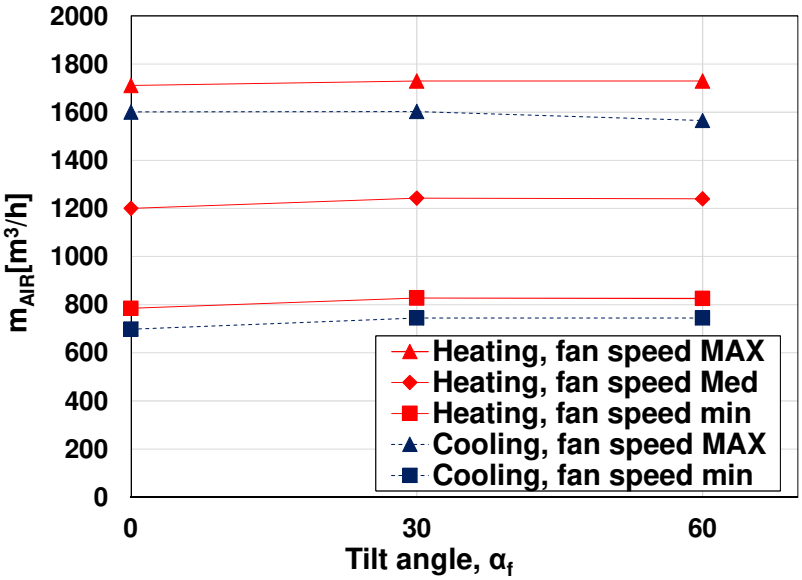

Figure 1.18. Volumetric flow rate of air versus tilt angle for different fan speeds and thermal conditions.

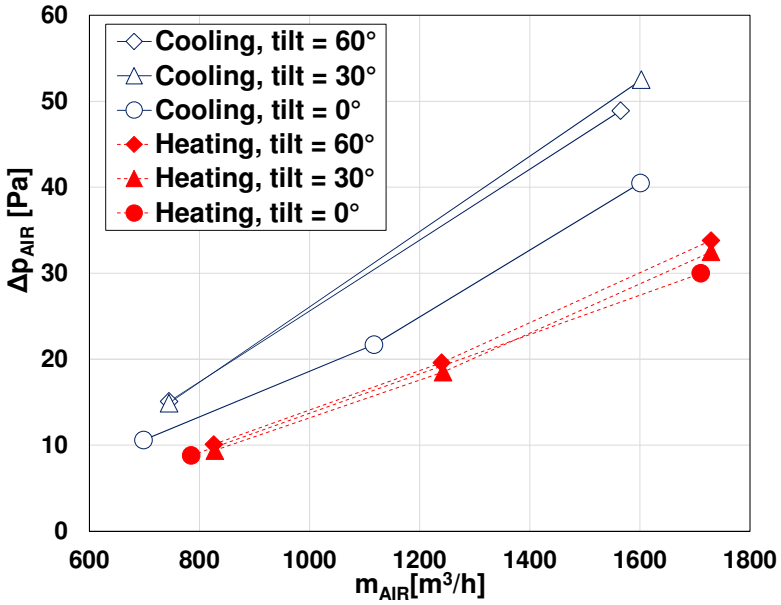

Figure 1.19. Pressure drop in the heat exchanger versus volumetric flow rate of air for different tilt angles and thermal conditions.

1.4.3 Heat flow rate measurements

Figure 1.20 and Figure 1.21 report the total and latent heat flow rate for the tested conditions versus the inclination angle of the heat exchanger.
Both graphs show that the effect of tilt angle on the performance of this heat exchanger is limited, and the maximum variation with respect to vertical position is 6%.

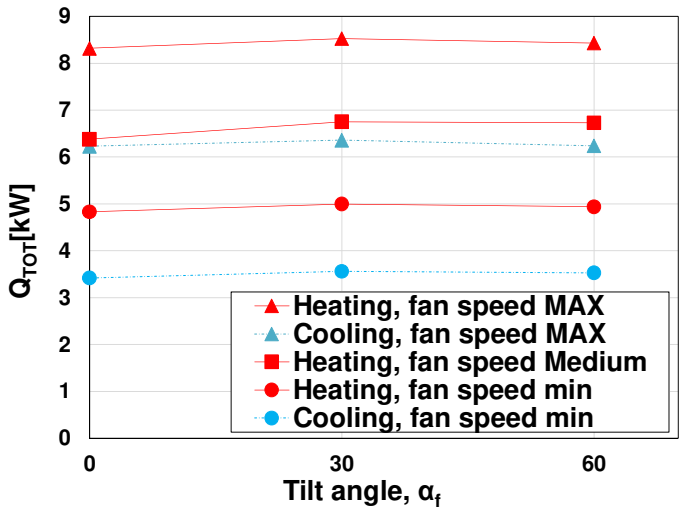

Figure 1.20. Total heat flow rate versus tilt angle for different fan speeds and thermal conditions.

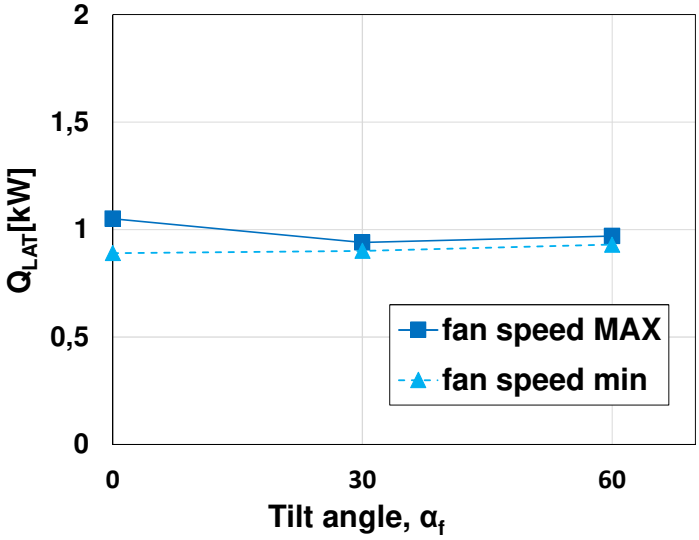

Figure 1.21. Latent heat flow rate versus tilt angle for different fan speeds in dehumidification tests.

2 Heat transfer in aluminium minichannels: experimentation

2.1 Introduction

Compact aluminium heat exchangers are used in various applications such as electronic cooling devices, cryogenic heat exchangers, automobile radiators, but their application in the field of air conditioning is still limited and little studied. The use of aluminium minichannels heat exchangers with high ratio of exchange surface area / volume for air conditioning application allows to obtain high performance of heat exchange with a limited refrigerant charge. Highly efficient heat transfer is critical to develop technologies with less environmental impact. In this case, an efficient and compact solution allows a reduction of greenhouse gas emissions resulting from electricity consumption and allows a reduction of the refrigerant charge resulting in lower potential emissions of refrigerants.

Bar-and-plate heat exchanger are a particular type of compact minichannels HX made of aluminium. These kind of heat exchangers are available in a wide variety of geometries: turbulator with perforated fins (Figure 2.2a) and turbulator with offset strip fins (Figure 2.2b) are the most used. In the literature, there are numerous studies on heat transfer in single-phase flow for aluminium compact heat exchangers. Kays (1972) presented an analytical model of the heat transfer and friction factor losses in offset strip fin surfaces. This is one of the first attempts to propose a model that includes the form drag contribution of the blunt fin edges.

Wieting (1975) evaluated the effect of fin length, height, thickness, spacing and hydraulic diameter on the performance and developed empirical relationships correlating experimental heat transfer and flow friction data for rectangular offset plate fin heat exchangers configurations given by London and Shah (1968), Walters (1969) and Kays and London (1964) for laminar or turbulent flow.

These correlations can be applicable only for air or gas as the heat transfer fluid and should be used only in completely turbulent or laminar regime.

Manglick and Bergles (1995) reanalysed the data reported in the literature for the rectangular offset strip fin compact heat exchangers and presented a generalized correlation for f (friction factor) and j (Colburn factor) that fit the experimental data for different airflows. Their correlations may be applicable for all gases and most liquids with moderate Prandtl number (fluids with Prandtl numbers ranging from 0.5 to 15) because the experimental data were obtained using air (Pr = 0.7) in the $120 < Re < 10^4$ range. Their equations represent the data continuously in the laminar, transition, and turbulent flow regions.

Min-Soo Kim et al. (2011) investigated the thermo-flow characteristics of a heat exchanger with offset strip fins for various fin geometries and working fluids. They observed that previous correlations underestimate *f* values in the laminar and turbulent regimes and overestimate *j* values in the laminar regime, as the blockage ratio increases. Therefore, they presented a new correlation for blockage ratios greater than 20%. While most previous correlations was limited to air, the study by Min-Soo Kim considered various working fluids, but all related to single phase heat transfer. Moreover, new *j* equations were suggested as functions of the Prandtl number to correlate the experimental values for various working fluids. Therefore, the correlations proposed could be available for a wide ranges of blockage ratios (0–35%) and Prandtl numbers (0.72–50).

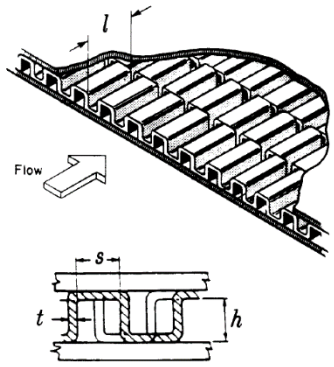

Figure 2.1. Offset strip fin turbulator (Manglick and Bergles, 1995).

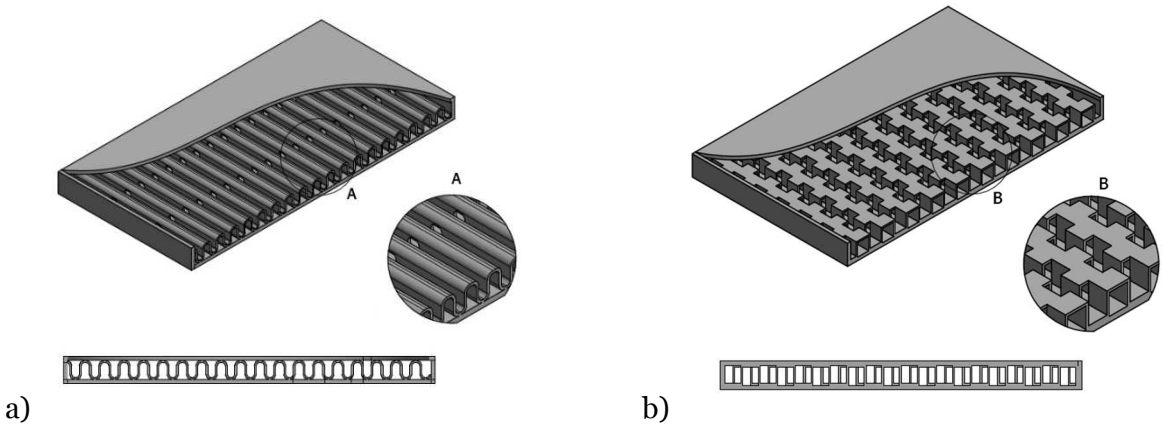

Figure 2.2. Perforated (a) and offset strip (b) fins turbulators.

Differently from the case of sensible heating and cooling, very limited studies are available with phase change in such geometries. Mandrusiak and Carey (1989) investigated different offset strip fins geometries, while Robertson and Clarke (1985) studied perforated fins with liquid nitrogen. Feldman et al. (1999) studied the heat flow rate in flow boiling for heat exchangers with vertical channels 'offset strip fins' and 'perforated fins' for the refrigerant CFC114. The vaporization of the fluid was obtained with foil resistances placed above and below the channel of the refrigerant: specific mass flow rates was varied up to 45 kg $s^{-1}m^{-2}$ while heat flow rate was equal to 3.5 kW m^{-2}. However, only few studies are reported in the literature regarding the performance in phase change heat transfer of these heat exchangers and their application in refrigeration and air conditioning equipment needs more extended investigation. For this purpose, a new test section is here presented. The test section has been designed with a refrigerant channel using perforated turbulators. In the present study, the heat transfer during vaporization, condensation and single phase flow with refrigerant R32 and R1234ze(E) is investigated. In the design of the test section, particular attention has been paid to the wall temperature measurement in order to determine the refrigerant heat transfer coefficient accurately.

Figure 2.2 shows the perforated and strip fins present in the refrigerant and water side of the test section, respectively.

2.2 Experimental apparatus and test section

2.2.1 Design of the experimental test section

A bar and plate heat exchanger consists of layers of corrugated aluminium fins separated from each other by thin sheets of aluminium. The core of these sheets is made of the same aluminium of the fins, while the outer part is a lower melting point aluminium, which performs the bond between the layers by melting and solidifying in the brazing furnace. During the process, the low melting point aluminium changes its position leading to the formation of a rough surface.

Water and refrigerant flow alternatively in the channels of the heat exchanger, as represented in Figure 2.3.

The goal of the experimental tests is to measure heat transfer coefficient and pressure drop during condensation, vaporization and single phase flow of refrigerant inside perforated turbulator. Thus, the test section can have only one channel with this kind of turbulator, it must have a system that allows to give or subtract heat and it should be instrumented in order the measure the wall temperature. The inlet and outlet manifolds should be able to ensure an evenly distributed flow of refrigerant and to measure the temperature and the pressure drop of the fluid.

The length and width of the prototype are the same of an existing heat exchanger already tested, in order to have the possibility to compare the results with a complete heat exchanger with the same geometry.

Many experimental studies use electrical resistances to heat the refrigerant during boiling tests, so that the measurement of the input thermal power is very accurate and the heat flux in the heat exchanger is uniform.

Another way to heat the refrigerant is to use a hot secondary fluid (i.e. water) that exchanges heat through the wall: in this case, the heat flow rate is measured with temperature and mass flow rate sensors placed on the secondary fluid circuit. The resulting uncertainty on the heat flow rate is higher than with the electrical heating, but there is no risk to burn the set up when dryout occurs, thus it is easier to investigate vapour qualities around or higher than the critical value, and the heat flux is similar to the one of water to refrigerant applications.

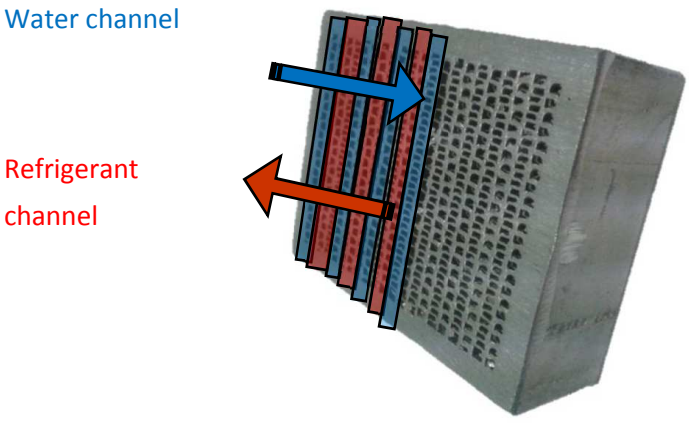

Figure 2.3. Schematic of the circuitry inside bar and plate heat exchangers: channel of water and refrigerant are alternated with a counter current flow.

Condensation tests are usually performed with a secondary fluid (i.e. water) that absorbs the heat of the refrigerant through the wall. A less used method involves Peltier cells for the heat removal and heat flux sensors for the heat flow rate measurements. This method could be used even in boiling applications, but the sensors and the cells are expensive.
The construction and instrumentation of the prototype requires an important effort, therefore we choose to use water to exchange heat during both condensation and vaporization processes in order to use the same test section for all the tests.
By measuring the wall temperature, the saturation temperature of the fluid and the heat flow rate, it is possible to determine the heat transfer coefficient according to the expression:

$$HTC = \frac{Q}{S\left(T_{wall} - T_r\right)} \tag{2.1}$$

with S equal to the heat transfer area on the refrigerant side.
In order to reduce the experimental uncertainty of the measurements, the difference between wall and refrigerant temperature must be higher than 1 K.
Moreover, the experimental apparatus allows a range of refrigerant mass flow rate between 18 and 120 kg/h (0.005÷0.033 kg/s) and a range of water mass flow rate from 40 to 300 kg/h (0.0111÷0.0833 kg/s), with water temperature in the test section lower than 60 °C, to avoid problem with the connecting pipes, and higher than 7 °C, to avoid frosting in the heat exchanger that cools the water.
After these considerations, we choose to build a test section composed by a single refrigerant channel 0.5 m long, as reported in Figure 2.4, and 14 water modules bonded on the external surface using an aluminium based conductive paste.
The refrigerant channel is 58 mm wide and 3 mm high, with perforated fins inside. A black and white image of the inlet of the test section, taken with a 12 megapixels camera, is reported in Figure 2.5. A decimeter close to the area of interest acted as a reference for the conversion from pixels to mm, while a CAD software allowed to detect the edge of each channel, evaluating its perimeter, area and hydraulic diameter. The resulting passage area is 110 mm² and the hydraulic diameter of the test section is 1.6 mm, evaluated as four times the total passage area divided by the total perimeter. Two grooves have been made on the refrigerant channel wall for each water module and 4 thermocouples have been placed before bonding the water modules to the refrigerant channel. The grooves were filled with an aluminium based conductive paste in order to reduce the thermal resistance between the thermocouples and the channel surface. The thermocouples positions at the 14th water modules are schematically indicated in Figure 2.4 by red dots.
On the whole, the refrigerant wall temperature is measured by means of 56 T-type thermocouples. These thermocouples were calibrated using a super-thermometer with a thermistor standard probe (± 0.001 K accuracy) and the zero reference for the cold junction is made using a Kaye Ice Point Temperature Reference device (KAYE 170), which has a typical stability of 0.02 K. All the thermocouples have been calibrated in situ, reaching an accuracy of ± 0.05 K for the entire measurement chain.
In each subsection (seven in total), the refrigerant exchanges heat with water in cross flow. The two water modules attached to the same refrigerant subsection are connected in parallel (as shown in Figure 2.4), while the connections between different water modules are represented in Figure 2.13. The resulting configuration for refrigerant and water is a nearly counter current flow. For each couple

of water modules a calibrated T-type thermopile (accuracy ±0.03 K) measures the water temperature variation, while the water volumetric flow rate is measured through a magnetic type flow meter (Endress Hauser, Promag A). Two T-type thermocouples, an absolute pressure transducer (Rosemount, 3051S) and a differential pressure transducer (Endress Hauser, PMD 235) are used to measure the refrigerant conditions at the inlet and outlet of the test section.

The cooling water modules are 0.156 m long, with a strip turbulator 0.067 m long, and a collector volume, which enables the water to be evenly distributed in all the channels. The thickness of the plate attached to the test section is 6 mm, while the other plate is 3 mm thick. Lateral bars of the water modules are 4.5 mm wide and there is a gap of 1 mm between two adjacent modules.
The choice of aluminium thickness is done to allow enough space for inserting the thermocouples.
It is noteworthy that this experimental configuration using a secondary fluid and specifically designed for condensation can also be used to study flow boiling when the secondary fluid is heating water.

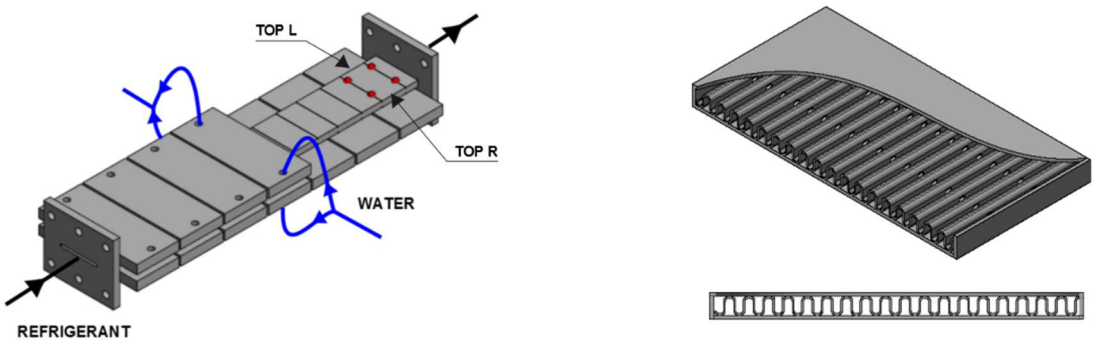

Figure 2.4. Picture of the test section. Left: refrigerant channel and water modules. The last three water modules on top are not depicted; for each water module, four thermocouples are embedded in the wall to measure the wall temperature (red dots represent the position of thermocouples). Right: detail of the refrigerant channel, with perforated fins inside.

Figure 2.5. Flow passage area of the inlet of the test section.

2.2.2 Construction of the experimental test section

The following sequence of pictures show some details of the test section during its building and instrumentation process.

Figure 2.6 shows the groove dug in the outer part of the refrigerant wall, which enables the installation of the T-type thermocouples composed by two wires of 0.124 mm of diameter. Figure 2.7 reports the 56 thermocouples, which are kept in position by a resin, while a thin layer of an aluminium based conductive paste (Figure 2.8) is used to perform the bonding between the refrigerant channel and the water modules.

In Figure 2.9 we can see how the test section looked like after the attachment of the water modules, obtained after two hours at 150°C.

Figure 2.10 shows a detail of the inlet of the test section, with a sheet of Teflon used to connect the inlet manifold preventing leakages.

In Figure 2.11 we can see the test section installed in the test rig, with the SuperThermometer and a thermostatic bath ready for the calibration of the thermocouples.

Finally, Figure 2.12 reports the test section connected to the refrigerant and the water circuits of the experimental apparatus.

a)  b) 

Figure 2.6. Groove to insert the thermocouples for the wall temperature measurement (a) and thermocouple in position (b).

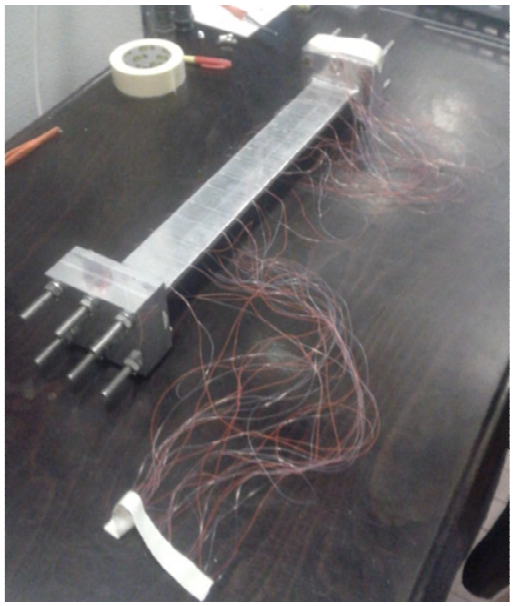

Figure 2.7. Picture of the refrigerant channel instrumented with all the 56 thermocouples.

Figure 2.8. Test section with aluminium based conductive paste before the attachment of water modules.

Figure 2.9. Test section with water module bonded after 2h at 150 °C.

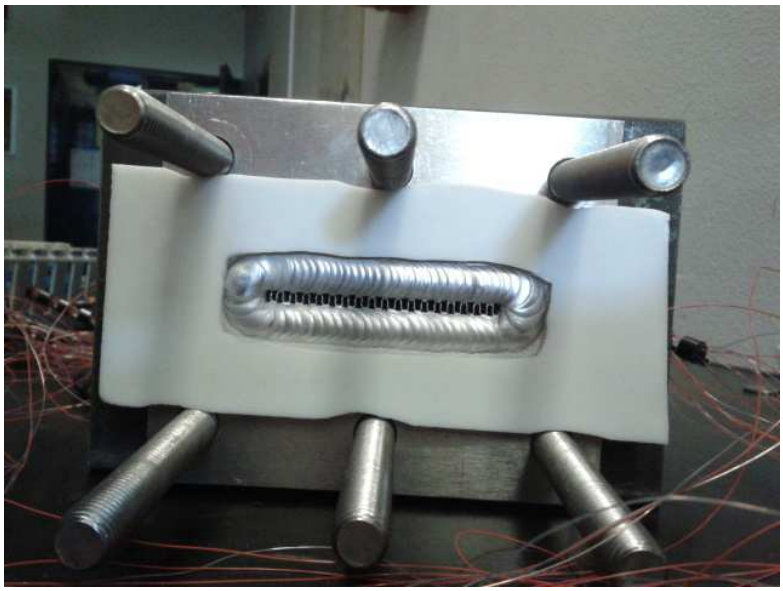

Figure 2.10. Detail of the inlet of test section with a sheet of Teflon to prevent leakages when connected to the test rig.

Figure 2.11. Test section and instrumentation used for on site calibration of the 56 thermocouples.

Figure 2.12. Test section with piping for the water modules.

2.2.3 *Experimental apparatus*

The tests have been performed at the Two-Phase Heat Transfer Laboratory of the Department of Industrial Engineering of the University of Padova. Figure 2.13 shows a schematic view of the experimental apparatus used for the present investigation. In the main loop the subcooled refrigerant flows driven by a magnetically coupled gear pump, then two tube in tube heat exchangers vaporize and superheat the fluid, which then exchanges heat with water coming from a thermostatic bath in another tube in tube heat exchanger (pre section) in order to reach the inlet of the test section with the desired conditions. Here water is sent at different temperatures and mass flow rates to perform the tests. After a brazed plate heat exchanger in which flows water and glycol, the refrigerant is again subcooled liquid and enters the pump. The inner pressure of the system can be varied by means of a bladder accumulator, while the speed of the pump can be controlled with an inverter. The refrigerant and water circuits are thermally insulated by an elastomeric closed-cell foam to minimize heat losses.

The expanded type B uncertainty of the different sensors is reported in Table 2.1.

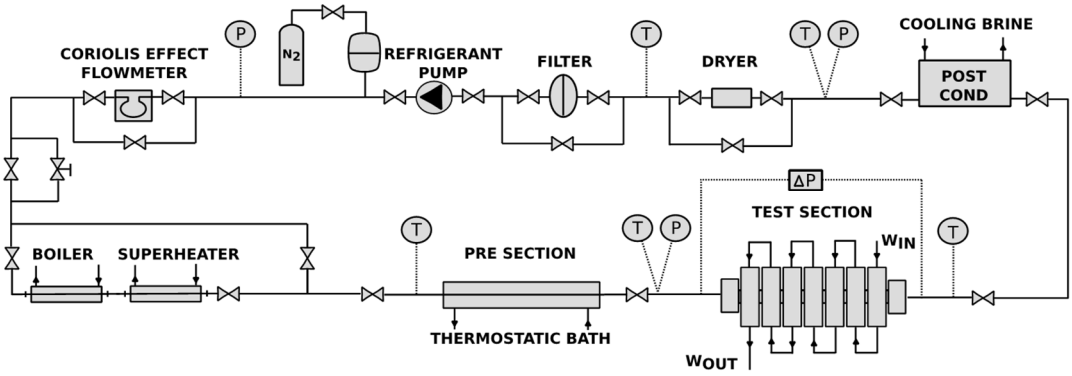

Figure 2.13. Schematic of the test rig.

Table 2.1. Type B expanded uncertainty (95% level of confidence) of sensors.

Absolute pressure transducer	±1 kPa
Differential pressure transducer	±200 Pa
Calibrated T-type thermocouples	±0.05 K
Calibrated T-type thermopiles	±0.03 K
Refrigerant mass flow meter	±0.2 %
Water volumetric flow meter	±0.2 %

2.3 Refrigerant pressure drop

2.3.1 *Experimental procedure*

Pressure drop tests are performed in adiabatic condition, thus the water in the secondary circuit is stopped. The refrigerant must enter the experimental test section in the desired conditions, so the boiler, superheater and the thermostatic bath are set in order to have subcooled liquid or superheated vapour during single phase tests, and the desired vapour quality during two phase adiabatic pressure drop tests. The range of mass flow rate that can be tested in the experimental apparatus led to a lack of data in the transition region, due to the big difference between the Reynolds number in single and two phase flow regime.

2.3.2 Data reduction

The frictional pressure drop is obtained by subtracting the local losses at the inlet and at the outlet of the test section to the total pressure drop measured during the tests.

$$\Delta p = \Delta p_{meas} - \Delta p_{in} - \Delta p_{out} \tag{2.2}$$

During single phase tests the pressure drop at inlet and outlet are estimated, according to Idel'chick (1996) for a similar geometry, equal to:

$$\Delta p_{in} = 2.5 \frac{G^2}{2\rho} \tag{2.3}$$

$$\Delta p_{out} = 0.5 \frac{G^2}{2\rho} \tag{2.4}$$

Inlet and outlet pressure drop during two phase tests is evaluated with the correlation proposed by Paliwoda (1992) for sudden contraction and expansion in circular section with blunt edges, as follows:

$$\Delta p_{in} = \frac{G^2}{2\rho_v \beta} \tag{2.5}$$

$$\Delta p_{out} = 0.5 \frac{G^2}{2\rho_v \beta} \tag{2.6}$$

With

$$\beta = \left(\theta + 1.21\left(1-\theta\right)x\right)\left(1-x\right)^{0.333} + x^{2.276} \tag{2.7}$$

$$\theta = \frac{\rho_v}{\rho_l}\left(\frac{\mu_l}{\mu_v}\right)^{0.25} \tag{2.8}$$

In order to reach the inlet of the test section with the desired vapour quality, the superheated vapour entering the pre section is partially condensed in the pre section and the refrigerant enthalpy at the inlet of the test section are evaluated as:

$$h_{in} = h_{in,pre\ sec} - \frac{Q_{pre\ sec}}{\dot{m}_r} \tag{2.9}$$

Where $h_{in,pre\ sec}$ is evaluated from the temperature and pressure at the inlet of the pre section and $Q_{pre\ sec}$ is the heat flow rate exchanged in the pre section. The vapour quality at the inlet of the test section is, then, calculated as:

$$x_{in} = \frac{h_{in} - h_l}{h_{lv}} \tag{2.10}$$

2.3.3 Experimental results and *comparison with models*

Single phase pressure drop

In Figure 2.14 the experimental single-phase friction factors are compared with the predictions by Hagen-Poiseuille and Churchill (1977) model from laminar to fully turbulent flow regime. The Churchill (1977) model is reported accounting for two different values of roughness. The relative roughness of the tube ε/d is equal to $2Ra/d$.

All the single phase pressure drop experiments reported here are performed in adiabatic conditions. The low Reynolds number tests are performed with liquid refrigerant, while the higher values of Reynolds number refer to tests with superheated vapour.

The trend of the experimental data in the transition region differs from the one predicted by Churchill for smooth tubes: this is probably due to holes present in the turbulator, which lead to an early transition to the turbulent flow regime, similarly to the behaviour predicted by Manglik and Bergles (1995) for offset strip fins with the same hydraulic diameter. The better agreement with the correlation of Churchill (1977) is reached considering a surface roughness equal to 2 μm.

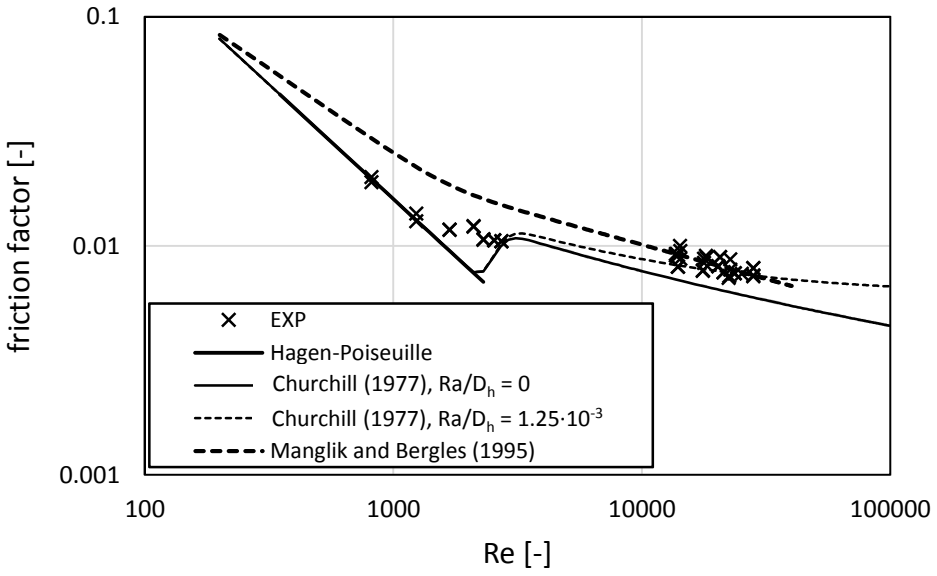

Figure 2.14. Friction factor versus Reynolds number for single phase tests with R1234ze(E).

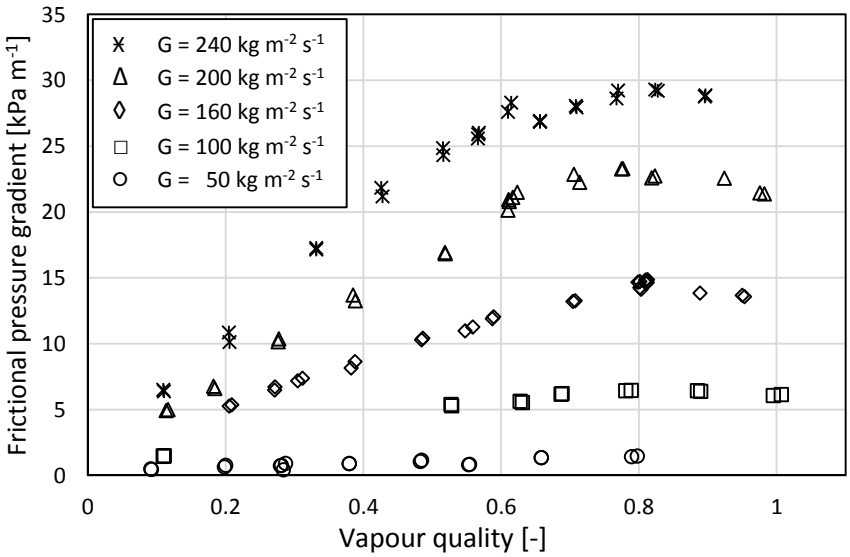

Figure 2.15. Pressure gradient versus vapour quality during adiabatic tests with different mass fluxes with R1234ze(E).

Adiabatic two phase pressure drop

Using the tube in tube heat exchanger placed before the test section it was possible to perform tests with different vapour quality in adiabatic conditions in order to measure the pressure drop during two-phase flow. Figure 2.15 shows the pressure gradient obtained with different mass fluxes versus the vapour quality. The pressure gradient increases with mass flux and has a maximum for a value of vapour quality close to 0.8.

Figure 2.16 depicts the comparisons among 10 prediction methods from literature and the experimental data for frictional pressure gradient taken under adiabatic conditions with R1234ze(E). These prediction methods have been evaluated according to the following criteria: the fraction of data predicted within ±20% and ±50% error band, ζ, and the mean absolute deviation, *MAD*, which is calculated as:

$$MAD = \frac{\sum_{i=1}^{n} |Err_i|}{n} \tag{2.11}$$

Where n is the number of tests performed and the error is evaluated as

$$Err = \frac{\gamma_{calc} - \gamma_{EXP}}{\gamma_{EXP}} \cdot 100 \tag{2.12}$$

With respect to the significant parameter γ, that here is the pressure gradient.

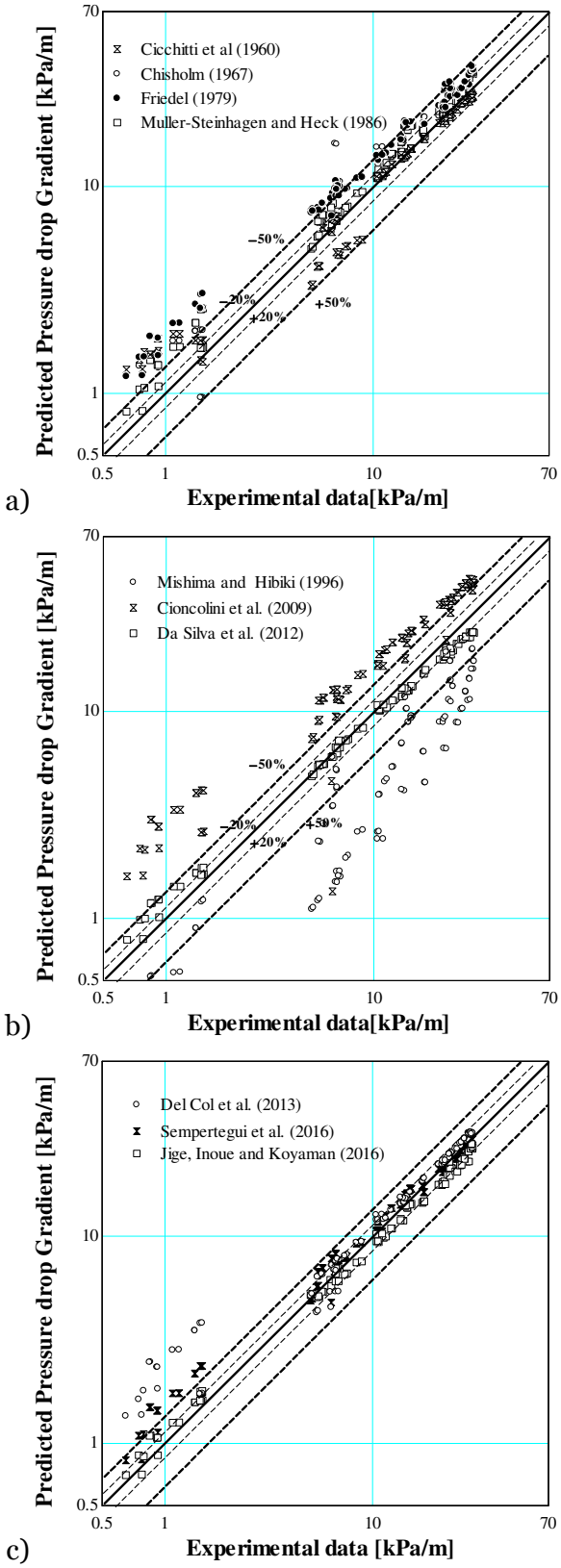

Figure 2.16. Comparison of frictional pressure drop experimental data with prediction methods from literature.

Table 2.2 presents the statistical parameters obtained by the assessment of 10 well-known prediction methods for frictional pressure drop available on literature. The prediction method proposed by Jige et al. (2016) provided the best predictions of the experimental results, with MAD = 11%, $\zeta_{20\%}$ = 95%

and $\zeta_{50\%}$ = 99%, followed by the method proposed proposed by Da Silva and Ribastki (2013), which was developed based on Muller-Steinhagen and Heck (1986) model, adjusted empirically by experimental data for single and mini-channel, providing reasonable predictions with MAD = 13%, $\zeta_{20\%}$ = 87% and $\zeta_{50\%}$ = 99%.

Figure 2.17 and Figure 2.18 present the deviation values of the results predicted by the most suitable prediction methods assessed for frictional pressure drop, displaying that deviation is higher at low mass velocity of 50 kg m^{-2} s^{-1}.

Table 2.2. Statistical parameters from the comparison between the pressure drop predictions and the experimental results.

Prediction methods	***MAD%***	$\zeta_{20\%}$	$\zeta_{50\%}$
Cicchitti *et al.* (1960)	19.73	71.68	87.61
Chisholm (1967)	23.33	61.06	87.61
Friedel (1979)	41.71	23.89	77.88
Muller-Steinhagen-Heck (1986)	21.68	57.52	92.92
Mishima and Hibiki (1996)	53.25	7.08	41.59
Cioncolini *et al.* (2009)	78.69	17.70	29.20
Da Silva and Ribatski (2013)	13.14	86.73	99.12
Del Col *et al.* (2013)	31.88	79.64	84.96
Sempertegui *et al.* (2016)	14.44	76.99	91.15
Jige, Inoue and Koyama (2016)	11.04	94.69	99.12

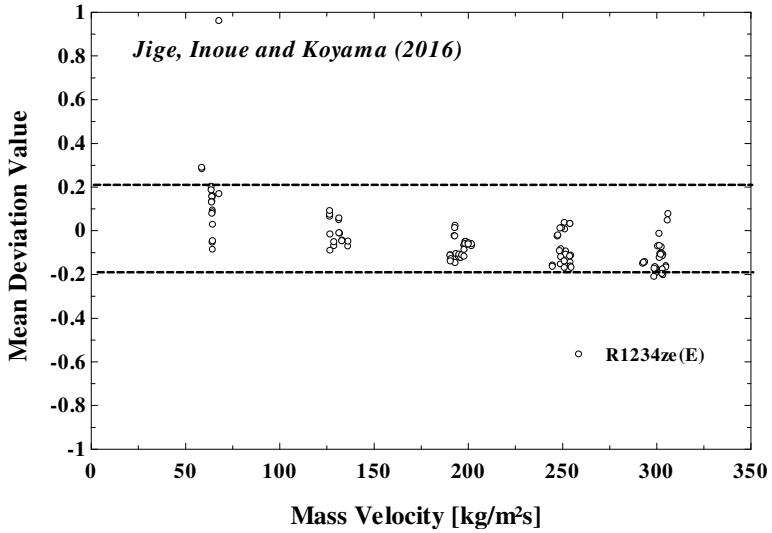

Figure 2.17. Evaluation of the deviation related to frictional pressure drop predicted results by Jige, Inoue and Koyama (2016).

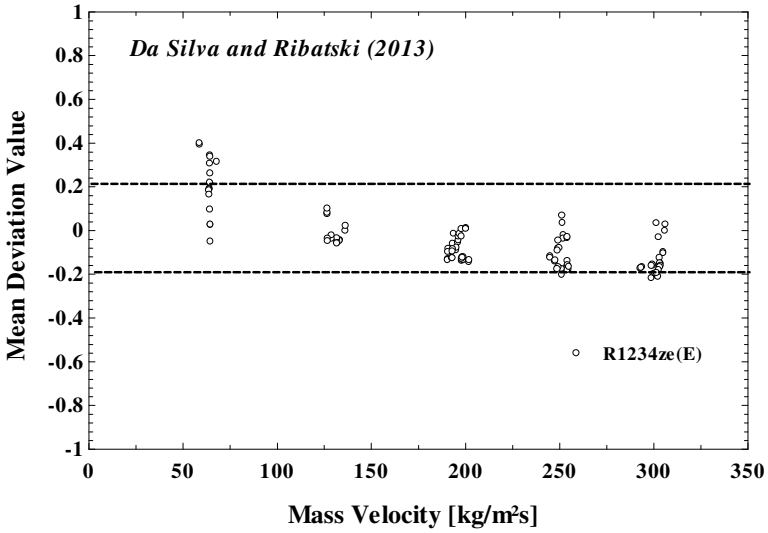

Figure 2.18. Evaluation of the deviation related to frictional pressure drop predicted results by Da Silva and Ribastki (2013).

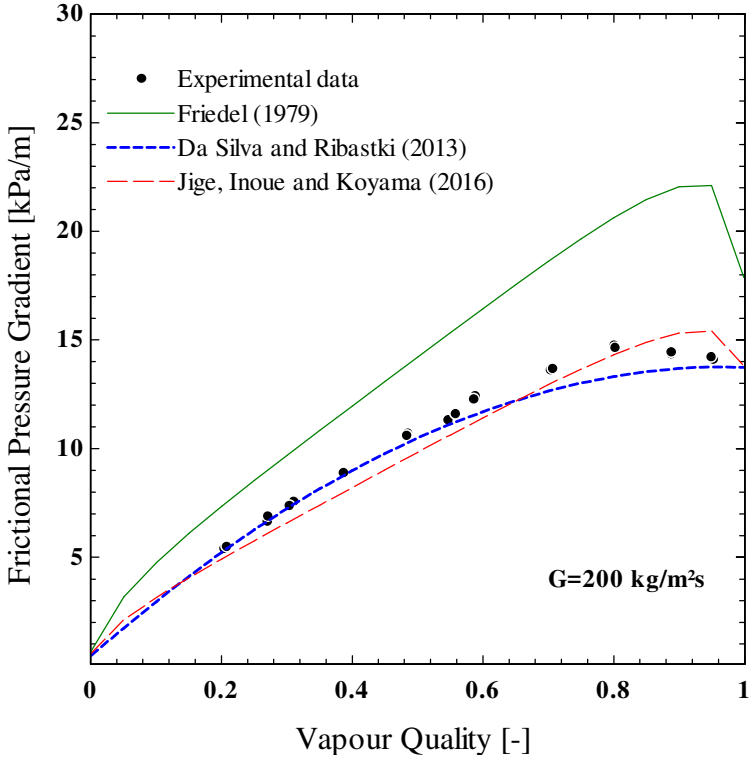

Figure 2.19. Comparison among prediction methods and the experimental results for R1234ze(E), Dh=1.6 mm, G=200kg/m²s.

According to Figure 2.19, the prediction methods proposed by Da Silva and Ribatski (2013) and Jige, Inoue and Koyama (2016), also captured reasonably the tendency of frictional pressure drop. On the other hand, the well-known prediction method developed by Friedel (1979) have failed on capturing the data behaviour; however, it was developed based on macrochannels, whereas the methods proposed by da Silva and Ribatski (2013) and Jige, Inoue and Koyama (2016) were developed based on microchannels.

Experimental tests in a specifically designed tests section have been performed in order to measure pressure drop in bar and plate heat exchangers with perforated fins.
It has been performed a comparison among these experimental data and predicted results by 10 well-known prediction methods available on literature for two-phase frictional pressure drop. The prediction methods proposed by Da Silva and Ribastki (2013) and Jige, Inoue and Koyama (2016) have predicted reasonably the experimental results, with MAD = 13.1%, $\zeta_{20\%}$ = 86.7% and MAD = 11.0%, $\zeta_{20\%}$ = 94.7%, respectively.

2.4 Single phase heat transfer with refrigerants

2.4.1 Experimental procedure

To measure the single phase heat transfer coefficient during single phase flow, we choose to send hot water to heat the liquid refrigerant. In order to avoid the evaporation of the refrigerant, the water temperature must be lower than the saturation temperature (during these tests at least 5 K of temperature difference have been maintained).
In order to have a high heat flow rate during this tests, the inlet temperature of the refrigerant was set as the lowest achievable with the apparatus (around 0°C) and the refrigerant pressure as the highest, so that the inlet water temperature could be high enough to ensure an accurate measurement of the HTC.

2.4.2 Data reduction

In order to evaluate the heat transfer coefficient the following expressions are used.
The heat flow rate exchanged in each refrigerant subsection (Q_{subsec}) is calculated from a thermal balance on the water side as:

$$Q_{subsec} = \dot{m}_w c_{pw} \Delta T_w \tag{2.13}$$

The heat transfer coefficient is then calculated for each subsection as

$$HTC = \frac{Q_{subsec}}{S_{subsec} \Delta T_{r,wall}} = \frac{q}{\Delta T_{r,wall}} \tag{2.14}$$

where q is the heat flux in the subsection, and $\Delta T_{r,wall}$ is the temperature difference between the refrigerant temperature and the wall temperature, $\Delta T_{r,wall} = T_r - T_{wall}$. During two phase tests, T_r is set equal to T_{sat}. S_{subsec} is the total heat transfer area on the refrigerant side for each subsection, which includes the surface of the perforated fins.
The wall temperature is calculated as the arithmetic average value of the 8 thermocouples positioned in the subsection corrected according to Fourier's Law, assuming one dimensional conduction to account for the thermal resistance of the aluminium. The temperature variation across the aluminium wall ΔT_{wall} is calculated as follows,

$$\Delta T_w = \frac{q}{\lambda_{al}} s_{wall} \tag{2.15}$$

where λ_{al} is the aluminium thermal conductivity and s_{wall} is the aluminium thickness.
The specific enthalpy of the refrigerant at the inlet of the test section results from the measured values of temperature and pressure of the superheated vapour. Since the heat transferred from the refrigerant in each subsection is equal to that exchanged by the water, it is possible to get the refrigerant enthalpy and the vapour quality at the exit of each subsection as reported in Eq. (10) and Eq. (11).

$$h_{out} = h_{in} - \frac{Q_{subsec}}{\dot{m}_r} \tag{2.16}$$

$$x_{out} = \frac{h_{out} - h_l}{h_{lv}} \tag{2.17}$$

All the fluid properties are calculated with NIST Refprop version 9.1 (Lemmon et al., 2013).

2.4.3 *Uncertainty analysis*

The experimental uncertainty analysis has been performed in agreement with the guidelines provided by JCGM (2008). The standard uncertainty is obtained by combining type A (u_A) and type B (u_B) uncertainties:

$$u = \sqrt{u_A^2 + u_B^2} \tag{2.18}$$

In order to get the standard uncertainty of indirect measurements the law of uncertainty propagation is used. For example, starting from Eq. (8) and Eq. (9), the standard uncertainty of the heat transfer coefficient is

$$u_{HTC} = \sqrt{\left(\frac{c_{p,w}\Delta T_w}{S_{subsec}\Delta T_{r,wall}} u_{\dot{m}_w}\right)^2 + \left(\frac{c_{p,w}\dot{m}_w}{S_{subsec}\Delta T_{r,wall}} u_{\Delta T_w}\right)^2 + \left(\frac{HTC}{\Delta T_{r,wall}} u_{(\Delta T_{r,wall})}\right)^2} \tag{2.19}$$

The HTC of the first and the last modules are not considered in the following analysis because of possible thermal dissipation since the heat transfer through axial conduction with the inlet and outlet chambers could affect the refrigerant heat flux and the heat transfer coefficient.
The uncertainties of the calculated parameter are given in Table 2.3.

Table 2.3. Uncertainty of main calculated parameters.

	Most of data	**MAX**
Vapour quality	< 0.015	0.03
HTC	< 12 %	14 %
Q	< 5 %	9 %
G	< 2 %	2 %

2.4.4 *Experimental results and comparison with models*

Figure 2.20 reports the heat transfer coefficient during single-phase tests performed with R32. During these tests, subcooled liquid refrigerant was heated by water at a temperature lower than saturation temperature, in order to avoid bubble formation. The dashed lines indicate the prediction by Gnielinski (1976) model, which is developed for smooth circular channels. The particular geometry of the test section lead to heat transfer coefficient 20% higher than the value predicted by Gnielinski (1976). The measurements with Reynolds number between 2000 and 3000 are more scattered, probably because in the transition region the holes of the turbulator affect the fluid flow so that slight differences in the mass flux lead to different flow regime, with appreciably different pressure drop, thus different heat transfer coefficient.

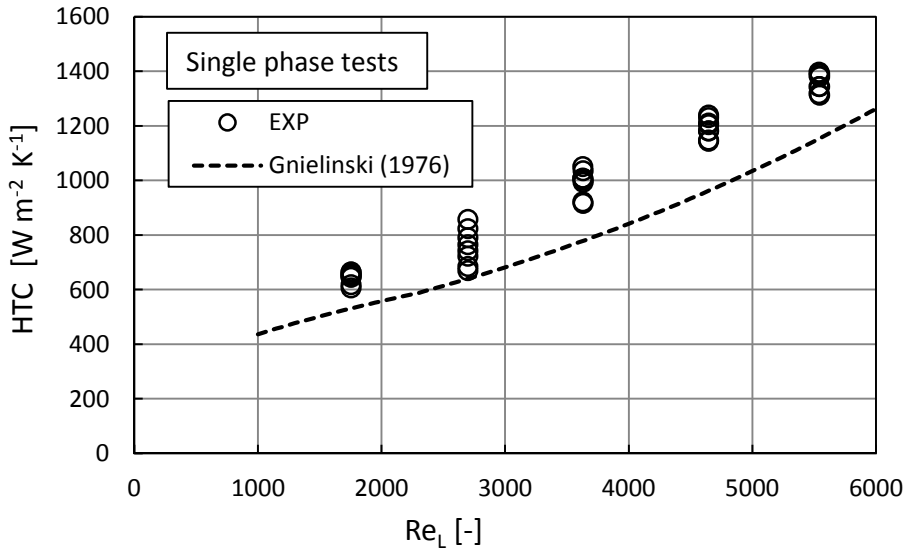

Figure 2.20. HTC versus Reynolds number during single phase tests with R32 and prediction by Gnielinski (1976).

2.5 Single phase heat transfer with water

In order to measure the thermal performance of bar and plate heat exchangers in real configurations, different tests have been carried out. A single heat exchanger has been tested in water/water configuration, in order to determine the global heat transfer coefficient and calculate the single phase heat transfer coefficient on both sides with the Wilson plot technique.

2.5.1 Experimental apparatus

A bar and plate heat exchanger have been used in water/water tests, with hot water that enters the perforated fins side and the cold water that flows in counter current inside the strip fins turbulator. The purpose of the tests was to measure the overall heat transfer coefficient, thus determining a correlation for the heat transfer coefficient in single-phase flow regime for channels with both perforated and strip turbulators.

2.5.2 Data reduction

During the tests the following parameters have been measured for both sides: water flow rate, inlet water temperature, temperature difference and water pressure drop between inlet and outlet.
By knowing the geometry of the heat exchanger the following parameters have been calculated:
Reynolds number:

$$Re = \frac{\rho \, u \, D_h}{\mu} \tag{2.20}$$

Prandtl number:

$$Pr = \frac{\mu \, c_p}{\lambda} \tag{2.21}$$

Heat flow rate exchanged at both sides, and average value:

$$Q_{strip} = \dot{m}_{strip} c_{p,strip} \left(t_{strip,out} - t_{strip,in} \right) = \dot{m}_{strip} c_{p,strip} \Delta T_{strip} \tag{2.22}$$

$$Q_{perf} = \dot{m}_{perf} c_{p,perf} \left(t_{perf,out} - t_{perf,in} \right) = \dot{m}_{perf} c_{p,perf} \Delta T_{perf} \tag{2.23}$$

$$Q_m = \frac{\left|Q_{strip}\right| + \left|Q_{perf}\right|}{2} \tag{2.24}$$

Overall heat transfer coefficient referred to the surface area of the strip turbulator side:

$$K_{strip} = \frac{Q_m}{S_{strip} \Delta T_{ml}} \tag{2.25}$$

2.5.3 Uncertainty analysis

An electromagnetic flow meter is employed for the measurement of the water volumetric flow rate (expanded uncertainty ±0.5% of flow rate). The water temperature is measured at the inlet of the heat exchanger (expanded uncertainty ±0.05 K), and the temperature gain of water is measured by T-type thermopiles (expanded uncertainty ±0.03 K). For all the expanded uncertainties, a coverage factor equal to 2 has been considered.

2.5.4 Experimental procedure

The tests were carried out maintaining one of the two sides at a constant Reynolds number and varying the mass flow rate on the other side.
During these tests, the Reynolds number range is between 500 and 2800 for the strip side, while from 350 to 5000 for the perforated side.
All tests were carried out with hot water on perforated side.

2.5.5 Experimental results

The values obtained from the tests are reported in Table 3.1.
In Figure 2.21, the overall heat transfer coefficient is a function of Reynolds number on the strip side, but it also depends on the operating conditions of the perforated side.
As shown in Figure 2.22 the overall heat transfer coefficient is almost entirely dependent on the Reynolds number of the perforated side, thus a variation of the operating conditions on the strip side has a minor effect.
The reason of this behaviour is the dominance of the thermal resistance on the perforated side with respect to the thermal resistance on the strip side.
Therefore, to understand how the heat transfer coefficient affects the overall heat transfer coefficient it is necessary to analyse the following expression, where the thermal resistances are reported:

$$K_{strip} = \left(\frac{1}{HTC_{strip}} + \frac{1}{HTC_{perf}} \frac{S_{strip}}{S_{perf}} + \frac{sp}{\lambda_{al}} \right)^{-1} = \left(R_{strip} + R_{perf} \frac{S_{strip}}{S_{perf}} + R_{al} \right)^{-1} \qquad (2.26)$$

In equation (2.26) the unknown variables are the heat transfer coefficients HTC_{strip} and HTC_{perf}. The next section reports the proposed correlations that determine the heat transfer coefficients during single phase flow.

Table 2.4. Results of single-phase flow tests with water on both strip and perforated side.

Test [-]	$T_{strip,in}$ [°C]	$T_{perf,in}$ [°C]	ΔT_{strip} [K]	ΔT_{perf} [K]	m_{strip} [kg/s]	m_{perf} [kg/s]	Re_{strip} [-]	Re_{perf} [-]	Q_m [W]	$K_{strip, EXP}$ [W/(m² K)]
1	15.03	24.95	8.74	-2.36	0.280	0.997	453	**1453**	10033	2384
2	15.01	24.92	7.62	-3.10	0.419	0.997	670	**1440**	13152	2589
3	15.00	24.87	6.58	-3.62	0.559	0.998	882	**1430**	15251	2699
4	15.00	24.95	5.86	-4.03	0.689	0.998	1077	**1426**	16857	2781
5	14.98	24.97	5.24	-4.37	0.829	0.998	1285	**1421**	18207	2873
6	15.02	26.43	6.06	-5.02	0.829	0.997	1300	**1458**	20979	2925
7	15.05	26.47	5.51	-5.39	0.969	0.997	1510	**1454**	22410	3065
8	15.02	26.35	4.94	-5.55	1.109	0.997	1714	**1447**	23036	3093
9	15.02	26.44	4.56	-5.78	1.248	0.997	1921	**1446**	23969	3141
10	15.02	26.47	5.93	-5.15	0.969	1.127	**1517**	1647	24156	3342
11	15.04	26.44	6.32	-4.97	0.969	1.237	**1525**	1810	25661	3657
12	14.95	26.40	4.93	-5.92	0.969	0.818	**1495**	1183	20120	2732
13	14.99	26.63	4.50	-6.54	0.969	0.688	**1488**	993	18536	2496
14	15.02	26.63	3.94	-7.13	0.969	0.549	**1479**	786	16170	2225
15	14.24	26.42	7.19	-5.04	0.969	1.386	**1511**	2026	29184	3970
16	14.26	26.38	7.47	-4.77	0.969	1.516	**1517**	2220	30261	4189
17	14.25	25.99	8.57	-3.85	0.689	1.526	1094	2239	24638	3886
18	14.22	25.96	10.17	-2.76	0.409	1.526	662	2265	17513	3365
19	14.89	38.80	22.99	-2.53	0.289	2.543	552	**4958**	27331	3431
20	10.25	40.30	27.70	-4.44	0.419	2.532	760	**4989**	47750	4003
21	17.33	40.00	19.82	-4.28	0.568	2.542	1106	**4988**	46266	4532
22	19.74	40.15	17.08	-4.51	0.687	2.532	1370	**4972**	48401	4914
23	22.36	40.24	14.14	-4.48	0.827	2.542	1689	**5001**	48222	5201
24	21.09	40.22	14.37	-5.34	0.966	2.533	1925	**4940**	57280	5508
25	23.30	40.22	11.96	-5.11	1.115	2.542	2271	**4970**	55026	5689
26	23.90	40.07	10.92	-5.25	1.245	2.533	2539	**4930**	56192	5925
27	26.21	40.47	3.86	-9.50	1.395	0.557	**2771**	1047	22299	2523
28	25.13	39.67	4.59	-9.05	1.395	0.696	**2728**	1295	26541	2889
29	25.29	40.46	5.45	-9.00	1.395	0.825	**2763**	1560	31398	3282
30	23.74	40.26	7.75	-8.72	1.395	1.222	**2740**	2308	44867	4426
31	22.10	40.28	10.20	-7.86	1.405	1.788	**2734**	3408	59328	5322
32	21.74	40.23	11.19	-7.01	1.405	2.196	**2742**	4214	65020	5749
33	21.00	40.04	12.06	-6.50	1.405	2.543	**2724**	4888	69961	6018

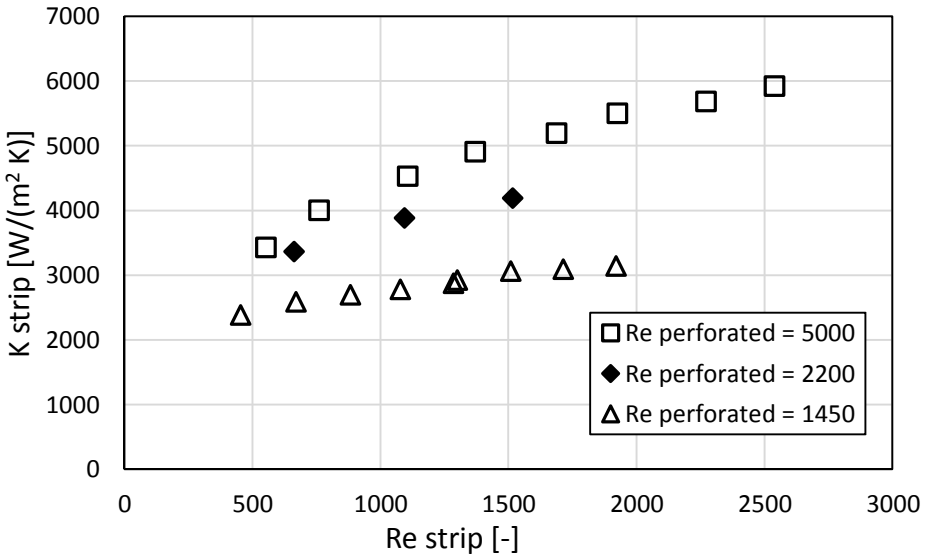

Figure 2.21. Experimental overall heat transfer coefficient as a function of Reynolds number on the strip side.

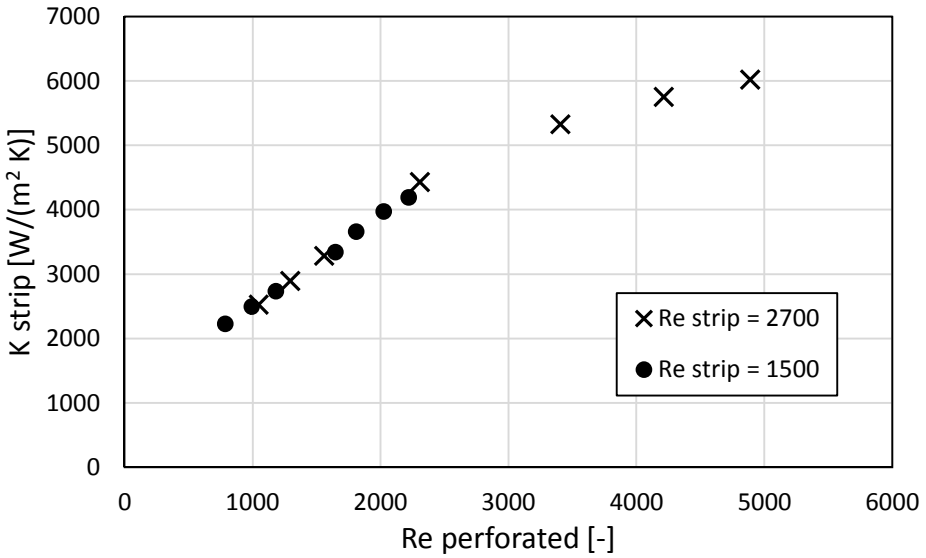

Figure 2.22. Experimental overall heat transfer coefficient as a function of Reynolds number on the perforated side.

2.5.6 Development of single phase heat transfer correlations

The heat transfer coefficient during single phase flow can be expressed as a function of Reynolds and Prandtl numbers as reported in the next equation

$$HTC = A\,Re^{B} Pr^{0.333} \frac{\lambda}{D_h}\left(\frac{\mu}{\mu_{wall}}\right)^{0.14} \tag{2.27}$$

with the constant values *A* and *B* that depend on the particular geometry of the heat exchanger.

Therefore, the development of single-phase correlations requires that the constants *A* and *B* are determined for each side from the interpolation of the experimental data.

The values that provide the best prediction of the overall heat transfer coefficients experimentally measured are:

$$A_{\text{strip}} = 0{,}1714$$

$$B_{\text{strip}} = 0{,}6694$$

$$A_{\text{perf}} = 0{,}0205$$

$$B_{\text{perf}} = 0{,}779$$

Thus, provided that μ/μ_p is set equal to 1, the equations for the HTC of strip and perforated turbulators are:

$$HTC_{strip} = 0.1714\,Re^{0.6694} Pr^{0.333} \frac{\lambda}{D_h} \tag{2.28}$$

$$HTC_{perf} = 0.0205\,Re^{0.779} Pr^{0.333} \frac{\lambda}{D_h} \tag{2.29}$$

In order to assess the agreement between the calculated and the corresponding experimental values, the MAD, MD and SD indexes, defined in the following equations, are considered.

Mean Absolute Deviation (MAD):

$$MAD = \frac{\sum_{i=1}^{n} |Err_i|}{n} \tag{2.30}$$

Mean Deviation (MD):

$$MD = \frac{\sum_{i=1}^{n} Err_i}{n} \tag{2.31}$$

Standard Deviation (SD):

$$SD = \sqrt{\frac{\sum_{i=1}^{n} \left(Err_i - MD\right)^2}{n-1}} \tag{2.32}$$

Where *n* is the number of tests performed and the error is evaluated as

$$Err = \frac{\gamma_{calc} - \gamma_{EXP}}{\gamma_{EXP}} \cdot 100 \tag{2.33}$$

With respect to the significant parameter γ, that here is the global heat transfer coefficient.

The results using the proposed correlations are reported in Table 2.5.

Table 2.5. Accuracy in the prediction of the overall heat transfer coefficient using Eq. (2.28) and Eq. (2.29).

MAD[%]	MD[%]	SD[%]	min[%]	MAX[%]
3.24	0.5	3.82	-8.59	5.04

2.5.7 Comparison with literature correlations

The experimental results have been also compared with the ones obtained using the correlation of Manglik and Bergles (1994) for the strip side and the correlation of Dittus and Boelter (1985) for the perforated side.

The comparison of the results is done in terms of overall heat transfer coefficient.

The heat transfer coefficient presented by Manglik and Bergles (1994) is calculated as:

$$\begin{aligned} Nu_{Manglik} = {} & 0.6522 Re^{-0.4597} \alpha^{-0.1541} \beta^{0.1499} \gamma^{-0.0678} \cdot \\ & \cdot \left(1 + 5.269 \cdot 10^{-5}\ Re^{1.34} \alpha^{0.504} \beta^{0.456} \gamma^{-1.055}\right)^{0.1} Pr^{0.333} \end{aligned} \tag{2.34}$$

$$HTC_{Man} = \frac{Nu_{Man}\,\lambda}{D_h} \tag{2.35}$$

While the Dittus and Boelter (1985) correlation evaluates the HTC as:

$$HTC_{DB} = 0.023\ Re^{0.8} Pr^{0.4} \frac{\lambda}{D_h} \tag{2.36}$$

The overall heat transfer coefficient that has been obtained is calculated as:

$$K_{Man-DB} = \left(\frac{1}{HTC_{Man}} + \frac{1}{HTC_{DB}} \frac{S_{strip}}{S_{perf}} + \frac{sp}{\lambda_{al}} \right)^{-1} \tag{2.37}$$

Table 2.6. Accuracy in the prediction of the overall heat transfer coefficient: Manglik and Bergles (1994) correlation is used for the strip side and Dittus and Boelter (1985) correlation is used for the perforated side.

MAD[%]	MD[%]	SD[%]	min[%]	MAX [%]
10.37	-5.5	10.60	-19.39	15.68

Table 4.2 reports the error indexes to assess the prediction accuracy of the overall heat transfer coefficient when Manglik and Bergles (1994) and Dittus and Boelter (1985) correlations are used to model the strip and the perforated side. The employment of these correlations results in a lower accuracy compared to Eq. (2.28) and Eq. (2.29).
For this reason, Eq. (2.28) and Eq. (2.29) will be used in the models presented in Chapter 5 to predict the behaviour of the heat exchanger during single phase heat transfer for the strip side and the perforated side, respectively.

2.6 Two phase heat transfer: flow boiling

2.6.1 Experimental procedure

The particular scheme adopted for the test section enables to measure the heat transfer coefficients varying vapour quality and heat flow rate. Differently from most flow boiling experiments, the heat flux cannot be independently varied because a secondary fluid is used to promote boiling instead of imposing Joule effect heating. During the tests, the heat flux is somehow governed by controlling the refrigerant saturation temperature and the inlet water temperature but it cannot be directly controlled.

During each flow boiling test run, seven data points corresponding to the seven subsections are recorded and therefore seven values of the heat transfer coefficient are measured, one for each experimental module. Data of the first and last modules are discarded because of heat conduction to the inlet and outlet manifolds.

The flow boiling test runs have been performed with R32 at 5°C saturation temperature, at mass velocity G = 50 - 200 kg $m^{-2}s^{-1}$, where $G = m/A$, being A the area of the channel perpendicular to the refrigerant flow, considering the obstruction of turbulators. The heat flux was varied between 10 and 30 kW m^{-2}.

In order to avoid possible maldistribution of the refrigerant in the test section, all two phase tests are performed with subcooled or superheated refrigerant at the inlet.

Data reduction and uncertainty analysis are performed as reported in 2.4.2 and 2.4.3 for single phase tests.

2.6.2 Experimental results

Figure 2.23 shows the temperature values measured along the section during a flow boiling test performed at G = 100 kg m^{-2} s^{-1}. From the temperatures profiles it can be seen that the thermal resistance on the water side is higher than the one on the refrigerant side up to a certain axial position. In the second graph of Figure 2.23 (from the top), the standard deviations of the wall temperature readings are plotted to detect temperature fluctuations in the wall: it can be seen that at the beginning of the flow boiling process, the standard deviation is very low while it starts to increase at around 0.25 m, corresponding to 0.6 vapour quality (third graph from the top). The standard deviation of the wall temperature is reported here because this parameter is sensitive to the occurrence of the dryout of the liquid film at the wall. As can be seen in the bottom graph of Figure 2.23, at the same position where the wall temperature fluctuations rise, the heat transfer coefficient decreases abruptly.

In Figure 2.24, it can be seen that such a decrease of the HTC is significant after 0.6 vapour quality. It is worth mentioning that a similar behaviour is reported also in Karayiannis et al. (2012), Del Col et al. (2013) and Ribatski (2013), which relates this to instabilities in the fluid flow that can be due to the presence of parallel channels and to the particular geometry of the bar and plate heat exchanger.

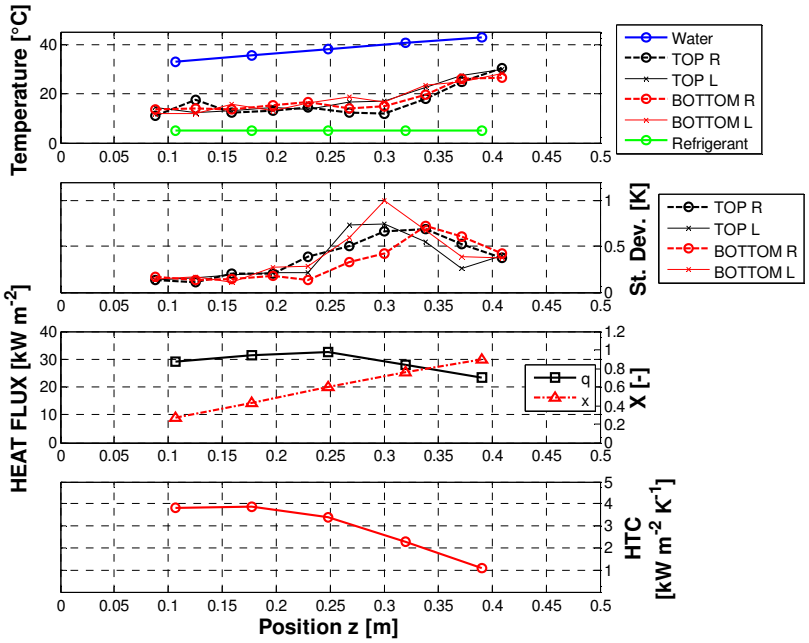

Figure 2.23. Measured values along the test section during a vaporization test performed at G = 100 kg m^{-2} s^{-1}. From top: temperature values, standard deviation of the wall temperature readings, heat flux and vapour quality and heat transfer coefficient.

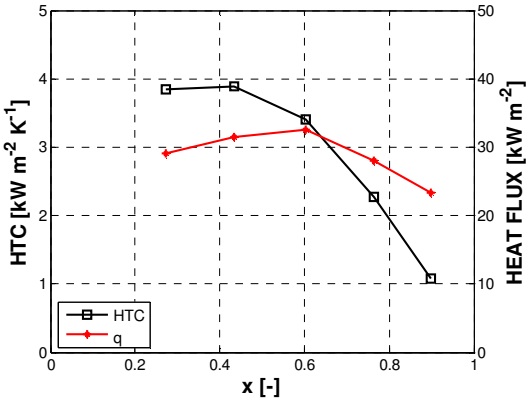

Figure 2.24. HTC and heat flux versus vapour quality for the vaporization test reported in the Figure 6 (G = 100 kg m^{-2} s^{-1}).

As previously seen, the heat flux is not an independent variable in the present measurements, thus it is not easy to separate the effect of heat flux from the effect of vapour quality. Therefore, much more data are needed to compare the experimental trends of the present heat transfer coefficients to those measured with Joule effect heating, at constant heat flux.

Figure 2.25 reports the heat transfer coefficients at constant heat flux for G = 50 kg m^{-2} s^{-1} and one can see that the heat transfer coefficient severely decreases after 0.6 vapour quality: this is in agreement with the information obtained from the standard deviation of the wall temperature readings.

Figure 2.26 and Figure 2.27 reports the same information for a mass velocity equal to 100 kg m^{-2} s^{-1} and 200 kg m^{-2} s^{-1} respectively: all the graphs show that the influence of heat flux on the HTC is limited for the tested conditions.

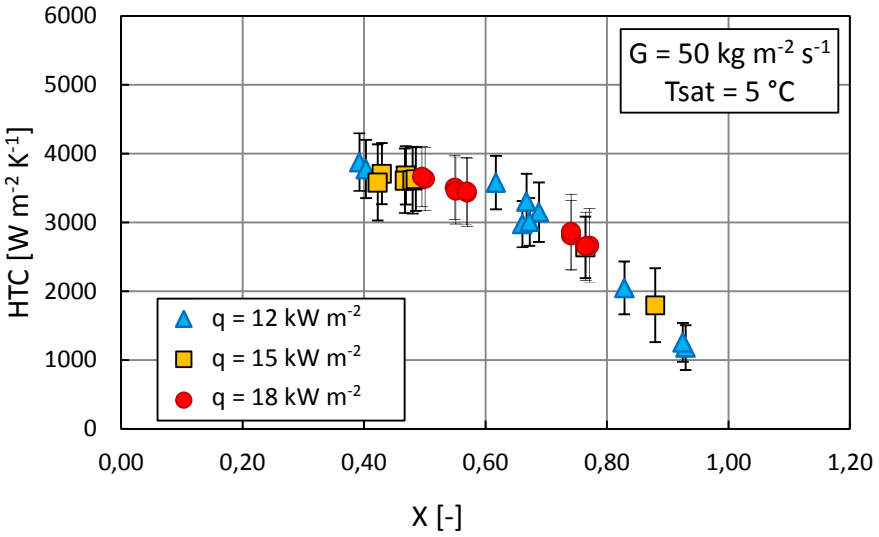

Figure 2.25. HTC versus vapour quality for different heat fluxes at G = 50 kg m⁻² s⁻¹.

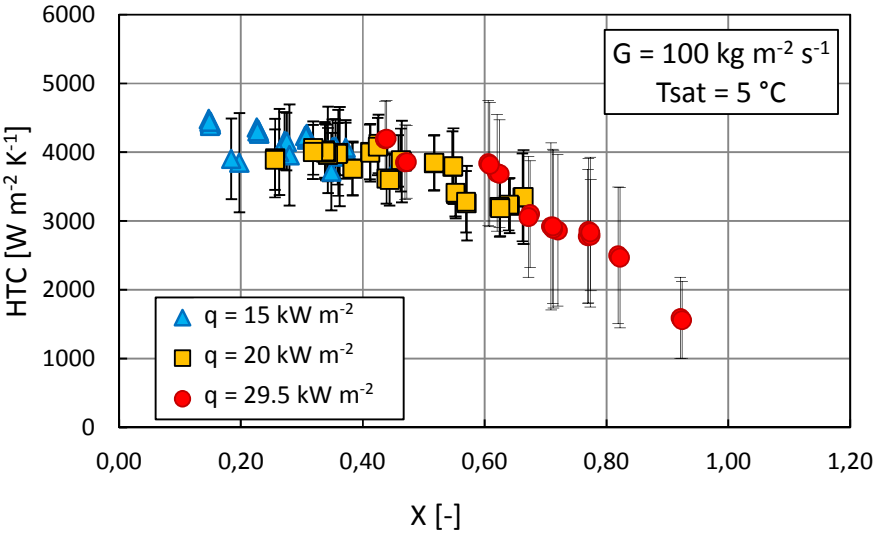

Figure 2.26. HTC versus vapour quality for different heat fluxes at G = 100 kg m⁻² s⁻¹.

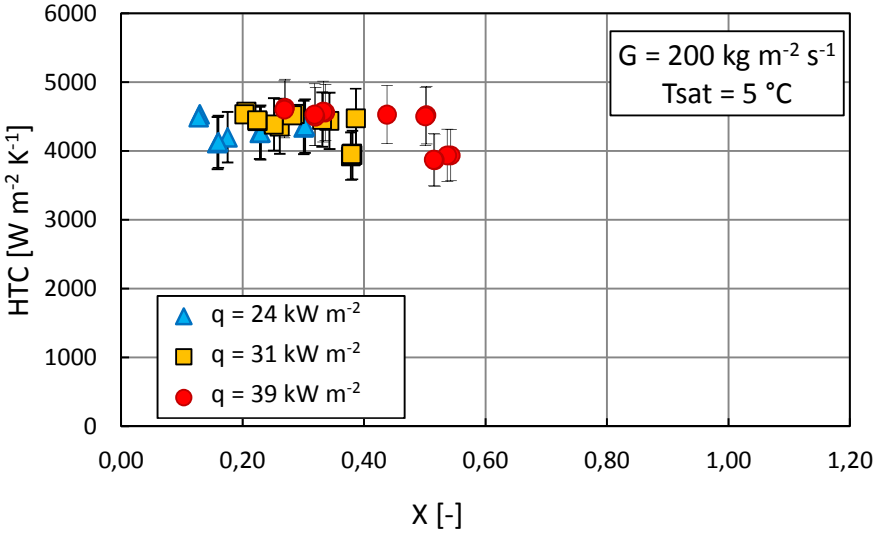

Figure 2.27. HTC versus vapour quality for different heat fluxes at G = 200 kg m⁻² s⁻¹.

2.6.3 Comparison with models

Because no predicting model has been developed for similar geometries, some comparison of the present preliminary data can be done with flow boiling models available in the open literature for conventional channels. Therefore, in the following, the heat transfer coefficients measured during vaporization tests have been compared with the predictions obtained from the Liu and Winterton (1991) correlation. This correlation, shown in Eq.(2.38), combines the Dittus Boelter (1985) equation for forced liquid convection of Eq.(2.39), multiplied by an enhancement factor *F*, Eq.(2.41), with the Cooper correlation, Eq.(2.40), for pool boiling inside tubes (thus the constant 55 is changed to 85), multiplied by a suppression factor *S*, Eq.(2.42).

$$HTC_{LW} = \left(\left(F\ HTC_F \right)^2 + \left(S\ HTC_{PB} \right)^2 \right)^{0.5} \tag{2.38}$$

$$HTC_F = 0.023\, Re^{0.8} Pr^{0.4} \left(\frac{\lambda}{D_h} \right) \tag{2.39}$$

$$HTC_{PB} = 85\ P_{red}^{\ 0.12} q^{2/3} \log_{10}\left(P_{red}^{\ -0.55} \right) M^{-0.5} \tag{2.40}$$

$$F = \left(1 + x\ Pr_l \left(\frac{\rho_l}{\rho_v - 1} \right) \right)^{0.35} \tag{2.41}$$

$$S = \left(1 + 0.055\ F^{0.1} Re_l^{0.16} \right)^{-1} \tag{2.42}$$

Figure 2.28 shows a comparison between experimental measurements and Liu and Winterton (1989) prediction for tests with R32 and vapour quality in the range 0.2 – 0.6.

The graphs highlight the fact that the experimental HTC is almost independent on heat and mass flux, while the correlation of Liu and Winterton (1989) predicts an important enhancement of HTC increasing these two parameters. Tests with G = 100 kg m^{-2} s^{-1} are predicted within ±25%, but the trend of data is not caught by the model.

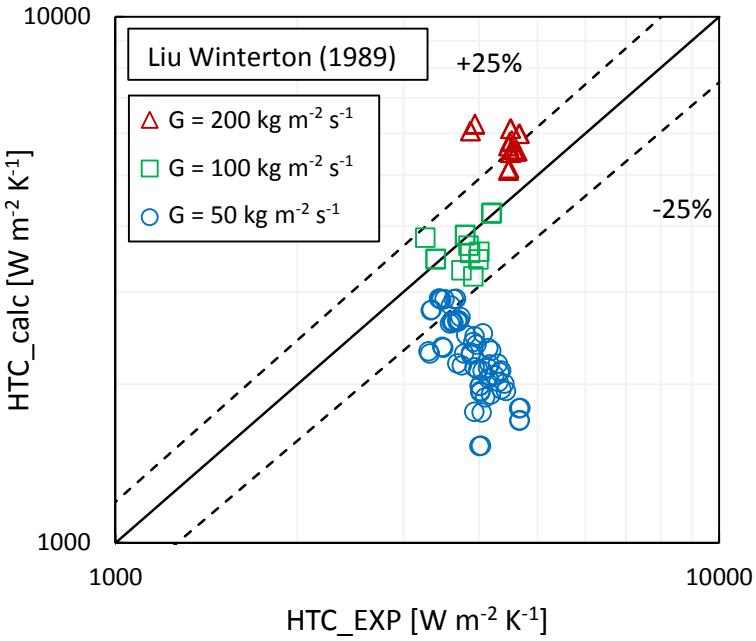

Figure 2.28. HTC during vaporization tests with R32 for different mass velocities: comparison between experimental measurements and Liu and Winterton (1989) correlation for data with vapour quality in the range 0.2 – 0.6.

2.7 Two phase heat transfer: condensation

The present study highlights the importance of parameters effects on heat transfer coefficient during condensation and on two-phase pressure drop, focusing on a better understanding of the condensation phenomena in minichannels. Furthermore, the experimental investigation are extremely important for the development of reliable predictive methods. For instance, Jige, Inoue and Koyama (2016) pointed out that some scientific studies have been proposed theoretical models and empirical correlations, however the local condensation heat transfer characteristics in the rectangular minichannel are not clarified sufficiently yet.

The heat transfer mechanism and pressure drop during condensation inside channels are intrinsically related to flow patterns , therefore, the flow patterns transitions have a strong effect on predicting heat and momentum transfer inside channels, as pointed out by several studies (Soliman, 1986; Garimella, 2004; Wang et al., 2002; Cavallini et al.; 2006; Park et al. 2011; Kim and Mudawar, 2012; Jige, Inoue and Koyama, 2016). Further, Coleman and Garimella (2003) has carried out experimental research on flow pattern transition, verifying that for similar hydraulic diameter, the flow pattern transitions are not strongly dependent on the tube shape or aspect ratio though.

The vapour shear stress and gravitational force are predominant effects during the condensation process inside conventional channels, instead of inside minichannels, the surface tension may be an important effect for low mass velocity. On the other hand, the vapour shear stress effect predominates under higher mass velocities for both micro- and macro-scale. Furthermore, a theoretical approach by Wang and Rose (2006, 2007, 2011) corroborates the influence of surface tension on liquid film thickness along the condensation inside micro-scale channels, by showing results solved numerically under the assumption of laminar condensate flow at low mass velocity. In this context, Da Riva et al. (2012) has reported a good agreement with the computational results by Wang and Rose (2006) for heat transfer coefficient at low mass velocities.

In addition, the condensation experimental results, reported by Wang et al. (2002), for rectangular minichannels suggest that surface tension may draw the condensate liquid into the corners, modifying the phase distribution along the channel, forming an annular liquid film at lower vapour velocity, and consequently, affecting the local average heat transfer coefficient. It would be expected an opposite tendency, as the condensate film decreases at lower vapour velocity. However, this behaviour have not been accurate on literature so far, as according to Derby et al. (2012), the shape of non-circular do not strongly affect the heat transfer coefficient.

Some experimental researches have been performed to study forced convective condensation heat transfer inside horizontal multiport minichannels including HCFC, HFC and CO_2, as presented by Yan and Lin, Wang et al. (2002), Koyama et al. (2003), Cavallini et al. (2005), Park and Hrnjak (2009), Agarwal et al. (2010), Derby et al. (2012), Kim and Mudawar (2012), Goss and Passos (2013), Heo et al. (2013), Sakamatapan et al. (2013), López-Belchi et al. (2015), Jige, Inoue and Koyama (2016). As expected, the heat transfer coefficient increases with mass velocity and vapour quality increasing. However, the tendencies of condensing heat flux and saturation temperature are not clearly consistent among studies from literature.

Yang and Webb (1996) and Sakamatapan et al. (2013) carried out an experimental study concerning condensation heat transfer inside multiport rectangular minichannels and they have observed the local heat transfer increases with local heat flux increasing, despite these studies have been used different technique for measuring the heat transfer coefficient.

Nevertheless, Yan and Lin (1999) has observed the opposite: local heat transfer coefficient increases with local heat flux decreasing. As pointed out by Ribatski and Da Silva and Ribastki (2016), the influence of local heat flux on heat transfer coefficient results is somewhat surprising, as expected that condensation heat transfer is dominated by convective effects, therefore, negligible effects of heat flux on heat transfer coefficient is expected as well. In addition, Shin and Kim (2004), Park et al. (2011), Derby et al. (2012) and Del Col et al. (2015) have found the local heat flux effect negligible on heat transfer coefficient during condensation.

Yan and Lin (1999), Park and Hrnjak (2009), Derby et al. (2012), Sakamatapan et al. (2013), Jige, Inoue and Koyama (2016) have performed experiments to investigate the effect of saturation temperature on condensation heat transfer coefficient for R134a and CO_2. Yan and Lin (1999), Park and Hrnjak (2009), Sakamatapan et al. (2013), Jige, Inoue and Koyama (2016) have found higher heat transfer coefficient at lower saturation temperature, even the experimental results by Park and Hrnjak (2009), which were performed for CO_2. According to the experimental results depicted by Yan and Lin (1999), it is possible to notice that saturation temperature effect enhanced at higher vapour quality condition, which is reasonable, considering that heat transfer coefficient enhances with two-phase mixture velocity increasing, due to augmenting the vapour specific volume, due to the saturation temperature decreasing. However, contradictory, Derby et al. (2012) has not found significant effect on condensation for R134a.

The heat transfer coefficient enhancement provided by micro-scale channels comes together with a pressure drop increasing, which brings negative impacts on the refrigerating system. The frictional pressure loss implies on decreasing the temperature saturation along the heat exchanger, which affects the driving temperature difference and, consequently, it decreases the overall efficiency of heat transfer rate.

Hence, many experimental studies have been performed to investigate the frictional pressure drop, and thus to developed prediction methods, such as proposed by Lockhart and Martinelli (1949), Chisholm (1967), Friedel (1979), Müller-Steinhagen and Heck (1986), based on empirical results for conventional channels, and Mishima and Ribiki (1996), Cioncolini et al. (2009), Del Col et al. (2013), Da Silva and Ribastki (2013), Jige, Inoue and Koyama (2016), which are based on micro-scale channels. Besides, fluid thermal characteristics are very relevant in two-phase heat transfer processes; however, the frictional pressure drop studies available on literature are mostly for HFC and HCFC refrigerants.

In the present paper, experimental results for quasi-local heat transfer coefficient during condensation and frictional pressure drop under adiabatic conditions inside multiport minichannels for R1234ze(E) and R32 are presented and compared to well-known prediction methods available on literature.

2.7.1 Experimental procedure

In order to obtain the HTC on the refrigerant side during condensation process, the superheater must ensure the complete vaporization of the refrigerant before the pre-section, in which the thermostatic bath allows to reach the desired superheating at the inlet of the test section. During these tests the saturation temperature is higher than ambient temperature, thus it is necessary to heat the tubes connected to the pressure transducers in order to avoid condensation, which can cause an incorrect measurement of pressure and pressure drop.
Data reduction and uncertainty analysis are performed as reported in 2.4.2 and 2.4.3 for single phase tests.

2.7.2 Experimental results

Condensation heat transfer coefficient: R1234ze(E)

The experimental values of the condensation heat transfer coefficient obtained with R1234ze(E) versus vapour quality are plotted in Figure 2.29: HTC decreases as vapour quality decreases, as expected, while the effect of mass flux is limited. Figure 2.30 to Figure 2.33 refer to different mass fluxes, showing the values of HTC versus vapour quality for different ΔT between saturation and wall temperature. This parameter seems to have an influence on the HTC for tests with the lowest mass flux (55 kg m^{-2} s^{-1}), while it does not affect the HTC in the other conditions.

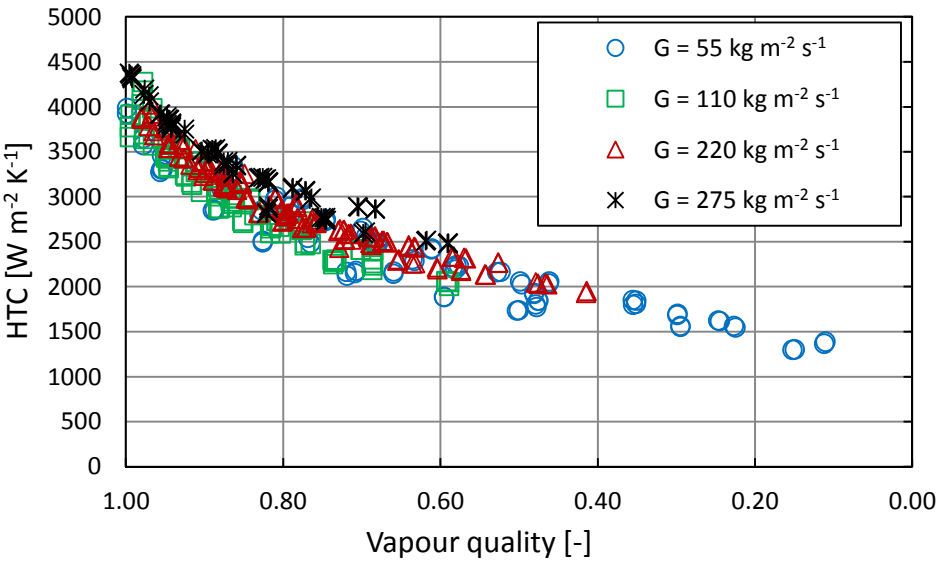

Figure 2.29. HTC versus vapour quality during condensation tests with R1234ze (E) with different mass fluxes.

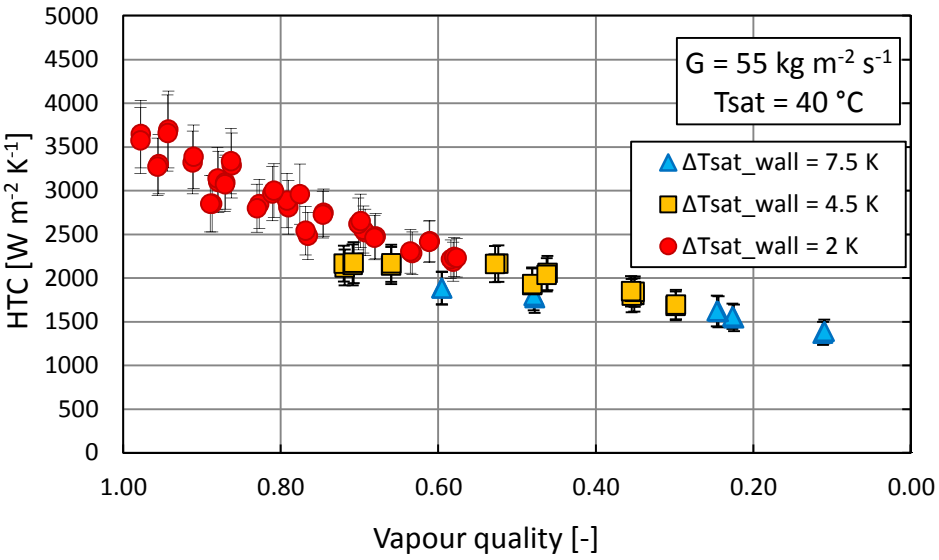

Figure 2.30. HTC versus vapour quality during condensation tests with R1234ze (E) at G = 55 kg m^{-2} s^{-1}. Series for three temperature differences between saturation and wall temperature.

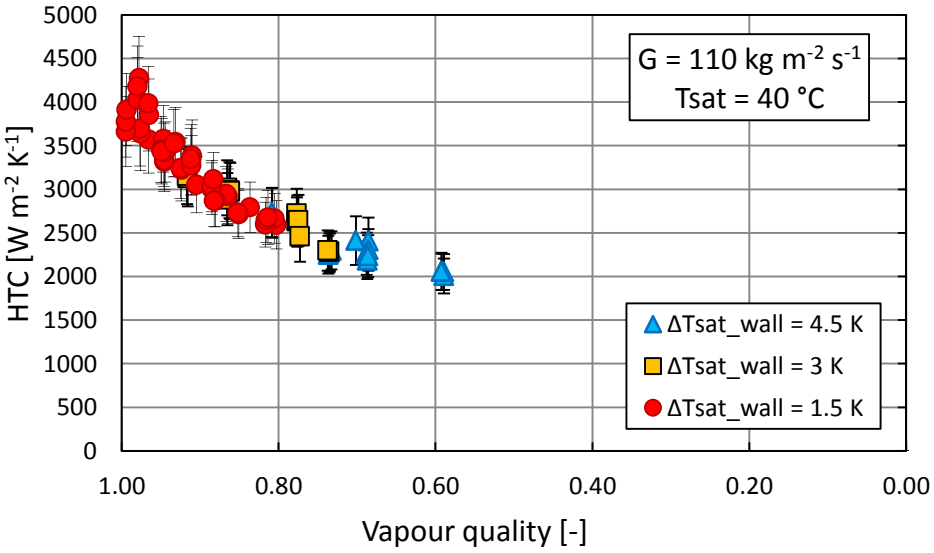

Figure 2.31. HTC versus vapour quality during condensation tests with R1234ze(E) at G = 110 kg m^{-2}s^{-1}. Series for three temperature differences between saturation and wall temperature.

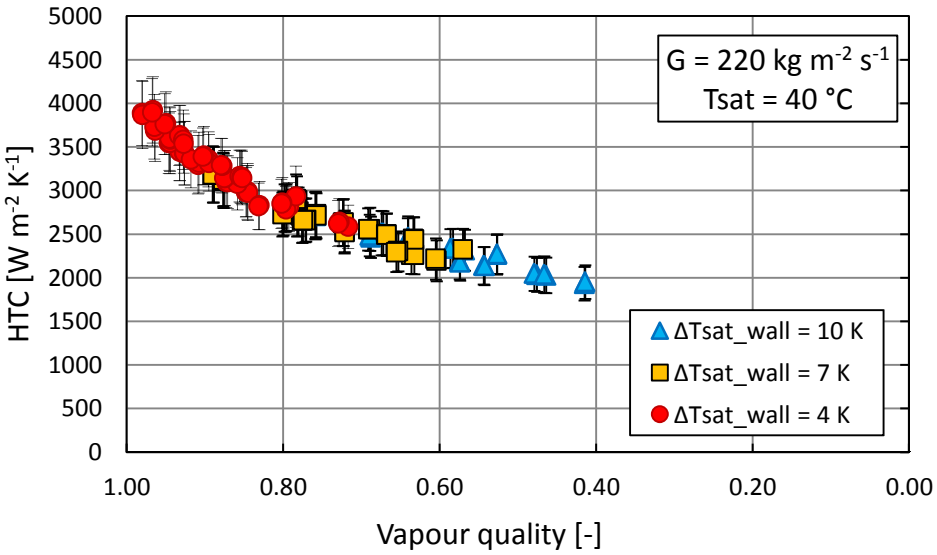

Figure 2.32. HTC versus vapour quality during condensation tests with R1234ze(E) at G = 220 kg m^{-2}s^{-1}. Series for three temperature differences between saturation and wall temperature.

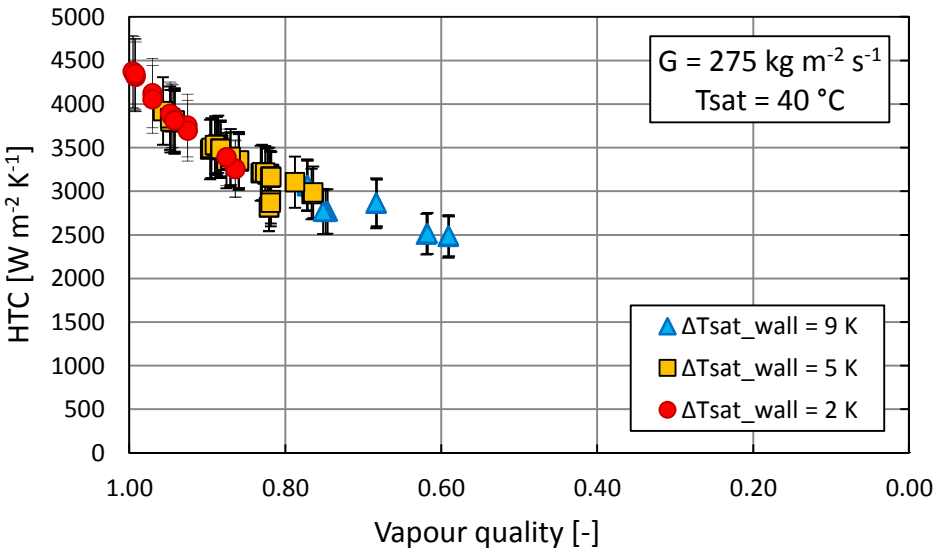

Figure 2.33. HTC versus vapour quality during condensation tests with R1234ze (E) at G = 275 kg m^{-2} s^{-1}. Series for three temperature differences between saturation and wall temperature.

Condensation heat transfer coefficient: R32

The next graphs report the experimental results obtained during condensation of R32. Figure 2.34 shows that HTC decreases as vapour quality decreases, while the effect of mass flux is limited, with the lowest mass flux that has slightly higher HTC. Figure 2.35 to Figure 2.37 refer to different mass fluxes, showing the values of HTC versus vapour quality for different ΔT between saturation and wall temperature. This parameter has a little influence on the HTC for tests with the lowest mass flux (55 kg m^{-2} s^{-1}), while it does not affect the HTC in the other conditions.

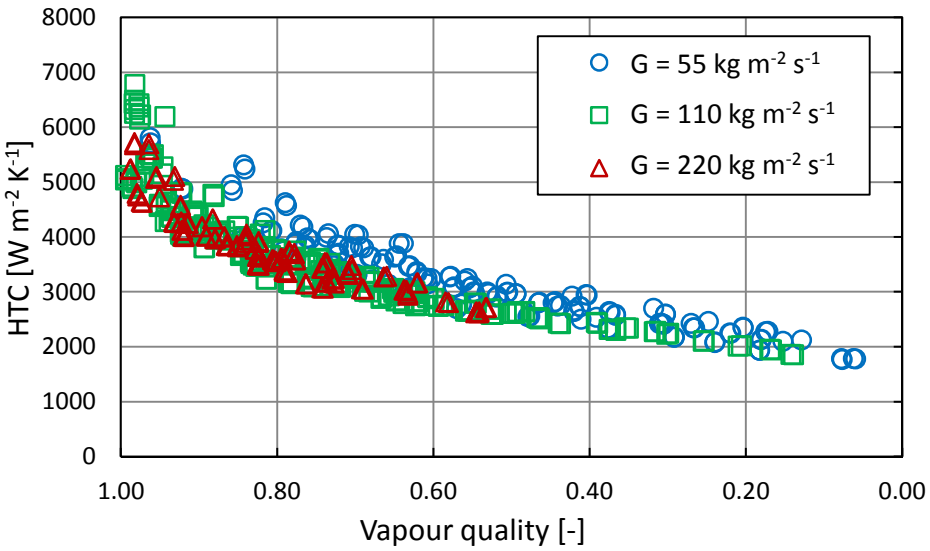

Figure 2.34. HTC versus vapour quality during condensation tests with R32 with different mass fluxes.

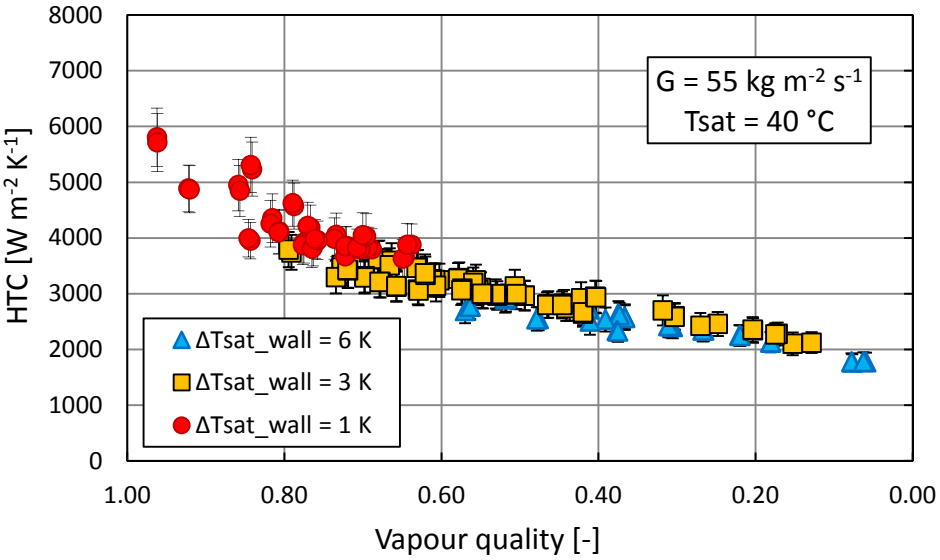

Figure 2.35. HTC versus vapour quality during condensation tests with R32 at G = 55 kg m^{-2} s^{-1}. Series for three temperature differences between saturation and wall temperature.

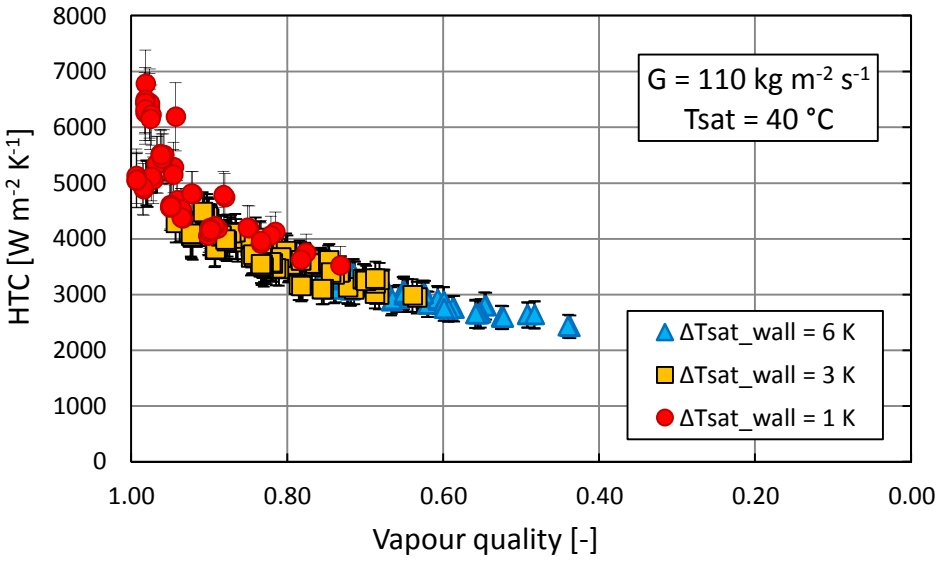

Figure 2.36. HTC versus vapour quality during condensation tests with R32 at G = 110 kg m^{-2} s^{-1}. Series for three temperature differences between saturation and wall temperature.

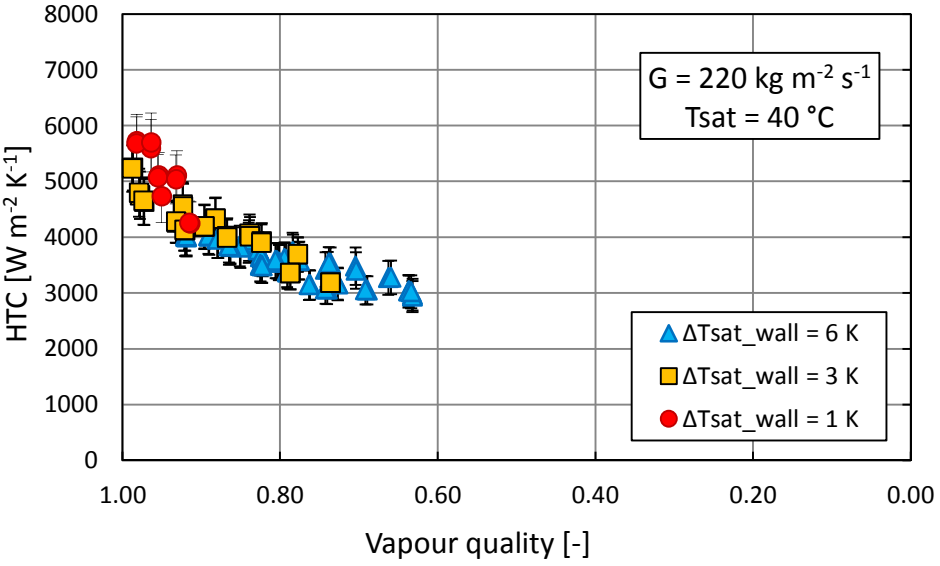

Figure 2.37. HTC versus vapour quality during condensation tests with R32 at G = 220 kg m^{-2} s^{-1}. Series for three temperature differences between saturation and wall temperature.

2.7.3 Comparison with models

The experimental database from the present study have been compared to predicted results of several semi-empirical methods and correlations for two-phase frictional pressure drop and condensation heat transfer coefficient available on literature. These prediction methods were developed based on macro and micro-scale channels, covering different channel shapes and sizes, working fluids, reduced pressure and aspect ratio.

Besides, in order to evaluate the prediction methods developed for heat transfer coefficients during condensation, a comparison among the experimental results for condensation of R32 and R1234ze(E) inside bar and plate heat exchanger with hydraulic diameter of 1.6 mm and 14 prediction methods available on literature is presented by Figure 2.38, Figure 2.39 and Figure 2.40.

The statistical results of all prediction methods in evaluation are shown by Table 2.7, which presents the mean absolute deviation *MAD*, calculated for the condensation heat transfer coefficient by Eq. (2.32) considering the heat transfer coefficient as the significant parameter γ.

The prediction method developed by Jige, Inoue and Koyama (2016) and Cavallini et al. (2006) provided the best predictions of the experimental results, with MAD = 17.5%, $\zeta_{20\%}$ = 77.6%, $\zeta_{50\%}$ = 94.4% and MAD = 17.7%, $\zeta_{20\%}$ = 62.2% and $\zeta_{50\%}$ = 97.8%, respectively. It is important to emphasize that the correlation proposed by Jige, Inoue and Koyama (2016) was developed based on experimental data characterized by parallel and multiport minichannel, despite of the correlation proposed by Cavallini et al. (2006), which also presented better predictions, it was developed based on macrochannel. However, the predictions obtained in general by the methods available on literature were not satisfactory, considering the predicted percentage fraction within ±20%. The characteristics regarding experimental parameters, such as channel geometry, scale and number of channel might affect the local heat transfer rate, which unable some correlations to predict well under certain conditions. Therefore, it is important to investigate experimentally further these effects on two-phase heat transfer characteristics, capturing the tendency and improving the predictions.

Table 2.7. Statistical parameters from the comparison between the HTC predictions and the experimental results.

Prediction methods	***MAD%***	$\zeta_{20\%}$	$\zeta_{50\%}$
Soliman (1968)	34.46	29.39	72.87
Traviss *et al.* (1973)	28.06	44.19	84.76
Cavallini and Zecchin (1974)	38.04	25.93	71.36
Shah (1979)	31.17	37.17	84.15
Soliman (1986)	30.58	41.74	78.14
Moser *et al.* (1998)	26.54	45.71	85.06
Dobson and Chato (1998)	40.73	26.36	66.42
Wang *et al.* (2002)	23.45	45.67	93.16
Koyama *et al.* (2003)	72.26	0.10	17.69
Cavallini *et al.* (2006)	17.71	62.15	97.79
Shah (2009)	30.33	37.71	85.69
Shah (2013)	24.59	52.08	89.94
Shah (2016)	26.67	40.91	91.60
Jige, Inoue and Koyama (2016)	17.54	77.65	94.41

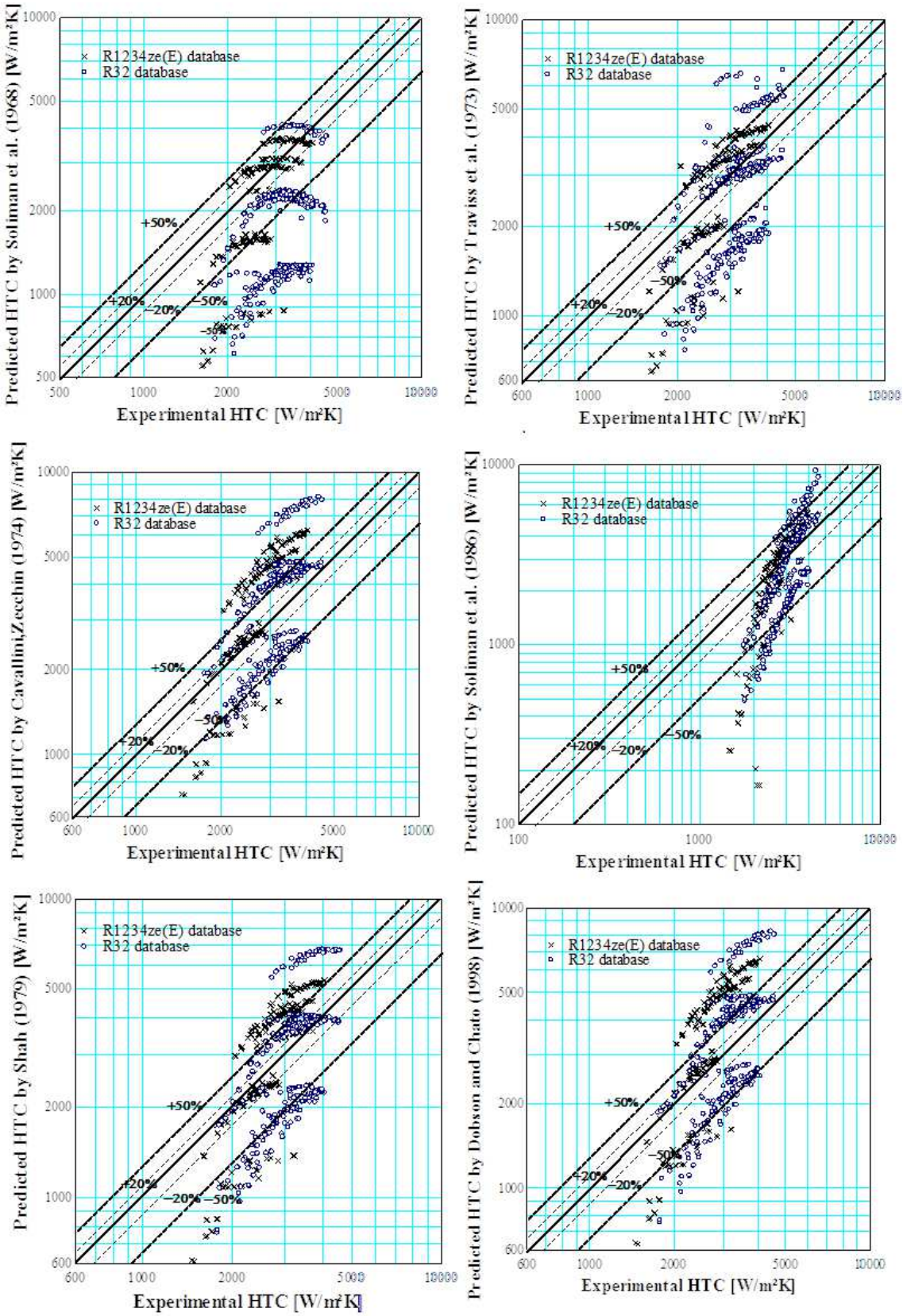

Figure 2.38. Comparison among experimental data for condensation heat transfer coefficient and prediction methods available on literature.

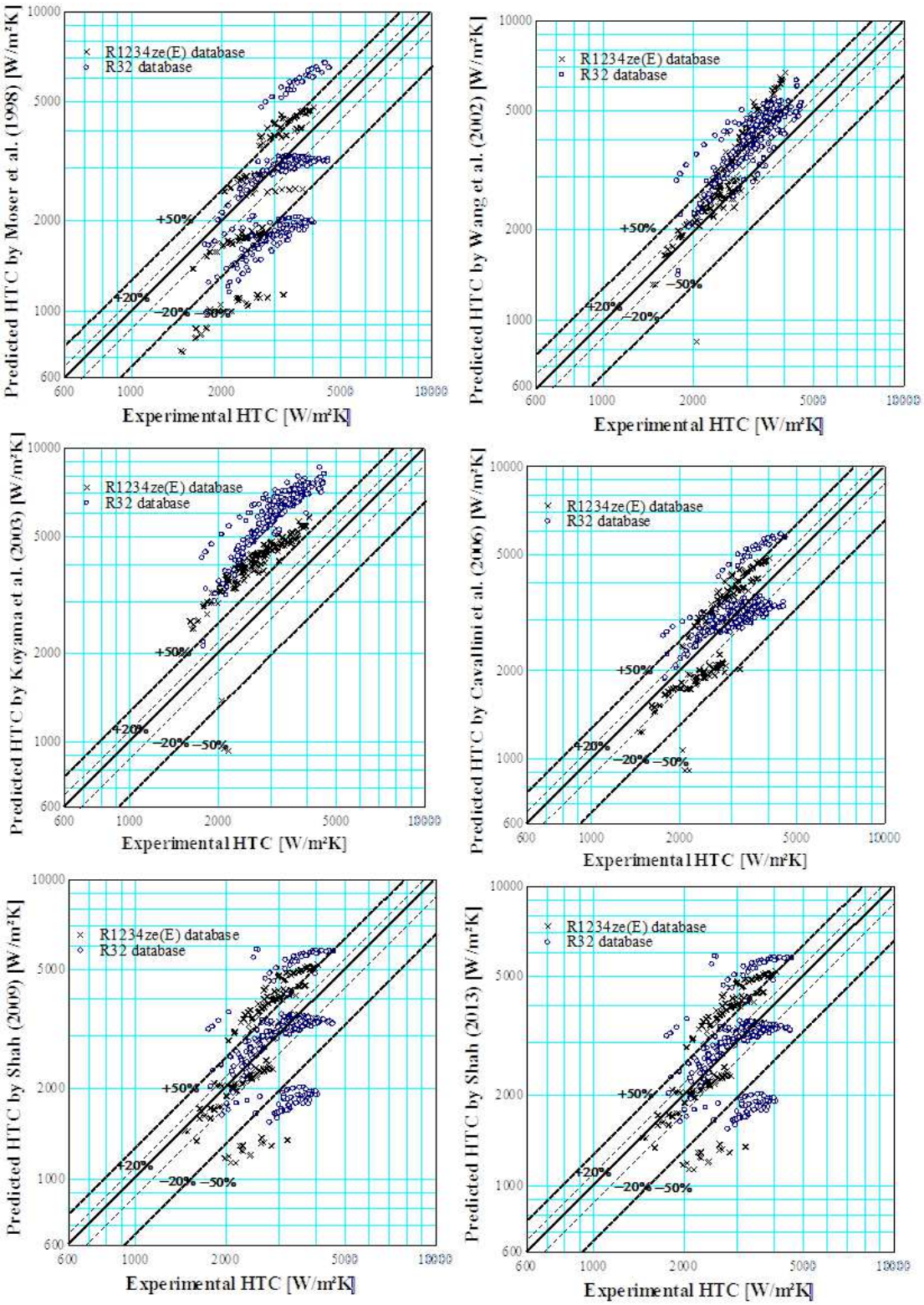

Figure 2.39. Comparison among experimental data for condensation heat transfer coefficient and prediction methods available on literature.

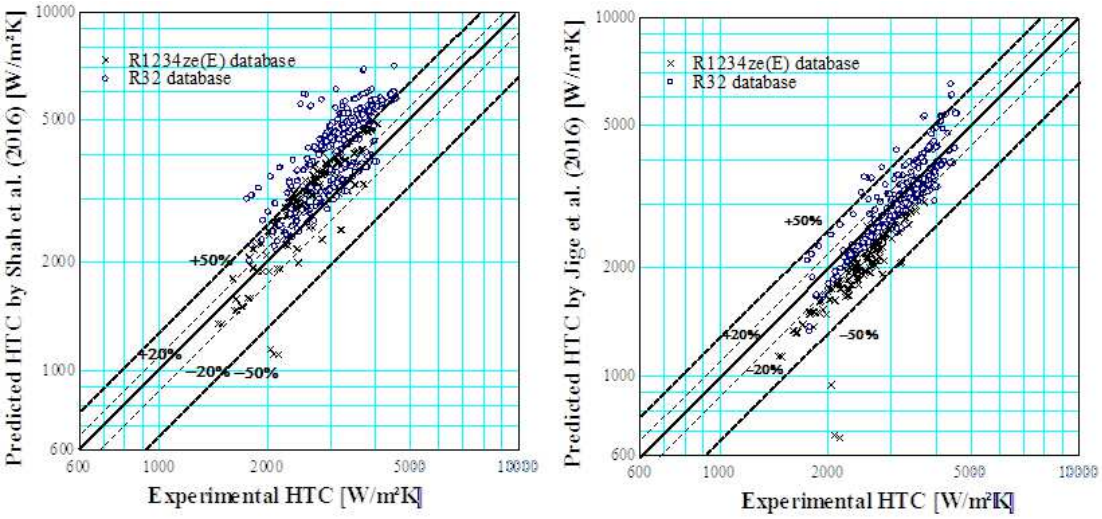

Figure 2.40. Comparison among experimental data for condensation heat transfer coefficient and prediction methods available on literature.

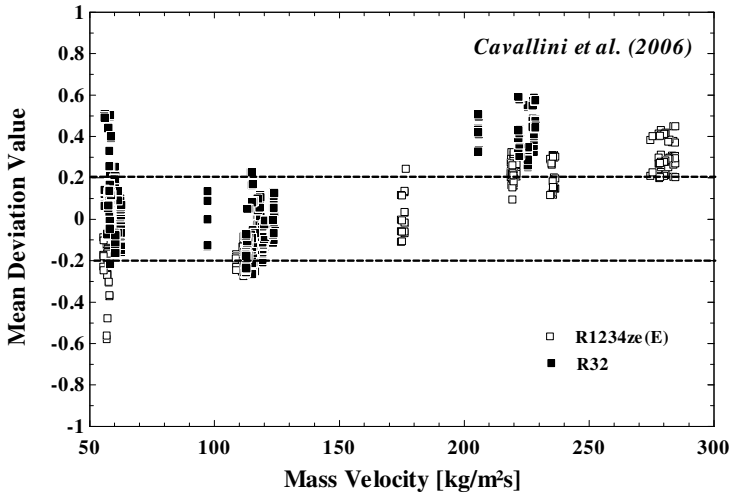

Figure 2.41. Evaluation of the deviation regarding the condensation heat transfer coefficient predicted results by Cavallini et al. (2006).

As presented previously for frictional pressure drop, the Figure 2.41 and Figure 2.42 present the deviation values of the results predicted by the best prediction methods assessed for local heat transfer coefficient during condensation inside micro-scale channels. The deviations are displayed by accordingly to mass velocity and fluid refrigerant.

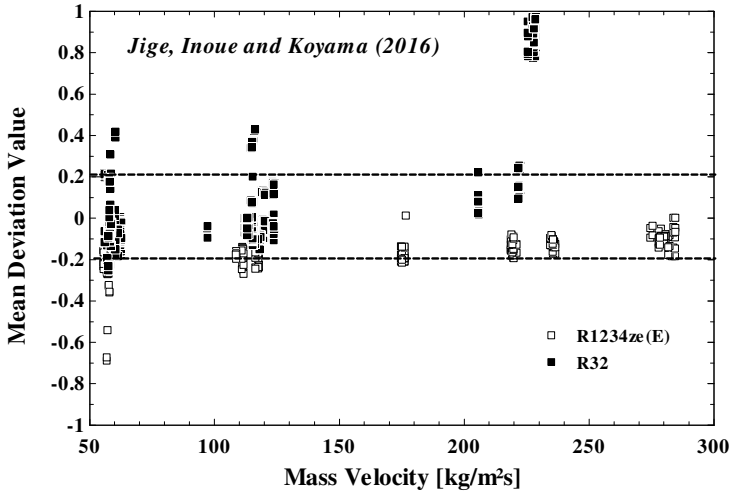

Figure 2.42. Evaluation of the deviation regarding the condensation heat transfer coefficient predicted results by Jige, Inoue and Koyama (2016).

2.7.4 Comparison between experimental HTC of R32 and R1234ze(E)

R1234ze(E) is a possible solution for the replacement of R134a due to its similar thermo physical properties and low GWP, but its performance are lower than R134a. As reported in Table 2.8, R32 has interesting thermo physical properties for condensation, like high latent heat and high liquid thermal conductivity, thus mixture of R32 and R1234ze(E) could be a way to replace R134a with a low GWP fluid that has similar or even higher performance. Figure 2.43 shows that in the present test section the HTC of R32 is 20 to 40% higher than that of R1234ze(E) during condensation at G = 110 kg m^{-2} s^{-1}. This experimental data can be used to assess the degradation of HTC in mixture of R32 and R1234ze(E) condensing in similar geometries.

Table 2.8. Thermo physical properties of R1234ze(E), R32 and R134a at 40°C of saturation temperature.

	P_{sat} [MPa]	ρ_L [kg m^{-3}]	ρ_V [kg m^{-3}]	h_{LV} [kJ kg^{-1}]	λ_L [mW m^{-1} K^{-1}]	Cp_L [kJ kg^{-1} K^{-1}]	μ_L [μPa s]	Pr_L [-]	GWP [-]
R1234ze(E)	0.77	1112	40.64	155	69	1.44	167	3.48	6
R134a	1.02	1147	50.09	163	75	1.50	161	3.24	1300
R32	2.48	893	73.27	237	115	2.16	95	1.79	550

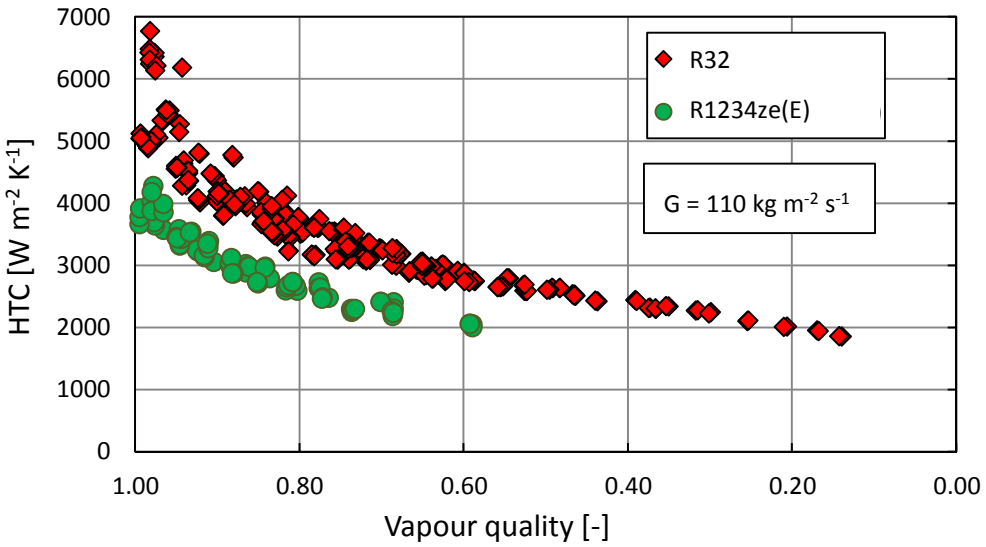

Figure 2.43. HTC versus vapour quality for condensation tests at G=110 kg m^{-2} s^{-1} with R32 and R1234ze(E).

2.7.5 Condensation of R1234ze(E) in the desuperheating region

During condensation tests, under conditions characterized by the presence of superheated vapor in the test section with a wall temperature lower than the saturation temperature, there is both latent and sensible heat transfer. Assuming the conventional driving temperature difference for condensation (T_{sat}-T_{wall}), as suggested by Webb (1998), leads to the experimental data reported in Figure 2.44a, where the HTC in the superheated region are smoothly connected to data with vapour quality lower than one. When the wall temperature is higher than the saturation temperature, the refrigerant temperature considered in the data reduction is the bulk temperature, thus, there is a sudden decrease in HTC that leads close to the values of single phase HTC predicted by Gnielinski (1976).

The same experimental data could be reduced using the refrigerant bulk temperature for all data with vapour quality higher than one. This leads to the HTC reported in Figure 2.44b, where experimental data in superheated region are compared to the prediction of HTC according to Kondou and Hrnjak (2012) for two different mass fluxes.

The prediction method proposed by Kondou and Hrnjak (2012) for the superheated region is expressed as

$$HTC = \left(HTC_{SH}\ \Delta T_{r\_sat} + HTC_{TP}\ \Delta T_{sat\_wall} \right) \Big/ \Delta T_{r\_wall} \tag{2.43}$$

Where HTC_{SH} is the single phase HTC evaluated with Gnielinski (1976) correlation with the correction factor proposed by Petukov (1970) and HTC_{TP} is the two-phase HTC evaluated with the correlation of Cavallini et al. (2006) assuming the same flow regime as vapour quality equal to one. The prediction by Kondou and Krnjak (2012) is in agreement with experimental data at the lowest mass flux, while data at G=220 kg m^{-2} s^{-1} are overestimated of 10 to 40%.

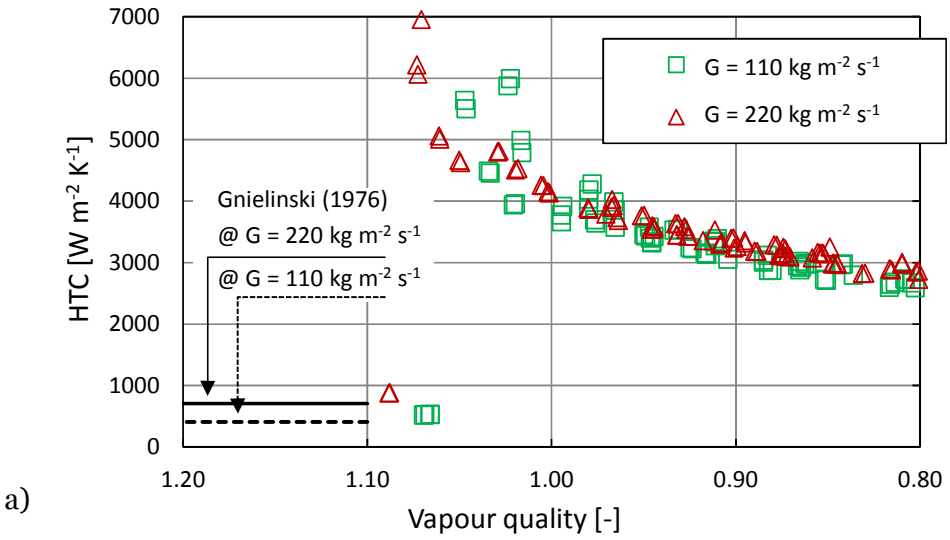

a)

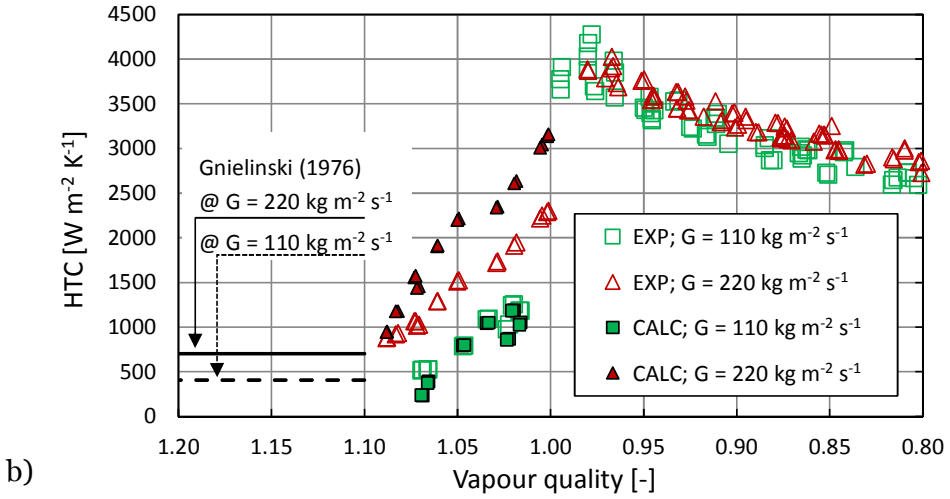

b)

Figure 2.44. HTC versus vapour quality close to saturated conditions for tests with R1234ze(E). Data reduction as suggested by: a) Webb(1998), b) Kondou and Hrnjak (2012).

3 Modelling of finned coil air to water heat exchangers

3.1 Air to water heat exchangers

3.1.1 Description of the model

This paragraph presents the numerical model developed in order to simulate the behaviour of finned coil heat exchangers working with air and water (or brine) in both winter and summer conditions. The method is based on the works of Fornasieri (1998), Casson (2000), Vardhan and Dhar (1997), where the heat exchanger is discretized in an arbitrary number of control elements and it is able to analyse the situations of completely dry or completely wet surface in each element.

To simplify the simulation model and decrease the computational effort, a number of simplifications are assumed. The first one is that the tubes disposition is considered inline, without any offset. The resulting error on the heat transfer performance is negligible. Thank to this assumption, it is possible to discretize the finned coil heat exchanger in a series of elementary sections composed by a portions of tube and the corresponding fins. The hypotheses underlying this approach are the following:

a) Each element can be analysed as an independent heat exchanger, neglecting the heat exchanged through the fins of two adjacent elements (this is true as long as the ΔT of the fluid inside the tubes is small, as in air conditioning applications);

b) The total finned area is equally divided between the elements;

c) An inline arrangement of the tubes is considered;

d) The air flow rate is supposed to be equally divided between the elements belonging to the first row;

e) All the air coming out from an element enters the following one along the air path;

f) The air properties are assumed to be uniform at the inlet of each element;

g) The elements are completely wet or completely dry;

h) In summer condition, where dehumidification occurs, the liquid film thickness is considered to be constant and the heat removed from the condensate moisture is neglected.

The arbitrary number of subdivisions of the tubes allows to change the number of elements in which the heat exchanger is divided. Table 3.1 reports the main input and output parameters of the model, while Figure 3.1 shows a schematic flow chart of the numerical model.

Table 3.1. Main input and output parameters of the numerical model.

INPUT	**OUTPUT**
Geometry; Thermal properties of tubes and fins; Inlet condition of fluids.	Total heat flow rate; Sensible and latent heat flow rate; Mass flow rate of condensate; Outlet condition of fluids.

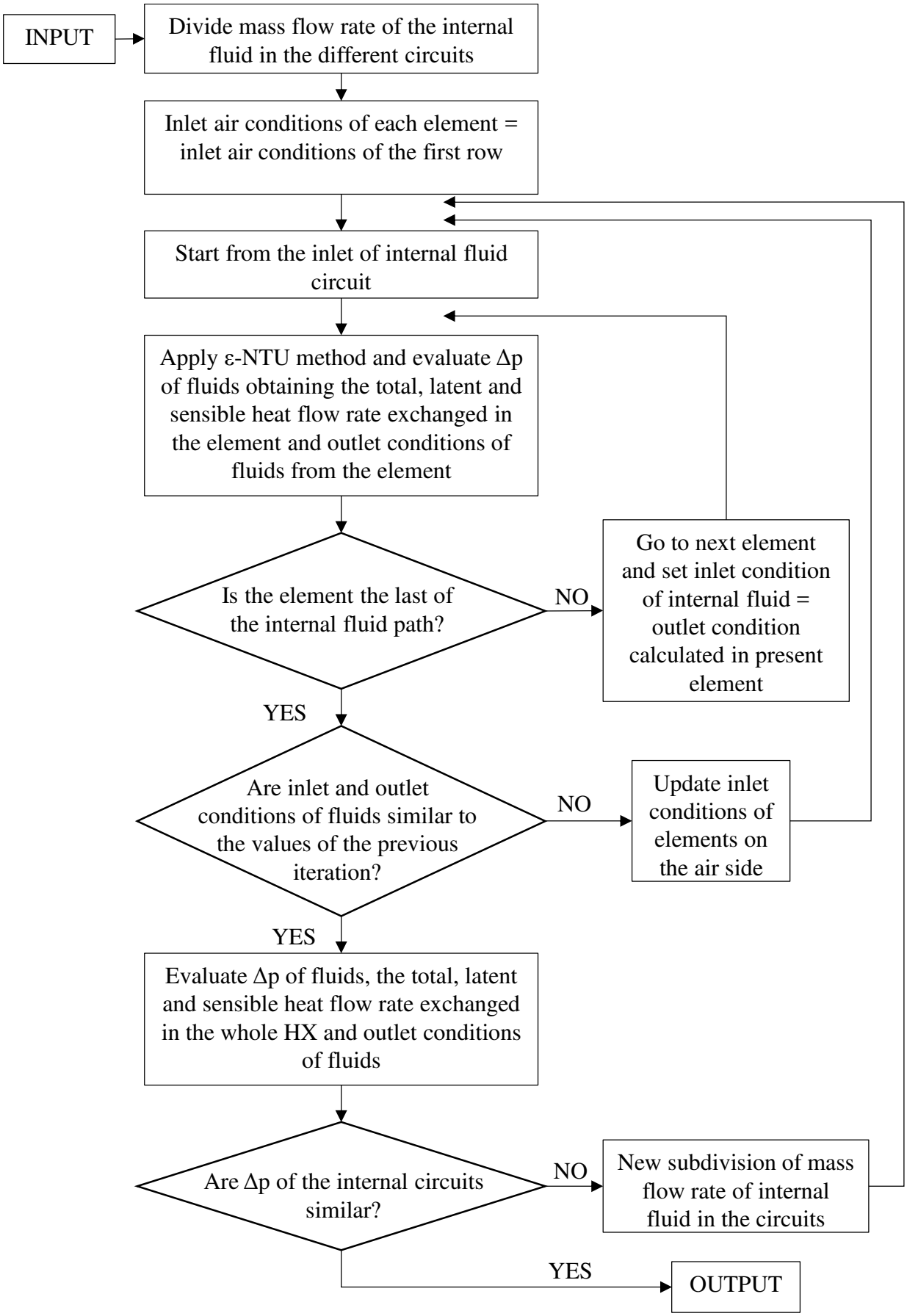

Figure 3.1. Flow chart of the numerical model for finned tube heat exchangers.

From the flow chart, it is possible to see that the model starts reading the input and evaluates a first guess for the distribution of the mass flow rate inside the tubes of the different circuits. The inlet conditions on the air side of each element are set equal to the inlet of the first row.
All the elements are considered as heat exchangers and the conditions of fluids at the outlet of each of them are evaluated through the ε – NTU method, using the correlations that will be later reported.
The resolution of the elements starts from the inlet of the internal fluid and follows its path through the finned tubes, setting the inlet conditions of the following element as the outlet conditions evaluated in the previous one.
Once the all the elements are considered, the inlet conditions of each element are compared to the inlet conditions of the previous iteration. If the difference of these parameters between the iterations is lower than specified values, the model evaluates the main output and the pressure drop of the internal fluid in the different circuits; otherwise, it updates the inlet conditions of all the elements on the air side and starts again from the inlet of the internal fluid.
The heat transfer process might change the temperature of the internal fluid in the model so that the pressure drop in the circuits differs from what expected in the first guess. Therefore, the program compares the pressure drop of the circuits and eventually updates the subdivision of the mass flow rate, starting again the calculations from the inlet of the internal fluid.
The following paragraphs explain the details of the calculations performed in the model.

Main geometrical parameters

The main geometrical input requested by the model are reported in Table 1.1.
The model reads the input and evaluates the fundamental geometric variables as follows.
Number of fins:

$$N_f = \frac{L}{X_f} \tag{3.1}$$

The fin height, H_f, and length, L_f, in the direction of air flow:

$$H_f = N_t \cdot X_t \tag{3.2}$$

$$L_f = N_R \cdot X_l \tag{3.3}$$

The frontal area of the entire heat exchanger:

$$A_{fr} = L \cdot H_f \tag{3.4}$$

The air passage area, which is affected by the physical presence of the tubes and the fins:

$$A_{pass,a} = \left(L \cdot H_f\right) - \left[\left(L - s_f N_f\right) D_e N_t - s_f N_f H_f\right] \tag{3.5}$$

The passage area of the internal fluid tubes:

$$A_{pass,fl} = \frac{\pi}{4} D_i^2 \tag{3.6}$$

Finally, the internal and external heat transfer areas of the heat exchanger are:

$$A_i = \pi D_i L N_t \tag{3.7}$$

$$A_e = \pi D_e \left(L - s_f N_a \right) + 2\left[\frac{\pi}{4} \left(D_f - D_e \right)^2 N_a \right] \tag{3.8}$$

Regarding a single element, the length *dL* of along the tube is calculated as:

$$dL = \frac{L}{Ndz} \tag{3.9}$$

Where Ndz is the number of subdivisions along the tube.
The internal and external heat transfer areas are, for each control element:

$$A_i = \pi D_i dL \tag{3.10}$$

$$A_e = \left\{ \pi D_e \left(L - s_f N_a \right) + 2\left[\frac{\pi}{4} \left(D_f - D_e \right)^2 N_a \right] \right\} \cdot \frac{dL}{L} \tag{3.11}$$

Maximum heat flow rate

Once the fundamental geometric values are calculated, the program starts calculating the mass flow rate of fluids. Since the input parameter for both sides is the volumetric flow rate, the model evaluates the density of the two fluids. The density of the internal fluid is evaluated with Refprop 9.1 (NIST), while the air density is given by:

$$\rho_{a,IN} = \left(1 - \frac{x_{a,IN}}{x_{a,IN} + 0.62198} \right) \cdot \left(1 + x_{a,IN} \right) \cdot \frac{p_a}{287,08 T_{a,IN}} \tag{3.12}$$

Where $x_{a,IN}$ is calculated as:

$$x_{a,IN} = 0.62198 \cdot \frac{p_{v,IN}}{p_a - p_{v,IN}} \tag{3.13}$$

And $p_{v,IN}$ is given by:

$$p_{v,IN} = p_{v,\mathrm{SAT}|\mathrm{T_{a,IN}}} \cdot \frac{UR}{100} \tag{3.14}$$

In order the find the total heat flow rate, the ε-NTU method evaluates the efficiency of the heat exchanger and multiplies this parameter for the maximum value of heat flow rate that can ideally be exchanged between the two fluids.
In an ideal heat exchanger, the outlet temperature of a fluid *A* is the inlet temperature of the other fluid *B*, and the maximum heat flow rate for the fluid *A* is

$$\dot{Q}_{A,MAX} = \dot{m}_A c_A \left| t_{B,\mathrm{IN}} - t_{A,\mathrm{IN}} \right| \tag{3.15}$$

For the fluid *B* we could write, similarly,

$$\dot{Q}_{B,MAX} = \dot{m}_B c_B \left| t_{B,\mathrm{IN}} - t_{A,\mathrm{IN}} \right| \tag{3.16}$$

If the products of mass flow rate times the thermal capacity of the two fluids are different, the two heat flow rates will be different and the maximum heat flow rate that can be exchanged would have two values.

This means that the maximum that we can obtain is the minimum between $\dot{Q}_{A,MAX}$ and $\dot{Q}_{B,MAX}$.

Thus, we need to evaluate the maximum value of heat flow rate on the internal and external side and pick up the minimum between the two values.

The maximum value of heat flow rate that can be reached on the internal side is:

$$\dot{Q}_{fl,MAX} = \left| \dot{m}_{fl} c_{fl} \left(T_{fl,\mathrm{IN}} - T_{\mathrm{a,IN}} \right) \right| \tag{3.17}$$

While the air, in the best case, can reach the inlet temperature of the internal fluid maintaining its absolute humidity (if $t_{fl,IN}$ is higher than the dew point temperature of the air), thus maximum heat flow rate is:

$$\dot{Q}_{a,MAX} = \left| \dot{m}_{a} c_{a} \left(T_{fl,\mathrm{IN}} - T_{\mathrm{a,IN}} \right) \right| \tag{3.18}$$

or with a relative humidity of 100% (if the inlet water temperature is lower than the dew point temperature of air), thus maximum heat flow rate is evaluated using the inlet enthalpy of air and the enthalpy of air in saturated conditions at the inlet temperature of the internal fluid:

$$\dot{Q}_{a,MAX} = \left| \dot{m}_{\mathrm{a}} \left(i_{\mathrm{a,IN}} - i_{\mathrm{a,SAT|T}_{fl,\mathrm{IN}}} \right) \right| \tag{3.19}$$

Finally, the maximum heat flow rate that can be exchanged in the unit is

$$Q_{MAX} = \min \left(Q_{air,MAX}, Q_{f,MAX} \right) \tag{3.20}$$

Definition of the circuitry

Each tube has an index number ranging between 1 and the product $N_R \cdot N_t$ (number of rows times the number of tubes per row). The paths of the internal fluid in the different circuits are described by the sequence of these numbers and are given as input to the model.

The heat exchanger is divided in a number of elements equal to:

$$N_{elements} = N_R \cdot N_t \cdot N\,dz \tag{3.21}$$

An index is assigned to each element depending on its position and the resolution of the model is performed examining the elements one by one, following the path of the internal fluid.

Mass flow rate of internal fluid inside the circuits

As described before, initially a mass flow rate and a mean temperature are hypothesized equal in each circuit:

$$\dot{m}_{fl,i} = \frac{\dot{m}_{fl,TOT}}{N_{circuits}} \tag{3.22}$$

$$T_{fl,mean,i} = T_{fl,IN} \tag{3.23}$$

The resolution method chosen in order to determine the internal fluid mass flow rate is the multidimensional method of Newton, which allows to identify real solutions of systems composed of

n non-linear equation with *n* unknown variables. An *X* array is then created: this array contains the values of the *n* mass flow rates.

$$X = \left(\dot{m}_{fl,1}, \dot{m}_{fl,2}, \dot{m}_{fl,3}, ..., \dot{m}_{fl,i}, ..., \dot{m}_{fl,n}\right) \tag{3.24}$$

A function $f(m)$ that evaluates the internal pressure drop is then defined. The function f_i is calculated as the difference between the Δp calculated in the circuit i and the one calculated in the n^{th} circuit:

$$f_i = f\left(\dot{m}_i\right) - f\left(\dot{m}_n\right) = \Delta p_{fl,TOT,i} - \Delta p_{fl,TOT,\mathrm{n}} \tag{3.25}$$

In the n^{th} circuit, the function is defined differently:

$$f_n = \dot{m}_{fl,TOT} - \left(\dot{m}_{fl,1} + \dot{m}_{fl,2} + ... + \dot{m}_{fl,n}\right) \tag{3.26}$$

Then the vector valued function $F(X)$ is defined as:

$$F(X) = \begin{bmatrix} f_1 \\ f_2 \\ \vdots \\ f_i \\ \vdots \\ f_{n-1} \\ f_n \end{bmatrix} \tag{3.27}$$

The next step is to approximate $F(X)$ with a first order Taylor series.

$$F(X) \sim F\left(X^{(k)}\right) + F'\left(X^{(k)}\right) \cdot \left(X - X(k)\right) \tag{3.28}$$

Where $F'\left(X^{(k)}\right)$ is the Jacobian matrix:

$$F'(X^{(k)}) = \begin{bmatrix} \frac{\partial f_1}{\partial x_1} & \cdots & \frac{\partial f_1}{\partial x_n} \\ \vdots & \ddots & \vdots \\ \frac{\partial f_n}{\partial x_1} & \cdots & \frac{\partial f_n}{\partial x_n} \end{bmatrix} \tag{3.29}$$

In this specific case, this matrix has values different from zero only in the diagonal, in the last row and in the last column.

$$F'(X^{(k)}) = \begin{bmatrix} \frac{\partial f_1}{\partial x_1} & 0 & \cdots & 0 & \frac{\partial f_1}{\partial x_n} \\ 0 & \frac{\partial f_2}{\partial x_2} & 0 & \cdots & \frac{\partial f_2}{\partial x_n} \\ \vdots & & \ddots & & \vdots \\ 0 & \cdots & & \frac{\partial f_{n-1}}{\partial x_{n-1}} & \frac{\partial f_{n-1}}{\partial x_n} \\ -1 & -1 & \cdots & -1 & -1 \end{bmatrix} \tag{3.30}$$

The iterative procedure uses the following expression to evaluate the new values of the mass flow rates:

$$X^{(k+1)} = X^{(k)} - \left[F'\left(X^{(k)}\right) \right]^{-1} F(X^{(k)}) \tag{3.31}$$

The convergence is controlled by the relative percentage difference of all values of the *X* array in two subsequent iterations.

$$\Delta m_{fl\%} = \max \left| \frac{X^{(k)} - X^{(k+1)}}{X^{(k+1)}} \right| \cdot 100 \tag{3.32}$$

The model stops the iterations when $\Delta m_{w\%} < 0.1\%$. Once the flow rate is calculated in each circuit, the model proceeds in the solution of the model, as will be described later. The same relative percentage difference is then calculated with the internal pressure drop in each circuit, defined as:

$$\Delta p_{\%} = \frac{\Delta p_{MAX} - \Delta p_{MIN}}{\Delta p_{MIN}} \cdot 100 \tag{3.33}$$

If $\Delta p < 0.1\%$ then the flow rate calculated is correct. Otherwise, it is necessary to calculate again the fluid flow rate with the sequence described before.

Resolution method and input assignment at first step

The characteristic of this program is to resolve each control element as a stand-alone heat exchanger, obtaining the output values, which are assigned as input of the following element for both internal and external fluid.

The first attempt is realized supposing the same temperature and humidity of air at the inlet of each element, assumed to be equal to the ones of the first row.

The variables that must converge for each element are the input air temperature, air humidity and the output water temperature. The minimum acceptable differences between the values of two iterations are:

$$dT_{a,IN} = 0.01\ K \tag{3.34}$$

$$dx_{a,IN} = 0.001 \frac{kg_v}{kg_{a.s.}} \tag{3.35}$$

$$dT_{fl,OUT} = 0.01\,K \tag{3.36}$$

In each element, the input variables are assigned equal to the output of the previous element. For each element, the ε - NTU method is applied to find the outlet conditions.

Internal side correlations for HTC

The first step in the study of the internal side is the evaluation of the Reynolds number:

$$Re_{fl} = \frac{\rho_{fl} u_{fl} D_i}{\mu_{fl}} \tag{3.37}$$

If the Reynolds number is equal or greater than 3000 then the flow is turbulent: the Gnielinski (1976) semi-empirical correlation is used in order to calculate the internal heat transfer coefficient.

$$Nu_{turb} = \frac{\frac{f_{fl}}{8}\left(\mathrm{Re}_{fl} - 1000\right) Pr_{fl}}{1 + 12.7\sqrt{\frac{f_{fl}}{8}}\left(Pr_{fl}^{2/3} - 1\right)} \cdot f_p \cdot \left[1 + \left(\frac{D_i}{dL}\right)^{\frac{2}{3}}\right] \tag{3.38}$$

Where $f_{w,el}$ is the Petukhov's friction factor:

$$f_{fl} = \left(1.82 \log\left(Re_{fl}\right) - 1.64\right)^{-2} \tag{3.39}$$

And f_p is the corrective Petukhov factor.

If the Reynolds number is lower than 2300, the Nusselt number is function of Graetz number which has two different definitions based on the value of Reyonlds number:

If $\mathrm{Re}_{fl} < 2300$

$$Gz = Re \cdot Pr \cdot \left(\frac{D_i}{dL}\right) \tag{3.40}$$

If $\mathrm{Re}_{fl} \geq 2300$

$$Gz = 2300 Pr \cdot \left(\frac{D_i}{dL}\right) \tag{3.41}$$

and the Shah and London (1978) correlation is used:

If $1/Gz > 0.03$

$$Nu_{lam} = 4.364 + 0.0722 \cdot Gz \tag{3.42}$$

If $1/Gz \leq 0.03$

$$Nu_{lam} = 1.953 \cdot Gz^{\frac{1}{3}} \tag{3.43}$$

In the transition between laminar and turbulent flow, when $2300 \le \mathrm{Re}_{fl} \le 3000$, the Nusselt number is calculated as a combination between the values for laminar and turbulent flow regime.

$$Nu = Nu_{lam} + \left(Re_{fl} - 2300\right) \cdot \left(\frac{Nu_{turb} - Nu_{lam}}{3000 - 2300}\right) \tag{3.44}$$

Once the Nusselt number is evaluated, the heat transfer coefficient of the internal side HTC_{fl} can be calculated:

$$HTC_{fl} = \frac{Nu\ \lambda_{fl}}{D_i} \tag{3.45}$$

Consequently, the global heat transfer coefficient, referred to the internal exchange area, is:

$$U_i = \frac{1}{\frac{1}{HTC_{fl}} + \frac{A_i \ln\left(\frac{D_e}{D_i}\right)}{2\pi\lambda_t\ dL}} \tag{3.46}$$

External side correlations for HTC

The external fluid that flow outside of the tubes is humid air. The correlation chosen to evaluate the heat transfer coefficient on the external side, HTC_a, is the one proposed by Abu Madi (1998). This correlation is among the most used in the study of finned coil heat exchangers. The characteristic length used in the evaluation of Reynolds number is the hydraulic diameter, defined as:

$$D_{h,a} = \frac{4\left(X_f - s_f\right)\left(X_t - D_e\right)X_l}{2\left(X_t X_l - \frac{\pi D_e^2}{4}\right) + \pi\left(X_f - s_f\right)D_e} \tag{3.47}$$

This correlation is applied when $200 \le \mathrm{Re}_{D_h,a} \le 6000$. The Colburn factor j for a 4-row finned coil is given by:

$$j_4 = \left(\mathrm{Re}_{D_{h,a}}\right)^{-0.44} \left(R_4\right)^{-3.07} \left(R_{5,1}\right)^{0.37} \left(R_7\right)^{-6.14} \left(R_9\right)^{-2.13} \tag{3.48}$$

And the same Colburn factor for a generic N_R number of rows is:

$$j_N = \frac{j_4}{0.87 + 0.0000143\left(\mathrm{Re}\right)^{0.55} \left(N_r\right)^{-0.67} \left(R_3\right)^{-3.13} \left(R_{5,1}\right)^{4.95}} \tag{3.49}$$

Where the dimensionless groups R_i are reported in Table 3.2.

Table 3.2. Dimensionless numbers used in the correlation of Abu Madi (1998).

R_i	*equation*	*validity field*
R_3	$\frac{D_e}{D_i}\left(1-\frac{s_f}{X_f}\right)+2\frac{X_t X_l}{\pi D_i X_f}-\frac{D_e^2}{2D_i X_f}+2\frac{X_f s_f}{\pi D_i X_f N_r}$	$7.26-19.3$
R_4	$\frac{X_t X_f}{\left(X_t-D_e\right)\left(X_f-s_f\right)}$	$1.77-2.25$
R_5	$\frac{\pi D_e N_r\left(1-\frac{s_f}{X_f}\right)}{X_t}+\frac{N_r}{X_t}\left(2X_l-\frac{\pi D_e^2}{2X_t}+\frac{2s_f}{N_r}\right)$	/
$R_{5,1}$	$\frac{R_5}{N_r}$	$11-21.8$
R_7	$\frac{1}{1+\frac{2\pi D_e\left(X_f-s_f\right)}{4X_t X_l-\pi D_e^2+\frac{4X_t s_f}{N_r}}}$	$0.86-0.95$
R_8	$\frac{X_f}{D_e}$	$0.16-0.27$
R_9	$\frac{X_l}{D_e}$	$1.6-2.21$

Then, the Nusselt number is:

$$Nu = j_N Re_{D_h,a}\, Pr^{\frac{1}{3}} \tag{3.50}$$

If $Re_{D_h,a} < 200$ then the Colburn factor is evaluated with the Gray correlation [8]:

$$j_4 = 0.14\left(Re_{D_e}\right)^{-0.328}\left(\frac{X_t}{X_l}\right)^{-0.502}\left(\frac{X_f}{D_e}\right)^{0.0312} \tag{3.51}$$

$$\frac{j_{N_r}}{j_4} = 0.911\left[2.24\left(\mathrm{Re}_{D_e}\right)^{-0.092}\left(\frac{row}{4}\right)^{-0.031}\right]^{0.607(4-row)} \tag{3.52}$$

Where "row" is used to indicate the number of the row the element belongs to. When the air side is considered, two different case must be studied: dry condition, with only sensible heat exchange, and wet condition, with dehumidification that causes mass and heat transfer. The distinction between the two cases depends on the interface temperature T_{int}, defined as:

$$T_{\text{int}} = \frac{T_{tube}A_{tube} + T_{fin}A_{fin}}{A_e} \tag{3.53}$$

Where:

$$T_{fin} = T_{a,IN} + \left(T_{tube} - T_{a,IN}\right) \cdot \frac{\cosh\left(m\frac{dL}{2}\right)}{\cosh\left(mdL\right)} \tag{3.54}$$

$$T_{tube} = T_{fl,mean} \pm \frac{\dot{Q}_{fl}}{U_i A_i} \tag{3.55}$$

NTU: dry surface

If $T_{\text{int}} \geq T_{a,dp}$, the external surface of the element is considered completely dry. The fin efficiency is evaluated as suggested by Schmidt (1949)

$$\eta_f = \frac{\tanh\left(mr_eZ\right)}{mr_eZ} \tag{3.56}$$

Where the parameter *Z* is defined as:

$$Z = \left(\frac{r_f}{r_e} - 1\right)\left(1 + 0.35\log\left(\frac{r_f}{r_e}\right)\right) \tag{3.57}$$

And r_f is the equivalent radius of the polygonal fin:

$$r_f = \sqrt{\frac{X_t X_l}{\pi}} \tag{3.58}$$

Values of the ratio r_f / r_e for the rectangular fin derive from Schmidt (1949). From the knowledge of the fin efficiency η_f the global finned surface efficiency can be calculated, η_S, and so the dry surface case, the external global coefficient is:

$$U_{e,\text{DRY}} = \frac{1}{\frac{1}{h_e\eta_S}} \tag{3.59}$$

The Number of Transport Unit for the dry case is:

$$NTU_a = \frac{U_{e,\text{DRY}}A_e}{\dot{C}_a} \tag{3.60}$$

NTU: wet surface

If $T_{\text{int}} < T_{a,dp}$, the surface of the element is considered completely wet and since the combined phenomena of heat and mass transfer occur, the fin performance can be considerably different from the dry surface case. The ARI Standard 401-81 (1972) applied a study previous of Ware and Hacha(1960). This approach is similar to the one lead from Threlkeld (1970), but does not account

for the additional resistance in the liquid film. The effective heat transfer coefficient that must be used in the fin efficiency equation is:

$$h_{e,eff} = \frac{h_e}{c_a} c_{SAT}(T) \tag{3.61}$$

Where $c_{SAT}(\mathrm{T})$ is:

$$c_{SAT}(\mathrm{T}) = \frac{i_{a,SAT}(T_{fl,OUT}) - i_{a,SAT}(T_{fl,\mathrm{IN}})}{T_{fl,OUT} - T_{fl,\mathrm{IN}}} \tag{3.62}$$

And all the calculations are carried out with the hypothesis of unitary Lewis number.

$$Le = \frac{h_e}{h_m c_a} \approx 1 \tag{3.63}$$

In the condition of wet surface, an additional conductive thermal resistance is present, because of the liquid film. In addition, the mass transfer coefficient h_m is used instead of the heat transfer coefficient h_e:

$$h_m = \frac{h_e}{c_a} Le^{-1} \tag{3.64}$$

The global heat transfer coefficient for a wet fin is defined as:

$$U_{e,WET} = \frac{1}{\frac{1}{h_m \eta_{S,WET}} + \frac{\frac{D_e}{2}\ln\left(\frac{D_e + s_t}{D_e}\right)}{\lambda_l}} \tag{3.65}$$

Once obtained $U_{e,WET}$, the Number of Transport Unit is:

$$NTU_{a,h\&m} = \frac{U_{e,WET} A_e}{\dot{m}_a} \tag{3.66}$$

Heat flow rate exchanged in the element

The program is able to evaluate the quantity NTU as a combination of NTU_a and NTU_{fl}

$$NTU_{h\&m} = \frac{NTU_{a,h\&m}}{1 + \frac{NTU_{a,h\&m}}{NTU_{fl}} \cdot m_r} \tag{3.67}$$

In the case of dry surface, $T_{\mathrm{int}} \geq T_{a,dp}$.

$$m_r = c_r = \frac{\dot{C}_{\min}}{\dot{C}_{\max}} \tag{3.68}$$

The efficiency is calculated with the Cabezas-Gomez (2015) correlations, and once determined:

$$\dot{Q}_{a,eff} = \varepsilon_a \cdot \dot{Q}_{a,\mathrm{MAX}} \tag{3.69}$$

The latent and sensible quotes are also calculated:

$$\dot{Q}_{a,sens} = \left| \dot{m}_{a,IN} c_{p,a} (T_{a,IN} - T_{a,OUT}) \right| \tag{3.70}$$

$$\dot{Q}_{a,lat} = \left| \dot{m}_{a,IN} h_{fg} (x_{a,IN} - x_{a,OUT}) \right| \tag{3.71}$$

And, in the case of condensation:

$$\dot{m}_{cond} = \frac{\dot{Q}_{a,lat}}{h_{fg}} \tag{3.72}$$

Internal pressure drop

The programs is able to evaluate the internal pressure drop, which is caused by 3 types of losses. The first loss calculated is the one relative to the distributed pressure drop, evaluated for every single element belonging to a specific circuit and then added together:

$$\Delta p_{fl,distributed} = \sum_{el=1}^{N_{nodes},Circ\_1} \Delta p_{fl,el} \tag{3.73}$$

After that, the concentrated losses are considered: these losses are the ones relative to the internal fluid entering and leaving the tubes.

$$\Delta p_{fl,in-out} = K_L \frac{\rho_{fl} u^2_{fl}}{2} \tag{3.74}$$

Where the value of the loss coefficient is $K_L = 0.8$ and comprehends the loss for sudden enlargements and restrictions. The last internal pressure drop evaluated by the model is the loss due to the presence of connection bends, calculated with the equation:

$$\Delta p_{fl,bend} = N_{bends} f_{fl} \left(\frac{L_{eq,curve}}{D_i} \right) \frac{\rho_{fl} u^2_{fl}}{2} \tag{3.75}$$

Where N_{bends} is the number of connection bends for a single circuit, while L_{eq} is the equivalent length assumed equal to 50 times the the internal diameter of the tube:

$$L_{eq} = 50 \cdot D_i \tag{3.76}$$

Therefore, the total internal pressure drop for each circuit is given from:

$$\Delta p_{fl,TOT} = \Delta p_{fl,distributed} + \Delta p_{fl,in-out} + \Delta p_{fl,bends} \tag{3.77}$$

This $\Delta p_{fl,TOT}$ refers to the portion of tubes in contact with the external air and characterized with heat exchange.

External pressure drop

The model is also able to calculate the external pressure drop in the air side. In order to calculate this pressure drop the model implements the formula:

$$\Delta p_{a,IN} = f_a \frac{\rho_a u^2_a}{2} \cdot \frac{A_e}{\left(\frac{A_{pass,TOT}}{N_t N dz} \right)} \tag{3.78}$$

Where the Fanning factor f_a is calculated in two different ways in the case of dry or wet surface. In the case of dry surface, the model makes use of the Abu Madi (1998) correlation:

$$f_a = \left(\mathrm{Re}_{D_h}\right)^{-0.25} \left(R_4\right)^{-1.43} \left(R_5\right)^{-1.37} \left(R_8\right)^{1.65} \left(R_9\right)^{3.05} \tag{3.79}$$

If the case of wet surface occurs, the Wang et al. (2003) correlation is used:

$$f_a = 28.209\left(\mathrm{Re}_{D_c}\right)^{-0.5653} \left(N_r\right)^{-0.1026} \left(\frac{X_f}{D_c}\right)^{-1.3405} \left(\frac{A_e}{A_t}\right)^{-1.3343} \tag{3.80}$$

Where the dimensionless groups R_i are the same of Table 3.2.

Main output of the numerical model

Once the model converges, the total, sensible and latent heat flow rate exchanged in the finned tube heat exchanger are calculated as a sum of the heat flow rate of the elements:

$$\dot{Q}_{eff,TOT} = \sum_{el=1}^{N_{nodi}} \dot{Q}_{eff,el} \tag{3.81}$$

$$\dot{Q}_{a,sens,TOT} = \sum_{el=1}^{N_{nodi}} \dot{Q}_{a,sens,el} \tag{3.82}$$

$$\dot{Q}_{a,lat,TOT} = \sum_{el=1}^{N_{nodi}} \dot{Q}_{a,lat,el} \tag{3.83}$$

$$\varepsilon_{TOT} = \frac{\dot{Q}_{eff,TOT}}{\dot{Q}_{\max,TOT}} \tag{3.84}$$

Moreover, the model evaluates the outlet conditions of both fluids as weighted average values of the parameters at the outlet of the circuits (for the air, at the outlet of the last row).

Alternative input: ΔT of internal fluid instead of mass flow rate of internal fluid

It is often interesting to use the model giving as input the ΔT of the fluid inside the tubes, instead of its mass flow rate. The model can solve the problem evaluating the results with an iterative procedure that involves the numerical model already presented.

A first guess of the mass flow rate of the internal fluid is made by Eq.(3.85)

$$\dot{m}_{fl} = 0.5\, Q_{MAX} = 0.5\, \dot{m}_a c_a \left| t_{a,in} - t_{f,in} \right| \tag{3.85}$$

Then, the numerical model previously described is run and the ΔT of the internal fluid is calculated. If this value matches the desired valued within ±0.1 K the calculated output are given as results, otherwise the mass flow rate is updated using the following equation.

$$\dot{m}_{fl\_NEW} = \dot{m}_{fl} \frac{\Delta T_{calc}}{\Delta T_{INPUT}} \tag{3.86}$$

3.1.2 Validation of the model

In order to choose the best predictive correlations, the experimental data reported in paragraph 1.3 have been used as references. In addition, other experimental data from previous tests made by Eurapo S.r.l. on different units have been used to verify the calculations of the model.
Moreover, another software for the evaluation of the thermal performance of these heat exchangers has been used to compare the results and assess the capability of the developed model.

3.1.2.1 Choice of best predictive correlations through MAD, MD and SD indexes

In order to assess the best predictive correlations on the water side and on the air side, where the main thermal resistance is, three indexes that evaluate the difference between the experimental results and the calculations of the model have been used.
Two correlations have been implemented for the heat transfer coefficient on the water side and eight for the air side. For each combination, the three indexes have been evaluated with Eq. (2.30), Eq. (2.31) and Eq.(2.32) for all the tests reported in 1.3, considering the total heat flow rate as the significant parameter in Eq.(2.33).
We are looking for the correlations that give the closer results to the experimental value, which are the ones that have the minimum values for the error indexes considered.
Table 3.3 reports a list of the correlations implemented for air side and water side.
Figure 3.2 shows the MAD, MD and SD values for the 16 combinations of correlations: the minimum of each index (2.1 %, -0.7 % and 2.4 % respectively) is reached with the correlation of Abu Madi (1998) on the air side and Gnielinski with Petukhov factor (1970) for the water side.
These two correlations are chosen for the comparison of the results of the model with the experimental data taken with different finned tube heat exchanger units.
All the experimental data provided by the company are within the range required by the correlation of Abu-Mahdi regarding geometry and fluid conditions.

Table 3.3. List of correlations for air side and water side.

Correlations for air side		**Correlations for water side**	
1	Rich (1973)	*1*	Gnielinski (1976)
2	Hilpert (1933)	*2*	Gnielinski with Petukhov factor(1970)
3	Gray and Webb (1986)		
4	Canton e Fornasieri (1983)		
5	Eckert e Drake (1959)		
6	Elmahdy e Biggs (1979)		
7	Abu Madi (1998)		
8	Eckert e Drake (1959)		

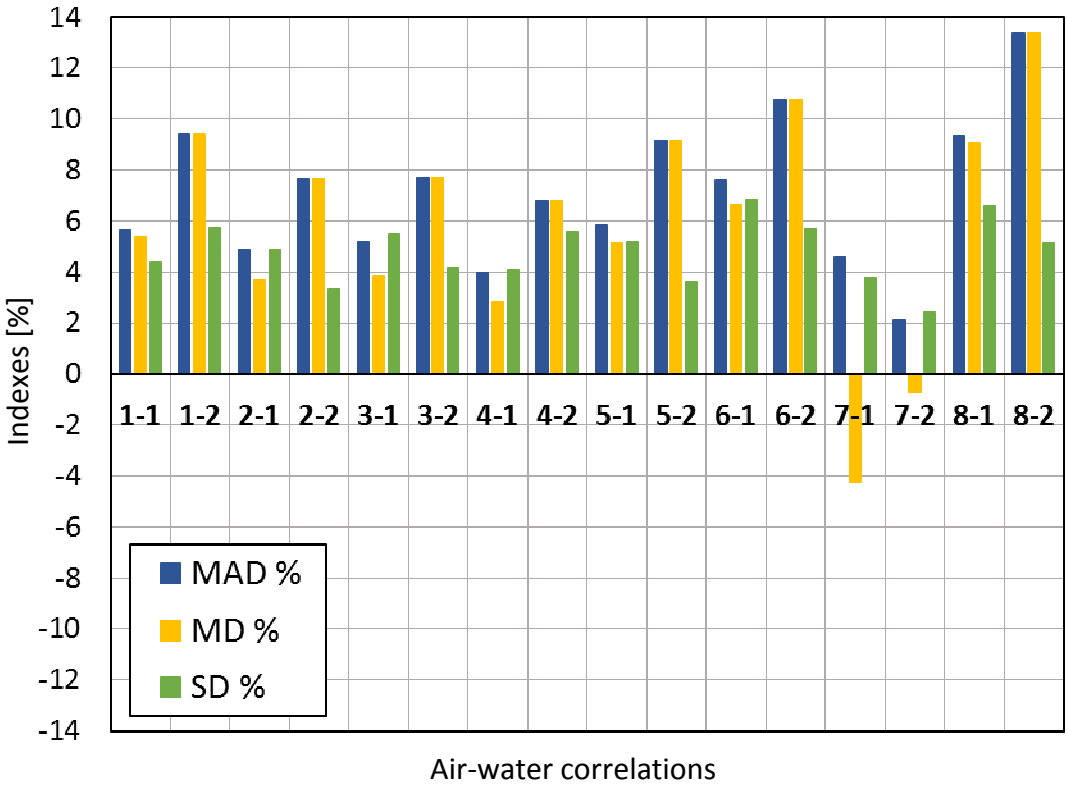

Figure 3.2. MAD, MD and SD indexes corresponding to the tested combinations of the implemented correlations.

3.1.2.2 Comparison with experimental data

The present paragraph present the comparison between the experimental data obtained in 1.3 and the results calculated with the developed model for the same conditions. In order to evaluate the ability of the model, the results of another software for finned coil simulation are plotted in the graphs.

The next paragraphs, however, present the comparison with other units, ducted unit and a fan coil model. This comparison will further validate the model, verifying its reliability not only for the different operating conditions, but also for different geometries and circuitries.

It is worth mentioning that $\dot{V}_{air}$ given as input to the model was not experimentally measured during the tests: $\dot{V}_{air}$ is measured in dry condition without heat exchange at different fan speeds for all the units, than the result obtained is considered for every test with that unit at that speed, regardless the fluid conditions (wet or dry fins). This can lead the model to different results, but it is a necessary assumption since the variation of $\dot{V}_{air}$ for different geometries during dehumidification process is unknown.

3.1.2.2.1 EBH 020 – 3R

The main dimensions of the finned coil heat exchanger are available in Table 3.4, while Figure 3.3 and Figure 3.4 show the real and the modelled circuitry of the heat exchanger, respectively.

Table 3.4. Dimensions of the tested finned tube heat exchanger (EBH 020 – 3R).

Number of Rows	[-]	N_R	3
Number of tubes in each row	[-]	N_t	12
Tube's length	[m]	L	0.875
Fin pitch	[m]	X_f	0.0021
Longitudinal tube pitch	[m]	X_l	0.022
Transverse tube pitch	[m]	X_t	0.025
Fin thickness	[m]	s_f	0.0001
Tube's external diameter	[m]	D_e	0.01009
Tube thickness	[m]	s_t	0.00028
Area on air side	[m²]	A_e	15.03
Area inside tubes	[m²]	A_i	0.943

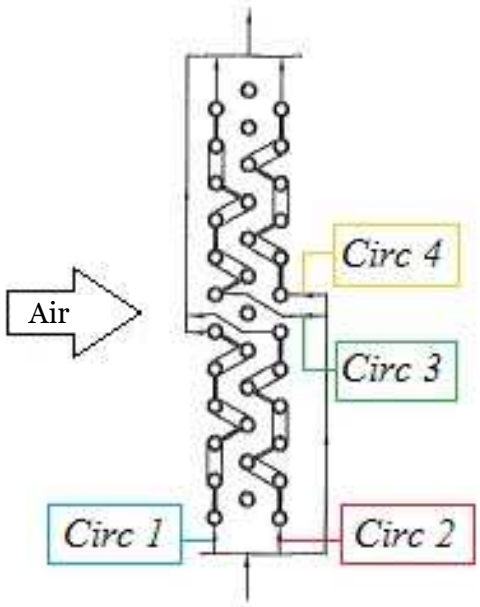

Figure 3.3. Schematic of the circuitry of the tested heat exchanger (020 – 3R).

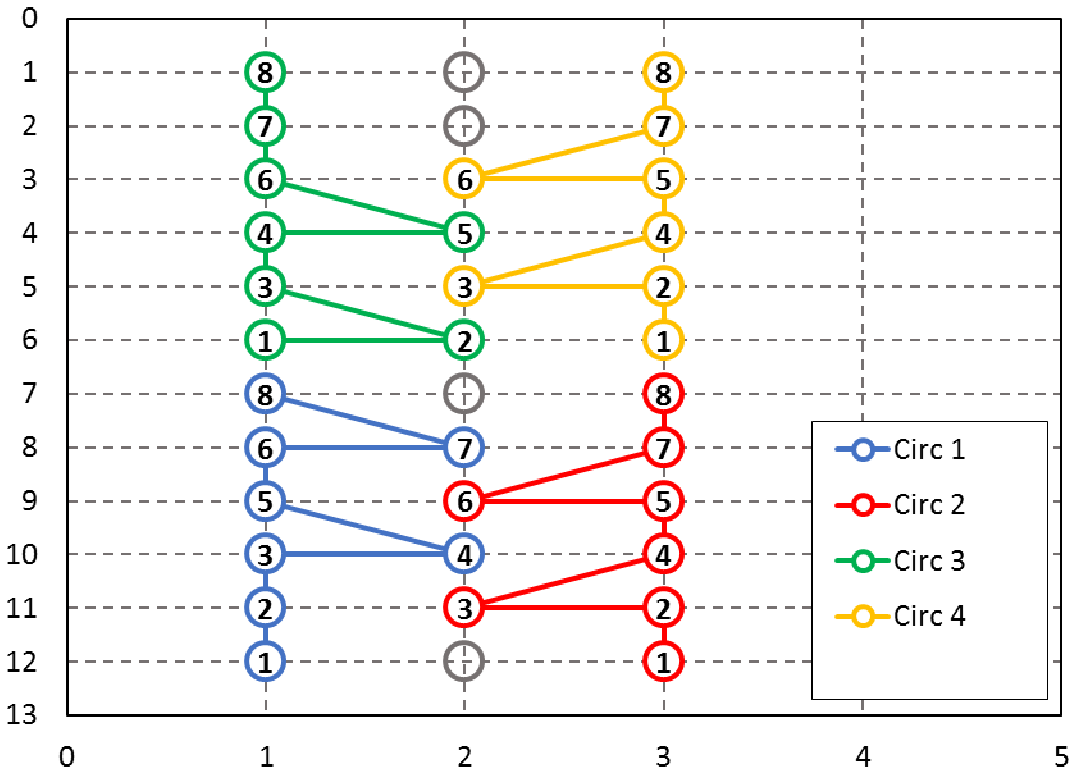

Figure 3.4. Heat exchanger 020 – 3R: considered circuitry for the model.

The main parameter for the comparison between numerical model and experimental results is the total heat flow rate. Figure 3.5 show that the agreement is within ± 5% for the present model during both dry and wet conditions, while the reference numerical model gives results within 15% for most of data, with same tests with higher error.

Considering the latent and sensible heat flow rate separately, it is possible to see from Figure 3.6 that the present model overestimates the condensate flow rate, especially when this value is low. On the other hand, the sensible heat flow rate is slightly underestimated, so that the total heat flow rate is well predicted.

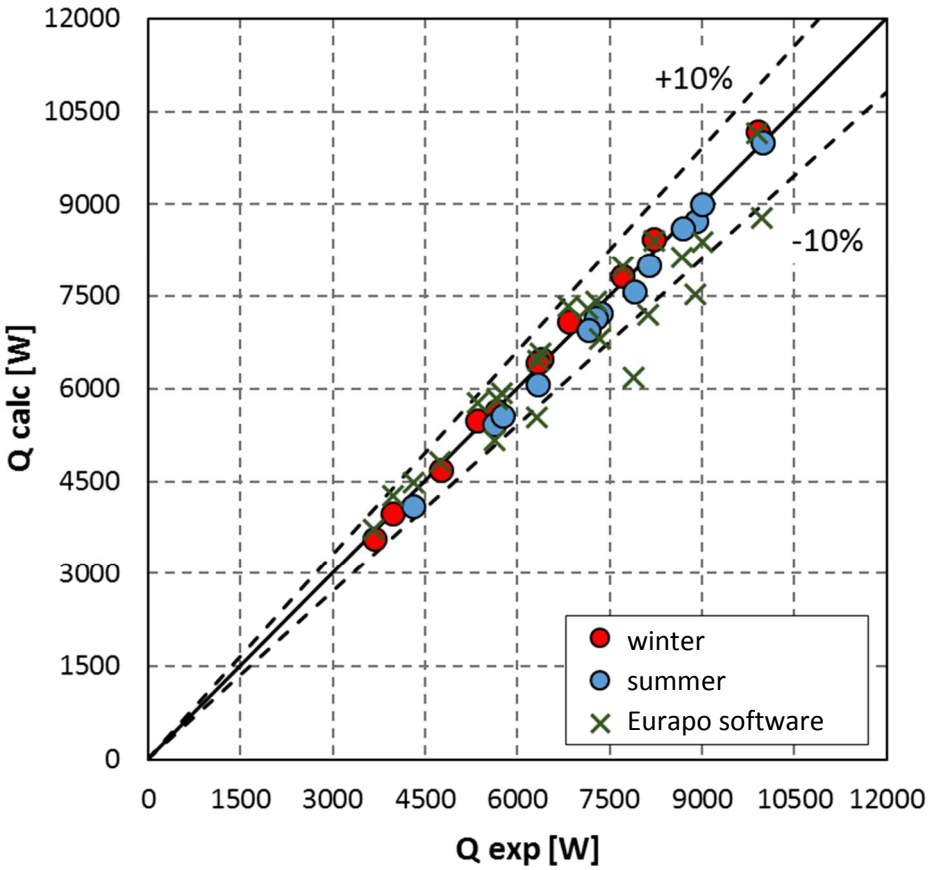

Figure 3.5. Total heat flow rate of unit EBH 020 – 3R: comparison between experimental data, results of the present model and results of the reference model.

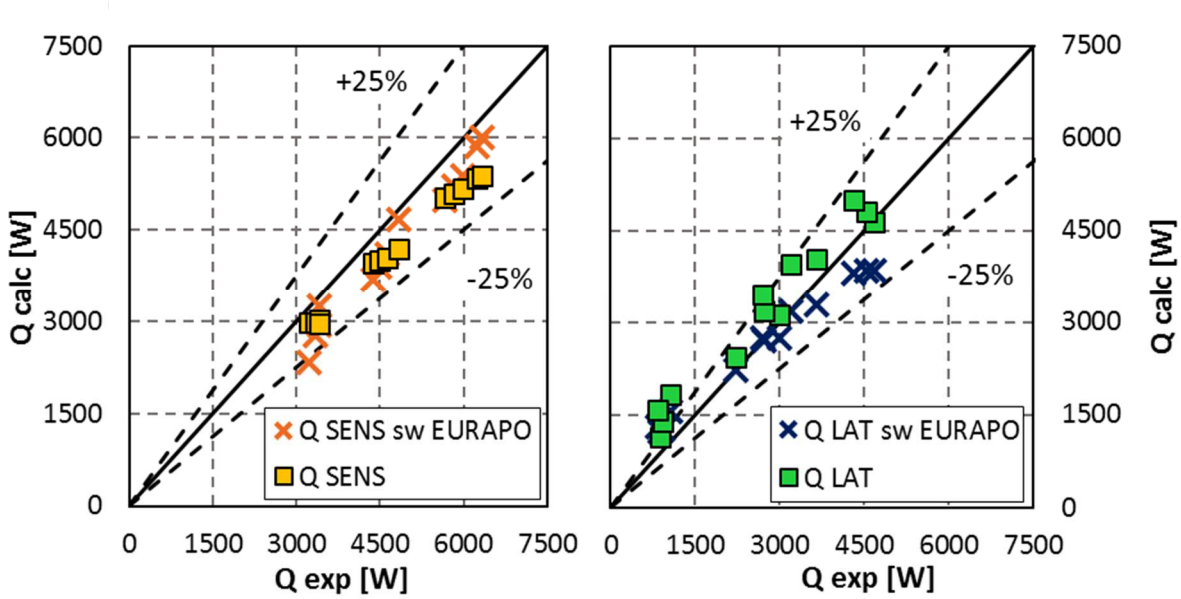

Figure 3.6. Sensible and latent heat flow rate of unit EBH 020 – 3R: comparison between experimental data, results of the present model and results of the reference model

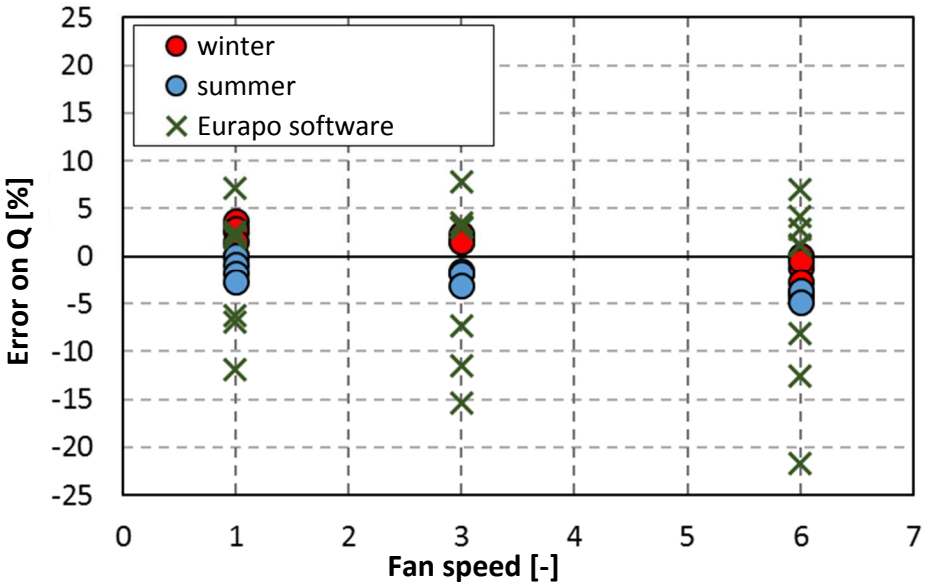

Figure 3.7. Error in the evaluation of the total heat flow rate versus fan speed for unit EBH 020 – 3R: comparison between results of the present model (divided in summer and winter conditions) and results of the reference model.

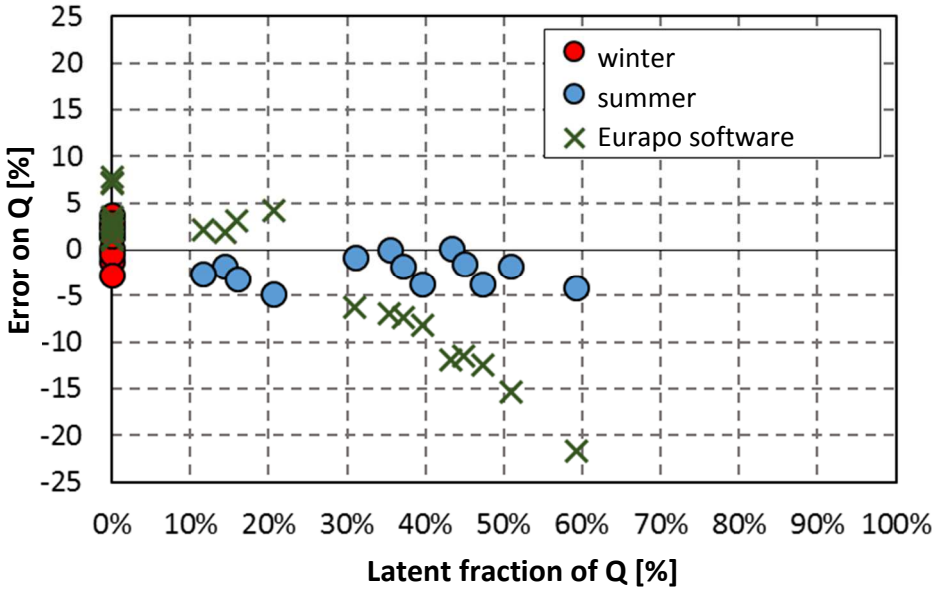

Figure 3.8. Error in the evaluation of the total heat flow rate versus the ratio between latent and total heat flow rate for unit EBH 020 – 3R: comparison between results of the present model (divided in summer and winter conditions) and results of the reference model.

Figure 3.7 reports the error on the heat flow rate versus the speed of the fan, showing that this parameter does not influence the capability of present and reference model. In order to understand if the mass flow rate of condensate influence the capabilities of the models Figure 3.8 reports the error on the total heat flow rate versus the ratio between latent and total heat flow rate: the present

model catches the trend of data with within 5% even in wet conditions, while the reference model shows that the dehumidification process is difficult to be modelled properly.

Figure 3.9 reports the comparison between internal pressure drop measured experimentally an calculated with the two numerical models. The present model is able to catch the trend of data and predicts all data within ±25%, while the reference model gives results with low accuracy, with errors up to 83%.
Figure 3.10 shows the internal pressure drop versus the water flow rate. It can be noticed that the trend of pressure drop during winter and summer tests is the same, but the red markers have slightly lower values than blue markers, because of the thermal properties of water at the two different temperature. This difference is more evident in the prediction of the present model, while it is really small in experimental data. The prediction of the reference model is less accurate than that of the present model.

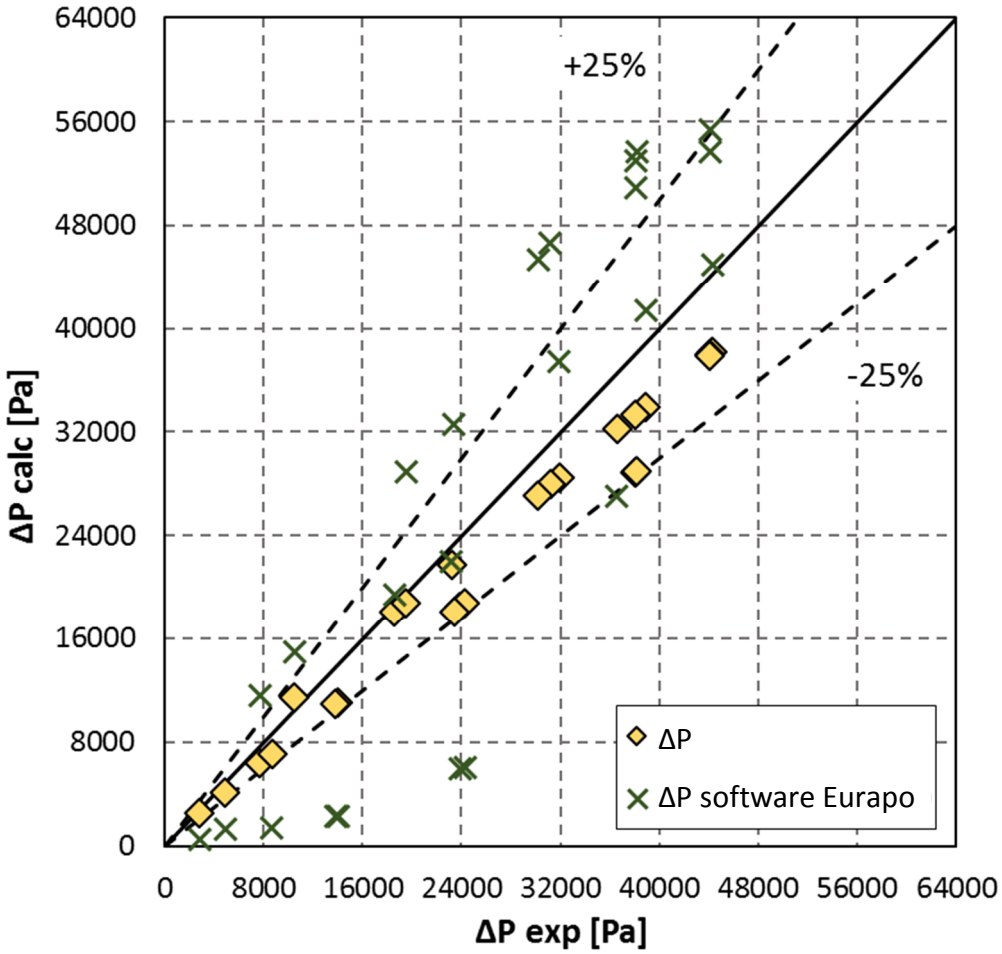

Figure 3.9. Pressure drop on the water side: comparison between experimental data, results of the present model and of the reference model for the unit EBH 020 – 3R.

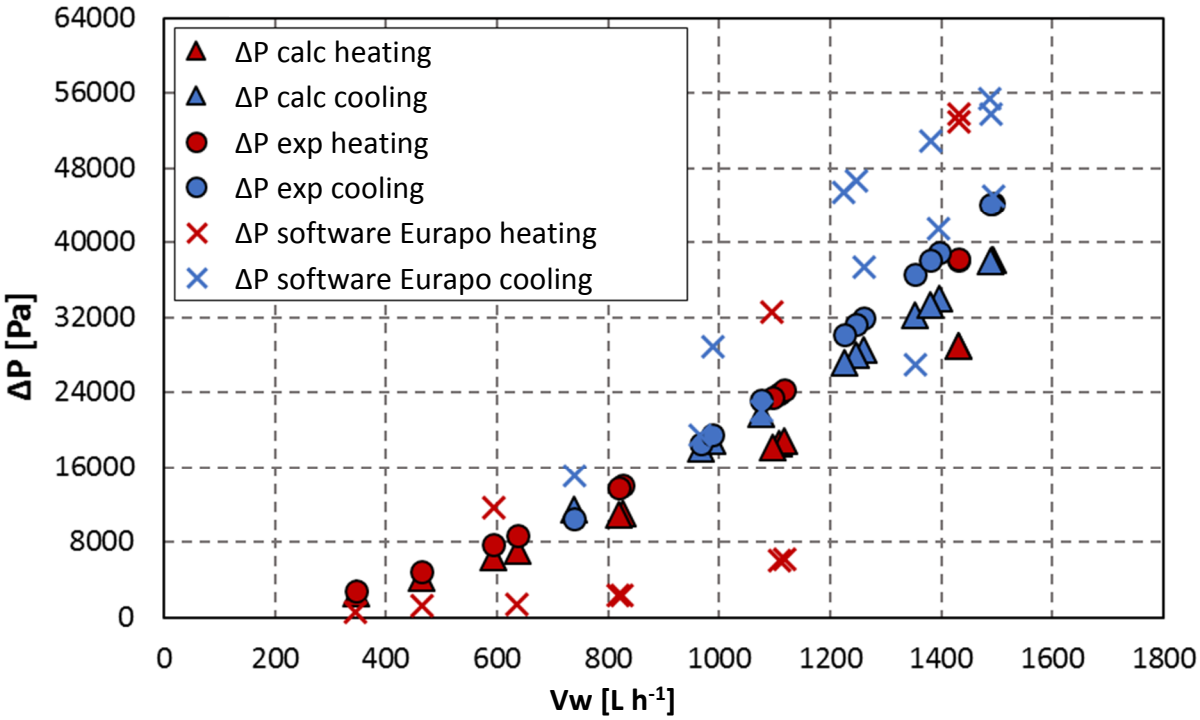

Figure 3.10. Internal pressure drop versus mass flow rate of water for unit EBH 020 – 3R: comparison between experimental results, results of the present model and results of the reference model (divided in summer and winter conditions).

As described in 1.2, ten thermocouples have been installed at the outlet of the heat exchanger in order to measure the air temperature and see the differences on vertical direction.

Figure 3.11 and Figure 3.12 reports the comparison between measured values and calculated ones for a dry and a wet condition respectively.

The model gives an outlet temperature value for each element in which the heat exchanger is divided, so that, after the last row of tubes, it calculates *Nt* times *Ndz* temperatures. In order to compare the model with the experimental measurements, an interpolation of the calculated values has been done to match the position of thermocouples. The results show that there is a good agreement between the two trends, and that the air temperature can be significantly different in the vertical direction, while along the tubes it is almost constant.

The differences between model and experimental values can be related to the mix of air in the real tests and to the simplified position if tubes in the model (that, according to Fornasieri and Zilio (1998) and Casson et al. (2000), is a simplification that does not affect the evaluation of the total heat flow rate significantly). Moreover, the air flow in the real situation is not perfectly homogeneous as modelled numerically, due to the position of the fans.

Overall, the results of the model can be interesting in order to assess the goodness of the circuitry, which should provide small differences in the air temperature at the outlet, which is an indication of a good matching of the temperature profile.

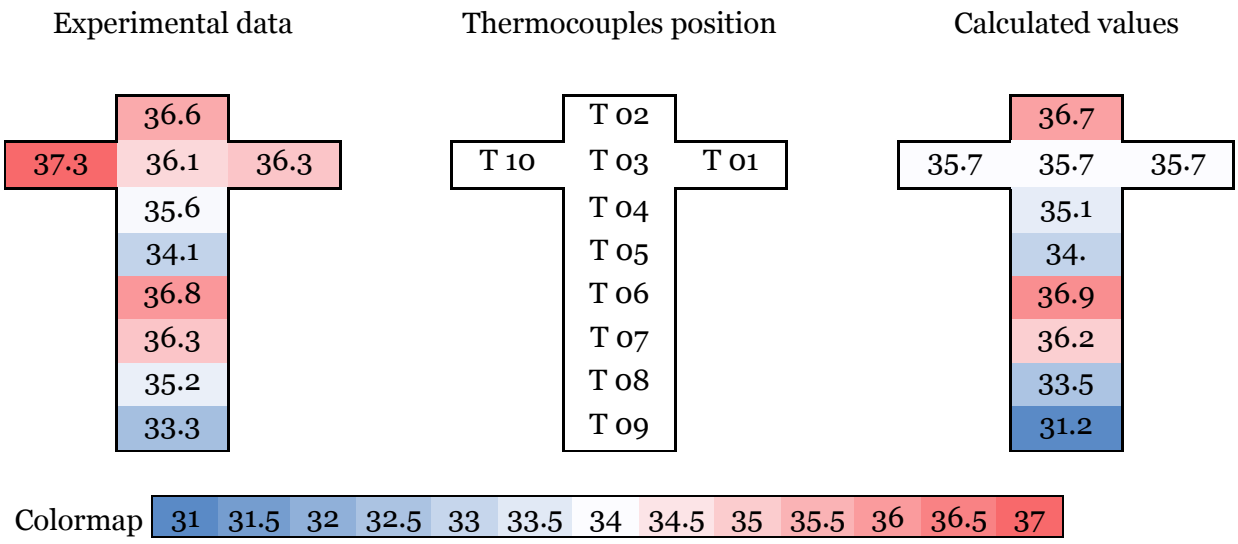

Figure 3.11. Air temperature at the outlet of the heat exchanger during a test in dry conditions: comparison between experimental data and results of the model.

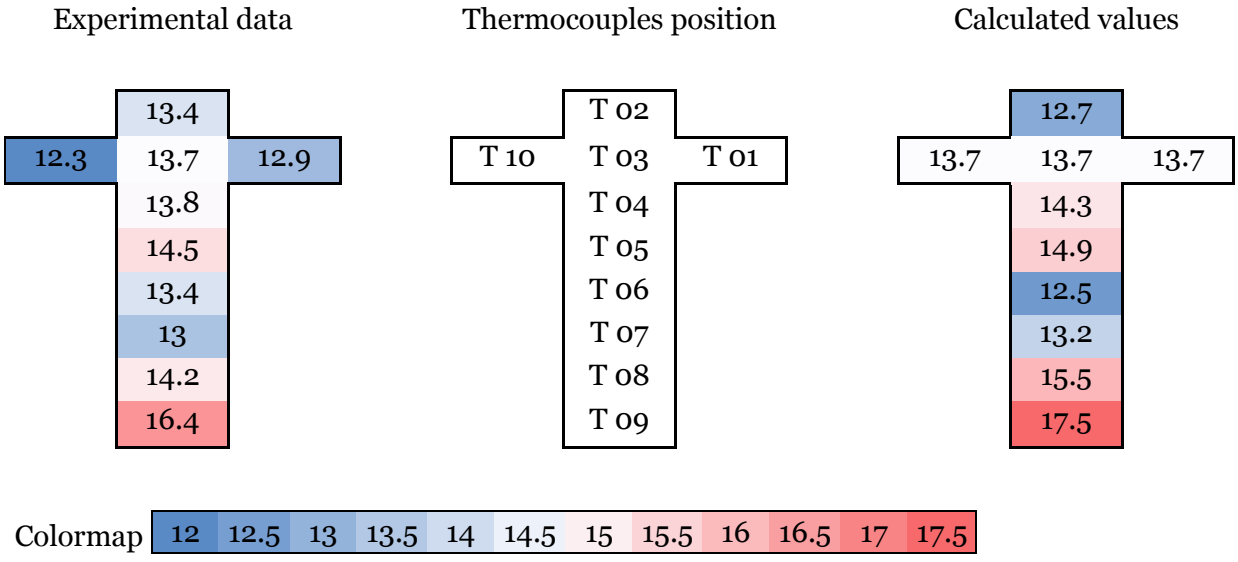

Figure 3.12. Air temperature at the outlet of the heat exchanger during a test in wet conditions: comparison between experimental data and results of the model.

3.1.2.2.2 EBH 020/030 – 4R

Hereafter, the experimental results obtained with different units will be compared with the results of the numerical model. Table 3.5 reports tests conditions, which are the standard for air treatment units.

As seen in Figure 1.15 dehumidification lead to a lower mass flow rate, due to the presence of liquid moisture that blocks the passage of air, but in the next experimental tests V_w was not measured, thus during tests in summer conditions the mass flow rate of air is assumed to be the same of that in dry conditions (which have been measured in the aeraulic tunnel).

Table 3.6 reports the main dimensions of the heat exchanger, while Figure 3.13 and Figure 3.14 show the real and the simplified circuitry of the unit.

Table 3.5. Standard conditions for tests in cooling and heating mode.

Cooling mode	
T_{air} *IN*	27 °C
RH IN	47 - 48 %
T_w *IN*	7 °C
ΔT_w	5 K
Fan speed	min – Med – MAX

Heating mode	
T_{air} *IN*	20 °C
T_w *IN*	50 °C
Fan speed	min – Med – MAX
V_w	Same as summer tests

Table 3.6. Dimensions of the tested finned tube heat exchanger (EBH 020/030 – 4R).

Number of Rows	[-]	N_R	4
Number of tubes in each row	[-]	N_t	12
Tube's length	[m]	L	0.875
Fin pitch	[m]	X_f	0.0021
Longitudinal tube pitch	[m]	X_l	0.022
Transverse tube pitch	[m]	X_t	0.025
Fin thickness	[m]	s_f	0.00012
Tube's external diameter	[m]	D_e	0.010225
Tube thickness	[m]	s_t	0.00035

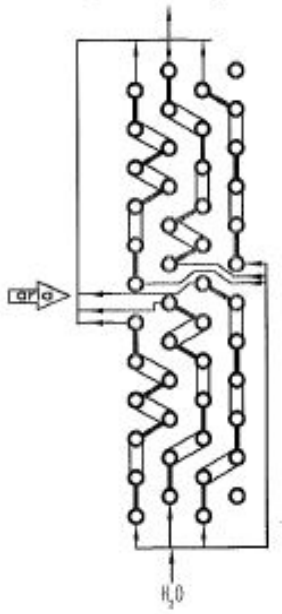

Figure 3.13. Schematic of the circuitry of the heat exchanger 020/030 – 4R.

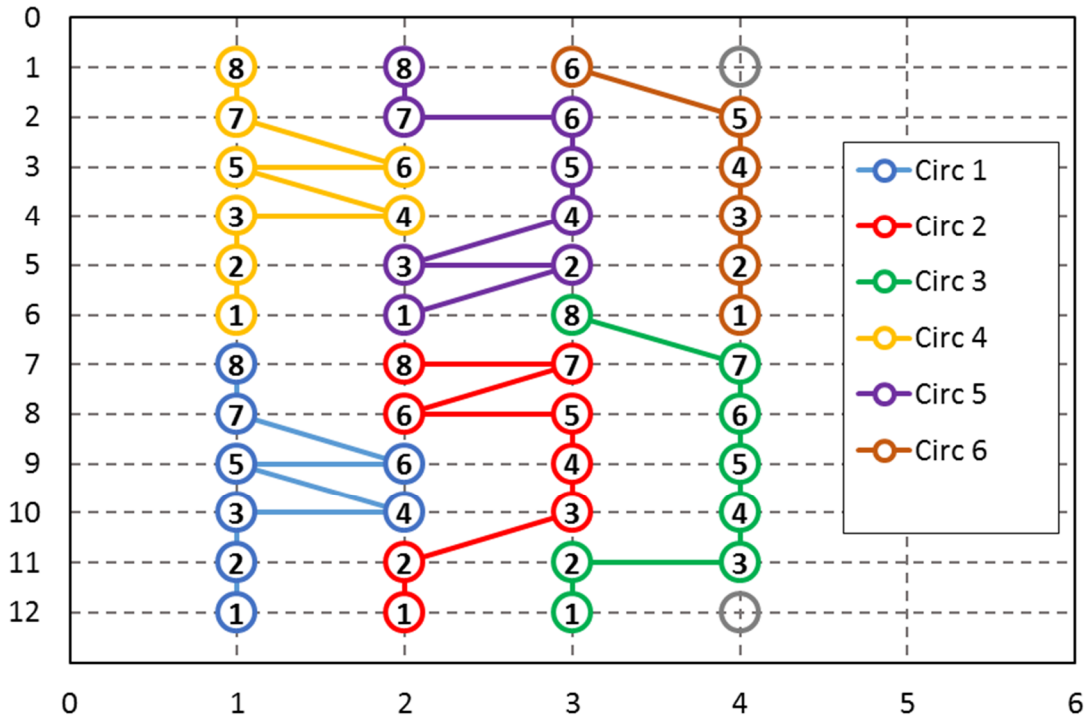

Figure 3.14. Heat exchanger 020/030 – 4R.

The available experimental data for this unit are 16 tests in winter conditions and 16 tests in wet conditions. The comparison between experimental heat flow rate and the calculation of the model are reported in Figure 3.15. Both conditions are predicted within ±16% and there is no evidence of an influence of the fan speed or of the latent heat in the capability of the model, as shown in Figure 3.16 and in Figure 3.17 by the absence of a clear trend of the error versus these two parameters.

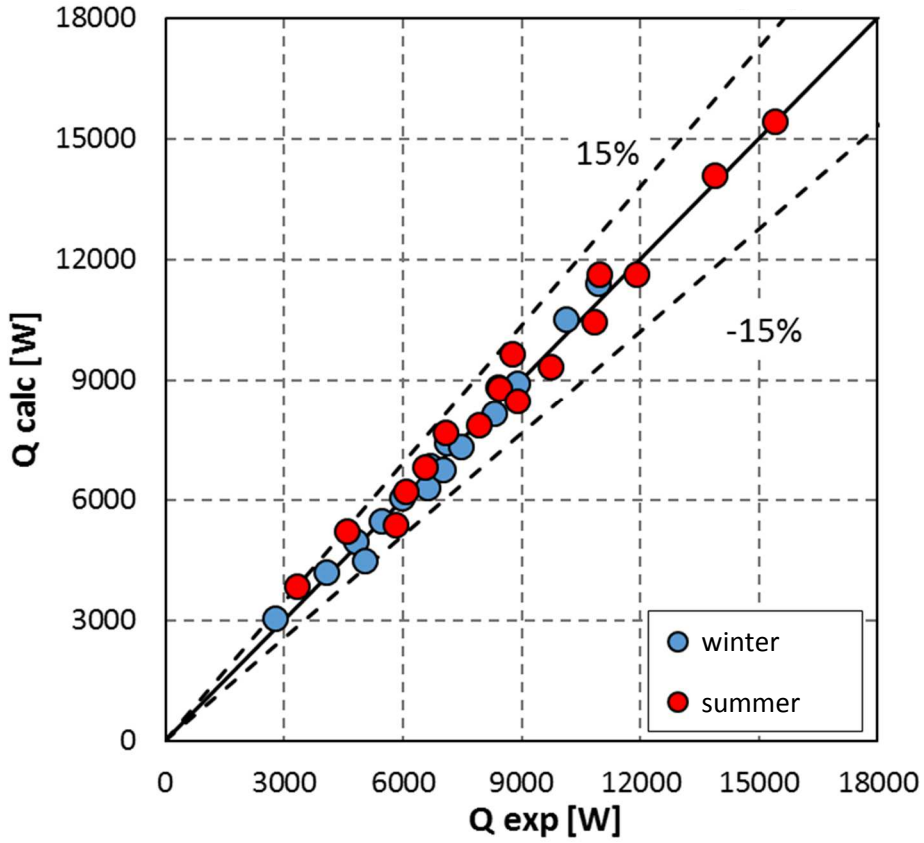

Figure 3.15. Total heat flow rate of unit EBH 020/030 – 4R: comparison between experimental data and results of the present model.

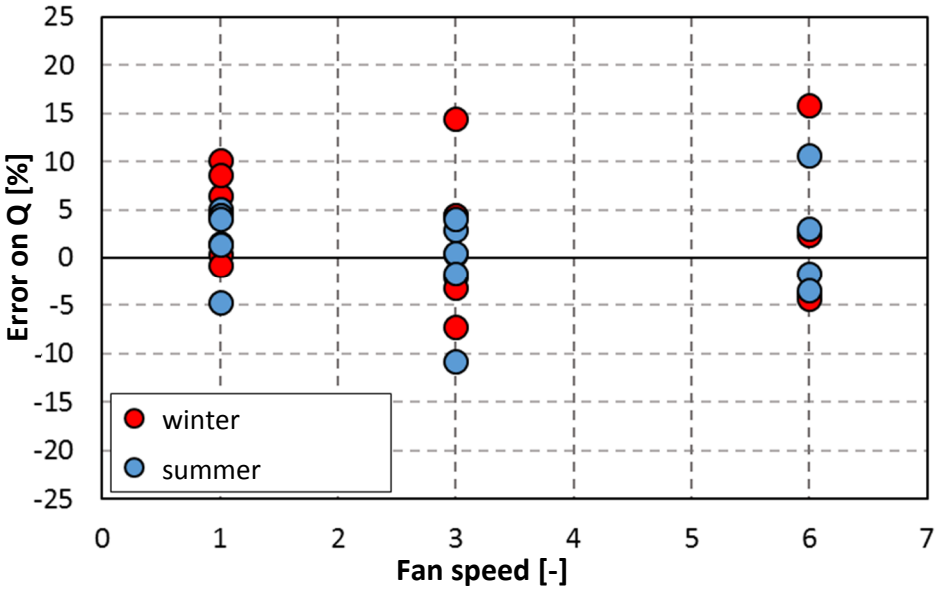

Figure 3.16. Error in the evaluation of the total heat flow rate versus fan speed for unit EBH 020/030 – 4R for the present model (divided in summer and winter conditions).

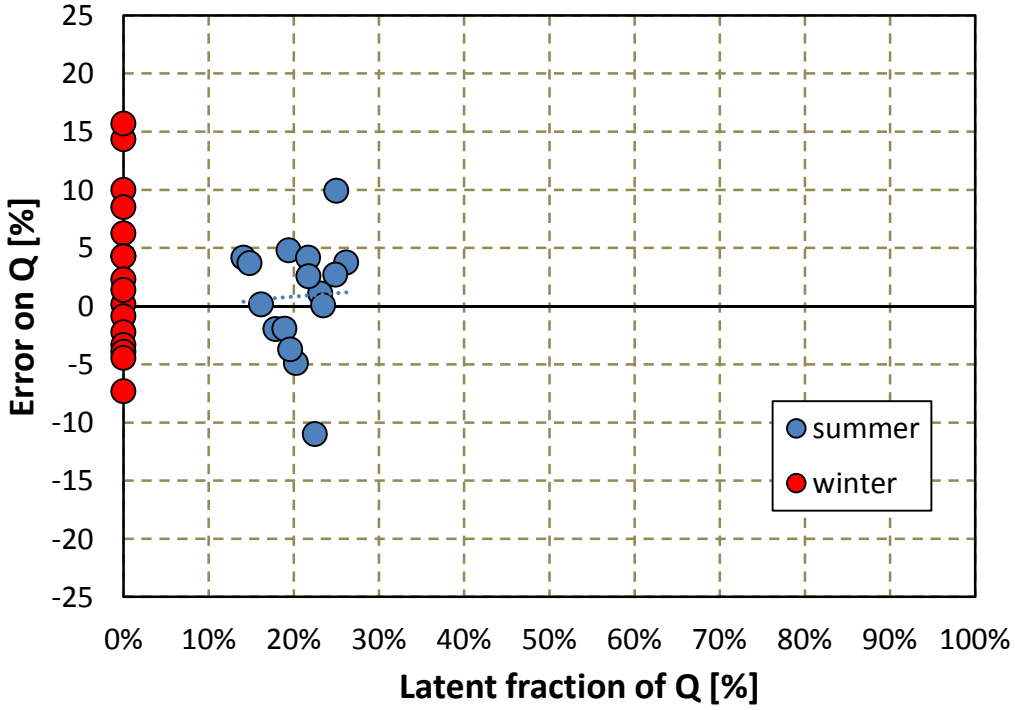

Figure 3.17. Error in the evaluation of the total heat flow rate versus the ratio between latent and total heat flow rate for unit EBH 020/030 – 4R for the present model (divided in summer and winter conditions).

Figure 3.18 represents the internal pressure drop experimentally measured versus the calculated one. The model underestimates this parameter by 30% – 40%, but the calculated values have the same trend as the measured ones, as shown by Figure 3.19. The lower pressure drop is probably related to the inlet at outlet manifolds, which are neglected by the model but have probably an important role at higher water mass flow rate.

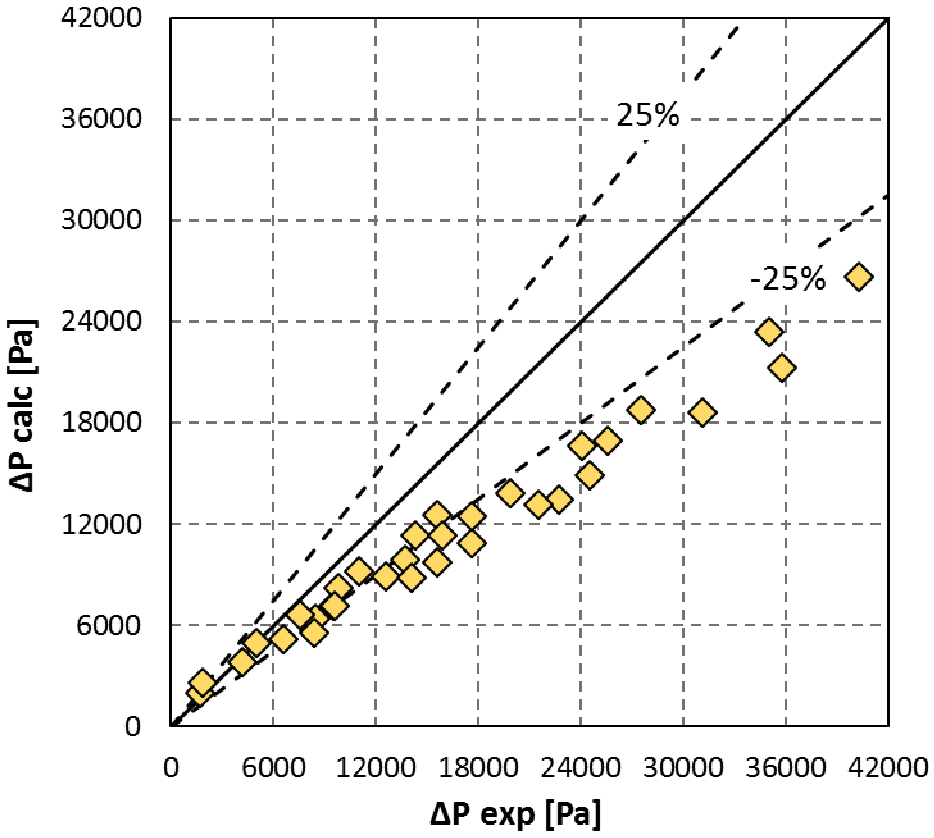

Figure 3.18. Pressure drop on the water side: comparison between experimental data and results of the present model for the unit EBH 020/030 – 4R.

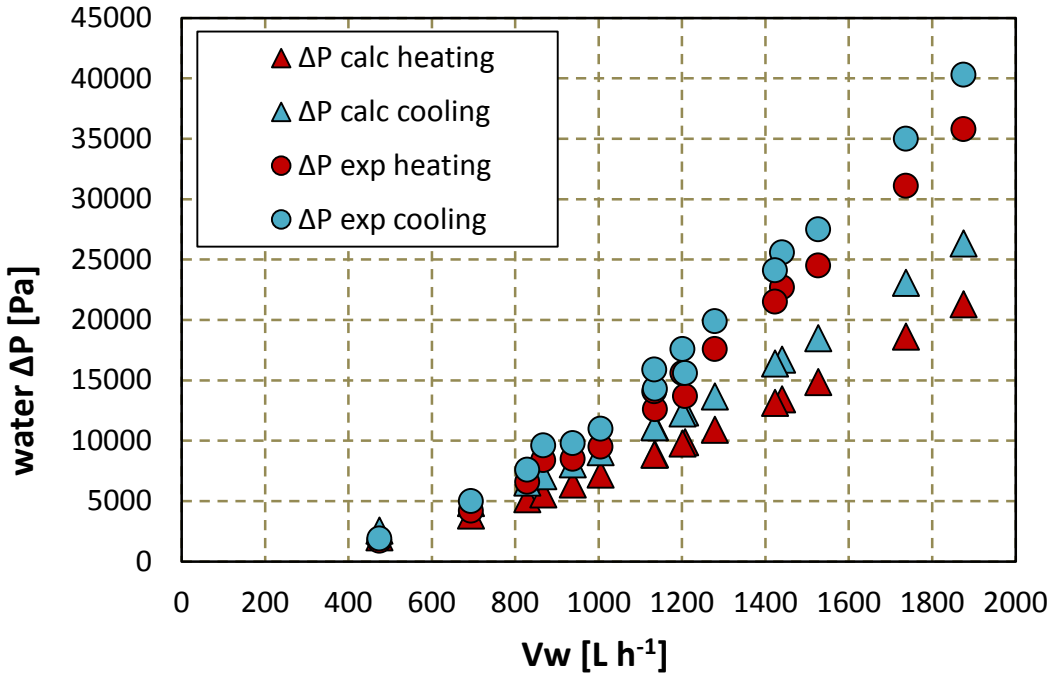

Figure 3.19. Internal pressure drop versus mass flow rate of water for unit EBH 020/030 – 4R: comparison between experimental results and results of the present model (divided in summer and winter conditions).

3.1.2.2.3 EBH 040/050 – 4R

Table 3.7 reports the main geometric characteristics of the heat exchanger in the unit EBH 040/050 – 4R, while Figure 3.20 and Figure 3.21 show the real and the simplified circuitry of the unit.

Table 3.7. Dimensions of the tested finned tube heat exchanger (EBH 040/050 – 4R).

Number of Rows	[-]	N_R	4
Number of tubes in each row	[-]	N_t	12
Tube's length	[m]	L	1.125
Fin pitch	[m]	X_f	0.0021
Longitudinal tube pitch	[m]	X_l	0.022
Transverse tube pitch	[m]	X_t	0.025
Fin thickness	[m]	s_f	0.00012
Tube's external diameter	[m]	D_e	0.010225
Tube thickness	[m]	s_t	0.00035

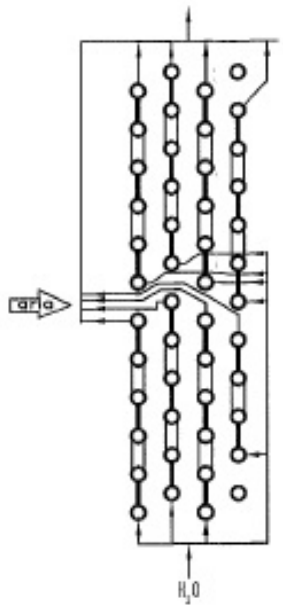

Figure 3.20. Schematic of the circuitry of the heat exchanger 040/050 – 4R.

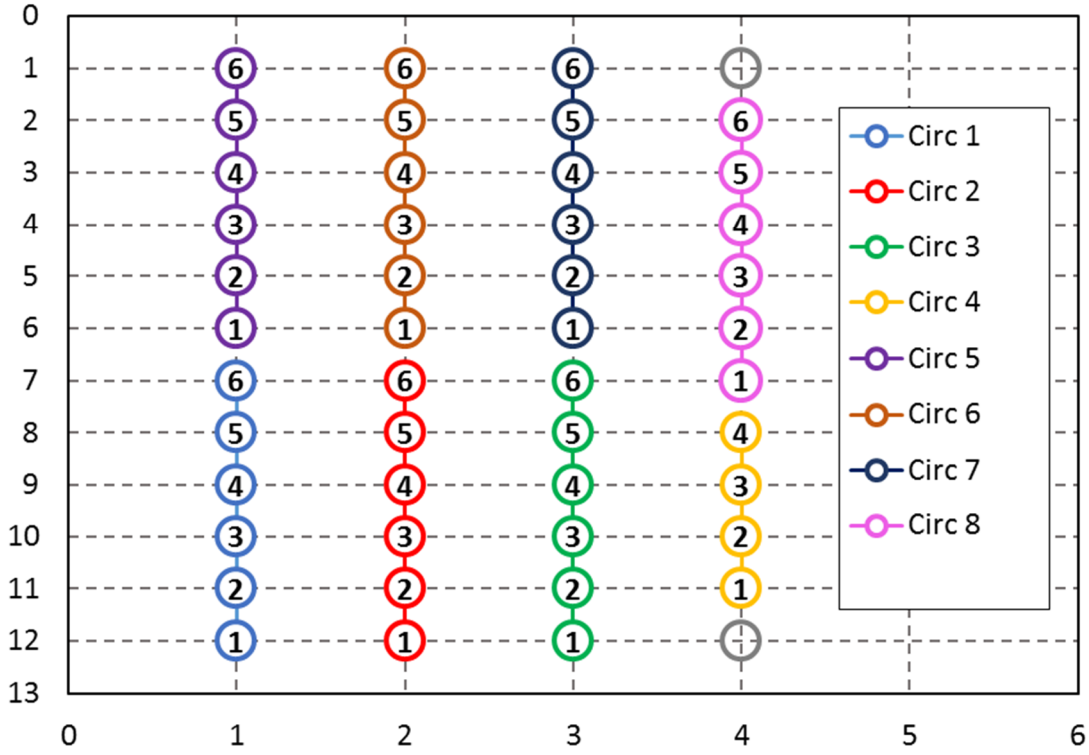

Figure 3.21. Heat exchanger 040/050 – 4R: considered circuitry for the model.

The available experimental data for this unit are 12 tests in winter conditions and 12 tests in wet conditions. The comparison between experimental heat flow rate and the calculation of the model are reported in Figure 3.22Figure 1.13 . Both conditions are predicted within ±9% and there is no evidence of an influence of the fan speed or of the latent heat in the capability of the model, as shown in Figure 3.23 and in Figure 3.24 by the absence of a clear trend of the error versus these two parameters.

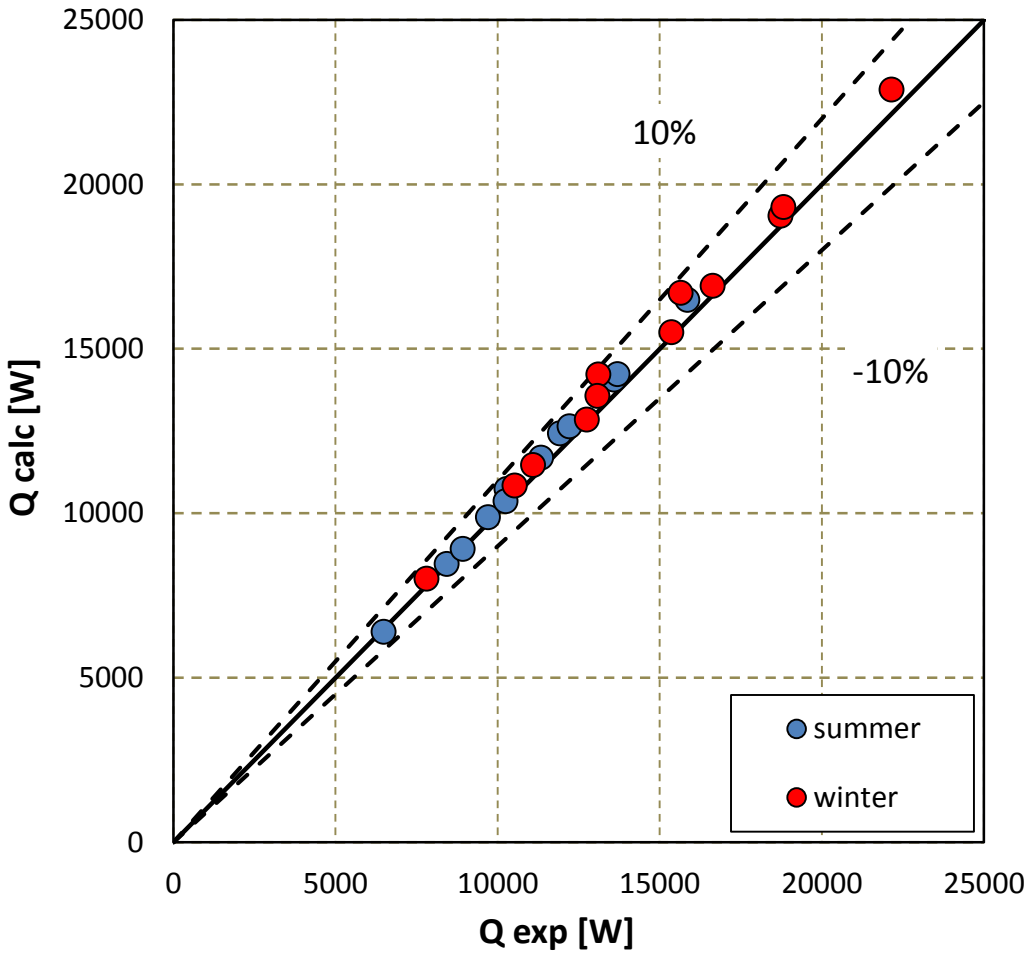

Figure 3.22. Total heat flow rate of unit EBH 040/050 – 4R: comparison between experimental data and results of the present model.

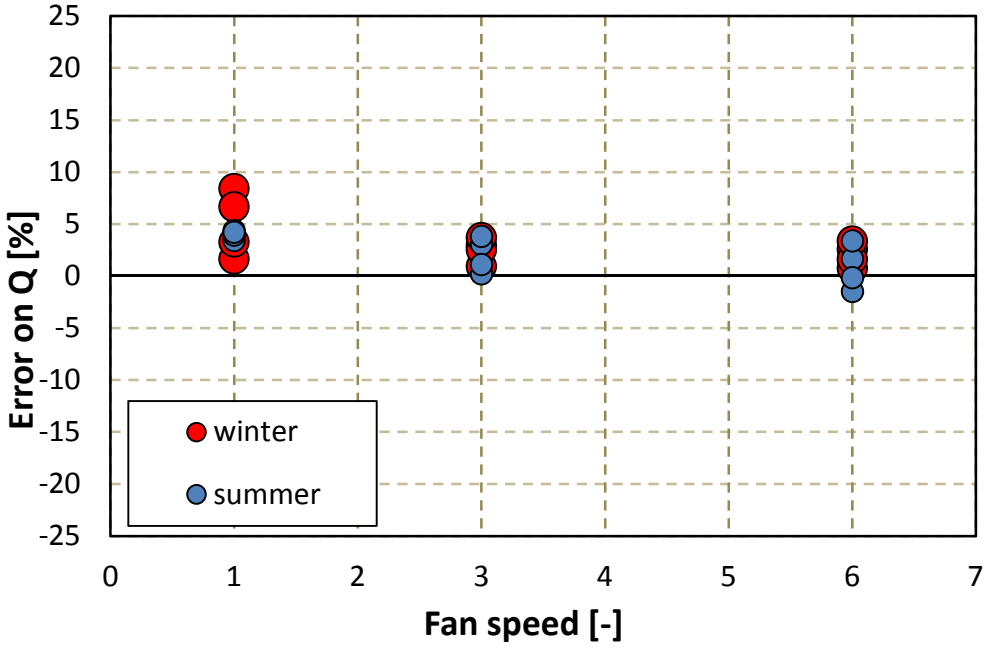

Figure 3.23. Error in the evaluation of the total heat flow rate versus fan speed for unit EBH 040/050 – 4R for the present model (divided in summer and winter conditions).

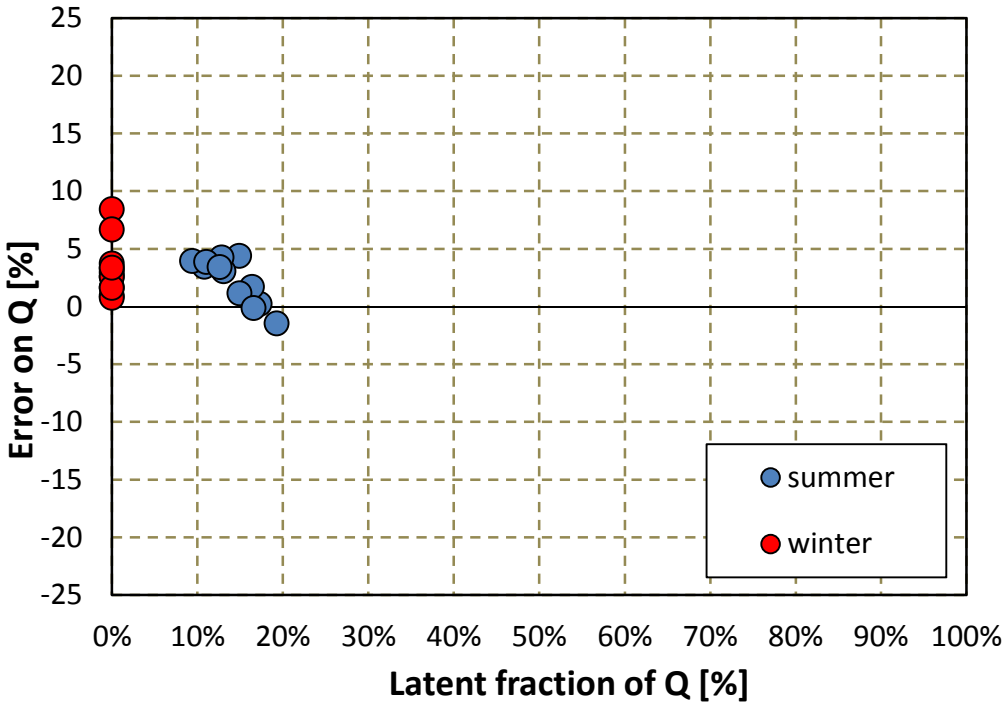

Figure 3.24. Error in the evaluation of the total heat flow rate versus the ratio between latent and total heat flow rate for unit EBH 040/050 – 4R for the present model (divided in summer and winter conditions).

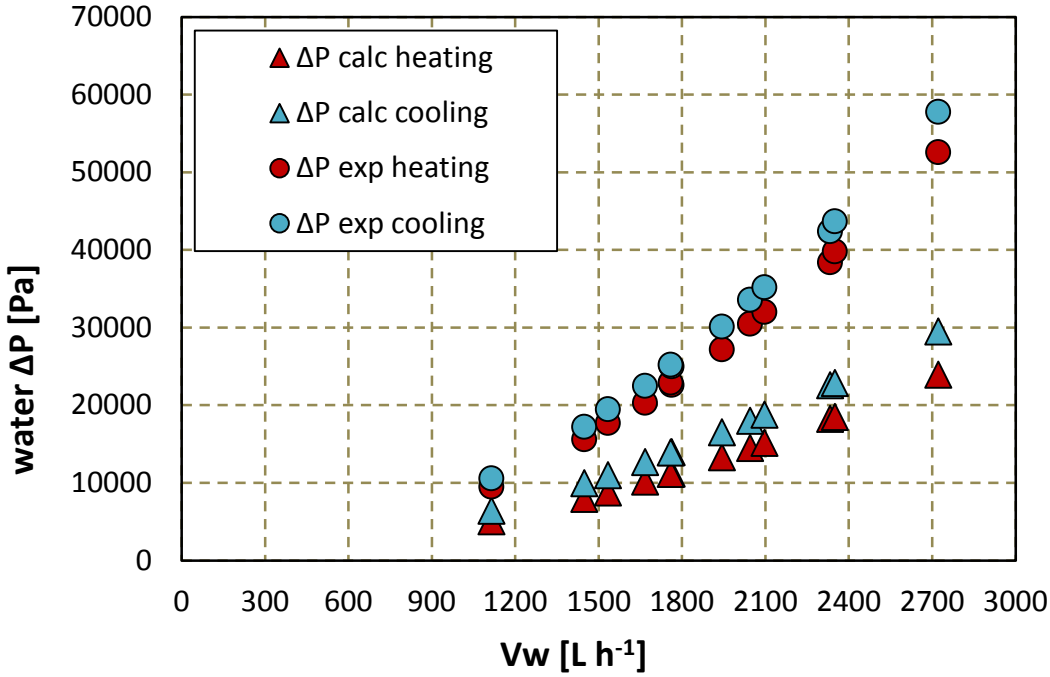

Figure 3.25. Internal pressure drop versus mass flow rate of water for unit EBH 040/050 – 4R: comparison between experimental results and results of the present model (divided in summer and winter conditions).

As with the previous unit, pressure drop are under predicted by the model, which is however able to catch the trend and predict that, with a lower temperature of water, the pressure drop are higher for the same water mass flow rate, due to the different properties of the fluid.

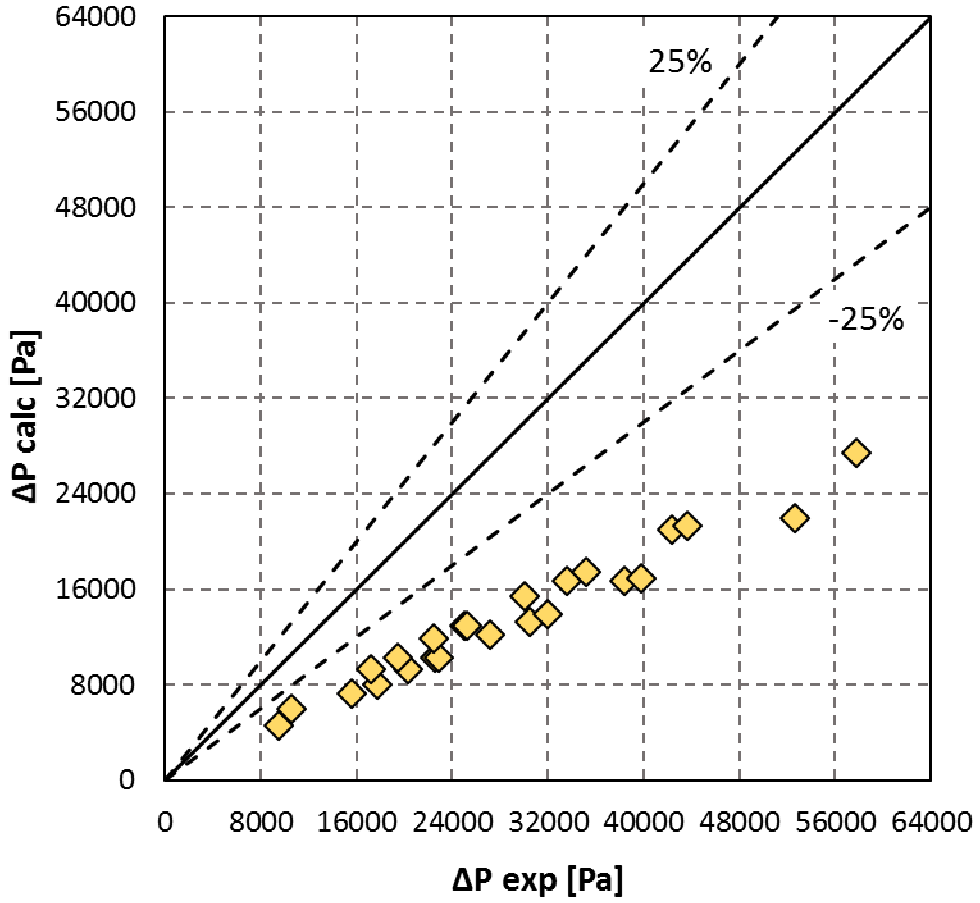

Figure 3.26. Pressure drop on the water side: comparison between experimental data and results of the present model for the unit EBH 040/050 – 4R.

3.1.2.2.4 EBH 060 – 4R

Table 3.8 reports the main dimensions of the heat exchanger, while Figure 3.27 shows the real and the simplified circuitry of the unit.

The main difference with the previous units is that the heat exchanger has a higher number of circuits, each of them with only 4 tubes arranged so that the overall configuration is similar to counter current. Six tests in winter and six tests in summer conditions are compared to the results of the model in Figure 3.28, which shows that the main error is lower than 6%.

Figure 3.29 and Figure 3.30 shows that there is no influence of the fan speed and of the latent heat in the capability of the model.

Table 3.8. Dimensions of the tested finned tube heat exchanger (EBH 060 – 4R).

Number of Rows	[-]	N_R	4
Number of tubes in each row	[-]	N_t	16
Tube's length	[m]	L	1.5
Fin pitch	[m]	X_f	0.0018
Longitudinal tube pitch	[m]	X_l	0.02165
Transverse tube pitch	[m]	X_t	0.025
Fin thickness	[m]	s_f	0.0001
Tube's external diameter	[m]	D_e	0.01008
Tube thickness	[m]	s_t	0.00028

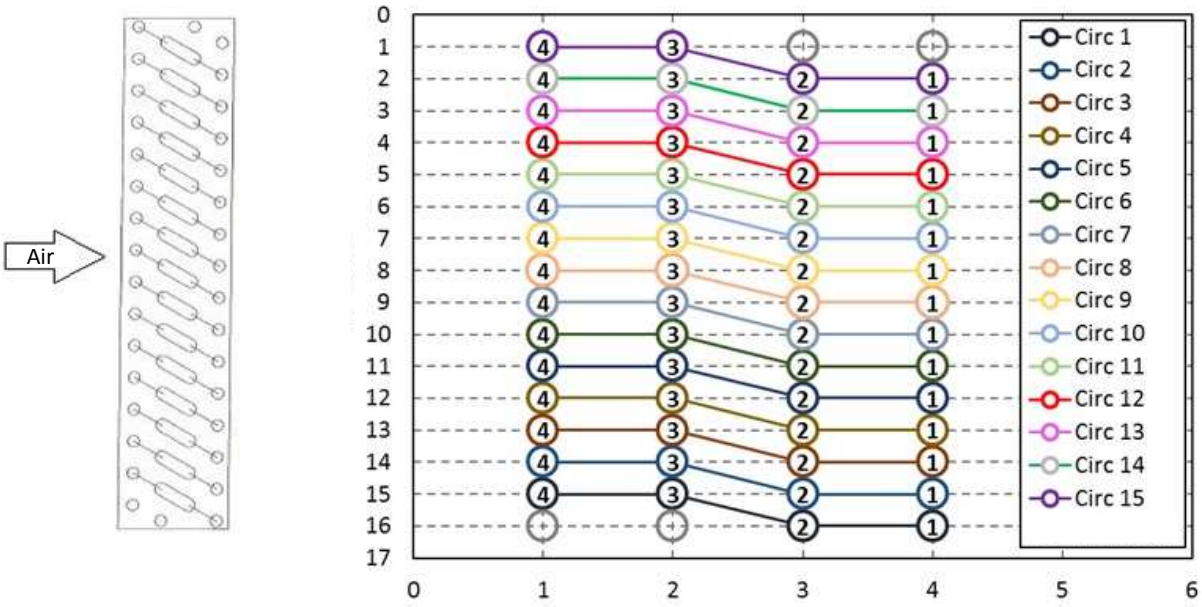

Figure 3.27. Heat exchanger 060 – 4R: schematic of the circuitry (left) and considered circuitry for the model (right).

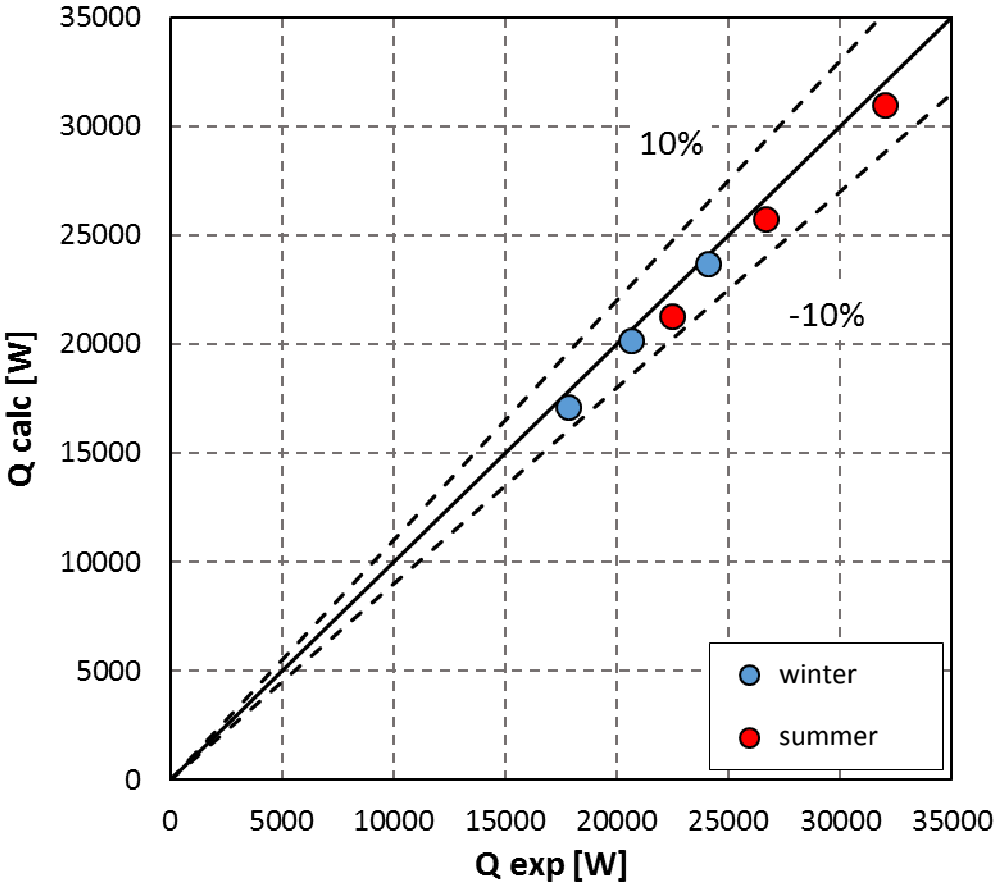

Figure 3.28. Total heat flow rate of unit EBH 060 – 4R: comparison between experimental data and results of the present model.

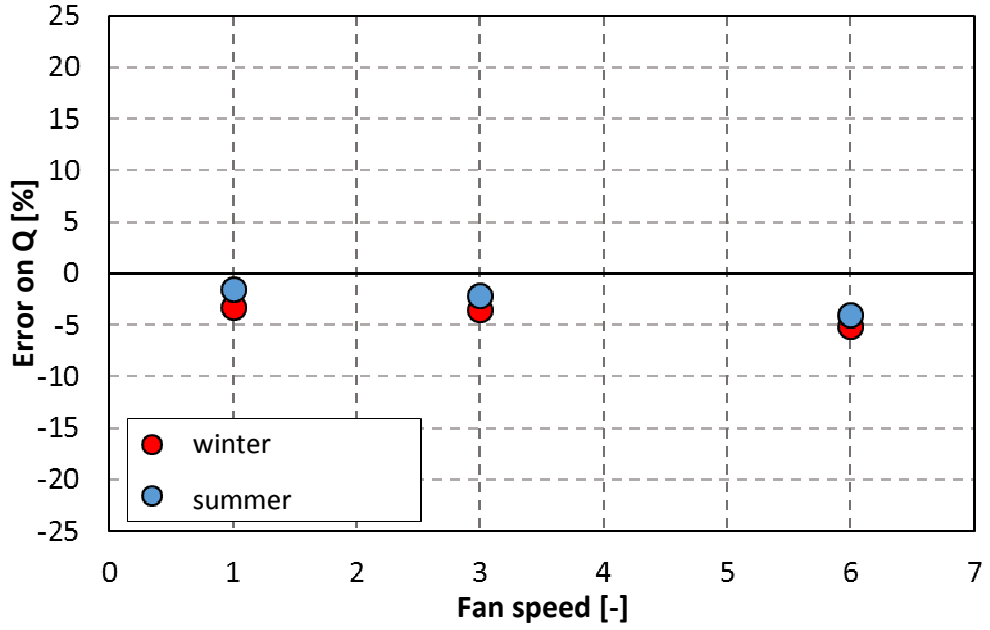

Figure 3.29. Error in the evaluation of the total heat flow rate versus the fan speed for unit EBH 060 – 4R for the present model (divided in summer and winter conditions).

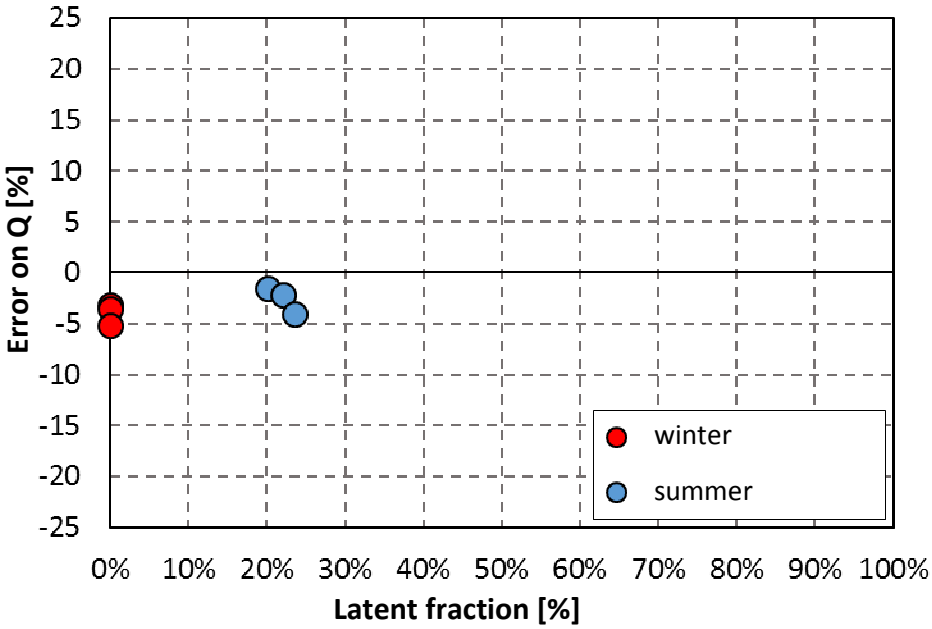

Figure 3.30. Error in the evaluation of the total heat flow rate versus the ratio between latent and total heat flow rate for unit EBH 060 – 4R for the present model (divided in summer and winter conditions).

Figure 3.31 and Figure 3.32 show that the pressure drop are under predicted by the model, but in this unit the length of each circuit is even lower than in the previous units, thus the value of inlet and outlet pressure drop is more important with respect to the total pressure drop.

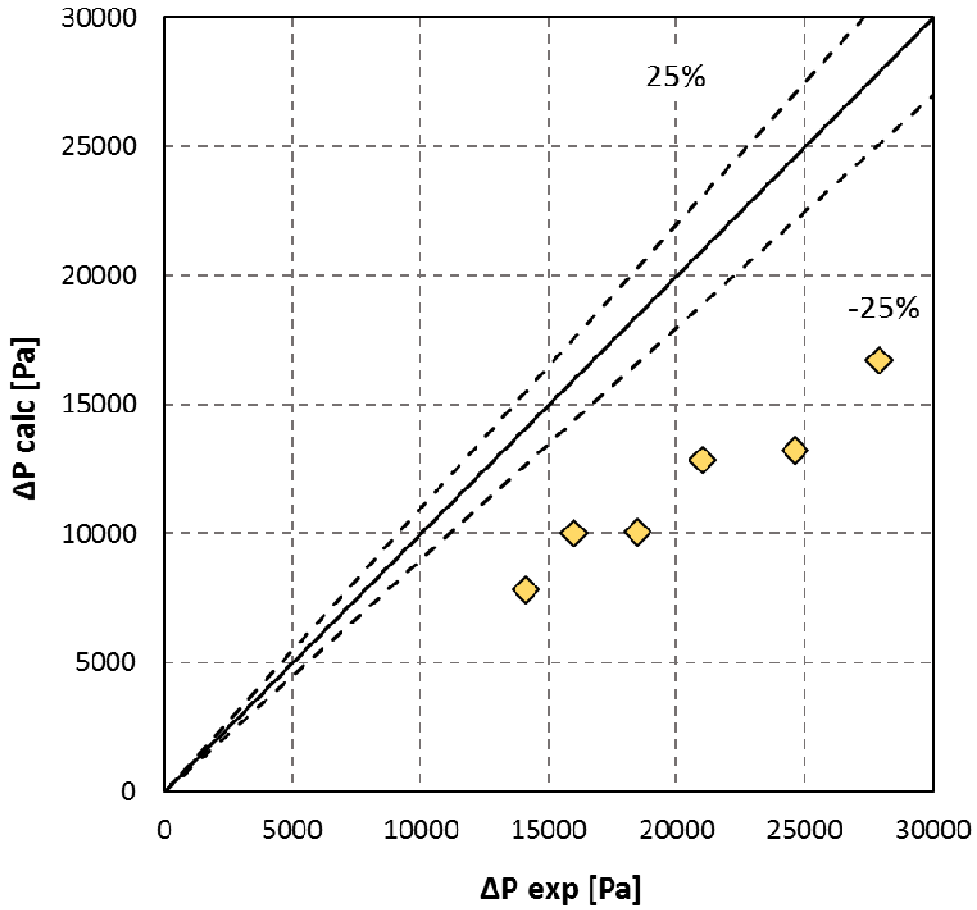

Figure 3.31. Pressure drop on the water side: comparison between experimental data and results of the present model for the unit EBH 060 – 4R.

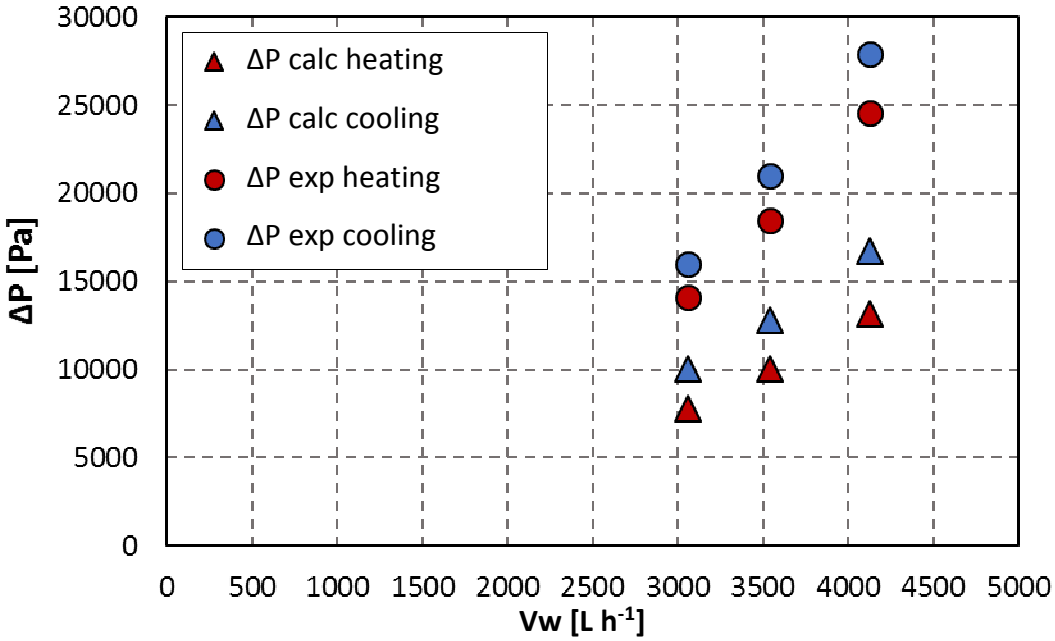

Figure 3.32. Internal pressure drop versus mass flow rate of water for unit EBH 060 – 4R: comparison between experimental results and results of the present model (divided in summer and winter conditions).

3.1.2.2.5 EBH 020/030 – 4R District Cooling

District cooling and district heating systems involve a central unit that provide the heat flow rate necessary for the thermal requirements of several buildings connected by a long grid of pipes. In order to decrease the power consumptions of the pumps, the mass flow rate of water is maintained at the minimum level, thus the temperature gain (or temperature loss) of water in the heat exchangers positioned in the buildings is increased with respect to the standard 5 K. The circuitry of the heat exchanger is changed because of this, so lower number of circuits with longer length are utilized. The temperature difference between inlet and outlet in these systems can vary in the range 9 – 20 K.

Table 3.10 reports the main geometric characteristics of the heat exchanger in the unit EBH 020/030 – 4R District Cooling, while Figure 3.33 and Figure 3.34 show the real and the simplified circuitry of the unit.

Table 3.9. Conditions for tests in cooling and heating mode with units for district cooling.

Summer mode	
T_{air} *IN*	27 °C
RH IN	50%
T_w *IN*	5.5 °C
ΔT_w	9 K
Fan speed	min – Med – MAX

Winter mode	
T_{air} *IN*	20 °C
T_w *IN*	60 °C
ΔT_w	15 - 20 K

Table 3.10. Dimensions of the tested finned tube heat exchanger (EBH 020/030 – 4R District Cooling).

Number of Rows	[-]	N_R	4
Number of tubes in each row	[-]	N_t	16
Tube's length	[m]	L	0.875
Fin pitch	[m]	X_f	0.0021
Longitudinal tube pitch	[m]	X_l	0.02165
Transverse tube pitch	[m]	X_t	0.025
Fin thickness	[m]	s_f	0.0001
Tube's external diameter	[m]	D_e	0.01008
Tube thickness	[m]	s_t	0.00028

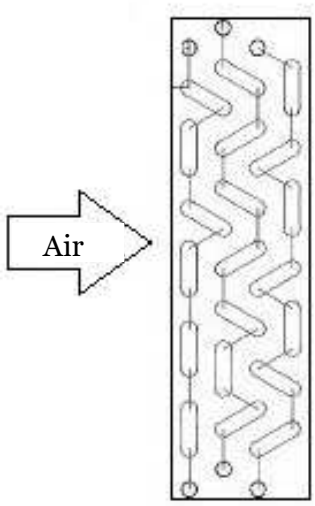

Figure 3.33. Schematic of the circuitry of the heat exchanger 020/030 – 4R District Cooling.

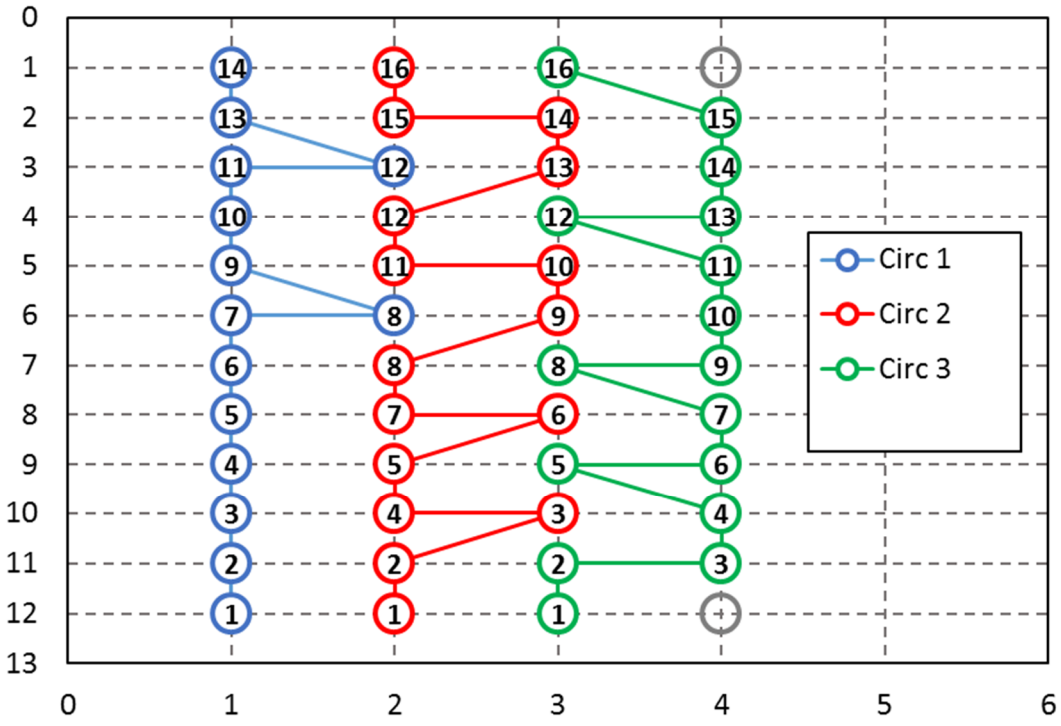

Figure 3.34. Heat exchanger 020/030 – 4R District Cooling: considered circuitry for the model.

Figure 3.35 shows that the total heat flow rate of the unit is predicted by the present model with an error lower than 8%. As with the previous units, Figure 3.36 shows that the speed of the fan does not influence the results of the model.

Figure 3.37 and Figure 3.38 show that the internal pressure drop of this unit are well predicted by the model (average error is 5%): this is due to the longer length of the circuits that lead to a lower importance of inlet and outlet pressure drop of the unit.

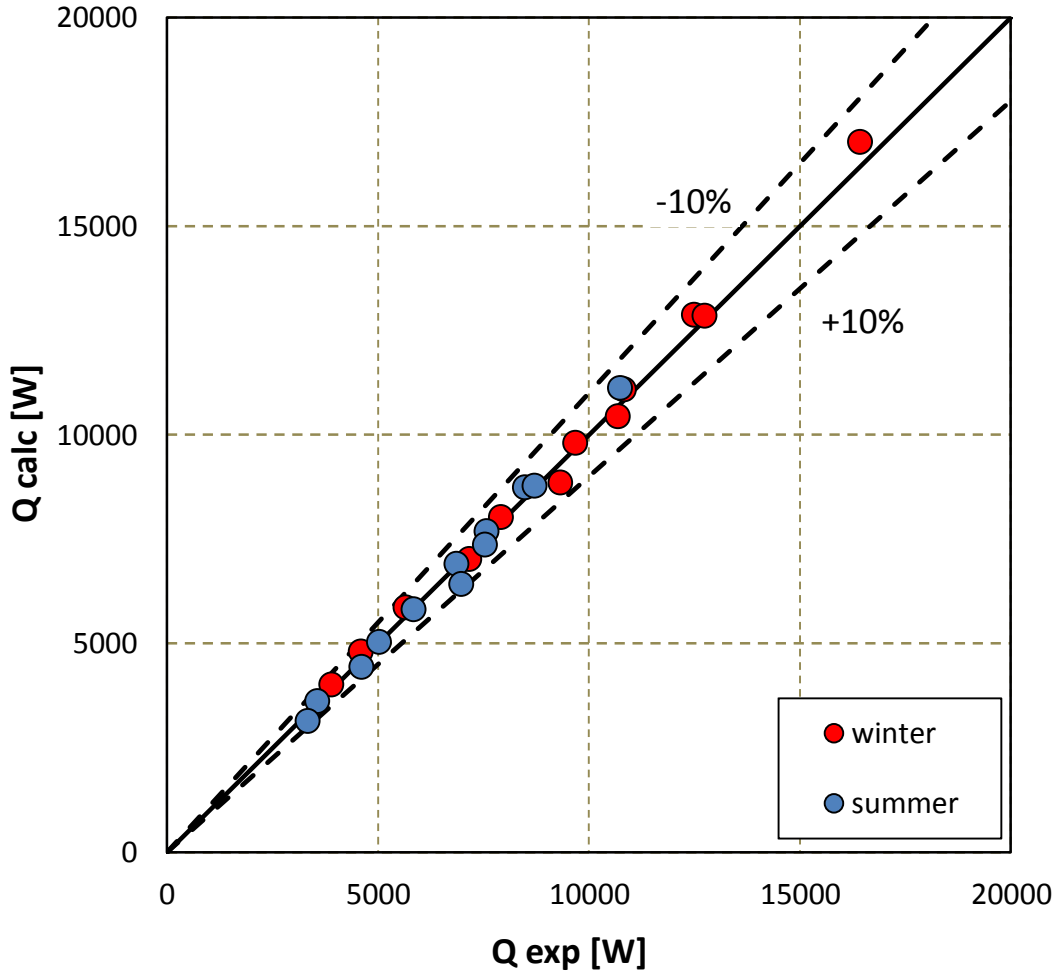

Figure 3.35. Total heat flow rate of unit EBH 020/030 – 4R District Cooling: comparison between experimental data and results of the present model.

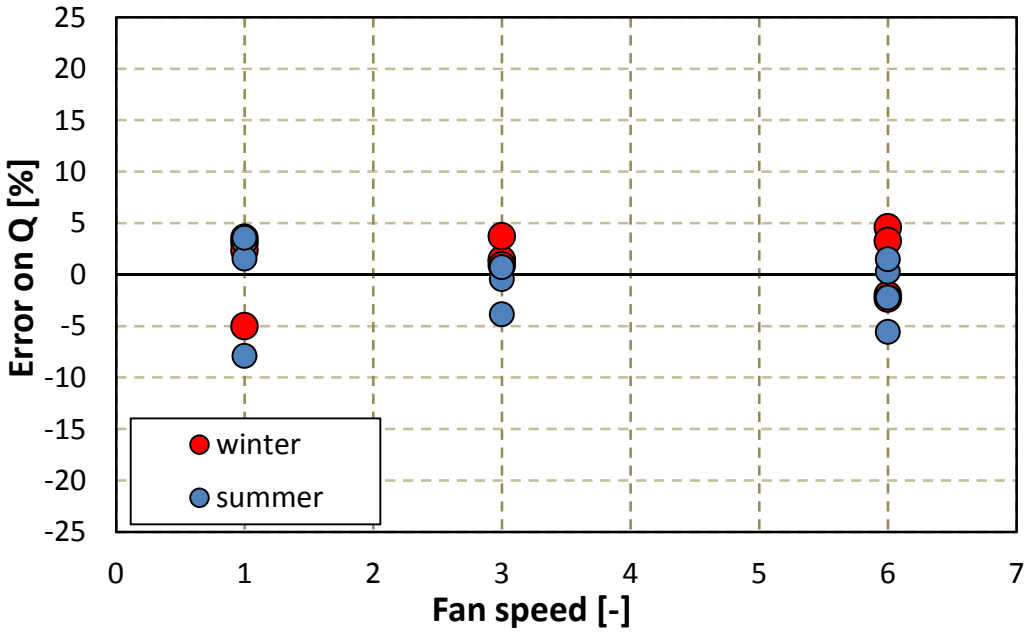

Figure 3.36. Error in the evaluation of the total heat flow rate versus the fan speed for unit EBH 020/030 – 4R District Cooling for the present model (divided in summer and winter conditions).

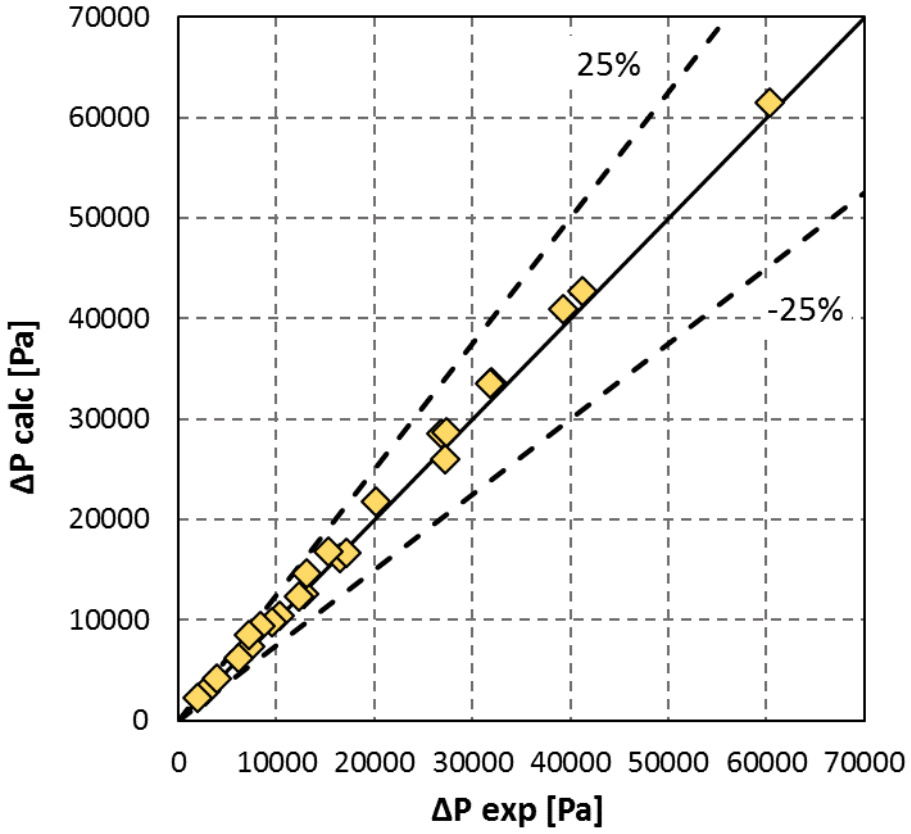

Figure 3.37. Pressure drop on the water side: comparison between experimental data and results of the present model for the unit EBH 020/030 – 4R District Cooling.

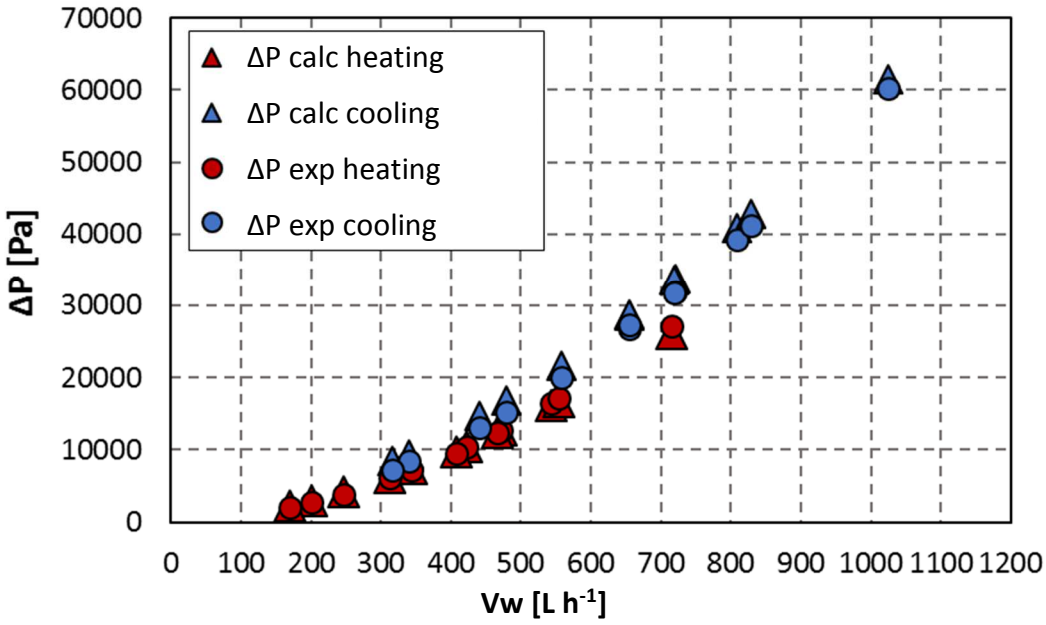

Figure 3.38. Internal pressure drop versus mass flow rate of water for unit EBH 020/030 – 4R District Cooling: comparison between experimental results and results of the present model (divided in summer and winter conditions).

3.1.2.2.6 EBH 040/050 – 4R District Cooling

As the previous units, these ones are used for district cooling, thus they have longer circuits and are tested in the conditions reported in Table 3.9.

Table 3.11 reports the main dimensions of the heat exchanger, while Figure 3.39 and Figure 3.40Figure 3.27 show the real and the simplified circuitry of the unit.

Table 3.11. Dimensions of the tested finned tube heat exchanger (EBH 040/050 – 4R District Cooling).

Number of Rows	[-]	N_R	4
Number of tubes in each row	[-]	N_t	16
Tube's length	[m]	L	1.125
Fin pitch	[m]	X_f	0.0021
Longitudinal tube pitch	[m]	X_l	0.02165
Transverse tube pitch	[m]	X_t	0.025
Fin thickness	[m]	s_f	0.0001
Tube's external diameter	[m]	D_e	0.01008
Tube thickness	[m]	s_t	0.00028

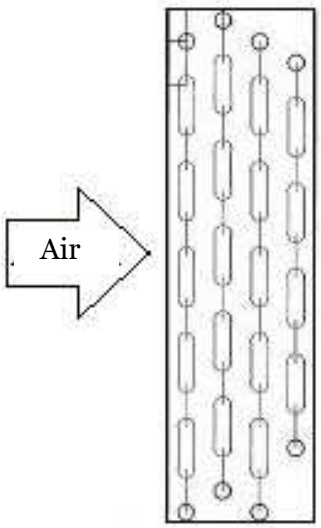

Figure 3.39. Schematic of the circuitry of the heat exchanger 040/050 – 4R District Cooling.

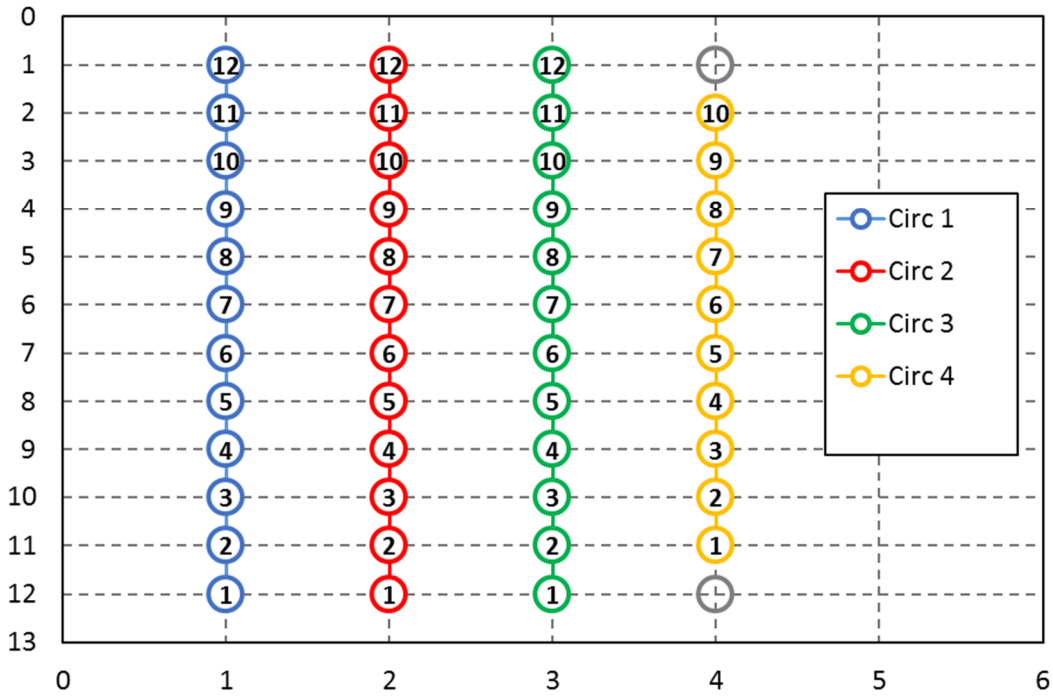

Figure 3.40. Heat exchanger 040/050 – 4R Direct Cooling: considered circuitry for the model.

Figure 3.41 and Figure 3.42 show that the heat flow rate is slightly over predicted by the model, with a maximum error of 15%.

The internal pressure drop results are shown in Figure 3.43 and Figure 3.44. The mean error is 5% while the maximum value of error is 13%. Again, the long circuits allow to have a reliable prediction of this parameter.

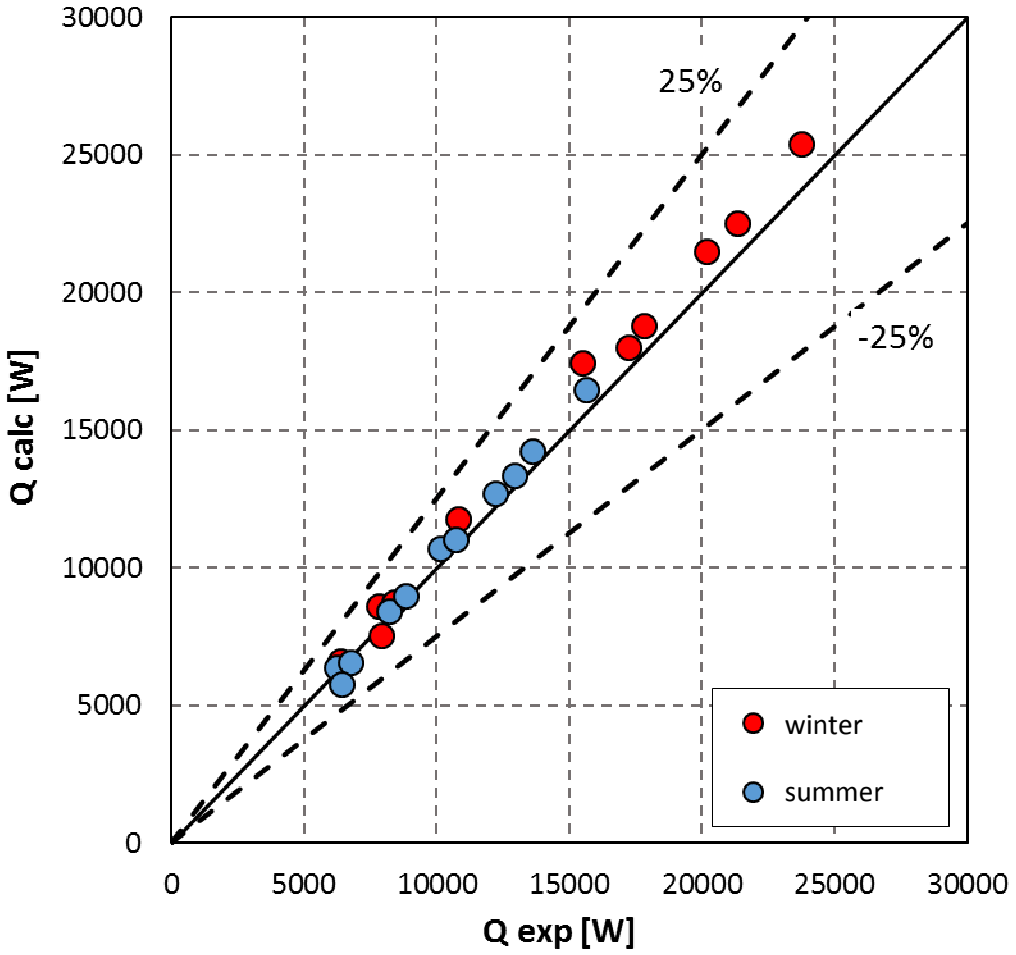

Figure 3.41. Total heat flow rate of unit EBH 040/050 – 4R District Cooling: comparison between experimental data and results of the present model.

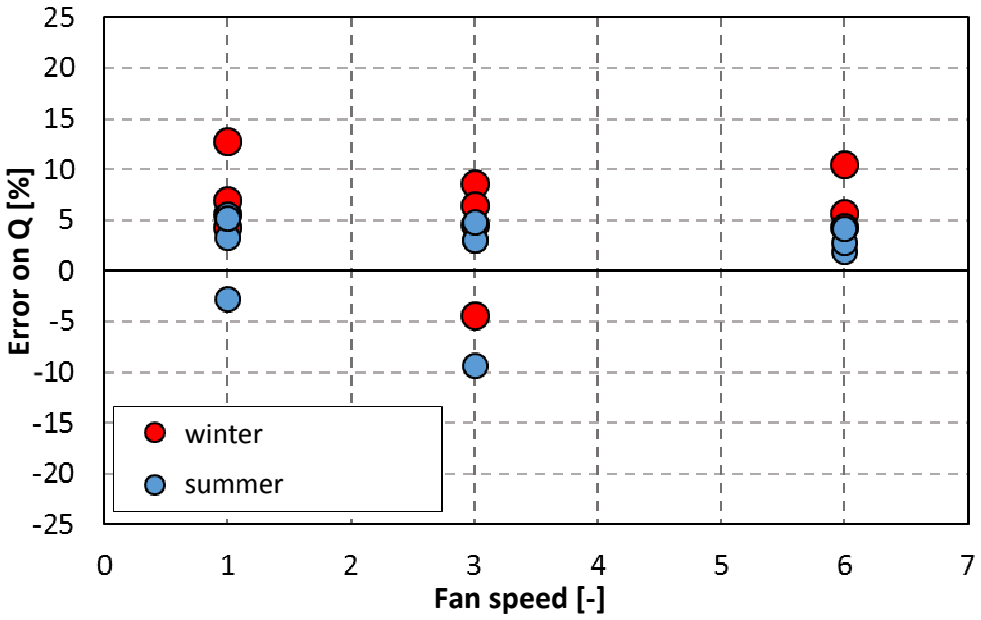

Figure 3.42. Error in the evaluation of the total heat flow rate versus the fan speed for unit EBH 040/050 – 4R District Cooling for the present model (divided in summer and winter conditions).

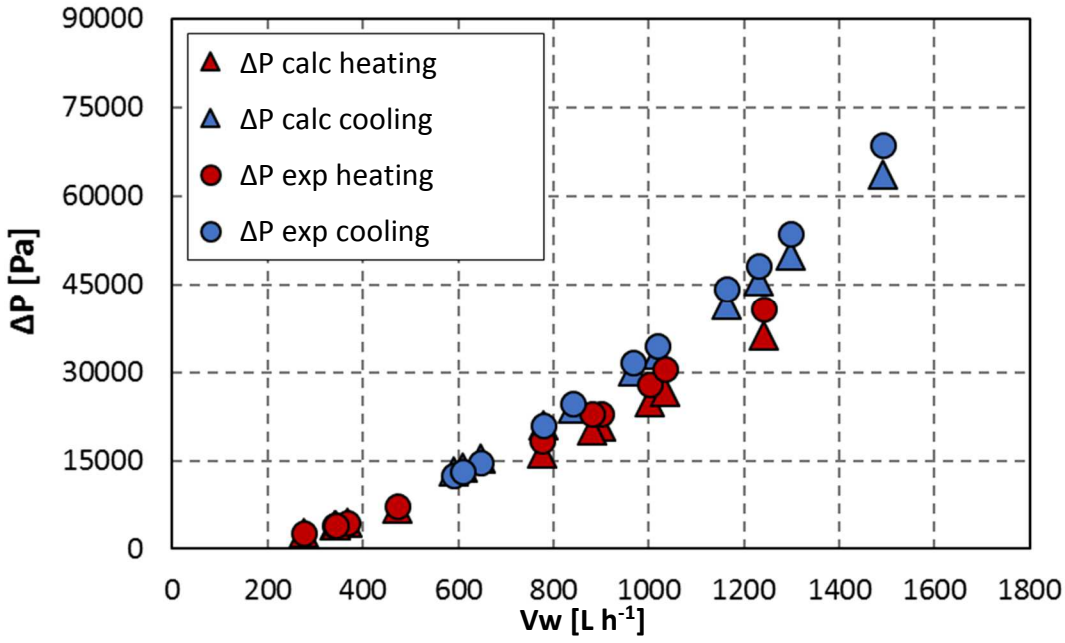

Figure 3.43. Internal pressure drop versus mass flow rate of water for unit EBH 040/050 – 4R District Cooling: comparison between experimental results and results of the present model (divided in summer and winter conditions).

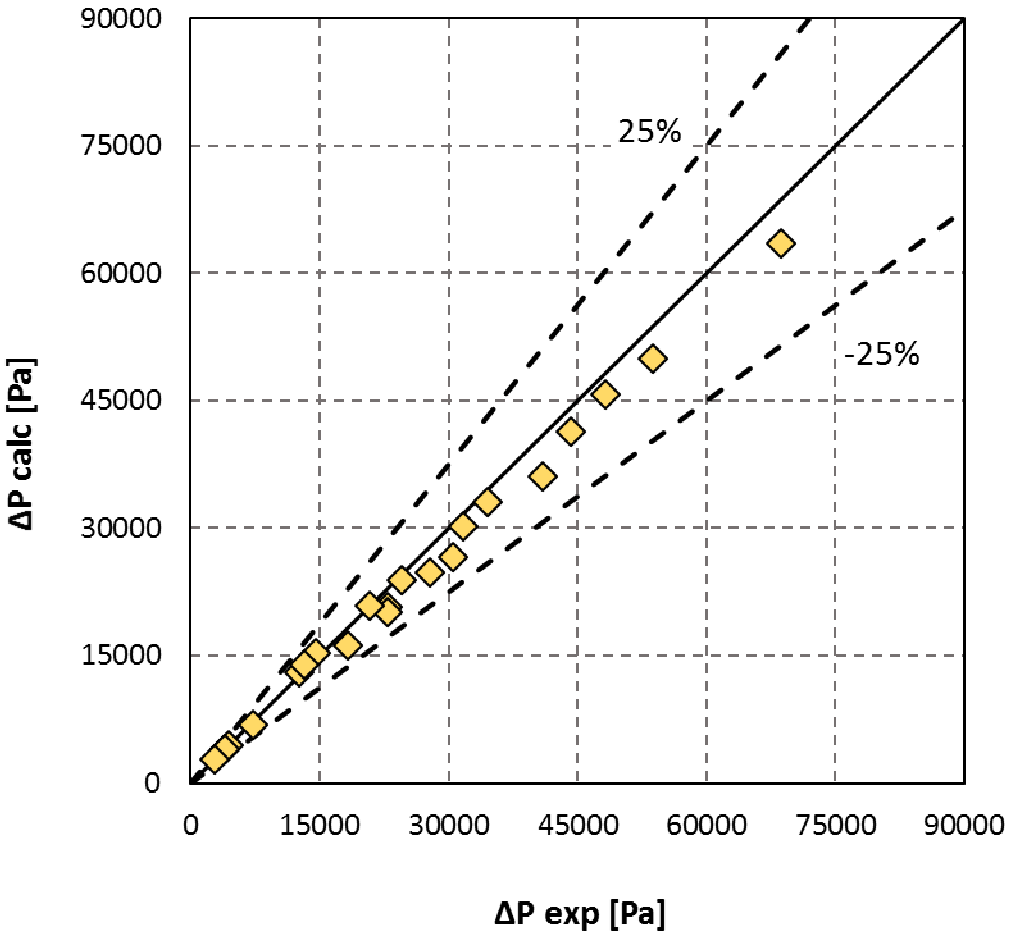

Figure 3.44. Pressure drop on the water side: comparison between experimental data and results of the present model for the unit EBH 040/050 – 4R District Cooling.

3.1.2.2.7 SV 220 – 4R District Cooling

This is a fan coil unit, which means that the heat exchanger is inclined with respect to the direction of the air flow. Figure 3.45 shows a photo and a schematic of the internal disposition of the two fans and of the finned tube heat exchanger in the unit.

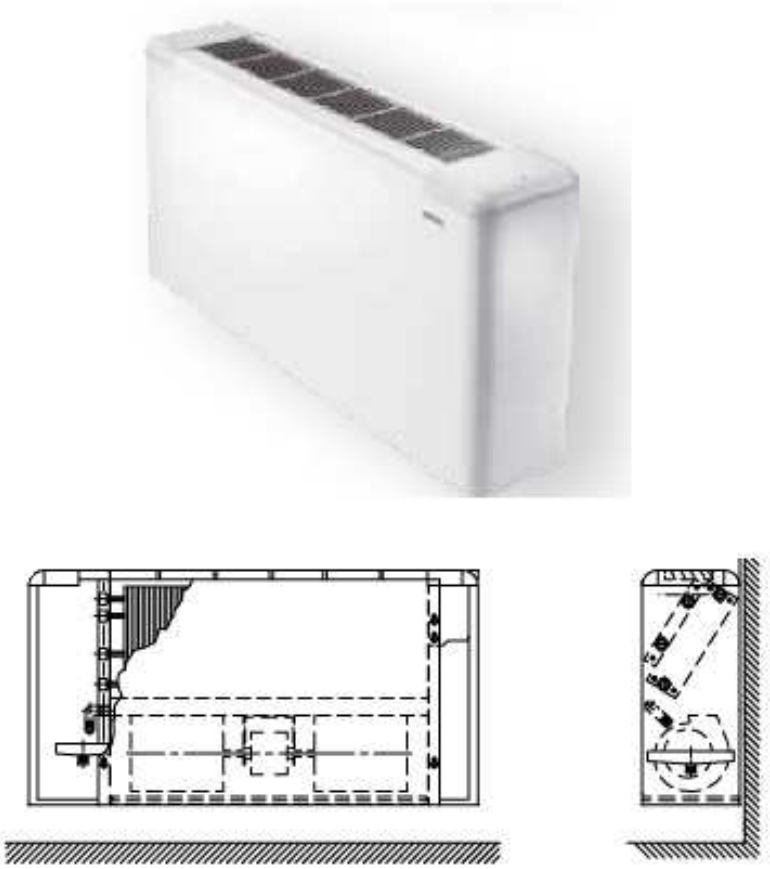

Figure 3.45. Fan coil unit SV 220 – 4R.

The heat exchanger is the same of unit EBH 020/030 – 4R District Cooling, thus Table 3.10 reports the main geometric characteristics, while Figure 3.33 and Figure 3.34 show the real and the simplified circuitry of the unit.

In the numerical model, the air flow direction is supposed to be orthogonal to the two main dimensions of the heat exchanger, as with the previous units.
Figure 3.46, Figure 3.47 and Figure 3.48 shows that the total heat flow rate of this unit is predicted within 3% by the present model, with no influence of the fan speed and latent heat.

Figure 3.49 and Figure 3.50 report the internal pressure drop of the unit, which is overestimated by the model of 10%.

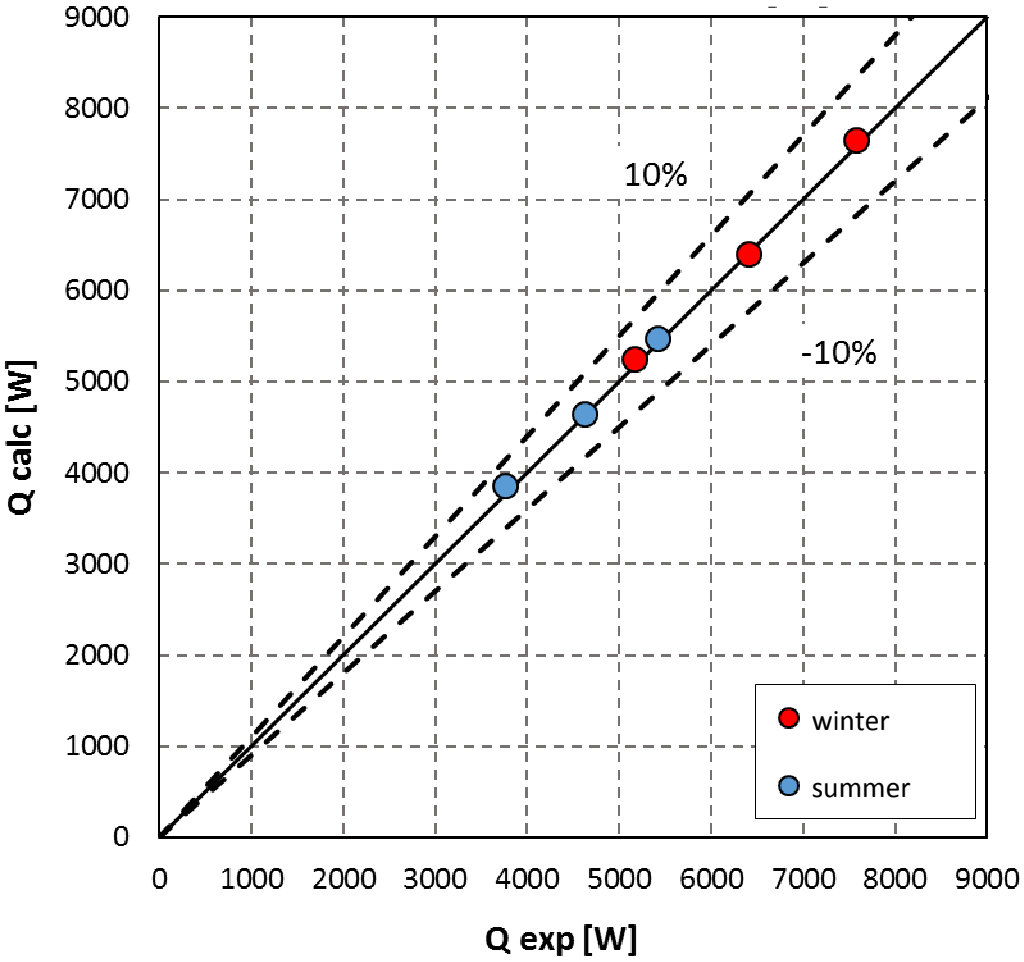

Figure 3.46. Total heat flow rate of fan coil unit SV 220 – 4R District Cooling: comparison between experimental data and results of the present model.

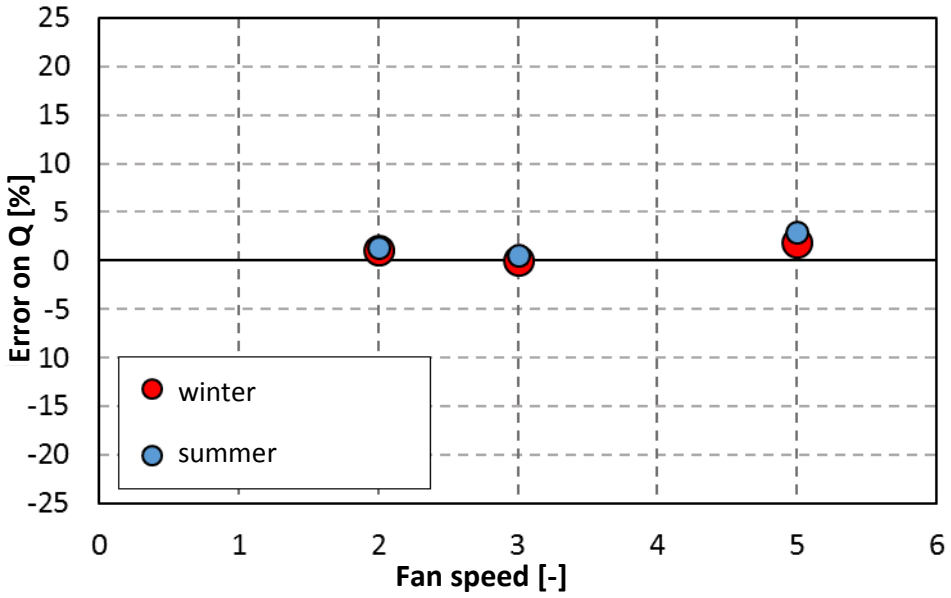

Figure 3.47. Error in the evaluation of the total heat flow rate versus the fan speed for fan coil unit SV 220 – 4R for the present model (divided in summer and winter conditions).

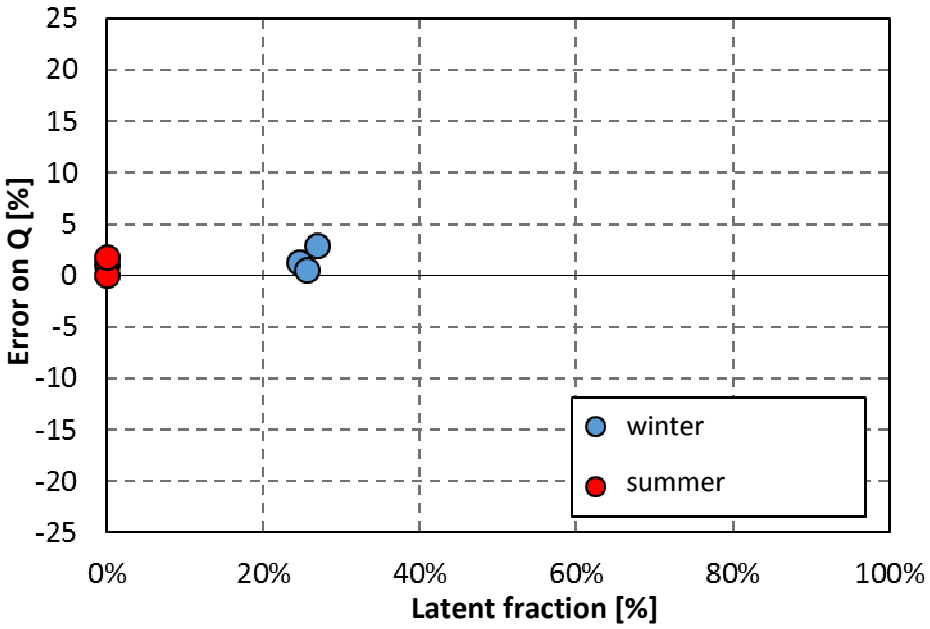

Figure 3.48. Error in the evaluation of the total heat flow rate versus the ratio between latent and total heat flow rate for fan coil unit SV 220 – 4R for the present model (divided in summer and winter conditions).

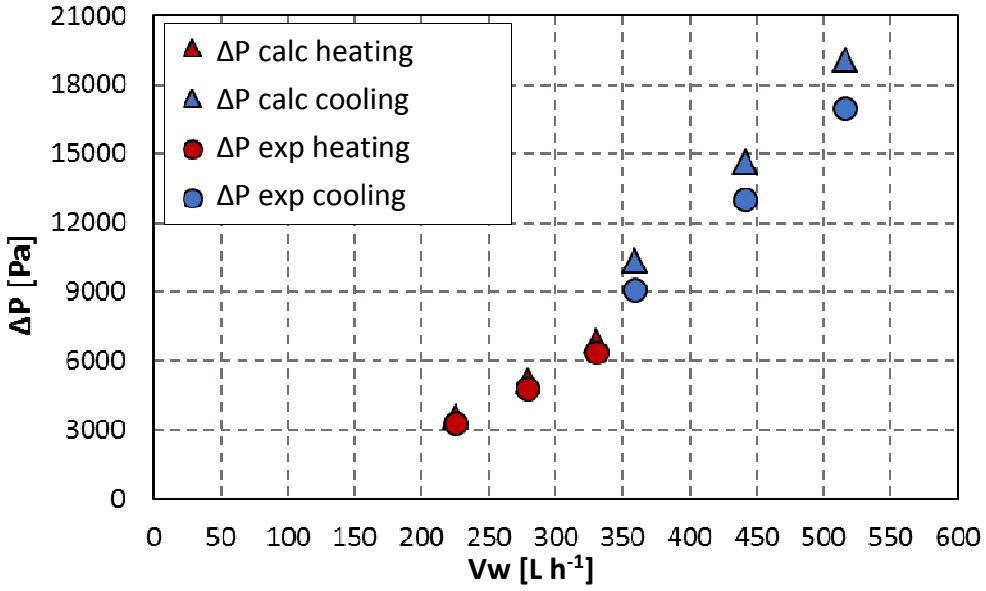

Figure 3.49. Internal pressure drop versus mass flow rate of water for fan coil unit SV 220 – 4R: comparison between experimental results and results of the present model (divided in summer and winter conditions).

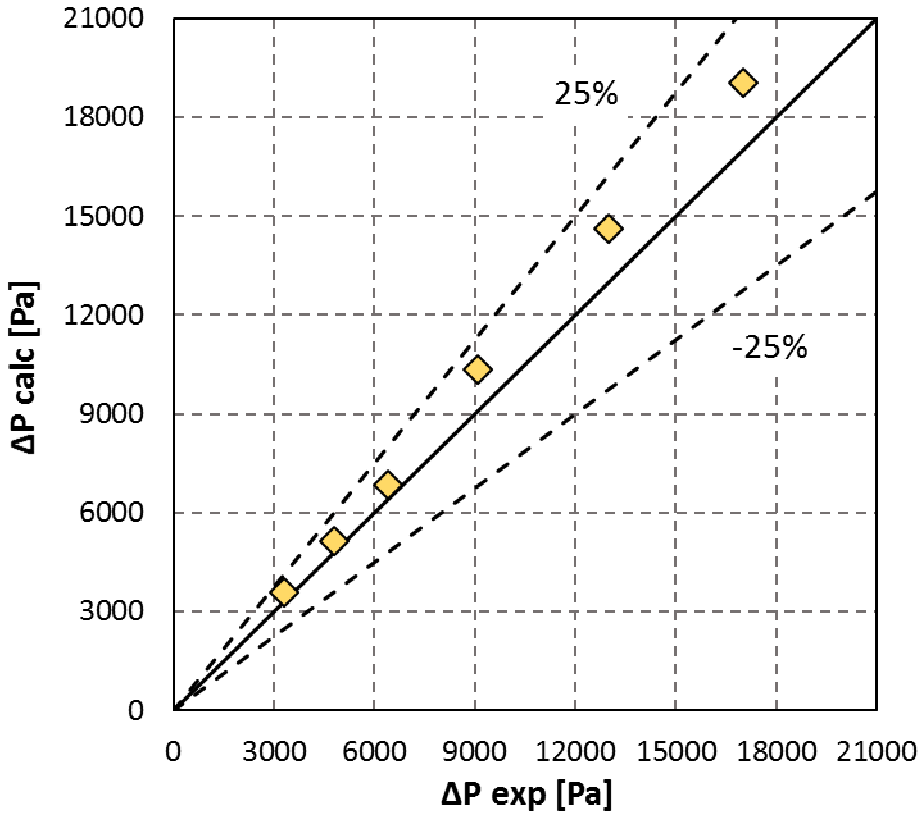

Figure 3.50. Pressure drop on the water side: comparison between experimental data and results of the present model for the fan coil unit SV 220 – 4R.

Figure 3.51 reports the MAD, MD and SD indexes as defined in equations (2.30), (2.31) and (2.32), for the total heat flow rate exchanged in the units described so far.
The first three indexes refer to the reference model compared with EBH 020 3R unit. The present model predicts the same unit with higher accuracy (MAD = 2.1 %; MD = -0.7%; SD = 2.4%).
The model predicts the total heat flow rate of the other 6 units with a maximum value of the three indexes equal to 5.9%.

Figure 3.52 reports the same information regarding the internal pressure drop: it is clear that the model is not able to catch the values of pressure drop in units with short circuits, while the situation is better with district cooling units.

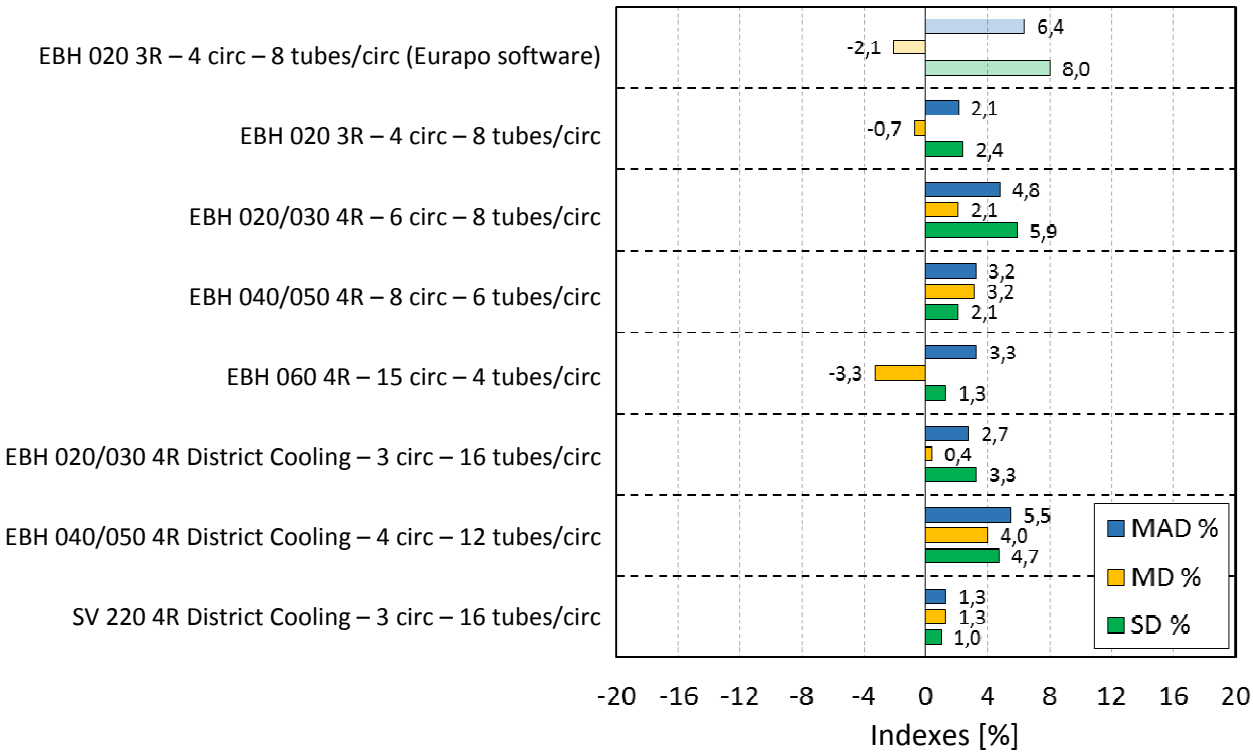

Figure 3.51. MAD, MD and SD indexes referred to total heat flow rate in the heat exchanger.

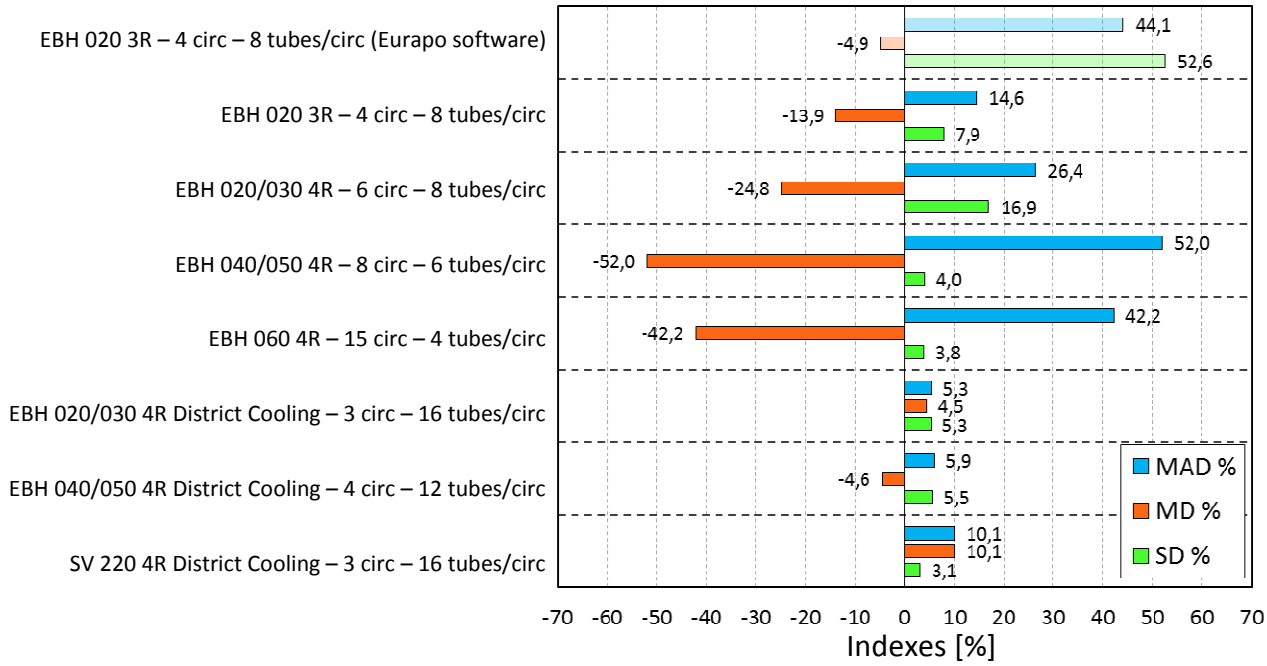

Figure 3.52. MAD, MD and SD indexes referred to pressure drop on the water side.

4 Modelling of finned coil evaporator

4.1 Description of the model

A model of finned coil heat exchangers working with an evaporating refrigerant inside the tubes has been implemented. The structure of the model is the same as the one described in Chapter 3, with the ε-NTU method applied in the same control elements, and the same correlations used to evaluate HTC and pressure drop on the air side.
The main difference lays in the evaluation of HTC and pressure drop inside the tubes.
Depending on the vapour quality of the refrigerant, different correlations are used:

- If the refrigerant is in single phase conditions, the HTC is evaluated with the correlation of Gnielinski with Petukhov factor (1970);
- If the vapour quality is between zero and the dryout value (evaluated with the correlation reported by Wojtan et al., 2005), the HTC on the refrigerant side is calculated with Liu and Winterton (1989) correlation, reported in Eq. (2.38);
- If vapour quality is between the critical value and 1, HTC is considered to be a linear interpolation between the value at the dryout and the value at saturated vapour conditions, as described in the following equation

$$HTC_x = HTC_{x=1} + \left(HTC_{DO} - HTC_{x=1}\right)\frac{(1-x)}{(1-x_{DO})} \tag{4.1}$$

In two phase flow conditions, pressure drop are evaluated with Friedel (1979) correlation, while Churchill (1977) correlation is used in single phase conditions.

The input parameters for the model are:

- Geometry of the finned tube heat exchanger;
- Air conditions at inlet: temperature, relative humidity, volumetric flow rate;
- Refrigerant inlet conditions: temperature, enthalpy (given by condensing temperature and subcooling at the outlet of a hypothetical condenser of a direct expansion system), mass flow rate of refrigerant.

Enthalpy and pressure are the parameters that pass the information about the refrigerant condition between the different elements of the heat exchanger.
The main output of the program is the total heat flow rate exchanged, divided in sensible and latent heat, and the air and refrigerant conditions at the outlet, with the corresponding pressure drop.
If there is more than one circuit on the refrigerant side, the total mass flow rate is uniformly divided assuming that there is an important pressure drop at the inlet of the tubes, so that the pressure drop inside tubes does not affect the distribution of the refrigerant.

4.2 Results of the model

The main results of the model are here analysed in order to assess the capability of the model to catch the involved phenomena and to give useful results.

The air side of the heat exchanger is modelled as presented in Chapter 3, so that the validation of the previous model ensures the ability of the present model to predict the behaviour of the heat exchanger on the air side.
Moreover, during flow boiling process, the thermal resistance on the air side is the dominant one, thus an error on the HTC on the internal side has a limited effect on the total performance of the evaporator. More attention should be paid when dryout occurs and in the superheating region.
Flow boiling in macro channels with circular cross section is a well studied phenomenon, with correlations developed to evaluate heat transfer coefficient, pressure drop and dryout vapour quality in different conditions.
The developed model allows to combine this knowledge with the results obtained in Chapter 3, so that the behaviour of a finned tube heat exchanger working as an evaporator can be simulated, with the possibility to study the influence of the circuitry on the thermal performance of these devices.

Table 4.1 reports the main geometric dimensions of the heat exchanger considered in the following simulations, while Figure 4.2 and Figure 4.3 show the configuration of its circuitry.
Inlet conditions of the fluids are reported in Table 4.2, while the main results are in Table 4.3.
These kind of evaporators are often employed in direct expansion systems, where the inlet conditions of the refrigerant depend on the outlet conditions at the condenser. Thus, the inlet enthalpy of the refrigerant at the evaporator is given as input to the model through the condensation temperature (Tcond) and subcooling (SC) at the outlet of the hypothetic condenser of the system.

Table 4.1. Dimensions of the finned tube heat exchanger modelled as evaporator (Evap1).

Number of Rows	[-]	N_R	3
Number of tubes in each row	[-]	N_t	12
Tube's length	[m]	L	1.5
Fin pitch	[m]	X_f	0.0021
Longitudinal tube pitch	[m]	X_l	0.022
Transverse tube pitch	[m]	X_t	0.025
Fin thickness	[m]	s_f	0.0001
Tube external diameter	[m]	D_e	0.01009
Tube thickness	[m]	s_t	0.00028

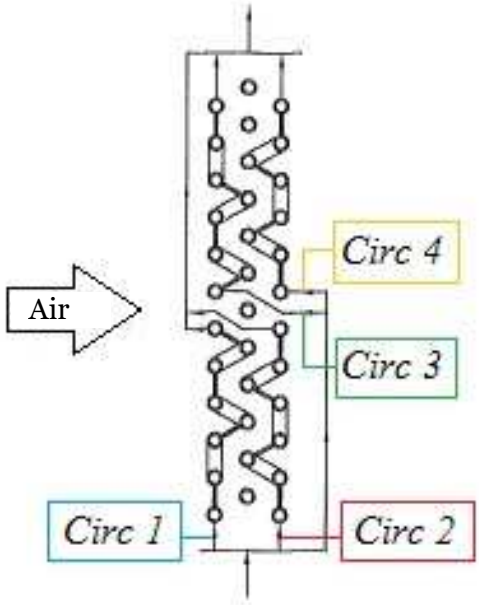

Figure 4.1. Schematic of the circuitry of the heat exchanger (Evap1).

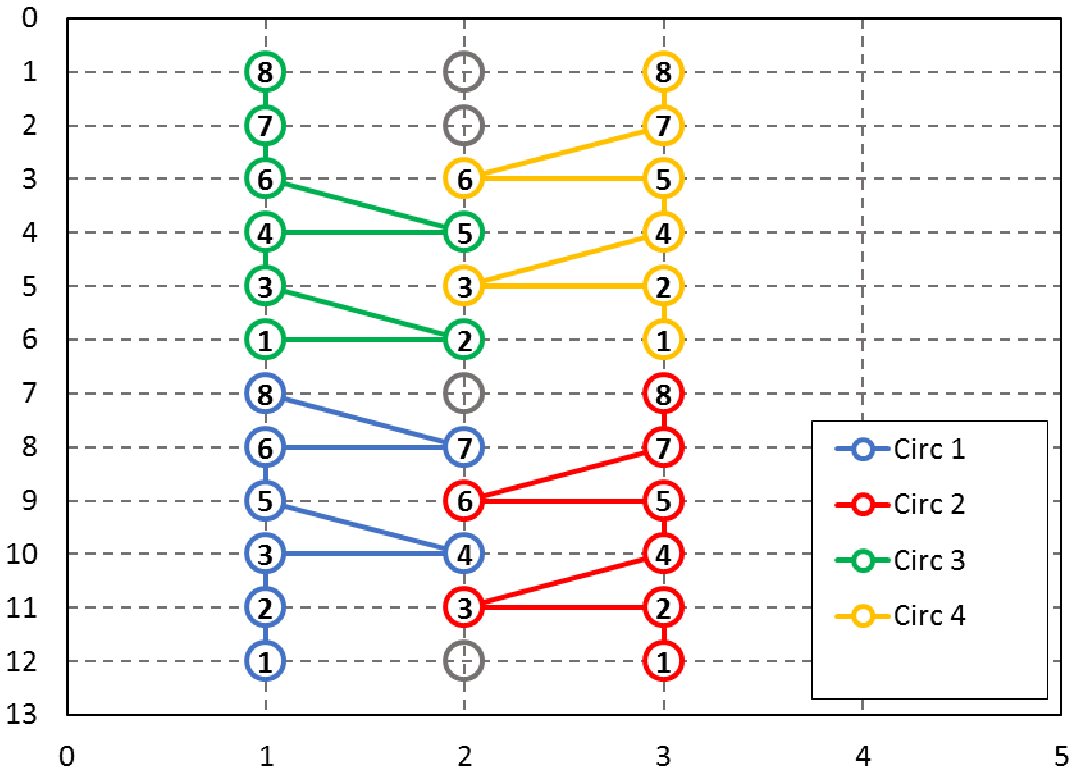

Figure 4.2. Heat exchanger (Evap1): considered circuitry for the model.

Table 4.2. Inlet conditions of simulation tests with the finned tube heat exchanger (Evap1).

T air IN	[°C]	27
RH	[%]	48
V air	[$m^3\ h^{-1}$]	2400
Refrigerant	-	R32
T evap IN	[°C]	7
SC	[K]	5
T cond	[°C]	40
G refr	[$kg\ m^{-2} s^{-1}$]	50 - 400

Table 4.3. Main results of simulation tests of Table 4.2.

G refr	[$kg\ m^{-2}\ s^{-1}$]	50	75	100	150	200	250	300	400
Q total	[kW]	3.8	5.8	7.6	10.5	11.7	12.3	12.7	13.4
Q sensible on air side	[kW]	2.6	3.9	5.1	6.9	7.7	8.0	8.3	8.7
Q latent on air side	[kW]	1.3	1.9	2.5	3.6	4.1	4.3	4.4	4.7
x OUT circuit 1	[-]	1.06	1.06	1.06	1.03	0.94	0.82	0.74	0.62
x dryout	[-]	0.97	0.97	0.96	0.94	0.93	0.92	0.91	0.88

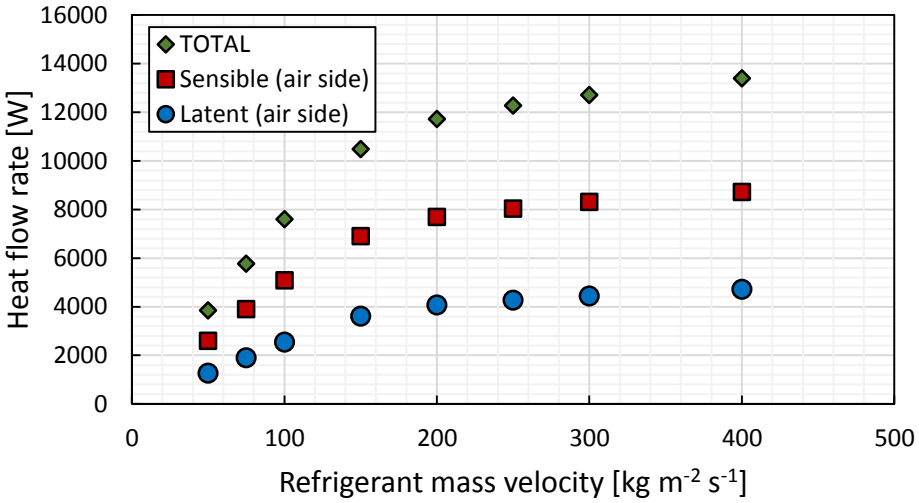

Figure 4.3. Total, latent and sensible heat flow rate versus refrigerant mass velocity during simulation tests of Table 4.2.

In Figure 4.3 the heat flow rate increases while the mass flux of R32 goes from 50 to 200 $kg\ m^{-2}\ s^{-1}$, but a further enlargement of mass velocity leads to a small variation of the heat exchanged. The ratio between sensible and latent heat exchanged is almost constant. The reason for the different trend at higher mass flux lays on the outlet condition of the refrigerant in the different tests: as reported in Table 4.3, the outlet vapour quality decreases with the mass flux and it is lower than 1 for tests with $G > 150\ kg\ m^{-2}\ s^{-1}$, meaning that the superheating zone plays an important role in the heat flow rate exchanged because of its lower HTC. When the superheating region is not present, the enhancement of HTC with mass flux slightly affects the total heat flow rate.

Figure 4.4 reports the heat transfer coefficient of the refrigerant along circuit number 1 for different mass velocities. Here we can see that with G=50 kg m^{-2} s^{-1} the first half of the evaporator has high HTC, due to the effectiveness of evaporation process, while the second half has low HTC, due to the gas–gas heat exchange in the superheating region. When the mass flux increases, the outlet vapour quality is lower, thus the superheating zone is shorter, leading to higher HTC on average.
For mass flux higher than 150 kg m^{-2} s^{-1}, the HTC increases with the mass flux, but the average HTC has a lower variation.
Figure 4.5 shows the temperature of the refrigerant along the circuit 1 for tests with different mass fluxes. With G=200 kg m^{-2} s^{-1} the vapour quality at the outlet is lower than one, thus the refrigerant outlet temperature is close to the inlet one. With G=150 kg m^{-2} s^{-1} the refrigerant superheating at the outlet is ≈6 K and lower mass fluxes has higher refrigerant temperature at the outlet.

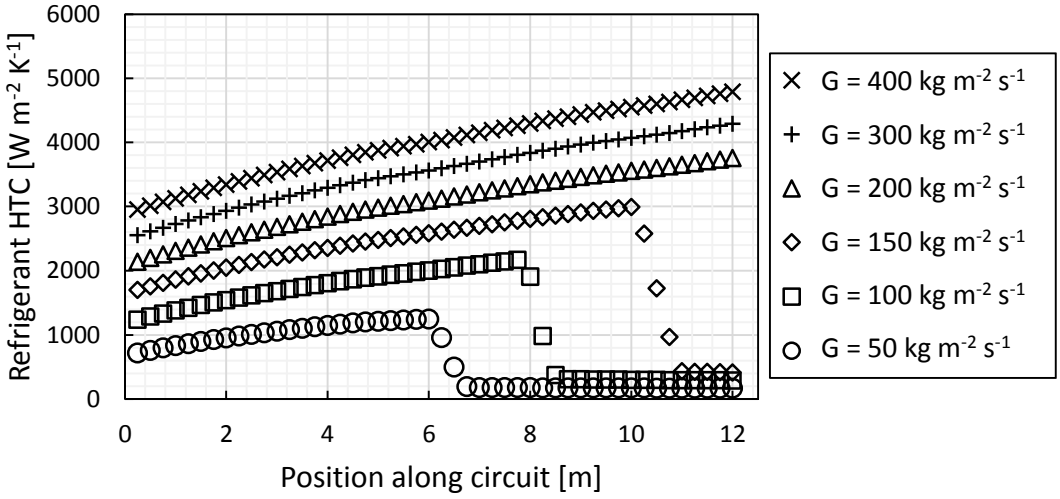

Figure 4.4. HTC of refrigerant along circuit 1 for different mass velocities during simulation tests of Table 4.2.

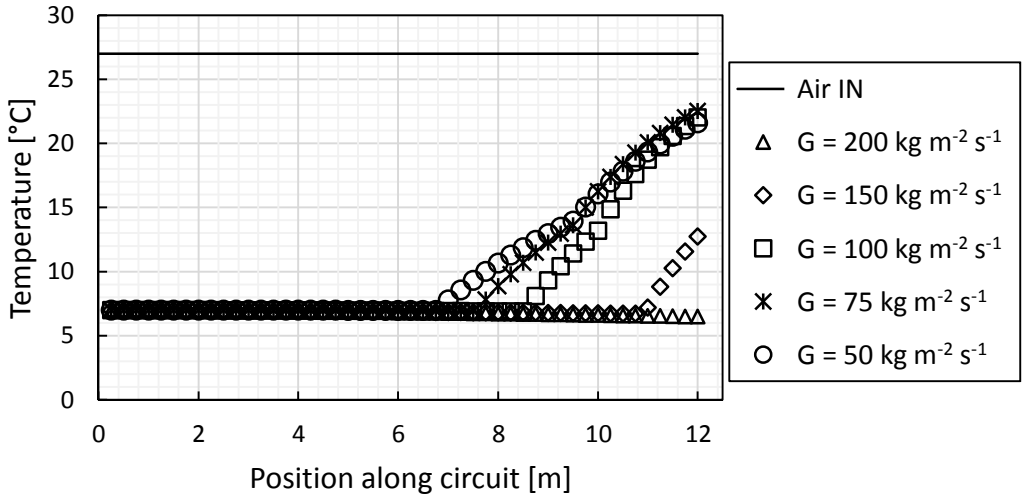

Figure 4.5. Refrigerant temperature profile along circuit 1 for different mass velocities during simulation tests of Table 4.2.

Figure 4.6 reports the refrigerant pressure gradient along the circuit 1 for tests with different mass fluxes. As expected, higher mass velocities means higher pressure drop. In the two-phase region, the trend of the pressure gradient reaches a maximum value before saturated vapour condition, as found in the experimental tests of Chapter 2, reported in Figure 2.15.

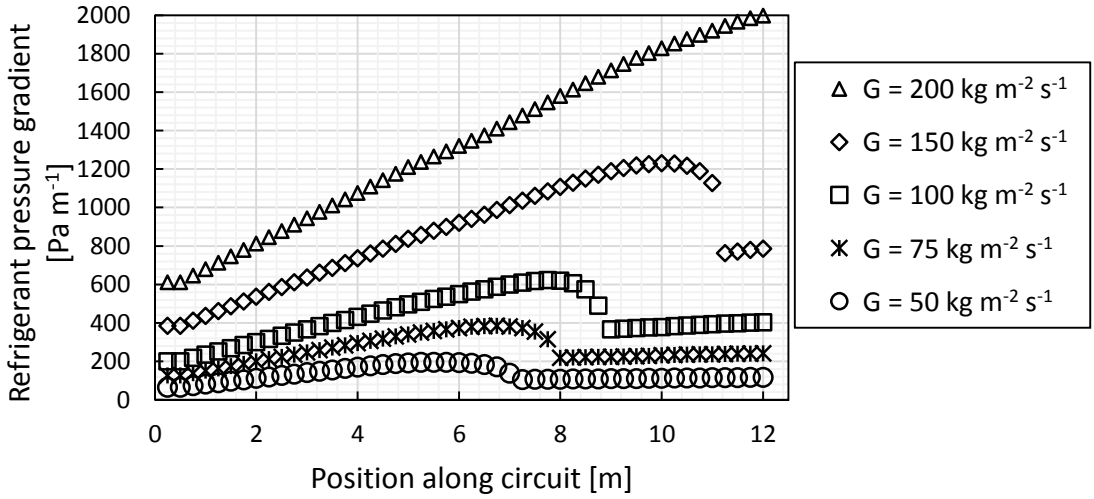

Figure 4.6. Refrigerant pressure gradient along circuit 1 for different mass velocities during simulation tests of Table 4.2.

Figure 4.7 reports the temperatures along the circuit 1 during a simulation test with G=50 kg m^{-2} s^{-1}. According to Figure 4.2, tube 4 and tube 7 belong to the second row, so their inlet air temperature differs from that of the other tubes.

In the first part of the circuit evaporation takes place, with the refrigerant slightly decreasing its temperature due to the pressure drop. In the fifth tube superheating starts and the refrigerant temperature increases. In tube #7 the refrigerant temperature reaches the dew point temperature of air and dehumidification of air ends, so that the following elements have an higher efficiency because of the absence of the thermal resistance of the liquid film on the fins: for this reason the trend of the refrigerant temperature increases its slope.

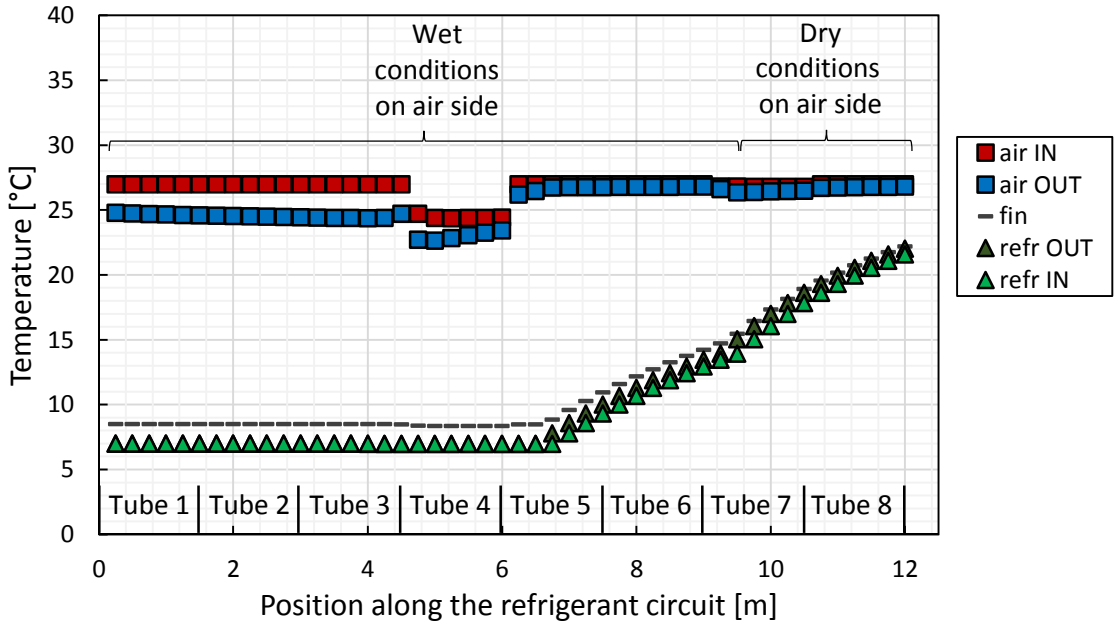

Figure 4.7. Temperature profile of air and refrigerant along circuit 1 during simulation tests of Table 4.2 at G=50 kg m^{-2} s^{-1}.

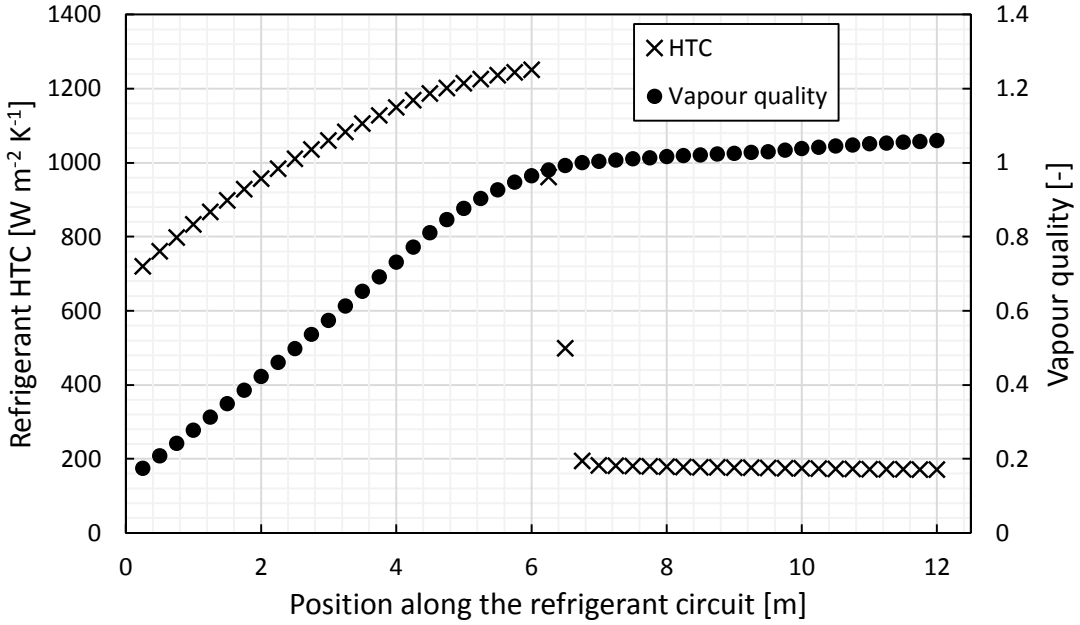

Figure 4.8. Refrigerant HTC and vapour quality along circuit 1 during simulation tests of Table 4.2 at G=50 kg m^{-2} s^{-1}.

Figure 4.8 shows the refrigerant heat transfer coefficient and vapour quality along the first circuit during a simulation performed at G=50 kg m^{-2} s^{-1}: after 6 meters of tubes the vapour quality reaches the critical value after which the dryout leads to an abrupt decrease in HTC towards the low values of the superheated vapour.

The present graphs show the capability of the model to investigate the values of several interesting parameters inside the heat exchanger while operating in different conditions.

5 Modelling of minichannel heat exchangers

Two models of the aluminium heat exchangers have been implemented in Matlab to simulate the behaviour of a bar and plate heat exchanger as condenser and as evaporator.
The correlations used for modelling the heat transfer derive from the experimental activity reported in Chapter 2. The experimental data used to validate the models have been performed on different water/R410A systems using bar and plate heat exchangers.

5.1 Minichannel heat exchangers in water to water systems

Experimental tests have been performed in direct expansion systems that work with R410A and bar and plate heat exchangers as evaporators and condensers with different sizes.
Figure 5.1 shows a schematic of the experimental apparatus used in the tests, while Figure 5.2 represent five of the different heat exchangers tested.
An electromagnetic flow meter is employed for the measurement of the water volumetric flow rate (expanded uncertainty ±0.5% of flow rate), at both evaporator and condenser. The water temperature is measured at the inlet and outlet with an expanded uncertainty of ±0.05 K. Resistance temperature detectors (RTDs, expanded uncertainty ±0.05 K) and pressure transducers (expanded uncertainty ±4 kPa) have been installed in the refrigerant lines before the inlet and after the outlet of the heat exchangers. For all the expanded uncertainties, a coverage factor equal to 2 has been considered.

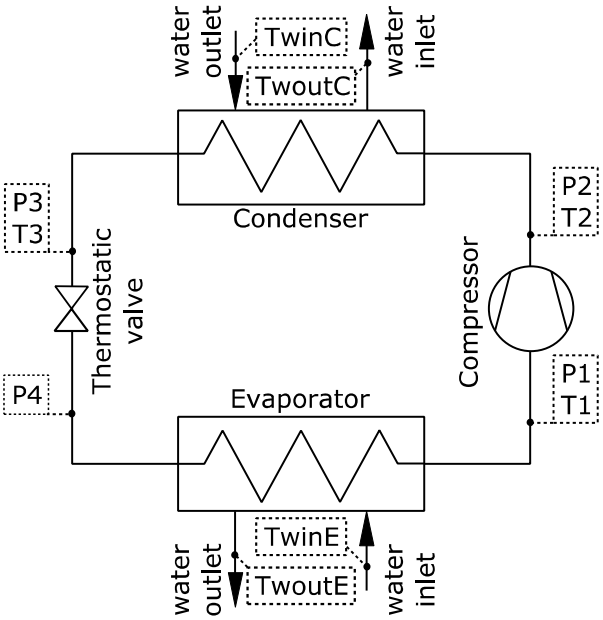

Figure 5.1. Schematic of the experimental apparatus used to test bar and plate heat exchangers as evaporators and condensers.

Figure 5.2. Bar and plate heat exchangers with different sizes that have been tested in direct expansion systems.

Table 5.1. Experimental conditions of the tests performed in the direct expansion systems with bar and plate heat exchangers.

		min	MAX	most of data
T evap	[°C]	1	15	5
T cond	[°C]	35	60	40
T water in evap	[°C]	25	50	30
T water in cond	[°C]	12	25	12
ΔT water cond	[K]	4	5	5
ΔT water evap	[K]	4	5	5
Superheating	[K]	4	12	5
Subcooling	[K]	2	8	5
Re water in the condenser	[-]	1400	3800	
Re water in the evaporator	[-]	1200	2800	

5.2 Water to refrigerant evaporator

5.2.1 Description of the model

The model of the evaporator takes as input:

- Inlet and outlet water temperature;
- Refrigerant superheat at the evaporator;
- Condensation temperature at the condenser;
- Refrigerant subcooling at the outlet of the condenser;
- Mass flow rate of refrigerant.

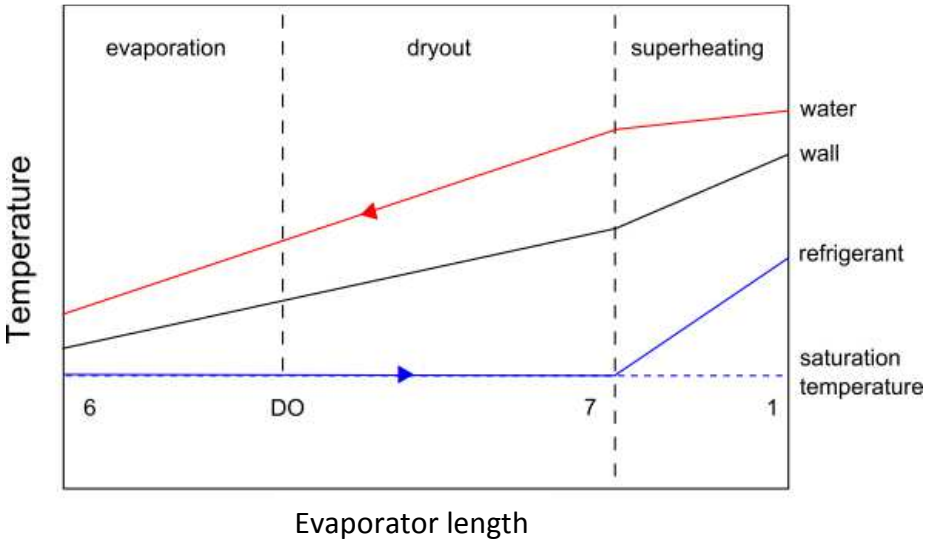

Figure 5.3. Refrigerant, wall and water temperature profile along the evaporator length.

The heat transfer coefficient on the water side is considered constant in all the heat exchanger, while on the refrigerant side this parameter variation is not negligible. The different processes that occurs along the heat exchanger on the refrigerant side lead to different HTC, thus the present model divides the total length of the heat exchanger into three sections, as shown in Figure 5.3: evaporation, dryout region and superheating region.

At first the program calculates the water flow rate for the thermal power with the given water temperatures.

$$m_w = \frac{Q_{evap}}{c_w \left(t_{w,out} - t_{w,in} \right)} \tag{5.1}$$

Then an iterative cycle runs, adjusting the evaporating temperature until the calculated heat flow rate at the evaporator is equal to the input value.
In each of the three parts, calculations are performed to evaluate the heat transfer coefficient and pressure drop. In the iterative cycle, a first attempt value of the evaporating temperature is initially set. The through a logarithmic mean temperature difference method, the model evaluates the length of the three section and compares the sum of the lengths of the three sections with the total length

of the evaporator given as input. The evaporator temperature is then modified in order to match the calculated length with the input value.

The model returns as results:

- Mass flow rate of water;
- Evaporating temperature necessary to obtain the desired heat flow rate at the given operating conditions;
- Heat flux actually exchanged in each section of the heat exchanger;
- Temperature profile of water and refrigerant along the heat exchanger;
- Heat transfer coefficient on the refrigerant and water side;
- Pressure drop on the water and refrigerant side;
- Refrigerant quality at the inception of dryout.

In order to evaluate the accuracy of the model to predict the present experimental data, the mean logarithmic temperature difference between water profile and evaporating refrigerant is here considered:

$$LMTD = \frac{\Delta_1 - \Delta_2}{\ln \frac{\Delta_1}{\Delta_2}} \tag{5.2}$$

Where Δ_1 and Δ_2 are defined as:

$$\Delta_1 = T_{w,in} - T_{evap} \tag{5.3}$$

$$\Delta_2 = T_{w,out} - T_{evap} \tag{5.4}$$

It is important to highlight that the heat transfer coefficient of the refrigerant side is much lower than that on the water side, so the phenomenon of heat transfer is driven by the heat transfer on the refrigerant side. The evaporating phenomenon is difficult to model since the heat transfer coefficient of refrigerant depends by many factors (i.e. quality, local heat flux, partial dry-out…) and this is why the present evaporators present some complexity during modelling.

Water correlations

The equation for strip turbulators has been used to estimate, on the water side, the heat transfer coefficient (HTC):

$$HTC_w = 0.1714 \cdot \mathrm{Re}^{0.6694} \cdot \mathrm{Pr}^{1/3} \frac{\lambda}{d_h} \tag{5.5}$$

For the estimation of the pressure drop the following equations can be used, to account for the frictional (DP_{fr}) and gravity effects (DP_{gr}) respectively:

$$DP_{fr} = \frac{2 \cdot f \cdot G_w}{D_h \cdot \rho} \tag{5.6}$$

$$DP_{gr} = g \cdot \rho \cdot \sin(\beta) \tag{5.7}$$

where the f value is the frictional factor and it is calculated with Manglik (1995) equation for strip turbulators.

Refrigerant correlations

As already mentioned the evaporator is divided in three zones, so for each one different correlations were used. In the evaporation region the Liu and Winterton (1991) correlation has been implemented to evaluate the heat transfer coefficient and the Del Col (2013) correlation for the frictional pressure drop terms. The Liu and Winterton correlation is reported in Eq.(2.38), while the model for pressure drop is reported in Annex A.

The inception of dryout is predicted using the correlation by Del Col et al. (2007), as shown below:

For Froude > 1500

$$x_{CR} = 0.4695 \cdot \left(\frac{4 \cdot q \cdot RLL}{G \cdot d_h \cdot h_{LV}} \right)^{1.472} \cdot \left(\frac{G^2 \cdot d_h}{\rho_L \cdot \sigma} \right)^{0.3024} \cdot \left(\frac{d_h}{0.001} \right)^{0.1836} \cdot (1 - p_{RED})^{1.239} \tag{5.8}$$

For Froude ≤1500

$$x_{CR} = 0.04377 \cdot \left(\frac{G \cdot h_{LV}}{q} \right)^{0.3161} \tag{5.9}$$

Where Froude number is defined as:

$$Froude = \left(\frac{G^2}{g \cdot d_h \cdot \rho_V{}^2} \right) \tag{5.10}$$

$$p_{RED} = \frac{p_{SAT}}{p_{CR}} \tag{5.11}$$

$$RLL = \left(0.437 \cdot \left(\frac{\rho_V}{\rho_L} \right)^{0.073} \cdot \left(\frac{\rho_L \cdot \sigma}{G^2} \right)^{0.24} \cdot d_h{}^{0.72} \cdot \left(\frac{G \cdot h_{LV}}{q} \right) \right)^{1/0.96} \tag{5.12}$$

In the dryout region, it is assumed that the heat transfer coefficient decreases linearly with the vapour quality, starting from the heat transfer coefficient obtained by Liu and Winterton (1991) at dryout quality and the one calculated using the single-phase correlation for the refrigerant (Eq. 39) at quality equal to 1.

Eq.(2.28) and (2.29), that have been developed based on the tests presented in 2.5, have been used to evaluate the single phase HTC on strip and perforated fins, respectively.

The Del Col (2013) correlation has been implemented to estimate the frictional pressure drop terms in dry-out zone and the correlation by Rohuani for the momentum variation and gravity pressure drop term (see Annex A).

Finally, in the superheating zone the single-phase correlation for the refrigerant was applied to calculate the heat transfer coefficient and the same correlation of water to estimate the frictional pressure drop term.

5.2.2 Validation of the model

In the following figures the calculated and experimental logarithmic mean temperature differences are shown for the strip perforated 12 kW, 22kW, 40kW, 120kW and the strip-strip 40kW heat exchangers.
Most of the data are predicted within 25%. Only two sets of data display higher disagreement (Figure 5.5).

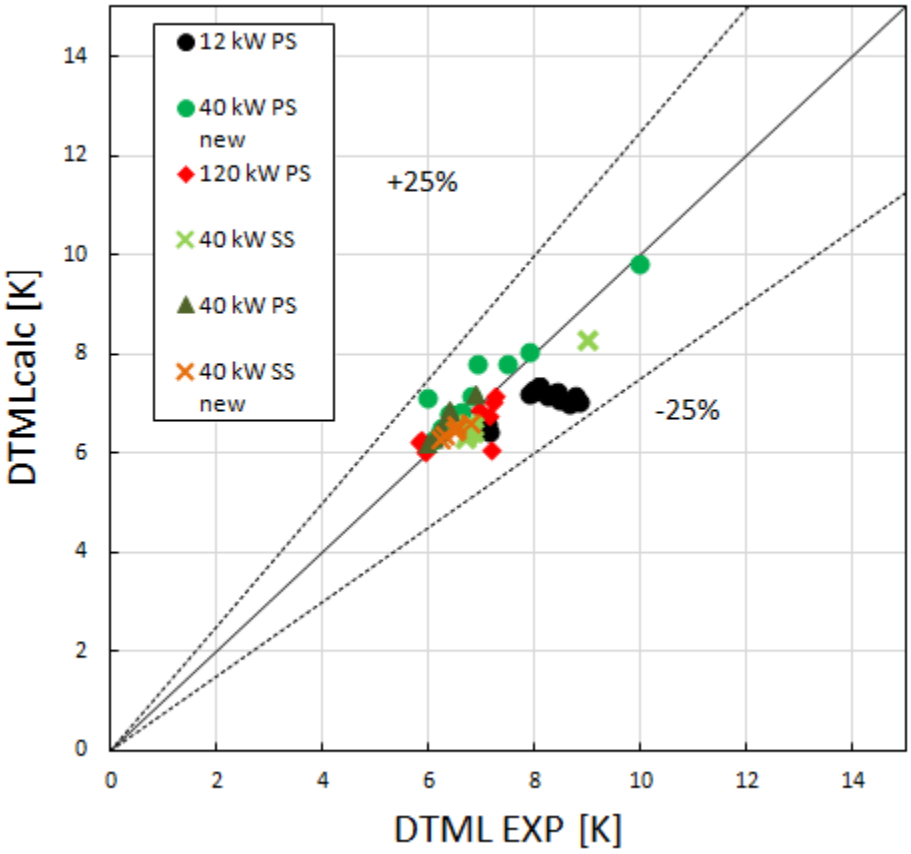

Figure 5.4. Logarithmic mean temperature difference: calculated vs. experimental values for 12 kW, 40kW, 120kW heat exchanger.

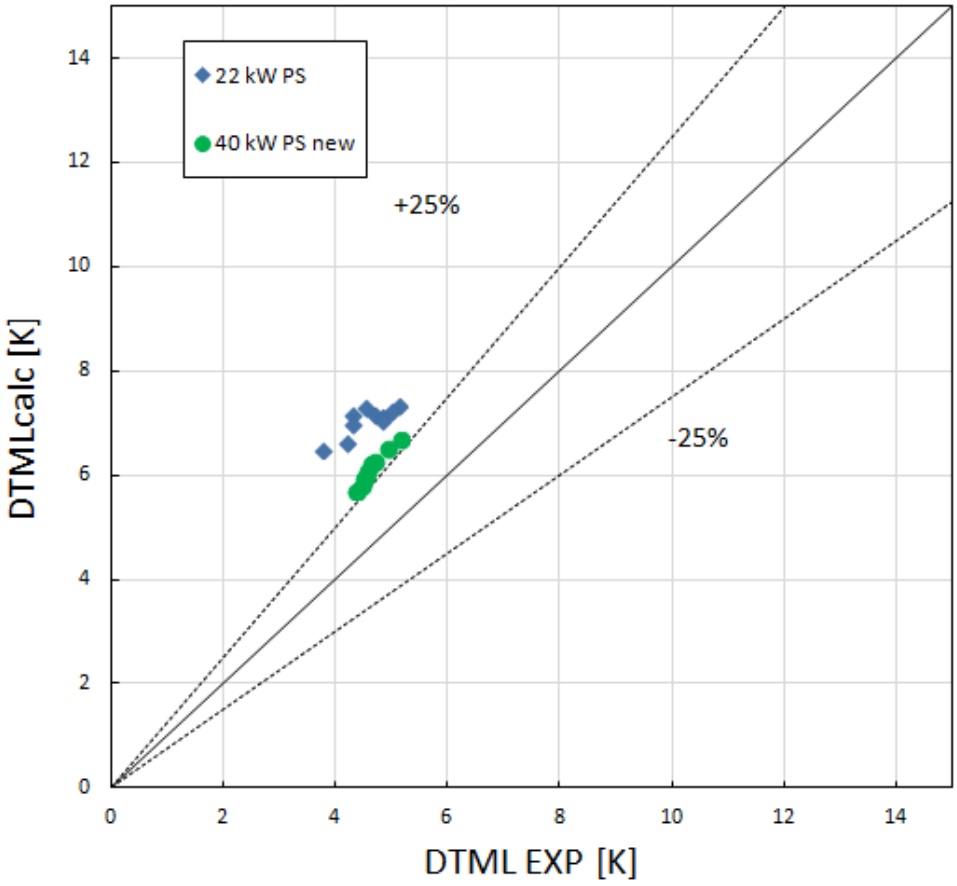

Figure 5.5. Logarithmic mean temperature difference: calculated vs. experimental values for 22 kW, 40 kW heat exchanger.

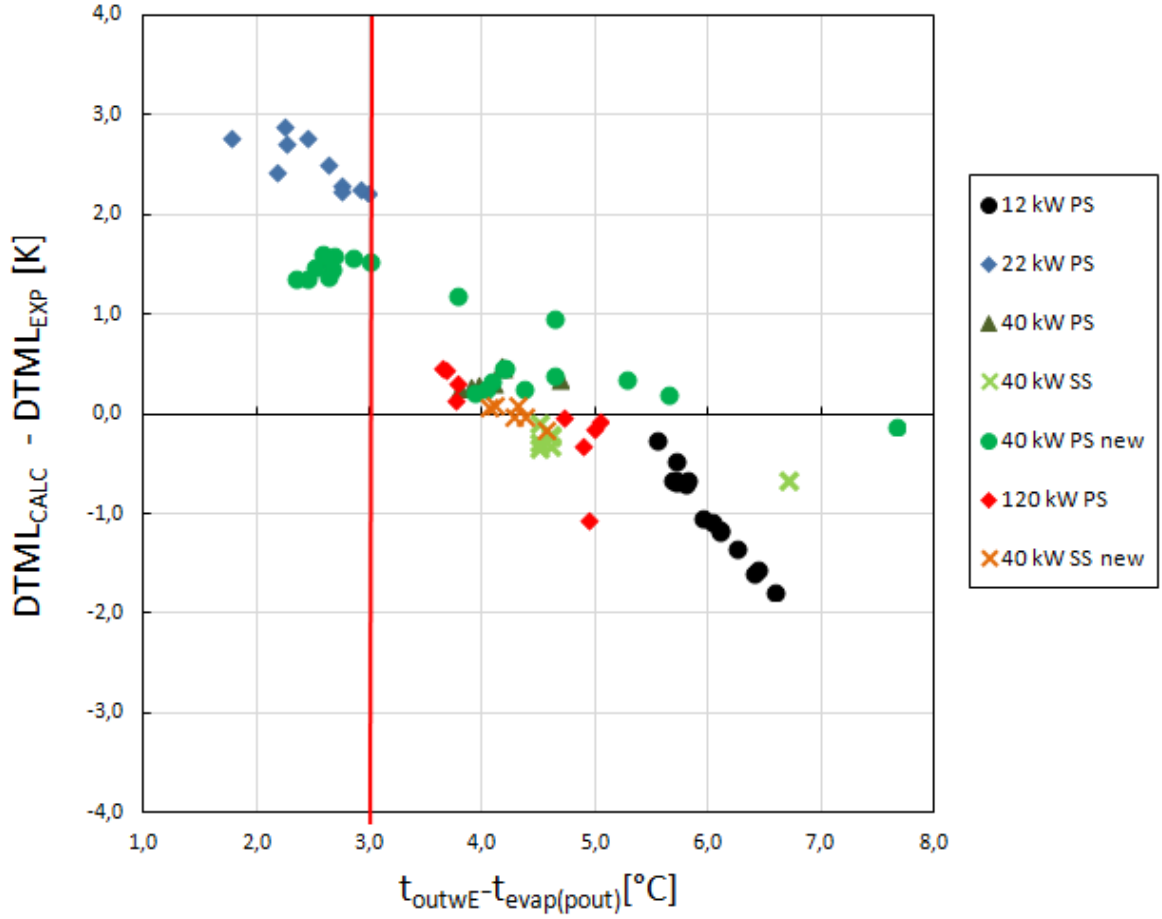

Figure 5.6. Calculated minus experimental logarithmic mean temperature difference versus the difference between outlet water temperature and evaporating temperature (at outlet refrigerant pressure) for 12 kW, 22 kW, 40 kW, 120 kW heat exchanger.

From Figure 5.6 one can see that this model predicts higher logarithmic mean temperature difference when the difference between outlet water temperature and evaporating temperature (at outlet refrigerant pressure) is below 3 K. It must be considered that this means predicting a lower evaporating temperature than the experimental value, thus being conservative in the final evaporation temperature estimation.

5.3 Water to refrigerant condenser

5.3.1 Description of the model

From the measurement of the heat transfer coefficient, the best predictive correlations where chosen to predict the behaviour of these heat exchangers.
A numerical model have been developed to simulate the performance of a condenser working with bar and plate heat exchangers.

The numerical model takes as input:

- The heat flow rate at the condenser;
- The subcooling at the outlet of the condenser;
- The refrigerant mass flux;
- The inlet and outlet water temperature;
- The geometry of the heat exchanger.

Similarly to the evaporator model, the heat transfer coefficient on the water side is considered constant in all the heat exchanger, while on the refrigerant side the variation of the HTC requires a distinction of different regions in the heat exchangers. The present model divides the total length of the heat exchanger into four main sections, as shown in Figure 5.7: de-superheating with dry wall, desuperheating with condensation, saturated condensation and subcooling.

In the four regions different heat transfer processes occur, as listed below:

1. When superheated vapour coming from the compressor enters the condenser, desuperheating occurs if the wall temperature is higher than the saturation one. Here, single phase heat transfer takes place and single phase correlations are used. (In all the experimental data used for validation, condensation starts immediately, thus this section length is zero);
2. When the wall temperature is below the saturation temperature, condensation starts even if the vapour is superheated. The condensation heat transfer coefficient is predicted using a model for condensation combined with a model for single phase heat transfer;
3. In the third region we have pure condensation. This section is divided into ten equal parts to increase the accuracy of the calculations, because of the strong dependence of vapour quality on HTC;
4. The last region accounts for the subcooling process, for which single-phase heat transfer correlations are implemented.

The numerical model is based on the logarithmic mean temperature difference method, thus it is an iterative procedure that:

- Evaluates the HTC on the water side;
- Starts with a first guess for the condensation temperature;
- Evaluates the HTC and the length of each region;
- Compares the available length with the sum of the calculated lengths;
- And eventually updates the condensation temperature in order to match the available length with the calculated one.

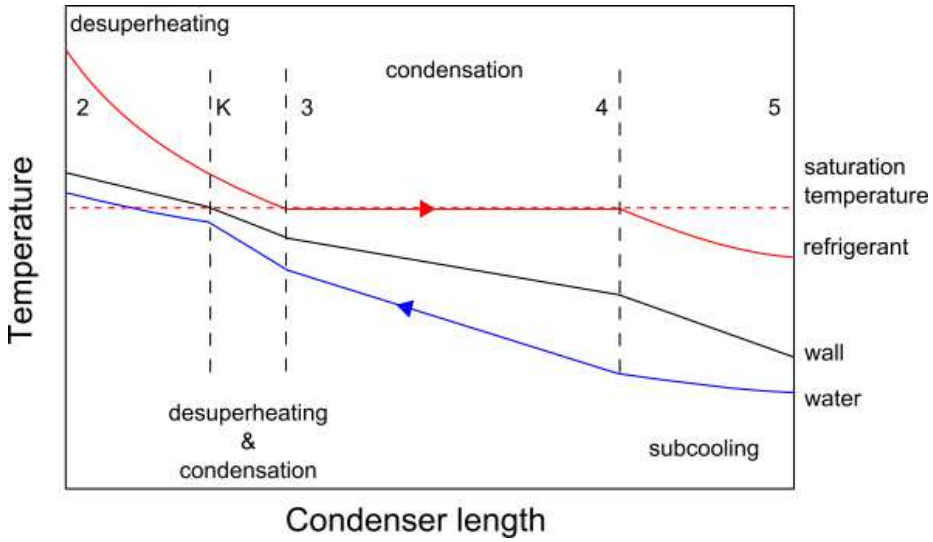

Figure 5.7. Refrigerant, wall and water temperatures along the condenser.

The thermophysical and thermodynamic properties of refrigerant and water are obtained from Refprop (NIST).
The model returns as results:

- The condensing temperature;
- Water flow rate;
- The heat flux actually exchanged in each section of the heat exchanger;
- The temperature profile of the refrigerant along the heat exchanger;
- The overall heat transfer coefficient;
- The heat transfer coefficient on the refrigerant and water side;
- The pressure drop on the refrigerant and water side.

At first, the model calculates the water mass flow rate required to exchange the nominal heat flow rate considering the input values of water temperature:

$$m_w = \frac{Q_{cond}}{c_w \left(t_{w,out} - t_{w,in} \right)} \tag{5.13}$$

Then the model calculates the HTC on the water side.
The condensation temperature is modified as reported in Eq. (22) at the end of every iteration until the condenser required length differs from the effective length less than 0.1%.

$$t_{cond,new} = t_{w,ave} + \left(t_{cond} - t_{w,ave} \right) \frac{L_{calc}}{L_{tot}} \tag{5.14}$$

The thermodynamic conditions at the condenser outlet are given by the saturation temperature and the subcooling. The conditions at inlet are calculated from:

$$h_{in} = h_{out} + \frac{Q_{cond}}{m_r} \tag{5.15}$$

The program is developed for a condenser working with superheated vapour at the inlet, thus if the calculated enthalpy at the inlet is lower than that of saturated vapour at the same pressure the program returns an error message. Otherwise, if this value is too high, the inlet temperature at the condenser section could be too high: the program returns an error message if the inlet temperature is higher than 140°C.
The program then calculates the wall temperature at inlet as

$$t_{wall,in} = t_{w,in} + \frac{K_w}{HTC_w}\left(t_{r,in} - t_{w,in}\right) \tag{5.16}$$

Where the global heat transfer coefficient referred to the heat exchange area on the water side is calculated as:

$$K_w = \left(\frac{S_w}{HTC_{r\_sp}\, S_r} + \frac{1}{HTC_w}\right)^{-1} \tag{5.17}$$

If the wall temperature is higher than the saturation temperature there is a first section of the condenser with single phase heat exchange on both sides. In order to evaluate the length of this section the program has to calculate the corresponding HTC and heat flow rate. Thus, the program evaluates these quantities starting from the following two equations:

$$m_r c_r \left(t_{r,in} - t_{r,k}\right) = m_w c_w \left(t_{w,out} - t_{w,k}\right) \tag{5.18}$$

$$HTC_w \left(t_{cond} - t_{w,k}\right) = HTC_{r\_sp} \left(t_{r,k} - t_{cond}\right) \tag{5.19}$$

The subscript 'k' indicates the point of the condenser where the wall temperature is equal to the saturation temperature.
From the previous two equations it is possible to determine the temperature of water and refrigerant at the point 'k' and then the heat flow rate of this section (Q_{des}). Hence, the desuperheating length is evaluated with Eq. (5.20):

$$L_{des} = \frac{Q_{des}\, L_{tot}}{K_w\, S_w\, LMTD_{des}} \tag{5.20}$$

In the following section, if the wall temperature is lower than the saturation temperature, condensation occurs on the wall surface. If the wall temperature at inlet is already lower than saturation temperature, point 'k' corresponds to the inlet of the condenser and the desuperheating length.
For each subsection, a mean logarithmic temperature difference between refrigerant and water is calculated. In the sections were some condensation occurs, the temperature difference is calculated using the condensing temperature for the refrigerant. This method is used even in the section where the refrigerant is superheated. However, since this assumption is made for simplification, it may not be acceptable when the vapour is highly superheated in comparison to the saturation to wall temperature difference.
For each section, the pressure variation of the fluid is also evaluated as the sum of three contributions: momentum, gravity and friction.
Some simulations were performed under the same operating conditions as in the experimental tests carried out in the laboratories of Blue Box / Swegon to validate the model.

The parameter chosen to compare the experimental tests with the model prediction is the logarithmic mean temperature difference between water and refrigerant:

$$LMTD = \frac{\left(T_{w,out} - T_{w,in}\right)}{\ln\left(\frac{T_{cond} - T_{w,in}}{T_{cond} - T_{w,out}}\right)} \tag{5.21}$$

where T_{cond} is the dew temperature at the pressure of the inlet of the condenser.

Heat transfer on water side

The HTC on the water side is considered to be constant along the heat exchanger and is evaluated from the single phase correlation developed in Section 2.5.6.

$$HTC_w = 0.1714 Re^{0.6694} Pr^{0.3333} \tag{5.22}$$

Heat transfer on the refrigerant side

The HTC for single phase on the refrigerant side is calculated as seen in Section 2.5.6:

$$HTC_{r\_sp} = 0.0205 Re^{0.779} Pr^{0.3333} \tag{5.23}$$

5.3.2 Validation of the model

From the comparison with the experimental performance of the whole condenser (data with 12 – 240 kW heat flow rate), it results that the refrigerant mass flow rate affects the condensation heat transfer coefficient much more than what expected from the experimental results reported in Section 2.7. For this reason, it was necessary to correct the predicting correlation used in the present code. Therefore, the program uses the Cavallini et al. (2006) correlation in the following way: HTC is initially evaluated at the refrigerant mass velocity G_0=50 kg m^{-2}s^{-1} and then calculated as shown in the following equation for the actual mass velocity:

$$HTC_{cond} = HTC_{Cavallini2006\_G_0} \left(\frac{G}{G_0}\right)^{0.8} \tag{5.24}$$

The following figures show the results using the correlations presented so far and calculating the HTC in the desuperheating region in which condensation occurs with:

$$HTC_{\text{desuperheating}} = HTC_{cond}\Big|_{x=1} \tag{5.25}$$

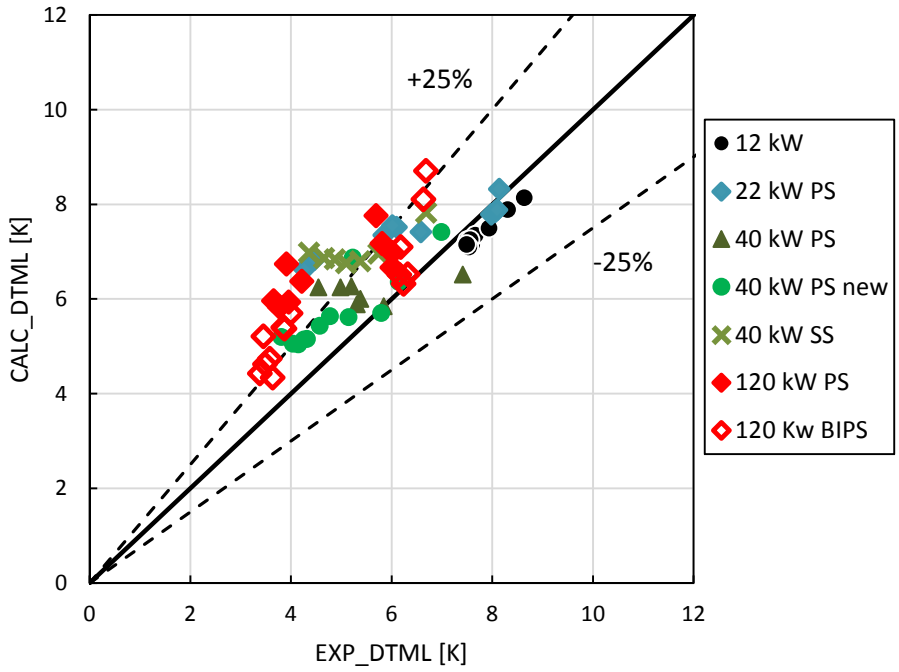

Figure 5.8. Calculated mean logarithmic temperature difference versus experimental measurements: values calculated without correction for de-superheating.

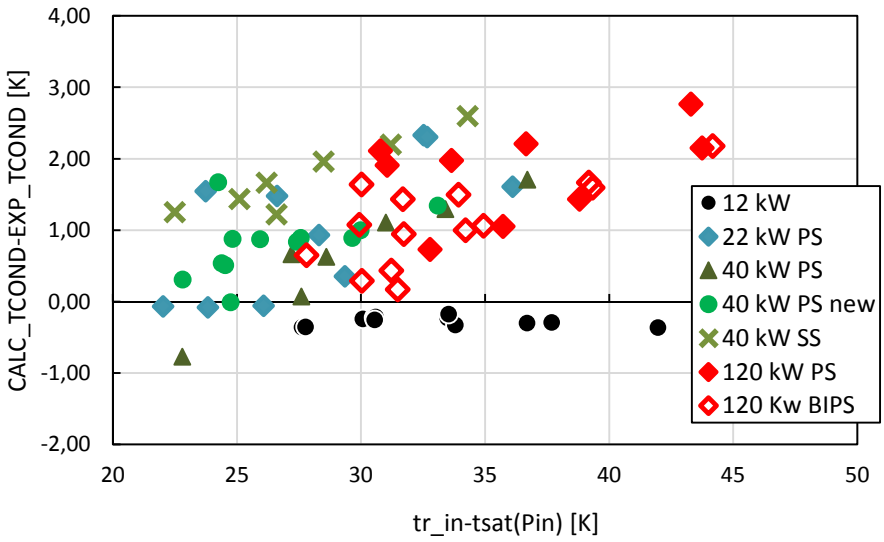

Figure 5.9. Difference between calculated and experimental condensation temperature versus superheating at the condenser inlet, without correction for desuperheating.

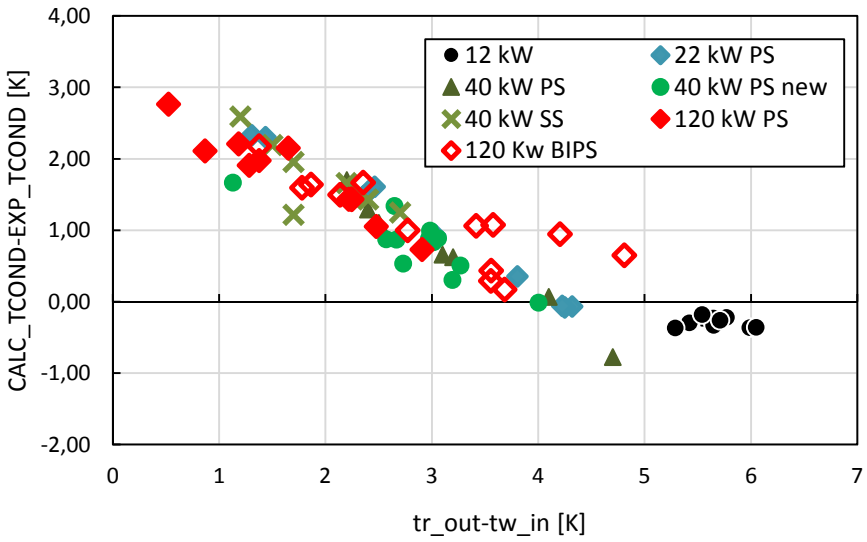

Figure 5.10. Difference between calculated and experimental condensation temperature versus temperature difference at the condenser outlet, without correction for desuperheating.

Heat transfer in the de-superheating region: Model by Webb (1998)

When condensation occurs with superheated vapour, the sensible heat must be added. The Webb correlation enhances the condensation HTC adding also the single phase HTC multiplied by the factor F, that accounts for the difference between bulk and saturation temperature.

The model presented by Webb (1998) is calculated as follows:

$$HTC_{Webb} = HTC_{cond}\big|_{x=1} + F \cdot HTC_{r\_sp} + \frac{c_r}{h_{lv}} HTC_{cond}\big|_{x=1} \left(t_r - t_{cond}\right) \tag{5.26}$$

where:

$$F = \frac{t_r - t_{cond}}{t_{cond} - t_{wall}} \tag{5.27}$$

The third part of Eq.34 accounts for the bulk convection of superheated vapour to the liquid-vapour interface.

This correlation has been implemented and the comparison with the experimental data is shown in Figure 5.11, Figure 5.12 and Figure 5.13.

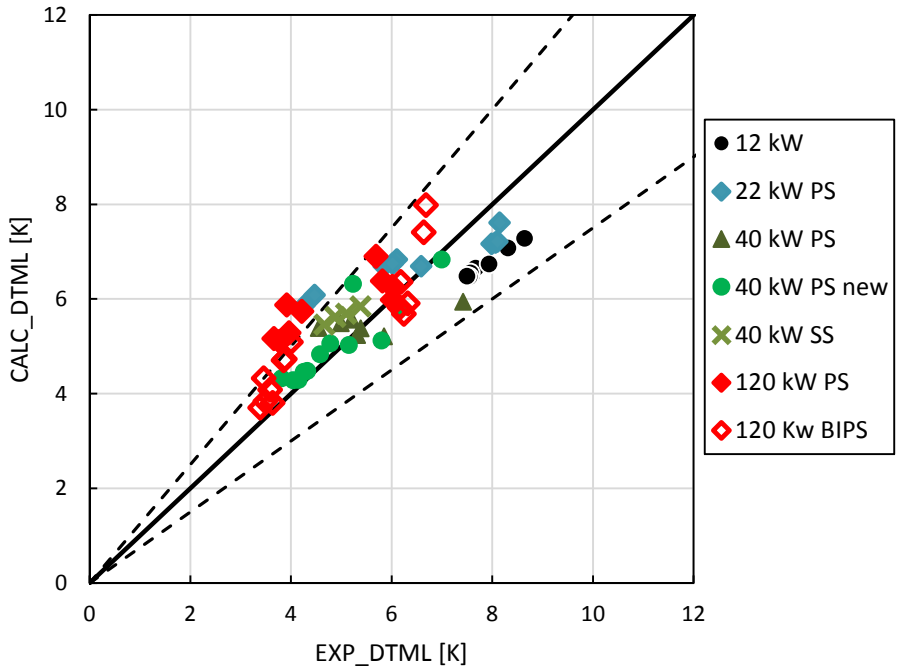

Figure 5.11. Mean logarithmic temperature difference: values calculated with Webb (1998) correction for sensible heat during desuperheating versus experimental measurements.

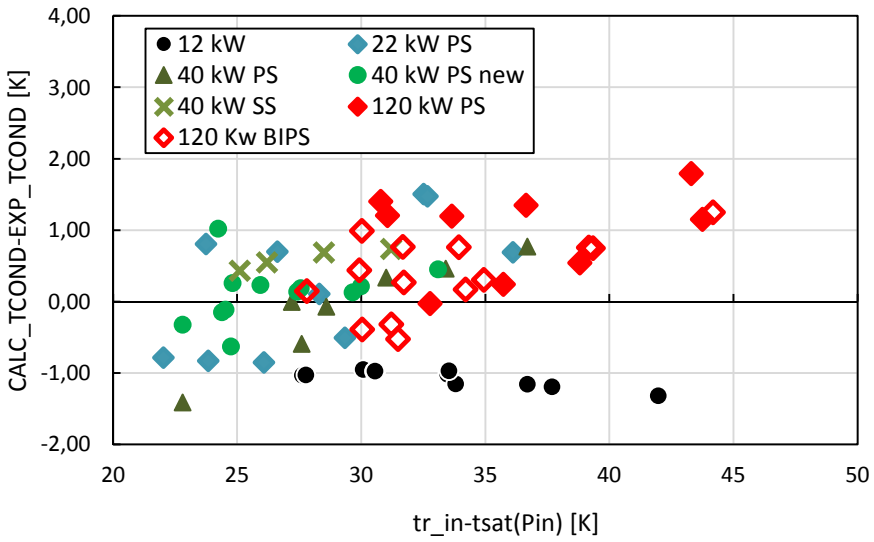

Figure 5.12. Difference between condensation temperature calculated with Webb (1998) correction for sensible heat during de-superheating and experimental temperature versus superheating at the condenser inlet.

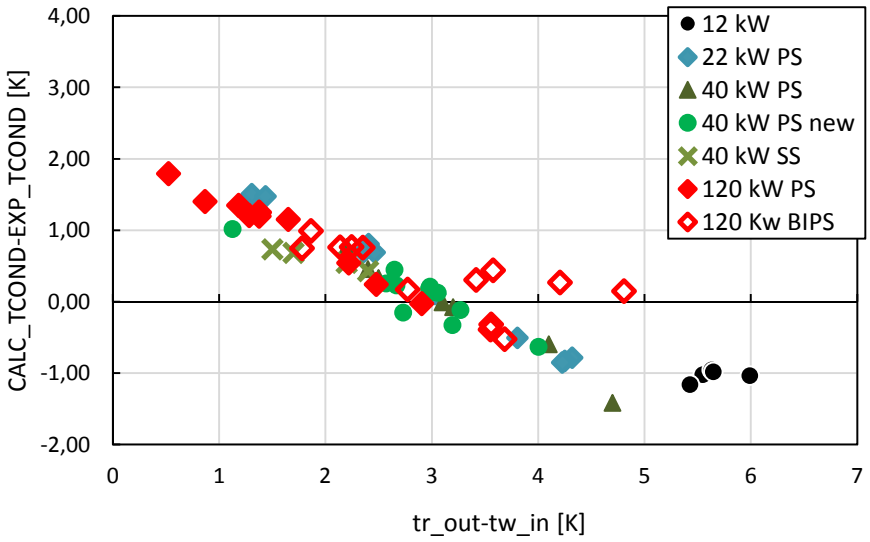

Figure 5.13. Difference between condensation temperature calculated with Webb (1998) correction and experimental temperature versus temperature difference at the condenser outlet.

Conclusions

Two different types of heat exchangers for application in refrigeration and air conditioning systems have been studied from the experimental and numerical point of view.

The first type of heat exchanger considered in the present work is a finned coil heat exchanger. Experimental tests on a finned tube heat exchanger have been carried out in the laboratory of Eurapo S.r.l. in order to validate the numerical model that has been developed to simulate these devices. The tests performed with different inclination angles highlighted that the influence of this parameter on the thermal performance of finned tube heat exchangers is limited. The main effect is related to the condensate moisture during dehumidification tests: with a tilted heat exchanger the condensate is drained slower and blocks the air passage causing higher pressure drop.

The numerical model is able to predict the behaviour of finned tube heat exchangers in which flows water or brine and it catches the dehumidification process on the air side maintaining a high level of accuracy in the prediction of the heat flow rate exchanged. The comparison with experimental data taken with 7 different finned coil heat exchangers, tested with and without dehumidification and with various speeds of the fan, shows that the model predicts the total heat flow rate of most of the data within ±6%.

A numerical model has been developed with a similar numerical approach in order to simulate a finned tube heat exchanger with vaporizing refrigerant inside the tubes. The prediction of the heat transfer coefficient of liquid water flowing in the tubes is rather simple and accurate, while the phenomena involved in the evaporating refrigerant process are more complex and they need to be carefully studied, since the heat transfer coefficient is strongly dependent on geometry, properties of the fluid, vapour quality, heat and mass flux. The developed tool is useful to design properly the evaporator of dehumidification units used to control the indoor humidity of air in winter conditions (e.g. in floor heating systems).

The second type of HX is a refrigerant-to-water minichannels HX. The experimental activity concerning heat transfer and pressure drop in bar-and-plate heat exchangers was carried out at the laboratory of the University of Padova allowing to assess the best predictive correlations to be implemented in the numerical models of evaporators and condensers.

A test section has been designed, built and instrumented for the measurement of quasi local heat transfer coefficient and pressure drop during both condensation and vaporization processes with refrigerants R1234ze(E) and R32. These two fluids are low GWP refrigerants that can have an important role in the future of refrigeration since they provide interesting thermal performance while reducing the greenhouse gas emissions. Evaporation tests showed that this kind of geometry might provide instabilities during the two phase flow leading to a limited effect of the heat flux on the heat transfer coefficient. The dryout occurs at a vapour quality of around 0.6, significantly reducing the performance of the heat transfer for higher values of vapour quality.

The condensation tests show that heat transfer coefficient decreases with vapour quality, as expected, but it is not influenced by the mass flow rate of refrigerant in the range tested. A comparison among experimental data and predicted results for condensation heat transfer coefficient and two-phase frictional pressure drop have been performed using 14 and 10 well-known prediction methods available on literature, respectively. The methods developed by Cavallini et al. (2006) and Jige et al. (2016) have provided the best predictions for heat transfer coefficient, showing

a Mean Absolute Error (MAE) = 17.7%, a percentage of data predicted within 20% ($\zeta_{20\%}$) = 62.2% and MAE = 17.5%, $\zeta_{20\%}$ = 77.6%, respectively. Additionally, the prediction methods proposed by Da Silva and Ribastki (2013) and Jige et al. (2016) have predicted the experimental results for two-phase frictional pressure drop reasonably well, with MAE = 13.1%, $\zeta_{20\%}$ = 86.7% and MAE = 11.0%, $\zeta_{20\%}$ = 94.7%, respectively. A comparison between experimental data obtained during condensation of R32 and R1234ze(E) at G=110 kg m^{-2} s^{-1} shows that R32 displays higher heat transfer coefficient than R1234ze(E) in the tested geometry by 10 to 40%. The analysis of the heat transfer coefficient in the superheated region shows that, when the wall temperature is lower than the saturation temperature, condensation occurs and thus the heat transfer coefficient is higher than that obtained during mere desuperheating. The correlation of Kondou and Hrnjak (2012) accounts for this effect and it is able to predict the results obtained at G=110 kg m^{-2} s^{-1}, while overestimates the results obtained at G=220 kg m^{-2} s^{-1}.

The numerical models developed for evaporators and condensers using bar-and-plate heat exchangers have been compared against experimental data of bar-and-plate heat exchangers. The comparison between the models and the experimental measurements taken in direct expansion units have pointed a fair agreement.

Nomenclature

A	flow passage area (m^2)
C	Hagen-Poiseuille constant (-)
$\dot{C}$	thermal capacity ($W\ K^{-1}$)
c_p	specific heat capacity ($J\ kg^{-1}\ K^{-1}$)
D, d_h	hydraulic diameter (m)
F_t	temperature factor (-)
f	friction factor (-)
G	mass velocity ($kg\ m^{-2}\ s^{-1}$)
G	Graetz number (-)
HTC	heat transfer coefficient ($W\ m^{-2}\ K^{-1}$)
h, i	specific enthalpy ($J\ kg^{-1}$)
j	Colburn factor (-)
L	tube length (m)
Le	Lewis number (-)
m	mass flow rate ($kg\ s^{-1}$)
N_f	number of fins (-)
N_t	number of tubes (-)
N_R	number of rows (-)
NTU	number of transfer units (-)
p	pressure (Pa)
q	heat flux ($W\ m^{-2}$)
RH	relative humidity (-)
Q	heat flow rate (W)
S	heat transfer area (m^2)
T	temperature (°C)
Ra	arithmetic mean deviation of the assessed profile according to EN ISO 4287:1998/A1 (μm)
Re	Reynolds number (-)
x	thermodynamic vapor quality (-)
u	uncertainty, velocity ($m\ s^{-1}$)
V	volumetric flow rate ($m^3\ h^{-1}$)
X_f	fin pitch (m)
X_l	longitudinal tube pitch (m)
X_t	transverse tube pitch (m)

Greek symbols

Δ	difference (-)
β	parameter in Eq.(5) (-)
ε	absolute roughness of the tube (m)
$\zeta_{20\%}$	data predicted within 20% (%)
θ	parameter in Eq.(6) (-)
θ_{ml}	logarithmic mean temperature difference (K)
η	efficiency (-)
λ	thermal conductivity ($W\ m^{-1}\ K^{-1}$)
μ	dynamic viscosity (Pa s)
ρ	density ($kg\ m^{-3}$)
τ	shear stress ($kg\ m^{-1}\ s^{-2}$)

Subscripts

a	air
al	aluminum
ave	average
e	external
EXP	experimental
i	internal
in	inlet
int	interface
L	liquid
LAT	latent
min	minimum
MAX	maximum
out	outlet
r	refrigerant
sat	saturation condition
sens	sensible
SH	superheated region
SP	single phase
subsec	referred to a single subsection
TP	two phase
v	vapour
w	water
wall	referred to aluminum wall

References

Abu Madi, M., Johns, R A. and Heikal, M. R, 1998, Performance Characteristics Correlation for Round Tube and Plate Finned Heat Exchangers, Int. J. Refrigeration, Vol. 21(7), pp. 507-517.

ARI Standanrd 410-81, 1972, Forced circulation air-cooling and air-heating coils, Air Conditioning and Refrigeration Institute.

Cabezas-Gomez, L., Navarro, H. A., Saiz-Jabardo, J. M., 2015. Thermal Performance Modeling of Cross-Flow Heat Exchangers, Springer, pp. 92-107.

Canton, P., and Fornasieri, E. , 1983, Sulla trasmittanza termica lato aria nelle batterie alettate, Condizionamento dell'aria, Riscaldamento, Refrigerazione, vol. 9, pp. 933-946.

Cavallini, A., Del Col, D., Doretti, L., Matkovic, M., Rossetto, L., Zilio, C., 2005. Condensation heat transfer and pressure gradient inside multiport minichannels. Heat Transfer Eng. 26 (3), 45-55.

Cavallini, A., Del Col, D., Doretti, L., Matkovic, M., Rossetto, L.,Zilio, C., 2006. Condensation in horizontal smooth tubes, a new heat transfer model for heat exchanger design. Heat Transfer Eng. 27 (8), 31–38.

Chisholm, D. 1967. A theoretical basis for the Lockhart-Martinelli correlation for two-phase flow. International Journal of Heat and Mass Transfer, 10 (12), 1767-1778.

Churchill, S. W., 1977. Friction factor equation spans all fluid-flow regimes, Chem. Eng. 45: 91-92.

Da Riva, E., Del Col, D., Garimella, S. V., Cavallini, A. 2012. The importance of turbulence during condensation in a horizontal circular minichannel. International Journal of Heat and Mass Transfer. 55, 3470–3481.

Da Silva, J. D., and Ribatski, G., 2013. Two-phase frictional pressure drop of halocarbons refrigerants inside small diameters tubes. Data analysis and the preposition of a new frictional pressure drop correlation. 8th International Conference on Multiphase Flow - ICMF 2013, Jeju, Korea.

Del Col, D., Azzolin, M., Bisetto, A., and Bortolin, S., 2015. Frictional Pressure Drop during Two-Phase Flow of Pure Fluids and Mixtures in Small Diameter Channels. International Journal of Chemical Reactor Engineering. 13 (4), 493-502.

Del Col, D., Bortolato, M., Azzolin, M., Bortolin, S. 2015. Condensation heat transfer and two-phase frictional pressure drop in a single minichannel with R1234ze(E) and other refrigerants. International Journal of Refrigeration. 50, 87-103.

Eckert, E. R. G., and Drake, R. M. , 1959, Heat and Mass Transfer, McGraw-Hill Inc., US.

Elmahdy, A. H., and Biggs, R. C., 1979, Finned tube heat exchanger: Correlation of dry surface heat transfer data, ASHRAE Transactions, vol. 85, pp. 262-273.

Dittus, F.W., and Boelter, L.M.K., 1985, Heat transfer in automobile radiators of the tubular type, International Communications in Heat and Mass Transfer, Volume 12, Issue 1, Pages 3-22

Fornasieri, E. and Mattarolo, L. , 1992, Scambio termico e perdite di carico lato aria nelle batterie alettate. Stato dell'arte, *La Termotecnica*, Università di Padova.

Friedel, L., 1979. Improved Friction Pressure Drop Correlations for Horizontal and Vertical Two-Phase Pipe Flow, European Two-Phase Flow Group Meeting, Ispra, June, Paper E2.

Garimella, S., 2004. Condensation Flow Mechanisms in Microchannels: Basis for Pressure Drop and Heat Transfer Models. Heat Transfer Engineering. 25 (3), 104–116.

Gnielinski, V., 1976. New equations for heat and mass transfer in turbulent pipe and channel flow, Int. Chem. Eng. 16: 359-368.

Gray, D. L. and Webb, R. L. , 1986, Heat transfer and friction correlations for plate-finned-tube heat exchangers having plain fins, In Proceedings of the 8th International Heat Transfer Conference, vol. 6, pp. 2745-2750.

Hilpert, R., 1933, Heat Transfer from Cylinders, *Forsch. Geb. Ingenieurwes*, 4:215.

Wang, H. S. and Rose, J. W. , 2011, Theory of Heat Transfer During Condensation in Microchannels, *Int. J. Heat Mass Transf.*, vol. 54, pp. 2525–2543.

Idel'chik, I. E., 1996. Handbook of Hydraulic Resistance, 3rd Ed., Begell House, New York.

JCGM, 2008. Evaluation of measurement data - Guide to the Expression of Uncertainty in Measurement, JCGM/WG 1, 134 pp.

Jige, D., Inoue, N. Koyama, S., 2016. Condensation of refrigerants in a multiport tube with rectangular minichannels. International Journal of Refrigeration. 67, 202-213.

Kondou, C., Hrnjak, P, 2012. Heat Rejection in Condensers: Desuperheating, Condensation in Superheated Region and Two Phase Zone. In: Int. Refr. And Air Conditioning Conf. at Purdue.

Lemmon, E. W., Huber, M. L., McLinden, M. O, 2013. NIST Standard Reference Database 23: Reference Fluid Thermodynamic and Transport Properties-REFPROP, Version 9.1, National Institute of Standards and Technology, Standard Reference Data Program, Gaithersburg.

Manglik, R. M., Bergles, A. E., 1995. Heat Transfer and Pressure Drop Correlations for the Rectangular Offset Strip Fin Compact Heat Exchanger, Experimental Thermal and Fluid Science 10: 171-180.

Nae-Hyun Kim, Jin-Pyo Cho, Jung-Oh Kim, Baek Youn, Condensation heat transfer of R-22 and R-410A in flat aluminum multi-channel tubes with or without micro-fins, International Journal of

Refrigeration, Volume 26, Issue 7, November 2003, Pages 830-839, ISSN 0140-7007, http://dx.doi.org/10.1016/S0140-7007(03)00049-5.

Paliwoda, A., 1992. Generalized method of pressure drop calculation across pipe components containing two-phase flow of refrigerants, Rev. Int. Froid 15(2): 119-125.

Park, I., Lee, H., Mudawar, I., 2015. Determination of flow regimes and heat transfer coefficient for condensation in horizontal tubes. Int. Journal of Heat and Mass Transfer, 80, 698-716.

Petukhov, B. S., 1970. Heat transfer and friction in turbulent pipe flow with variable physical properties, in Advances in heat transfer, vol. 6, New York, Academic Press, pp. 504-577.

Ribatski G., 2013, A Critical Overview on the Recent Literature Concerning Flow Boiling and Two-Phase Flows Inside Micro-Scale Channels, Experimental Heat Transfer, 26:2-3, 198-246, DOI: 10.1080/08916152.2012.737189.

Ribatski, G. and Da Silva, J. D., 2016. Condensation in Microchannels. Microchannel Phase Change Transport Phenomena, First Edition, 287-324.

Rich, D. G., 1973, The effect of fin spacing on the heat transfer and friction performance of multi-row, smooth plate fin-and-tube heat exchangers, ASHRAE Trans., vol. 79, pp. 137-145.

Schmidt, T. E., 1949. Heat transfer calculations for extended surfaces, Refrigerating Engineering, vol. 57, pp. 351-357.

Shah, R., K., London, A. L., 1978. Laminar Flow Forced Convection in Ducts, A Source Book for Compact Heat Exchanger Analytical Data, ACADEMIC PRESS, INC., New York.

Shin, J. S., and Kim, M. H., (2004). An Experimental Study of Condensation.

Soliman, H., 1986. M., Mist–annular transition during condensation and its influence on the heat transfer mechanism. Int. J. Multiphase Flow, 12, (2), 277–288.

Threlkeld, J. L., 1970. Thermal Environmental Engineering, 2ed., New York USA: Prentice-Hall Inc.

Wang, H. S., Ding, J., and Rose, J. W., 2007. Heat Transfer During Annular Film Condensation in Microchannels: Calculations for R152a, R134a, R22, R410, Propane, Ammonia and Carbon Dioxide, Proceedings of the 6th International Conference on Enhanced, Compact and Ultra Compact Heat Exchanger, Potsdam, Germany. 12–16.

Wang, H.S., and Rose, J. W. (2006). Film condensation in horizontal microchannels: Effect of channel shape. International Journal of Thermal Sciences, Vol. 45, pp. 1205–1212.

Wang, J., Hihara, E., 2003. Prediction of air coil performance under partially wet and totally wet cooling conditions using equivalent dry-bulb temperature method, Int. J. Refrigeration, vol. 26, pp. 293-301.

Wang, W. W., Radcliff, T. D., Christensen, R.N., 2002. A condensation heat transfer correlation for millimeter-scale tubing with flow regime transition. Experimental Thermal and Fluid Science. 26, 473-485.

Ware, C. D. and Hacha, T. H., 1960. Heat transfer from humid air to fin and tube extended surface cooling coils, ASME Paper 60-HT-17.

Webb, R. L., 1998. Convective condensation of superheated vapor. Trans. ASME, J. Heat Transf. 120, 418-421.

Wojtan, L., Ursenbacher, T., Thome, J. R., 2005. Investigation of flow boiling in horizontal tubes: Part I – A new diabatic two-phase flow pattern map, Int. J. of Heat and Mass Transfer. 48, 2955 – 2969.

Annex A. Model for calculating pressure gradient during two phase flow

The frictional pressure gradient during adiabatic flow when the dimensionless gas velocity $J_G > 2.5$ can be calculated from Eqs. (A.1)-(A.12) (Del Col et al., 2013).

$$\left(\frac{\mathrm{d}p}{\mathrm{d}z}\right)_f = \Phi_{LO}^2 \left(\frac{\mathrm{d}p}{\mathrm{d}z}\right)_{f,LO} = \Phi_{LO}^2 \frac{2 f_{LO} G^2}{D_h \rho_L} \tag{A.1}$$

The liquid-only friction factor is evaluated as follows:

$$f_{LO} = 0.046\left(\mathrm{Re}_{LO}\right)^{-0.2} + 0.7 RR \cdot X \tag{A.2}$$

In Eq. (D.2) $RR = 2Ra/D_h$ is the relative roughness of the tube. The factor X relates the effects of the wall superficial roughness to the liquid-only Reynolds number:

$$X = \begin{cases} 0 & if \quad \mathrm{Re}_{LO} \le \mathrm{Re}_{LO}^{+} \\ 1 & if \quad \mathrm{Re}_{LO} \ge 3500 \\ 1 + \dfrac{A - 0.046\,\mathrm{Re}_{LO}^{-0.2}}{0.7 \cdot RR}, & if \quad \mathrm{Re}_{LO}^{+} < \mathrm{Re}_{LO} < 3500 \end{cases} \tag{A.3}$$

$$A = 0.046\left(3500^{-0.2}\right) = 8.9938 \cdot 10^{-3} \tag{A.4}$$

Re_{LO}^{+} is the Reynolds number at which the smooth tubes friction factor (Eq. (A.2) with $RR = 0$) is equal to the one for rough tubes (Eq. (A.2)) evaluated at $\mathrm{Re}_{LO} = 3500$

$$\mathrm{Re}_{LO}^{+} = \left(\frac{A + 0.7 RR}{0.046}\right)^{-5} \tag{A.5}$$

$$\Phi_{LO}^2 = Z + 3.595 \cdot F \cdot H \cdot \left(1 - E\right)^W \tag{A.6}$$

$$W = 1.398\, p_R \tag{A.7}$$

$$Z = \left(1 - x\right)^2 + x^2 \frac{\rho_L}{\rho_V}\left(\frac{\mu_V}{\mu_L}\right)^{0.2} \tag{A.8}$$

$$F = x^{0.9525}\left(1 - x\right)^{0.414} \tag{A.9}$$

$$H = \left(\frac{\rho_L}{\rho_V}\right)^{1.132}\left(\frac{\mu_V}{\mu_L}\right)^{0.44}\left(1 - \frac{\mu_V}{\mu_L}\right)^{3.542} \tag{A.10}$$

The entrainment ratio E used in Eq. (D.6) is calculated as suggested by Paleev and Filippovich (1966)

$$\begin{cases} E = 0.015 + 0.44 \log\left[\left(\dfrac{\rho_{GC}}{\rho_L}\right)\left(\dfrac{\mu_L j_G}{\sigma}\right)^2 10^4\right] \\ E = 0 \qquad if \;\; E \le 0 \\ E = 0.95 \quad if \;\; E \ge 0.95 \end{cases} \tag{A.11}$$

The homogeneous gas core density ρ_{GC} is given by

$$\rho_{GC} = \frac{x+(1-x)E}{\frac{x}{\rho_V}+\frac{(1-x)E}{\rho_L}} \tag{A.12}$$

The model can be extended to lower vapour qualities and mass velocities (J_G < 2.5), by taking the higher value between $(\mathrm{d}p/\mathrm{d}z)_f$ evaluated through Eq. (A.1)-(A.12) and the all-liquid frictional pressure gradient $(\mathrm{d}p/\mathrm{d}z)_{f,LO}$ for the considered channel geometry.

$$\left(\frac{\mathrm{d}p}{\mathrm{d}z}\right)_{f,LO} = \frac{2 f_{LO} G^2}{D_h \rho_L} \tag{A.13}$$

$$\begin{cases} f_{LO} = 0.046\left(\dfrac{GD_h}{\mu_L}\right)^{-0.2} & if\ \mathrm{Re}_{LO} > 2000 \\ f_{LO} = \dfrac{C}{\left(\dfrac{GD_h}{\mu_L}\right)} & if\ \mathrm{Re}_{LO} < 2000 \end{cases} \tag{A.14}$$

C = 16 for circular cross section, C = 14.3 for square cross section.

The static and momentum pressure gradients can be calculated as in Eqs. (A.15-A.16).

$$\left(\frac{\mathrm{d}p}{\mathrm{d}z}\right)_{static} = \rho g \sin(\beta) \tag{A.15}$$

$$\left(\frac{\mathrm{d}p}{\mathrm{d}z}\right)_{momentum} = G^2 \frac{d}{dz}\left[\frac{(1-x)^2(1-E)^2}{\varepsilon\rho_L} + \frac{\left[x+(1-x)E\right]^2}{(1-\varepsilon)\rho_{GC}}\right] \tag{A.16}$$

The void fraction in the previous equation can be calculated using the correlation by Rohuani.

$$\varepsilon = \frac{x\rho_L}{Co\cdot(x\rho_L+(1-x)\rho_G)+(\rho_L\rho_G\cdot u_{gj})/\mathrm{G}} \tag{A.17}$$

$$Co = 1+0.2\cdot(1-x)\cdot\left[\frac{g\cdot D_h\cdot {\rho_L}^2}{G^2}\right]^{0.25} \quad \text{for } \varepsilon > 0.1,\ Co\to 0\ \ \varepsilon\to 0 \tag{A.18}$$

$$u_{gj} = 1.18\cdot(1-x)\cdot\left(\sigma\cdot g\cdot\frac{(\rho_L-\rho_G)}{{\rho_L}^2}\right)^{0.25} \tag{A.19}$$

Annex B. Evaluation of the Hagen-Poiseuille constant for the test section

The following analysis was conducted according to Shah and London (1978), in order to evaluate the Hagen-Poiseuille constant for the particular geometry tested, thus allowing to evaluate properly the friction factor in laminar flow regime presented in the experimental results.

Laminar flow in a two-dimensional stationary straight duct is designed as *hydrodynamically fully developed* when the fluid velocity distribution at a cross section is independent of the axial distance *x,* and

$$u = u(y, z) \tag{A1}$$

$$v, w = 0 \tag{A2}$$

where u is the fluid axial velocity, in x direction, y and z are Cartesian coordinates across the flow cross section, while v is the fluid velocity component in y direction and w is the fluid velocity component in z direction.

Consider a fully developed, steady-state laminar flow in a two-dimensional multiply connected stationary duct with the boundary Γ. The fluid is idealized as liquid or low-speed gas with constant fluid properties (independent of fluid temperature). Moreover, body forces such as gravity, centrifugal, Coriolis and electromagnetic do not exist. The applicable momentum equation is

$$\nabla^2 u = \frac{\partial^2 u}{\partial^2 y} + \frac{\partial^2 u}{\partial^2 z} = c_1 \tag{A3}$$

The boundary condition for the velocity problem is the no-slip condition, namely,

$$u = 0 \text{ on } \Gamma \tag{A4}$$

where c_1 is defined as a pressure drop parameter.

The pressure drop in fully developed flow is caused by the wall shear. Fluid mean axial velocity and wall shear stress are two important physical quantities in the laminar flow problem. The fluid mean axial velocity is defined as the integral average axial velocity with respect to the flow area A:

$$u_m = \frac{1}{A}\int_A u\, dA \tag{A5}$$

where the velocity distribution u for a given duct geometry is determined from the following equation

$$\tau_x = -\mu\left(\frac{\partial u}{\partial n}\right)_{w,m} \tag{A6}$$

The local wall shear stress for a Newtonian fluid flowing through the duct is expressed as the average wall shear stress with respect to the perimeter of the duct:
The flow length average wall shear stress is then defined as:

$$\tau_m = \frac{1}{x}\int_0^x \tau_x \, dx \tag{A7}$$

The ratio of wall shear stress τ to the kinetic energy per unit volume is defined as the Fanning friction factor. The peripheral average axially local Fanning friction factor in then expressed as:

$$f_x = \frac{\tau_x}{\rho u_m^2/2} \tag{A8}$$

For the case of fully developed flow through a duct, the velocity profile is invariant across any flow cross section. Consequently, the wall shear stress does not change axially, and the average friction factor is the same as the local friction factor. In this case, the constant-density pressure drop across two flow sections, separated by a distance *L*, takes the following form:

$$\frac{\Delta p}{\rho u_m^2/2} = f\frac{4L}{d_h} \tag{A9}$$

In the fully developed region, the last equation may be rearranged using the definition of Re and using the constant c_1, so that

$$f\,Re = -\frac{c_1 d_h^2}{2\,u_m} = -2\left[\frac{\partial\left(u/u_m\right)}{\partial\left(n/d_h\right)}\right] \tag{A10}$$

Also, based on the solution of the differential equation (A3), it can be shown that

$$f\,Re = C \tag{A11}$$

where *C* is a constant value dependent on the geometry of the channel cross section.
Steady state fully developed laminar flow of an incompressible fluid through a stationary circular duct is referred to as Hagen-Poiseuille flow. For a circular tube the friction factor-Reynolds number product is:

$$f\,Re = 16 \tag{A12}$$

This procedure has been used for determining the *C* constant for the inlet and outlet of the test section. A Matlab® code was written in order to solve the differential equation in Eq. (A3), with an arbitrary value of the constant c_1 and the boundary conditions given by Eq. (A4). Once the real geometry profile was imported, the partial differential equation in Eq. (A3) was resolved using finite elements method.
The resulting velocity field for the inlet section is reported in Figure B.1. The fluid mean axial velocity u_m has been calculated by Eq. (A5) and finally the friction factor-Reynolds product has been obtained by Eq. (A10) for the inlet and outlet sections.
Considering a hydraulic diameter of 1.6 mm the average coefficient C between inlet and outlet is 15.9.

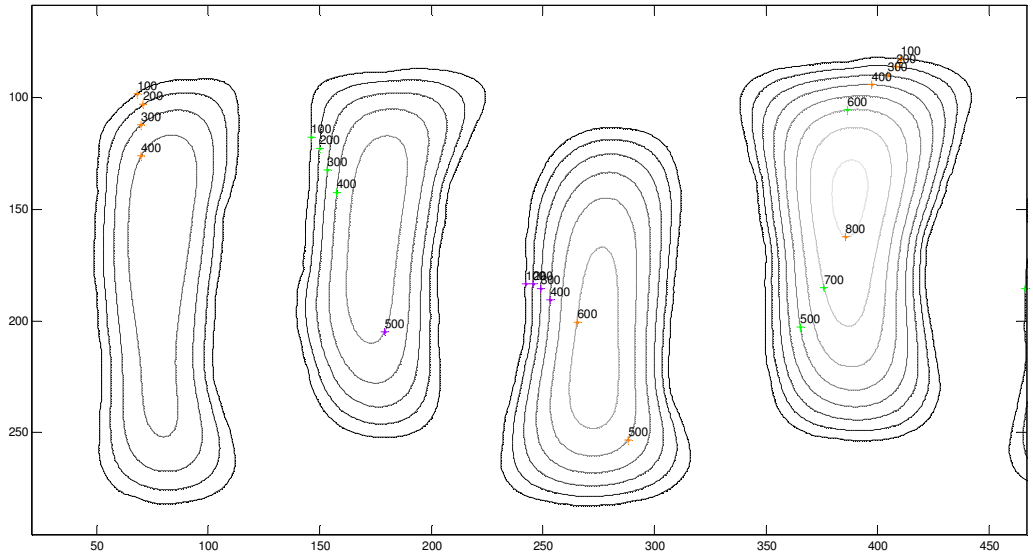

Figure B.1. Velocity profile of four representative channels of the inlet of the test section obtained through the solution of Eq.(A3). The velocity is represented in Pixels/s.

Grazie a...

...Eurapo S.r.l., per aver reso concretamente possibile questo mio percorso;
...Davide Del Col, per aver saputo creare un ambiente di lavoro allegro e stimolante;
...tutti gli altri membri dello S.T.E.T., (Stefano, Andrea, Marco, Matteo, Paolo, Alberto, Simone, David, Riccardo, Andrea), ricorderò sempre con il cuore sorridente questi tre anni trascorsi insieme;
...Jaqueline, Han, Malte, Ahmed e Phuong per avermi permesso di fare il mio periodo all'estero stando comodamente a Padova;
...tutti i laureandi che pensando di imparare da me, hanno molte volte finito per essere loro stessi ad insegnarmi qualcosa;
...i tecnici Marco Rampin e Roberto Squarcina per l'aiuto durante le prove sperimentali;
...il vecchio Leone, per aver allenato la mia pazienza e la mia capacità di ragionare;
...tutti i miei amici, per avermi dato modo di pensare anche ad altro;
...mamma, papà, Elena e Laura, per avermi saputo sempre sostenere;
...Benedetta, perché è più facile lavorare potendo ogni giorno abbracciare la propria motivazione.